RISK ANALYSIS FOR RISK INSIGHTS PROGRESS REPORT

Prepared for

U.S. Nuclear Regulatory Commission
Contract NRC–02–02–012

Prepared by

S. Mohanty, R. Benke, R. Codell,[1] K. Compton,[1] D. Esh,[1] D. Gute, L. Howard, T. McCartin,[1] O. Pensado, M. Smith, G. Adams, T. Ahn,[1] P. Bertetti, L. Browning, G. Cragnolino, D. Dunn, R. Fedors, B. Hill, D. Hooper, P. LaPlante, B. Leslie,[1] R. Nes, G. Ofoegbu, R. Pabalan, R. Rice,[2] J. Rubenstone,[1] J. Trapp,[1] B. Winfrey, L. Yang

[1]U.S. Nuclear Regulatory Commission
[2]Consultant

Center for Nuclear Waste Regulatory Analyses
San Antonio, Texas

May 2005

The MECHFAIL module (Gute, et al., 2003), as implemented in the latest version of the TPA code, includes three mechanisms. These mechanisms, which may cause the drip shield to transmit rockfall loads to the waste package, are buckling, creep, and discrete rock block impacts. To account for the three mechanisms, the MECHFAIL module uses TPA code input parameters that are dependent on the drip shield design. The TPA code input parameters utilized in this analysis are appropriate for the CRWMS M&O (2000a) drip shield design.

The first MECHFAIL module mechanism that may cause the drip shield to interact with the waste package is buckling under accumulated rockfall rubble loads. The amount of accumulated rockfall rubble load that may cause the drip shield to buckle is estimated to be strongly dependent on the amount of additional structural support provided by the rockfall rubble that has accumulated on the sides of the drip shield. Because the amount of additional drip shield structural support is expected to exhibit significant spatial variation, the drip shield buckling load distribution is a TPA code input parameter appropriate for the drip shield design (CRWMS M&O, 2000a) evaluated in this analysis.

Creep of the drip shield materials caused by the stresses created by the accumulation of rockfall rubble is the second mechanism accounted for in the MECHFAIL module that may cause the drip shield to transmit accumulated rockfall rubble loads to the waste package. The amount of rockfall rubble, which may be needed to create stresses exceeding the creep initiation threshold, is strongly dependent on the drip shield design (CRWMS M&O, 2000a) and its buckling load. The TPA code input parameters for this potential failure mode are incorporated in the parameters for buckling.

The third potential drip shield failure mechanism evaluated within the MECHFAIL module is impacts from individual rock blocks that have been dislodged from the drift ceiling. For this analysis, the occurrence of discrete rock blocks of sufficient size to damage the drip shield and, possibly, the waste package is estimated to be limited to the nonlithophysal rock unit. Because (1) the nonlithophysal rock unit is estimated to represent approximately 15 percent of the repository footprint and (2) the percentage of this rock unit comprised of individual rock blocks of sufficient size to compromise the drip shield is estimated to be small, this potential drip shield failure mechanism is likely to have a negligible affect on engineered barrier system performance. The TPA code input parameters for this failure mechanism control the occurrence, spatial extent, and size of discrete rock blocks for the drip shield design (CRWMS M&O, 2000a) evaluated in this analysis.

In the MECHFAIL module, any increases in the accumulated rockfall rubble loads created by a seismic event are considered as well. Potential interactions between the drip shield and waste package are only assessed when it has been determined the drip shield (CRWMS M&O, 2000a) has either buckled or experienced creep failure after being subjected to accumulated rockfall rubble loads. The MECHFAIL module in the latest version of the TPA code does not consider either drip shield and waste package corrosion or reduced drip shield and waste package mechanical properties for temperatures greater than 150 °C [300 °F]. The rationale and methodologies used for accommodating the temporal, spatial, and magnitude variabilities of the accumulated rockfall rubble loads are documented in Gute, et al. (2003). It should be noted that the allowable waste package deflection/penetration depth is uncertain. Also, note that the effects of accumulated rockfall rubble on the near-field temperature are addressed in Chapter 11.

ABSTRACT

The U.S. Nuclear Regulatory Commission (NRC) staff and their technical support contractor, the Center for Nuclear Waste Regulatory Analyses (CNWRA), conducted 12 analyses to enhance the staff understanding of specific features, events, and processes and associated uncertainties as identified in NRC (2004). The specific areas identified for these analyses include (i) repository near-field environment, (ii) extrusive volcanism, (iii) radionuclide transport in the saturated zone, and (iv) radionuclide inventory.

Analyses addressing the significance of features, events, and processes associated with the repository system near-field environment include estimates of the impact of (i) near-field chemical environments on waste package corrosion, (ii) thermohydrological (i.e., seepage and evaporative) processes in the drift, (iii) accumulated rockfall on mechanical degradation of the waste package, (iv) thermal effects resulting from accumulated rockfall on the waste package, and (v) fluoride on drip shield corrosion. Results of these analyses for 10,000 years estimate that (i) few waste package failures will occur from localized corrosion if there is no drip shield protection; (ii) better integration of seepage and evaporation may reduce waste package localized corrosion failure and radionuclide release rates; (iii) waste package failure from accumulated rockfall increases dose by a factor of nearly seven [assuming there is no localized corrosion failure and using a drip shield design from CRWMS M&O (2000)]; (iv) convection in accumulated rockfall may lower waste package temperature substantially; and (v) drip shields are not expected to fail by fluoride-enhanced corrosion.

Analyses to assist staff in understanding the significance of features, events, and processes associated with extrusive volcanism include estimates of the impact of (i) wind-field variability assumptions, (ii) ash deposition and remobilization, (iii) ash mass loading, (iv) assumptions regarding spent nuclear fuel incorporation and initial plume velocity, and (v) drift degradation on magma-waste package interactions. Results of these analyses for 10,000 years indicate (i) current assumptions for ash mass loading and wind-field speed and direction are reasonable; the assumptions have the potential to affect the dose estimate by approximately one order of magnitude, (ii) alternative mass loading reduces dose estimates by approximately a factor of two, (iii) current and alternative models for spent nuclear fuel incorporation and initial plume velocity cause only small differences in dose estimates, and (iv) no effects on the peak eruptive risk are estimated from coupling drift degradation with the number of entrained waste packages. Ash remobilization and wind variations are implemented in an alternative model.

The analysis related to radionuclide transport in the saturated zone focuses on an alternative model evaluation of radionuclide sorption via a modified response surface representation and an evaluation of modified chemistry ranges. Results based on this analysis indicate less than an order of magnitude decrease in dose estimates.

The analysis related to radionuclide inventory focuses on an evaluation of the impact of alternative models for various burnup rates of spent nuclear fuel on the radionuclide inventory. The results from this analysis indicate dose estimates increase by less than a factor of two.

These analyses are expected to support staff efforts to risk-inform the NRC prelicensing activities and interactions with the U.S. Department of Energy (DOE) and assist in preparing for review of a license application for a potential repository at Yucca Mountain, Nevada.

REFERENCES:

CRWMS M&O. "Design Analysis for the Ex-Container Components." ANL–XCS–ME–000001. Rev. 00. Las Vegas, Nevada: CRWMS M&O. 2000.

NRC. "Risk Insights Baseline Report." ML0405601620. Washington, DC: NRC. April 2004. <www.nrc.gov/waste/hlw-disposal/reg-initiatives/resolve-key-tech-issues.html>

CONTENTS

Section			Page
ABSTRACT			iii
FIGURES			ix
TABLES			xiii
EXECUTIVE SUMMARY			xv
METRIC TO ENGLISH SYSTEM CONVERSION FACTORS			xix
ACKNOWLEDGMENTS			xxi
1	INTRODUCTION		1-1
	1.1	Report Organization	1-10
	1.2	Caveats	1-10
2	ROCKFALL DAMAGE TO WASTE PACKAGE		2-1
	2.1	Background and Purpose	2-1
	2.2	Methodology	2-3
	2.3	Assumptions	2-4
	2.4	Results	2-4
	2.5	Conclusions	2-7
3	WASTE PACKAGE CORROSION AND NEAR-FIELD CHEMISTRY		3-1
	3.1	Background and Purpose	3-1
	3.2	Methodology	3-2
	3.3	Assumptions	3-7
	3.4	Results	3-8
	3.5	Conclusions	3-9
4	ASH REDISTRIBUTION AND WIND-FIELD VARIABILITY		4-1
	4.1	Background and Purpose	4-1
	4.2	Methodology	4-2
		4.2.1 Conditional Dose Analysis	4-3
		4.2.2 Probability-Weighted Dose Analysis	4-3
	4.3	Assumptions	4-5
		4.3.1 Conditional Dose Analysis	4-5
		4.3.2 Probability-Weighted Dose Analysis	4-6
	4.4	Results	4-6
		4.4.1 Conditional Dose Results	4-6
		4.4.2 Probability-Weighted Dose Results	4-8
	4.5	Conclusions	4-10
5	RESUSPENSION OF VOLCANIC ASH		5-1
	5.1	Background and Purpose	5-1
	5.2	Methodology	5-2
	5.3	Assumptions	5-4
	5.4	Results	5-7
	5.5	Conclusions	5-9

CONTENTS (continued)

Section			Page
6	ASH REMOBILIZATION MODELING FOR EXTRUSIVE VOLCANISM		6-1
	6.1	Background and Purpose	6-1
	6.2	Methodology	6-2
		6.2.1 Subtask 1—Alternative Model	6-2
		6.2.1.1 Contribution from the Initial Deposit at the Receptor Location	6-7
		6.2.1.2 Contribution from Fluvial Remobilization	6-9
		6.2.1.3 Contribution from Eolian Remobilization	6-11
		6.2.1.4 Execution of the Modified TPA Code	6-12
		6.2.2 Subtask 2—Detailed Analyses for Generating Data for the Alternative Model and Obtaining Risk Insights	6-13
	6.3	Assumptions	6-15
	6.4	Results	6-16
	6.5	Conclusions	6-16
7	CREDIT ATTRIBUTED TO ALLUVIUM		7-1
	7.1	Background and Purpose	7-1
	7.2	Methodology	7-2
		7.2.1 Subtask 1—Evaluate the Effect of Modifications Made to the Implementation of the TPA Code Data File	7-2
		7.2.2 Subtask 2—Verify Modified TPA Code Parameter Ranges Used to Determine the Neptunium Retardation Factors	7-3
		7.2.2.1 Mineral Content	7-3
		7.2.2.2 Water Chemistry	7-3
		7.2.2.3 Specific Surface Area	7-3
	7.3	Assumptions	7-4
	7.4	Results	7-4
		7.4.1 Subtask 1—Evaluate the Effect of Modifications Made to the Implementation of the TPA Code Data File	7-4
		7.4.2 Subtask 2—Verify Modified TPA Code Parameter Ranges Used to Determine the Neptunium Retardation Factors	7-5
		7.4.2.1 Mineral Content	7-5
		7.4.2.2 Water Chemistry	7-5
		7.4.2.3 Specific Surface Area	7-5
	7.5	Conclusions	7-7
8	FUEL INCORPORATION AND INITIAL PLUME VELOCITY		8-1
	8.1	Background and Purpose	8-1
		8.1.1 Part 1—Alternative Model for Incorporation of Spent Nuclear Fuel into Tephra	8-1
		8.1.2 Part 2—Alternative Model for Initial Plume Velocity	8-1
	8.2	Methodology	8-1
		8.2.1 Part 1—Alternative Model for Incorporation of Spent Nuclear Fuel into Tephra	8-2

CONTENTS (continued)

Section			Page
		8.2.1.1 Current Source Term Model	8-2
		8.2.1.2 Alternative Conceptual Source Term Model	8-3
	8.2.2	Part 2—Alternative Model for Initial Plume Velocity	8-6
8.3		Assumptions	8-8
	8.3.1	Part 1—Alternative Model for Incorporation of Spent Nuclear Fuel into Tephra	8-8
	8.3.2	Part 2—Alternative Model for Initial Plume Velocity	8-9
8.4		Results	8-9
	8.4.1	Part 1—Alternative Model for Incorporation of Spent Nuclear Fuel into Tephra	8-9
	8.4.2	Part 2—Alternative Model for Initial Plume Velocity	8-11
		8.4.2.1 Tephra Deposition on Ground Surface	8-11
		8.4.2.2 Estimated Peak Dose	8-14
8.5		Conclusions	8-14
	8.5.1	Part 1—Alternative Model for Incorporation of Spent Nuclear Fuel into Tephra	8-16
	8.5.2	Part 2—Alternative Model for Initial Plume Velocity	8-17
9		HIGH BURNUP SPENT NUCLEAR FUEL	9-1
9.1		Background and Purpose	9-1
9.2		Methodology	9-2
9.3		Assumptions	9-4
9.4		Results	9-4
9.5		Conclusions	9-5
10		NATURAL BACKFILL AND IGNEOUS CONSEQUENCES	10-1
10.1		Background and Purpose	10-1
10.2		Methodology	10-2
	10.2.1	Estimate of the Fraction of Waste Packages Buried by Natural Backfill	10-2
	10.2.2	Estimate Igneous Risk Curves With and Without the Effects of Natural Backfill	10-6
10.3		Assumptions	10-6
	10.3.1	Assumption 1—Degradation Rates	10-6
	10.3.2	Assumption 2—Elliptical Drift Degradation Geometry	10-6
	10.3.3	Assumption 3—1-m [3.28-ft] Minimum Degraded Void Height	10-8
10.4		Results	10-8
10.5		Conclusions	10-9
11		NEAR-FIELD TEMPERATURE AND NATURAL BACKFILL	11-1
11.1		Background and Purpose	11-1
11.2		Methodology	11-2
	11.2.1	Determination of the Heat Transfer Regime	11-2
	11.2.2	Estimation of Natural Backfill Permeability	11-3
	11.2.3	Determining the Significance of the Convection Regime	11-5

CONTENTS (continued)

Section			Page
		11.2.4 Temperature Calculation	11-6
		11.2.5 Implementation in the TPA Code	11-8
	11.3	Assumptions	11-8
		11.3.1 Heat Transfer Assumptions	11-8
		11.3.2 Geometric Simplifications	11-8
		11.3.3 Backfill Material Assumptions	11-9
	11.4	Results	11-10
		11.4.1 Air Flow Characteristics of the Natural Backfill Material	11-10
		11.4.2 Temperature Calculations	11-13
		11.4.3 Dose Consequence Calculations	11-15
	11.5	Conclusions	11-17
12		NEAR-FIELD THERMAL, HYDROLOGICAL, AND CHEMICAL INTEGRATION	12-1
	12.1	Background and Purpose	12-1
	12.2	Methodology	12-1
	12.3	Assumptions	12-2
	12.4	Results	12-2
	12.5	Conclusions	12-5
13		DRIP SHIELD AND FLUORIDE	13-1
	13.1	Background and Purpose	13-1
	13.2	Methodology	13-2
		13.2.1 Water Mass Balance	13-4
		13.2.2 Fluoride Mass Balance	13-4
		13.2.3 Solution Algorithm	13-6
	13.3	Assumptions	13-7
	13.4	Results	13-8
		13.4.1 Example 1—Detailed Results	13-9
		13.4.2 Example 2—Monte Carlo Analysis for a Range of Input Parameters	13-9
		13.4.3 Example 3—Higher Evaporation and Reflux Plus Infiltration	13-12
		13.4.4 Example 4—Maximum Fluoride Concentration Allowed to Reach 0.18 mol/L	13-12
	13.5	Conclusions	13-14
14		CONCLUSIONS	14-1
15		REFERENCES	15-1
APPENDIX A		DERIVATION OF THE DRIP SHIELD AND WASTE PACKAGE INTERACTION CONTACT AREA	A–1

FIGURES

Figure		Page
2-1	Estimated Total Effective Dose Equivalent (TEDE) with Localized Corrosion Averaged Over 450 TPA Code Realizations	2-6
2-2	Estimated Total Effective Dose Equivalent (TEDE) with Localized Corrosion Eliminated Averaged Over 450 TPA Code Realizations	2-6
2-3	Mean Number of Estimated Waste Package Failures with Localized Corrosion Averaged Over 450 Realizations	2-7
2-4	Mean Number of Estimated Waste Package Failures with Localized Corrosion Eliminated Averaged Over 450 Realizations	2-8
3-1	Comparison of Computed Corrosion Potential (Continuous Line) As a Function of pH and Temperature to Experimental Data (Diamonds)	3-4
3-2	Estimated Cumulative Distribution Functions (CDFs) for (a) Relative Humidity at 100 °C [212 °F] Waste Package Temperature, Derived from 100 Realizations	3-6
3-3	Estimated Cumulative Distribution Function (CDF) of Times at Which the Waste Package Temperature Reaches 100 °C [212 °F]	3-8
4-1	Sensitivity of Estimated Peak Conditional Dose to Initial Level and Persistence of Mass Loading about Ash Blanket	4-7
4-2	Sensitivity of Estimated Peak Conditional Dose to Wind Speed and Wind Direction	4-8
4-3	Sensitivity of Estimated Peak Probability-Weighted Dose to Persistence of Ash Deposits and Mass Loadings	4-9
4-4	Sensitivity of Estimated Peak Probability-Weighted Dose and Conditional Dose to Wind Speed	4-10
4-5	Sensitivity of Estimated Peak Probability-Weighted Dose and Conditional Dose to Wind Direction	4-11
4-6	Sensitivity of Estimated Peak Probability-Weighted Dose to Dispersion of Ash Deposition	4-11
6-1	Schematic Representation of the Time Evolution of the Total Airborne Concentration of High-Level Waste at the Receptor Location	6-4
7-1	Estimated Np-237 Total Effective Dose Equivalent for Original Basecase and Modified Basecase (Modified Np-237 Ka′ Curve Fit Coefficients)	7-6
7-2	Estimated Np-237 Total Effective Dose Equivalent for Modified Basecase Including Modified pH and CO_2 and Modified Basecase	7-6
7-3	Histogram of Estimated Nonsorbing Tracer Transport Times in the Saturated Zone for Modified Basecase Including Modified Porosity Range and Modified Basecase	7-7
7-4	Estimated Np-237 Total Effective Dose Equivalent for Modified Basecase Including Modified Porosity Range and Modified Basecase	7-8
7-5	Estimated Np-237 Total Effective Dose Equivalent for Modified Basecase Including All Parameter Changes (pH, CO_2, and Porosity) and Modified Basecase	7-8
8-1	Probability Density Functions for Median Tephra and Course and Fine Fuel Particle Diameters. Tephra Cutoff is Maximum Tephra Particle Size Use in Calculations	8-4

FIGURES (continued)

Figure		Page
8-2	Estimated Particle Density Distribution for Median Dose Vector and Coarse Fuel Distribution	8-12
8-3	Estimated Peak Dose for 100 Vectors from the Alternative Model and the Current TPA Code Model for Fine Fuel Particle-Size Distribution	8-13
8-4	Estimated Peak Dose for 100 Vectors from the Alternative Model and the Current TPA Code Model for Coarse Fuel-Size Distribution	8-13
8-5	ASHPLUME Results and Cerro Negro Tephra Thickness Data for Tephra Density As a Function of Distance along the Centerline of Tephra Plume.	8-14
8-6	Areal Distribution of the Ash Thickness Computed By ASHPLUME, Using the Alternative Vent Velocity Model and β = 10	8-15
8-7	Estimated Peak Volcanic Dose for 50 Vectors Computed Using the Alternative and Current TPA Code Vent Velocity Models	8-15
8-8	Estimated Mean Doses for 500 Years from ASHPLUME Computed Using the Alternative and Current TPA Code Vent Velocity Models	8-16
9-1	ORIGEN-ARP Code Version 2.00 Radionuclide Inventory Showing Decay of 65-GWd/MTU Fuel Throughout 10,000 Years from Reactor	9-3
9-2	High Burnup Fuel Decay Heat Comparison—ORIGEN-ARP Code Version 2.00-Calculated Values, TPA Code Profile, and Data Extracted	9-6
10-1	Cross-Sectional View of the Emplacement Drift Showing the Minimum Area of Rock Debris Required to Fill the Voids on the Sides of the Drip Shield	10-5
10-2	Unburied Fraction of Waste Packages As Estimated by the Numerical Model for Drift Degradation	10-9
10-3	Estimated Contributions to Eruptive Risk with an Annual Volcanic Probability of 10^{-7} (a) Neglecting Natural Backfill and (b) Accounting for Natural Backfill	10-10
10-4	Estimated Effect of Natural Backfill on the Eruptive Risk With an Annual Volcanic Probability of 10^{-7} for the Alternative Model with Dog-Leg Flow	10-11
11-1	Equivalent Drift Radius and Backfill Radius As a Result of Drift Degradation and Natural Backfilling of the Drift	11-9
11-2	Schematic Showing (a) Natural Backfilling from Drift Degradation and (b) Idealization of Natural Backfilling for Computing Heat Transfer	11-10
11-3	Estimated Variation in Waste Package Surface Temperature at Different Mean Particle Diameters of the Natural Backfill	11-14
11-4	Estimated Variation in Waste Package Surface Temperature at Different Porosities of the Natural Backfill	11-14
11-5	Estimated Evolution of Waste Package Temperature for Subarea 1 As a Function of Various Assumptions Regarding Heat Transfer in the Natural Backfill	11-16
11-6	Estimated Average, Minimum, and Maximum Waste Package Surface Temperatures for Subarea 1 from 450 Monte Carlo Realizations	11-16
11-7	Estimated Expected Groundwater Dose As a Function of Time for Various Heat Transfer Assumptions in the Natural Backfill	11-17

FIGURES (continued)

Figure		Page
12-1	Selected Environmental Variable Response (Realization 1)	12-3
13-1	Schematic Showing a Dent on the Crest of the Drip Shield	13-3
13-2	Evaporation Rates of Water from a Drip Shield Dent in 10,000 Years	13-5
13-3	Estimated Infiltration and Reflux Rate of Water to a Drip Shield Dent in 10,000 Years	13-5
13-4	Drip Shield Corrosion Rate As a Function of Fluoride Concentration	13-7
13-5	Estimated Water Surface Area of a Drip Shield Dent in 10,000 Years	13-10
13-6	Estimated Fluoride Concentration in a Drip Shield Dent in 10,000 Years	13-10
13-7	Estimated Drip Shield Corrosion Rate from Fluoride in 10,000 Years	13-11
13-8	Estimated Corroded Thickness of the Drip Shield in 10,000 Years As a Function of Input Concentration of Fluoride with No Reconcentration of Infiltrating Water	13-12
13-9	Estimated Corroded Thickness of the Drip Shield in 10,000 Years As a Function of Input Concentrations of Fluoride with High Evaporation and Reflux	13-13
13-10	Estimated Drip Shield Corrosion Thickness in 10,000 Years for an Upper Internal Fluoride Concentration Limit of 0.18 Molar	13-13
A–1	Drip Shield Bulkhead Contact with the Waste Package Outer Barrier, x-y Plane	A–2
A–2	Drip Shield Bulkhead Contact with the Waste Package Outer Barrier Showing the Bulkhead Penetration into the Barrier, y-z Plane	A–2

TABLES

Table		Page
1-1	Description of Analyses, Significance to Waste Isolation, and Results	1-2
3-1	Concentrations at 85.8-Percent Relative Humidity and 100 °C [212 °F]	3-6
4-1	Peak Conditional Dose Sensitivity Analysis Parameter Set	4-4
4-2	Peak Probability-Weighted Dose Sensitivity Analysis Parameter Set	4-4
5-1	Activity-Specific Breathing Rates, Times, and Daily Inhaled Volumes	5-3
5-2	Estimated Composite Values of Mass Loading for Outdoor Activities Assuming Fresh Ash Conditions	5-5
5-3	Estimated Composite Values of Mass Loading for Indoor Activities Assuming Fresh Ash Conditions	5-5
5-4	Estimated Composite Values of Mass Loading for Outdoor Activities Assuming Soil Conditions	5-6
5-5	Estimated Composite Values of Mass Loading for Indoor Activities Assuming Soil Conditions	5-6
5-6	Estimated Daily Mass Inhaled from Outdoor and Indoor Exposures to Fresh Ash Conditions Assuming a Low Composite Mass Loading	5-8
5-7	Estimated Daily Mass Inhaled from Outdoor and Indoor Exposures to Fresh Ash Conditions Assuming a Medium Composite Mass Loading	5-8
5-8	Estimated Daily Mass Inhaled from Outdoor and Indoor Exposures to Fresh Ash Conditions Assuming a High Composite Mass Loading	5-9
5-9	Estimated Daily Mass Inhaled from Outdoor and Indoor Exposures to Soil Conditions Assuming a Low Composite Mass Loading	5-9
5-10	Estimated Daily Mass Inhaled from Outdoor and Indoor Exposures to Soil Conditions Assuming a Medium Composite Mass Loading	5-10
5-11	Estimated Daily Mass Inhaled from Outdoor and Indoor Exposures to Soil Conditions Assuming a High Composite Mass Loading	5-10
6-1	Format for the Lookup Table Consisting of *n* Realizations of the TEPHRA Code.	6-5
6-2	Summary Table of the Input Parameters for the Alternative Remobilization Model	6-6
6-3	Modifications to Igneous Activity Parameters in the TPA Code Input File	6-14
8-1	Parameters for Vent Velocity Model	8-10
8-2	Volcanic Parameters and Probability Distributions Relevant to Source Term Models	8-11
8-3	Estimated Fraction of Fuel in Dense Tephra Particles from Alternative Model	8-12
9-1	Comparison of Calculated High Burnup Inventory to TPA Code Inventory for Nuclides Important to Long-Term Performance	9-4

TABLES (continued)

Table		Page
10-1	Input Parameters Used in the Mathematica® Simulations for Natural Backfill	10-3
10-2	TPA Code Input Parameter Values for the Two Calculational Sets	10-7
11-1	Input Parameter Names and Values	11-11
12-1	Summary of Environmental Variable Responses for the Basecase TPA Code	12-4
13-1	Input Ranges for Monte Carlo Runs with All Distributions Uniform	13-11

EXECUTIVE SUMMARY

In support of and preparation for the regulatory review activities outlined in the Nuclear Waste Policy Act (1982), the NRC staff, with support from the Center for Nuclear Waste Regulatory Analyses (CNWRA), are conducting system-level performance assessments (Codell, et al., 1992; Westcott, et al., 1995; Mohanty, et al., 2002, 1999) to assist in their independent understanding of the important waste isolation characteristics and capabilities of the potential repository system at Yucca Mountain. Based on their experience conducting and reviewing performance assessments, staff have documented a set of system-level and detailed risk insights related to the postclosure performance of the potential geologic repository system at Yucca Mountain (NRC, 2004). This report communicates the current staff independent understanding of the significance of specific features, events, and processes to waste isolation capabilities of the potential repository system and summarizes analyses supporting the risk insights and their associated uncertainties.

This report documents 12 continued analyses that enhance the staff understanding in specific areas identified in the risk insights baseline (NRC, 2004). The analyses were intended to support the staff understanding of the impact of uncertainties associated with specific features, events, or processes identified in the risk insights baseline. The specific areas identified for these analyses include (i) repository near-field environment, (ii) extrusive volcanism, (iii) radionuclide transport in the saturated zone, and (iv) radionuclide inventory.

Five analyses were conducted to enhance the staff understanding of the repository near-field processes and their impact on waste isolation.

- An alternative model was developed to estimate the consequence of accumulated rockfall rubble from drift degradation on waste package failure. Analysis with the alternative model, which uses a drip shield design from CRWMS M&O (2000) and results in impingement of the drip shield onto the waste package with no corrosion failure, indicates estimated dose could increase by a factor of nearly seven (Chapter 2).

- The TPA code near-field model that accounts for seepage and evaporation conditions in the drift was refined to better integrate the waste package corrosion abstraction with near-field chemistry. Estimates indicate that if protection by the drip shield is ignored, a few waste packages will experience localized corrosion failures in 10,000 years (Chapter 3).

- Integration of the thermal, hydrological, and chemical model abstractions was assessed to support the analysis described in Chapter 3. Results suggest both the number of waste packages impacted by localized corrosion and radionuclide release rates may be reduced by better integration of these model abstractions (Chapter 12).

- An alternative thermal model was developed to account for conductive and convective heat transfer in accumulated rockfall rubble resulting from drift degradation. Results indicate that by including both conduction and convection, the estimated peak waste package temperature may be substantially lower than the previously estimated temperature of 351 °C [664 °F], which was calculated assuming conduction-only heat transfer (Chapter 11).

- An alternative model was developed to account for the corrosion of titanium by dripping water containing fluoride that collects in dents on the drip shield. Results indicate that although fluoride-enhanced corrosion is expected to contribute to corrosion degradation of the drip shield, it alone will not fail the drip shield in 10,000 years (Chapter 13).

Five analyses were conducted to enhance the staff understanding of processes associated with extrusive volcanism and their associated uncertainties.

- The effects on dose estimates of current assumptions for ash redistribution, wind speed, and wind direction were evaluated. A likely bounding analysis that encompassed the uncertainties associated with these assumptions assessed more persistent mass loads and used an approach that represented a temporally variable, heterogenous wind field. Results of the analysis indicated assumptions for ash mass loading and fixed southern wind direction and wind speed are reasonable to account for ash remobilization. The assumptions have the potential to increase the estimated probability-weighted dose by approximately one order of magnitude (Chapter 4).

- To support the analyses described in Chapter 4, an alternative model was developed and detailed analytical work was conducted to account for variations in the wind speed and wind direction along the height of the tephra column and for first-order processes affecting fluvial and eolian remobilization of ash. The alternative model calculates the time history of the airborne concentrations of high-level waste at the receptor location. Results from the detailed analytical work provide input data to the alternative model (Chapter 6).

- Mass loading, related to inhalation of volcanic ash, was evaluated for both fresh ash and soil conditions. Using a wide range of surface disturbance levels and transience in mass loads, the mass loading estimates varied by approximately a factor of two. Alternative mass loading values decreased the estimated peak dose by a factor of approximately two. The analysis supported development of the alternative model and input data in Chapter 6 (Chapter 5).

- Alternative models were developed to account for the spent nuclear fuel incorporation into magma and the initial plume velocity. The alternative spent nuclear fuel incorporation model allowed a range of fuel concentrations, while the alternative plume velocity model accounted for the effects of volatile components in the magma. Results from these analyses indicate small changes in the estimated peak dose. The results support assumptions in the current TPA code models and suggest both models are likely conservative (Chapter 8).

- An analysis was conducted with an alternative model to estimate the effect of natural rockfall rubble on the spent nuclear fuel entrainment for the dog-leg flow of magma in the drift. Results indicate that natural backfill has no effect on the eruptive risk estimates for the basecase source term (i.e., a vertical conduit for magma flow). With the alternative model, whereby magma flows along a drift before continuing its vertical ascent to the surface, natural backfill has no effect on the peak of the estimated eruptive risk (peak occurs at approximately 250 years after repository closure). At times beyond 750 years, however, natural backfill results in a factor of 10 or more decrease in the estimated eruptive risk for the alternative dog-leg model compared with estimates of the eruptive risk if natural backfill is excluded (Chapter 10).

Additional analyses involved evaluating radionuclide transport in the saturated zone alluvium and the effect of higher burnup on radionuclide inventory.

- Transport in the saturated zone alluvium was analyzed with an alternative surface complexation model and with modified pH and partial pressure of CO_2 ranges. Results from the alternative model estimate less than a twofold decrease in the peak Np-237 dose in 10,000 years. Results using modified ranges for pH and partial pressure of CO_2 estimate a decrease of nearly one order of magnitude in the peak Np-237 dose in 10,000 years (Chapter 7).

- An analysis was conducted to understand the effects of variations in the degree of spent nuclear fuel burnup on radionuclide inventory and the subsequent effects on dose estimates. The calculations indicate that a change in the fuel burnup could lead to differences in the radionuclide inventory and estimate that the effects on the peak dose for the nominal scenario (i.e., no extrusive volcanism) would increase by less than a factor of two (Chapter 9).

The results of these analyses are expected to complement the risk insights baseline and assist staff in further understanding the significance of specific features, events, or processes regarding waste isolation capabilities of the potential repository system. Additionally, these results are expected to support the staff in risk-informing the ongoing prelicensing activities and interactions with DOE and other stakeholders.

REFERENCES:

Codell, R.B., N. Eisenberg, D. Fehringer, W. Ford, T. Margulies, T. McCartin, J. Park, and J. Randall. NUREG–1327, "Initial Demonstration of the NRC's Capability to Conduct a Performance Assessment for a High-Level Waste Repository." Washington, DC: NRC. May 1992.

CRWMS M&O. "Design Analysis for the Ex-Container Components." ANL–XCS–ME–000001. Rev. 00. Las Vegas, Nevada: CRWMS M&O. 2000.

Mohanty, S., R. Codell, J.M. Menchaca, R. Janetzke, M. Smith, P. LaPlante, M. Rahimi, and A. Lozano. "System-Level Performance Assessment of the Proposed Repository at Yucca Mountain Using the TPA Version 4.1 Code." CNWRA 2002-05. Rev. 1. San Antonio, Texas: CNWRA. 2002.

Mohanty, S., R. Codell, R.W. Rice, J. Weldy, Y. Lu, R.M. Byrne, T.J. McCartin, M.S. Jarzemba, and G.W. Wittmeyer. "System-Level Repository Sensitivity Analyses Using TPA Version 3.2 Code." CNWRA 99-002. San Antonio, Texas: CNWRA. 1999.

NRC. "Risk Insights Baseline Report." Rev. 00. Washington, DC: NRC. 2004.

Nuclear Waste Policy Act of 1982. Pub. L. 97–425. 96 Stat. 2201 (1982).

Wescott, R.G., M.P. Lee, N.A. Eisenberg, T.J. McCartin, and R.G. Baca, eds. NUREG–1464, "NRC Iterative Performance Assessment Phase 2." Washington, DC: NRC. October 1995.

METRIC TO ENGLISH SYSTEM CONVERSION FACTORS

The following table provides the appropriate conversion factors to allow the user to switch between the System Internationale (metric system) and the English system of measure. Not all units or methods of conversions are shown. Unit abbreviations are shown in brackets. All conversion factors are approximate. Multiply quantity in metric units by the appropriate conversion factor to obtain English unit equivalents. For additional unit conversions, refer to C.J. Pennycuick (1988).

Conversion Factors			
	To Convert	**To**	**Multiply By**
Length	Microns or micrometer [µm]*	Inches [in]*	3.9370×10^{-5}
	Microns or micrometer [µm]*	Feet [ft]*	3.2808×10^{-6}
	Millimeters [mm]*	Inches [in]*	3.9370×10^{-2}
	Millimeters [mm]*	Feet [ft]*	3.2808×10^{-3}
	Centimeters [cm]*	Inches [in]*	3.9370×10^{-1}
	Centimeters [cm]*	Feet [ft]*	3.2808×10^{-2}
	Meters [m]	Inches [in]	3.9370×10^{1}
	Meters [m]*	Feet [ft]*	3.2808
	Meters [m]	Yards [yd]	1.0936
	Kilometers [km]	Miles [mi]	6.2137×10^{-1}
Area	Square centimeters [cm^2]	Square inches [in^2]	1.5500×10^{-1}
	Square meters [m^2]*	Square feet [ft^2]*	10764×10^{1}
	Square meters [m^2]	Square yards [yd^2]	1.1960
	Square kilometers [km^2]	Square miles [mi^2]	3.8610×10^{-1}
Volume	Cubic centimeters [cm^3]	Cubic inches [in^3]	6.1024×10^{-2}
	Cubic meters [m^3]*	Cubic feet [ft^3]*	3.5315×10^{1}
	Cubic meters/year [m^3/yr]*	Cubic feet/year [ft^3/yr]*	3.5315×10^{1}
	Cubic meters [m^3]	Cubic yards [yd^3]	1.3080
	Liters [L]	Pints [pt]	2.1134
	Liters [L]	Quarts [qt]	1.0567
	Liters [L]	Gallons [gal]	2.6417×10^{-1}
Specific Surface Area	Square meters/gram [m^2/g]*	Square feet/pound mass [ft^2/lbm]*	4.8824×10^{3}
Specific Volume	Milliliters/gram [ml/g]*	Gallons/pound mass [gal/lbm]*	1.1983×10^{-1}
Velocity	Meters/second [m/s]*	Feet/second [ft/s]*	3.2808
	Centimeters/second [cm/s]	Inches/second [in/s]	3.9370×10^{-1}
	Centimeters/second [cm/s]*	Feet/second [ft/s]*	3.2808×10^{-2}
Acceleration	Meters/second [m/s^2]	Feet/second [ft/s^2]	3.2808
Mass	Milligrams [mg]*	Pounds [lb]*	2.2046×10^{-6}
	Grams [g]	Ounces [oz]	3.5274×10^{-2}
	Kilograms [kg]	Pounds [lb]	2.2046
	Metric tons [t]	Tons [long]	1.1023

Conversion Factors (continued)			
	To Convert	**To**	**Multiply By**
Density	Milligrams/cubic meter [mg/m^3]*	Pounds/cubic foot [lb/ft^3]*	6.2428×10^{-8}
	Grams/cubic centimeter [g/cm^3]*	Pounds/cubic foot [lb/ft^3]*	6.2428×10^{1}
	Grams/cubic meter [g/m^3]	Pounds/cubic foot [lb/ft^3]	6.2428×10^{-5}
	Kilograms/cubic meter [kg/m^3]*	Pounds/cubic foot [lb/ft^3]*	6.2428×10^{-2}
Force	Newton [N]	Pound-force [lbf]	2.2481×10^{-1}
	Dyne [dyn]	Pound-force [lbf]	2.2481×10^{-6}
Pressure	Pascals [Pa]*	Pounds/square inch [psi]*	1.4504×10^{-4}
	Kilopascals [kPa]*	Pounds/square inch [psi]*	1.4504×10^{-1}
	Dyne/square centimeter [dyn/cm^2]	Pound-force/square foot [lb/ft^2]	2.0885×10^{-3}
	Kilopascals [kPa]	Atmosphere [atm]	9.8692×10^{-3}
	Megapascals [MPa]*	Kilo pounds/square inch [kpsi]*	1.4504×10^{-1}
Power	Kilowatts [kW]	Horsepower [hp]	1.3405
Temperature	Celsius [°C]*	Fahrenheit [°F]*	(see footnote)†
	Kelvin [K]*	Fahrenheit [°F]*	(see footnote)‡
Temperature Difference	Celsius [°C]*	Fahrenheit [°F]*	1.8
Thermal Conductivity	Watts/(meter-K) [W/(m-K)]*	British Thermal Unit/ (hour-foot-Fahrenheit) [BTU/(hr-ft-°F)]*	5.7779×10^{-1}
Activity	Becquerels [Bq]	Curies [Ci]	2.7000×10^{-11}
Absorbed Dose	Gray [Gy]	Rad	100
Dose Equivalent	Sievert [Sv]	Rem	100
	Millisievert [mSv]*	Millirem [mrem]*	100
Permeability	Square meters [m^2]*	Darcy *	1.0133×10^{12}
	Square millimeters [mm^2]*	Darcy *	1.0133×10^{6}

*Conversions with an asterisk are used in this report.

†The formula for converting temperature in Celsius to Fahrenheit is $T_F = (1.8)T_c + 32$

‡The formula for converting temperature in Kelvin to Fahrenheit is $T_F = (1.8)(T_K - 273.15) + 32$

REFERENCE:

Pennycuick, C.J. "Conversion Factors: S.I. Units and Many Others." Chicago, Illinois: University of Chicago Press. 1988.

ACKNOWLEDGMENTS

This report was prepared to document work performed by the Center for Nuclear Waste Regulatory Analyses (CNWRA) for the U.S. Nuclear Regulatory Commission (NRC) under Contract No. NRC–02–02–012. The activities reported here were performed on behalf of the NRC Office of Nuclear Material Safety and Safeguards, Division of High-Level Waste Repository Safety. The report is a joint CNWRA and NRC project. It does not necessarily reflect the views or regulatory position of NRC.

The authors wish to thank G. Wittmeyer, R. Codell (NRC), and D. Esh (NRC) for technical reviews and A. Campbell (NRC) and B. Sagar for programmatic reviews. The authors also thank B. Goodwin for an informal review of selected chapters prior to finalization of the report. The template prepared by C. Grossman, the NRC Program Element Manager, greatly improved consistency in the presentation of information from 12 different independent teams. Thanks also are expressed to J. Danna (NRC) and G. Wittmeyer for the strong support they provided at the planning stage of this effort. Appreciation also is expressed to C. Cudd, C. Gray, and B. Long for editorial reviews and to R. Mantooth for skilled secretarial support.

QUALITY OF DATA, ANALYSES, AND CODE DEVELOPMENT

DATA: CNWRA-generated data contained in this report meet quality assurance requirements described in the CNWRA Quality Assurance Manual. Data from other sources are freely used. The respective sources of non-CNWRA data should be consulted for determining levels of quality assurance.

ANALYSES AND CODES: The TPA Version 4.1j and 5.0 codes and variations of the TPA Version 5.0 code used in the risk analyses in this report were developed according to procedures described in the CNWRA Technical Operating Procedure (TOP)–18, which implements the quality assurance requirements contained in the CNWRA Quality Assurance Manual. Some calculations documented in this report demonstrate proof of concept. Many computations resulted in modification to the TPA code. Supporting computations are implemented in software such as Microsoft® Excel 97, Mathematica® Version 4.1.0.0, ORIGEN-ARP code Version 2.00, or written as FORTRAN scripts. These computations are documented in scientific notebooks (numbers 650, 612–6E, 410, 612–8E, 631, 493, and 377) and stored in electronic form in quality assurance records for this report.

1 INTRODUCTION

In accordance with the provisions of the Nuclear Waste Policy Act (1982), the U.S. Nuclear Regulatory Commission (NRC) is responsible for evaluating any license application for a potential geologic repository constructed for the emplacement of high-level waste [e.g., commercial spent nuclear fuel; several types of U.S. Department of Energy (DOE)-owned high-level waste from the production of nuclear weapons; and spent nuclear fuel from weapon production reactors, research reactors, and U.S. Navy reactors] at Yucca Mountain, Nevada. In support of and preparation for the regulatory review activities outlined in the Nuclear Waste Policy Act, the NRC staff are conducting performance assessments to assist in their independent understanding of the important isolation characteristics and capabilities of the potential repository system at Yucca Mountain.

The performance assessment activity is part of an ongoing iterative process at NRC to prepare for the review of any DOE license application. As part of these iterative performance assessment activities, the NRC staff and their technical support contractor, the Center for Nuclear Waste Regulatory Analyses (CNWRA), have developed a system-level model, the Total-system Performance Assessment (TPA) code (Mohanty, et al., 2002a), and conducted independent system-level performance assessments, uncertainty and sensitivity analyses, and auxiliary analyses to improve understanding of the repository system (Codell, et al., 1992; Wescott, et al., 1995; Mohanty, et al., 2002b, 1999). Each iteration of the independent system-level performance assessment reflects the evolution of both the design of the potential repository and the understanding of features, events, and processes related to postclosure performance of the potential repository system gained through prelicensing issue resolution activities. These quantitative analyses support the staff in risk-informing the prelicensing interactions with DOE and other stakeholders, as well as the staff preparation for review of a potential license application.

Based on their experience conducting and reviewing performance assessments, the staff prepared a set of system-level and detailed risk insights (NRC, 2004) related to postclosure performance of the potential geologic repository system at Yucca Mountain. This NRC report communicates the current staff independent understanding of the significance of specific features, events, and processes to waste isolation capabilities of the potential repository system and summarizes analyses supporting the risk insights and their associated uncertainties.

This progress report documents continued analyses to enhance the staff understanding of specific areas identified in the risk insights baseline (NRC, 2004). The analyses described herein were intended to support staff in understanding the impact of uncertainties associated with specific features, events, or processes identified in the risk insights baseline. This progress report describes 12 analyses—most are identified in Mohanty (2003). Several analyses initially identified were combined to focus the scope of this project. Some analyses were added later to assist in understanding areas not initially identified in the original plan. Table 1-1 provides brief descriptions of these analyses, summarizes the relationship to the risk insights baseline, and reports results. The results are expected to complement the risk insights baseline and assist staff in further understanding the significance of specific features, events, or processes regarding waste isolation capabilities of the potential repository system.

Table 1-1. Description of Analyses, Significance to Waste Isolation, and Results			
Chapter	**Task Description**	**Significance** †	**Result**
2	Evaluate potential waste package mechanical failures caused by accumulated rockfall rubble load.	**Effects of Accumulated Rockfall on Engineered Barriers**: Medium Significance to Waste Isolation Mechanical loading from rockfall rubble accumulated from drift degradation over time may lead to failure of the drip shields and waste packages. The failure of the drip shields and waste packages will depend on the rate of accumulation of rockfall rubble in the drift (building static load on the drip shield) and the threshold load-bearing capacity of the drip shields and the waste packages. The accumulation of rockfall rubble in the drift outside the drip shield will also increase the waste package and drip-shield temperatures.	Using a drip shield design from CRWMS M&O (2000a), analysis estimates that an average of approximately 363 mechanically-induced waste packages failures from impingement of the drip shield onto the waste package with no localized corrosion failures results in a factor of nearly seven increase in the peak mean dose.
3	Integrate waste package corrosion abstraction and near-field chemistry.	**Persistence of a Passive Film**: High Significance to Waste Isolation The persistence of a passive film on the surface of the waste package is anticipated to result in very low corrosion rates of the waste package. High temperatures and aggressive water chemistry conditions have a potentially detrimental effect on the stability of the passive film and may accelerate corrosion over extended surface areas. **Chemistry of Seepage Water**: High Significance to Waste Isolation Evaluating the range in chemistry of water seeping into the drift and contacting the drip shield and waste package is important for determining corrosion rates of the engineered materials.	The TPA code near-field model that accounts for seepage and evaporation conditions in the drift was refined. Analysis estimates localized corrosion may affect 0.1 percent of the waste packages on mill-annealed areas and 19 percent on welded areas if drip shield protection is ignored. These estimates indicate that a few waste packages will experience localized corrosion failures in 10,000 years.

Table 1-1. Description of Analyses, Significance to Waste Isolation, and Results (continued)			
Chapter	**Task Description**	**Significance** †	**Result**
3 (continued)		**Waste Package Failure Mode**: Medium Significance to Waste Isolation The failure mode of the waste package (uniform corrosion, localized corrosion, or stress corrosion cracking) and its morphology (e.g., pits, cracks, or large corrosion holes or patches) is important for determining the amount of water that can enter the waste package.	
4	Evaluate the relative sensitivity of the peak probability-weighted dose to parameters relevant to modeling posteruption ash redistribution.	**Remobilization of Ash Deposits**: Medium Significance to Waste Isolation After a potential eruption, contaminated ash could be deposited over hundreds to perhaps thousands of square kilometers (tens to perhaps hundreds of square miles). Over time, some of this ash can be eroded and transported by wind and water, with later deposition at or near the reasonably maximally exposed individual location. An influx of remobilized ash could affect the airborne mass loads at the reasonably maximally exposed individual location, depending on the rate of remobilization and dilution with existing soils. **Wind Vectors During an Eruption**: Medium Significance to Waste Isolation Both wind speed and wind direction affect the transport of contaminated ash from the eruption source to the location of the reasonably maximally exposed individual. Wind speed has been	Sensitivity of TPA code assumptions for ash redistribution and wind-field direction was evaluated by comparing results from analyses using likely bounding assumptions for mass loads and a variable wind field. Analyses suggest that assumptions for ash mass loading and a fixed southern wind direction and wind speed are reasonable; the assumptions have the potential to affect estimates of the probability-weighted dose by approximately one order of magnitude.

Table 1-1. Description of Analyses, Significance to Waste Isolation, and Results (continued)			
Chapter	**Task Description**	**Significance** †	**Result**
4 (continued)		shown to be an influential parameter in the sensitivity studies conducted with performance assessment codes. A distribution of wind speeds appropriate to model eruption columns 2 to 7 km [1.2 to 4.4 mi] high needs to be considered. The current total system performance assessment approach also fixes the wind direction toward the reasonably maximally exposed individual to simulate potential effects of posteruption ash remobilization.	
5	Verify assumptions regarding the amount of fine ash particles resuspended in the air and the influence on estimated dose.	**Inhalation of Resuspended Volcanic Ash**: High Significance to Waste Isolation Inhalation of resuspended volcanic ash dominates the total dose for the igneous scenario. Thus, assumptions regarding the amount of fine ash particles in the air significantly influence the calculated dose. The thickness of the deposited ash layer and extent of potential mixing with the underlying soil affects the proportion of ash in the airborne particle load.	Using a wide range of surface disturbance levels and transcience in mass loads, analysis estimates mass loading changed by a factor of approximately two. Analysis with these composite mass loading estimates compared to the TPA code basecase suggests that the composite mass loading values decrease the estimated dose by a factor of approximately two.
6	Develop an alternative model to estimate the risk of extrusive volcanism, taking into account ash remobilization and assumptions of wind speed and direction.	**Inhalation of Resuspended Volcanic Ash**: High Significance to Waste Isolation Inhalation of resuspended volcanic ash dominates the total dose for the igneous scenario. Thus, assumptions regarding the amount of fine ash particles in the air significantly influence the calculated dose. The thickness of the deposited ash layer and extent of potential mixing with the underlying soil affect the proportion of ash in the airborne particle load.	An alternative model was developed for ash remobilization based on the initial deposit of ash and subsequent fluvial and eolian remobilization of ash. Detailed modeling yielded TPA code data for a lookup

Table 1-1. Description of Analyses, Significance to Waste Isolation, and Results (continued)			
Chapter	**Task Description**	**Significance** †	**Result**
6 (continued)		**Remobilization of Ash Deposits**: Medium Significance to Waste Isolation After a potential eruption, contaminated ash could be deposited over hundreds to perhaps thousands of square kilometers (tens to perhaps hundreds of square miles). Over time, some of this ash can be eroded and transported by wind and water, with later deposition at or near the reasonably maximally exposed individual location. An influx of remobilized ash could affect the airborne mass loads at the reasonably maximally exposed individual location, depending on the rate of remobilization and dilution with existing soils. **Wind Vectors During an Eruption**: Medium Significance to Waste Isolation Both wind speed and wind direction affect the transport of contaminated ash from the eruption source to the location of the reasonably maximally exposed individual. Wind speed has been shown to be an influential parameter in the sensitivity studies conducted with performance assessment codes. A distribution of wind speeds appropriate to model eruption columns 2 to 7 km [1.2 to 4.4 mi] high needs to be considered. The current total system performance assessment approach also fixes the wind direction toward the reasonably maximally exposed individual to simulate potential effects of posteruption ash remobilization. **Volume of Ash Produced by an Eruption:** Medium Significance to Waste Isolation The concentration of radionuclides in ash is affected by the volume of ash released during an igneous event. Relative to small-volume eruptions, larger-volume eruptions dilute the concentration of high-level waste in the volcanic deposit.	table and values for input parameters.

Table 1-1. Description of Analyses, Significance to Waste Isolation, and Results (continued)			
Chapter	**Task Description**	**Significance** †	**Result**
7	Reassess the credit attributed to the alluvium unit in delaying movement of sorbing radionuclides.	**Retardation in the Saturated Alluvium**: High Significance to Waste Isolation Retardation in the alluvium unit has the potential to delay the movement of most radionuclides for very long time periods (e.g., thousands to tens of thousands of years and longer) for nuclides that tend to sorb onto porous materials (e.g., Np-237, Am-241, and Pu-240). In this context, Np-237 is the most significant radionuclide affected by retardation in the alluvium because of its large inventory and long half-life. **Saturated Alluvium Transport Distance**: Medium Significance to Waste Isolation The saturated zone flow path is composed of both fractured tufaceous rock and porous alluvium. Alluvium comprising a portion of the flow path is important because of the large capacity of the alluvium to retard a majority of the radionuclides. To have a significant influence on retarded radionuclides, the alluvium needs to comprise at least 500 m [1,640 ft] of the total flow path of 18 km [11.2 mi].	Assumptions were investigated for flow path length in saturated zone alluvium and sorption coefficients, including ranges for pH and partial pressure of CO_2. Analysis indicates that the alternative surface complexation model decreases the estimated Np-237 dose in 10,000 years by less than a factor of two. Modified chemistry ranges for pH and partial pressure of CO_2 decrease the estimated Np-237 dose in 10,000 years by nearly one order of magnitude.
8	Evaluate sensitivity of the ASHPLUME model assumptions for spent nuclear fuel incorporation into tephra and initial plume velocity on dose estimates.	**Volume of Ash Produced by an Eruption**: Medium Significance to Waste Isolation The concentration of radionuclides in ash is affected by the volume of ash released during an igneous event. Relative to small-volume eruptions, larger-volume eruptions dilute the concentration of high-level waste in the volcanic deposit.	Alternative models for spent nuclear fuel incorporation into ash and for vent velocity were investigated. For either alternative model, analyses estimate a small change in the peak dose. Analyses support assumptions in the current TPA code models and suggest that both models are likely conservative.

Table 1-1. Description of Analyses, Significance to Waste Isolation, and Results (continued)			
Chapter	**Task Description**	**Significance** †	**Result**
9	Evaluate the disposal of spent nuclear fuel with a wide variation in the degree of burnup and compare peak expected dose with estimates from the use of an average representative inventory.	**Cladding Degradation**: Medium Significance to Waste Isolation Zircaloy cladding exhibits extremely low uniform corrosion rates in aqueous environments and could substantially delay the release of radionuclides from commercial spent nuclear fuel if it remains intact. Performance assessments estimate a high correlation between dose and fraction of failed cladding. Cladding, however, is thin and not physically strong. Cladding failure can occur as a result of localized corrosion, stress corrosion cracking, and hydride reorientation, under a combination of adverse environmental and stress conditions. Cladding may also fail as a result of creep caused by hoop stresses due to internal pressure or mechanically, when subjected to loads associated with seismic events and rockfall.	Analysis evaluated the effects of variations in burnup rates of spent nuclear fuel on radionuclide inventory. Results estimate a factor of less than two increase in peak dose compared with the basecase TPA inventory.
10	Evaluate the effects of natural backfill on igneous consequences.	**Number of Waste Packages Affected by an Eruption**: High Significance to Waste Isolation The consequences of extrusive igneous activity are directly proportional to the number of waste packages intersected by an erupting volcanic conduit. At present, this number is estimated based on observed conduit size at analog volcanoes. Alternative models of how a volcano may interact with repository drifts and develop a conduit could increase the number of entrained waste packages and, thus, increase the concentration of radionuclides in erupted ash.	Analysis with an alternative model for dog-leg flow of magma along a drift, which includes the effects of rockfall rubble on the entrainment of spent nuclear fuel in magma, indicates that natural backfill has no effect on the estimated peak eruptive risk. At times greater than 750 years, however, natural backfill reduces estimated eruptive risk by more than a factor of 10 compared to no natural backfill.

Table 1-1. Description of Analyses, Significance to Waste Isolation, and Results (continued)			
Chapter	**Task Description**	**Significance** †	**Result**
11	Evaluate the dose consequence of increased waste package and drip shield temperatures resulting from natural backfilling by drift degradation.	**Effects of Accumulated Rockfall on Engineered Barriers**: Medium Significance to Waste Isolation The accumulation of rockfall rubble in the drift outside the drip shield will increase the waste package and drip-shield temperatures.	Analysis using an alternative model accounting for heat transfer through the natural backfill estimates that convection in accumulated rockfall may lower waste package temperature substantially.
12	Evaluate the integration of the thermal, hydrological, and chemical abstraction models for physical consistency.	**Persistence of a Passive Film**: High Significance to Waste Isolation The persistence of a passive film on the surface of the waste package is anticipated to result in very low corrosion rates of the waste package. High temperatures and aggressive water chemistry conditions have a potentially detrimental effect on the stability of the passive film and may accelerate corrosion over extended surface areas. **Chemistry of Seepage Water**: High Significance to Waste Isolation Evaluating the range in chemistry of water seeping into the drift and contacting the drip shield and waste package is important for determining corrosion rates of the engineered materials.	Analysis addresses integration of the thermal, hydrological, and chemical environments and supports the Chapter 3 analysis that refines the near-field chemistry and waste package corrosion model. Results suggest better integration of seepage and evaporative processes may reduce waste package localized corrosion failure and radionuclide release rates.

Table 1-1. Description of Analyses, Significance to Waste Isolation, and Results (continued)			
Chapter	**Task Description**	**Significance** [†]	**Result**
13	Evaluate the potential for failure of the drip shield within 10,000 years by general corrosion caused by fluoride in infiltrating water.	**Drip Shield Integrity**: Medium Significance to Waste Isolation The integrity of the drip shield will influence the quantity and chemistry of the water that can develop on the waste package and the potential effects on corrosion modes and rates.	Analysis estimates, from an alternative model that accounts for corrosion of titanium by dripping water containing fluoride that collects in dent on the drip shield, suggest it is unlikely the drip shield will fail by fluoride corrosion alone in 10,000 years.
[†]Risk Insights Baseline Report (NRC, 2004).			

Additionally, these results are expected to support staff in risk-informing the ongoing prelicensing activities and interactions with DOE and other stakeholders.

1.1 Report Organization

Chapters 2 through 13 are organized in a consistent format. The task description, authors and contributors, background and purpose, methodology, assumptions, results, and conclusions are presented in each chapter. A summary of the conclusions is presented in Chapter 14, and the references cited throughout this progress report are provided in Chapter 15.

The background and purpose in each of these chapters present the rationales, objectives, and scopes of the tasks. The linkage of the task is shown to at least one of the following documents: Risk Insights Baseline Report (NRC, 2004), Total-system Performance Assessment (TPA) Version 4.0 Code: Module Description and User's Guide (Mohanty, et al., 2002a), System-Level Performance Assessment of the Proposed Repository at Yucca Mountain Using the TPA Version 4.1 Code (Mohanty, et al., 2002b), and relevant DOE, NRC, and CNWRA reports. The methodology section in each chapter describes the model development, if any, and execution of the analyses, which includes a description of the software, input data, and modifications to the TPA code. The assumptions and likely conservatism employed in the analysis are described in the assumptions section of each chapter to support any alternative analysis.

Each chapter includes sections with results and conclusions. Discussions of the quantitative analyses and interpretation of these analyses are provided. Details for alternative models also are provided. Outcomes include discussions of the results and the effects of uncertainty and likely conservatism of the analyses, where applicable. Some analyses provide context for understanding the likelihood that the scenario will exist or occur during the 10,000-year period. The scenario consequence and its beneficial or adverse effects regarding waste isolation capabilities of the potential repository system are described to the extent possible.

1.2 Caveats

This report provides results from various risk analyses geared toward supporting the NRC staff in understanding the effects of specific features, events, and processes regarding waste isolation capabilities of the potential repository system and the associated uncertainties. The following caveats, therefore, should be kept in mind regarding the results presented in this progress report.

- Analysts used the TPA code to perform many of the analyses. The underlying assumptions, limitations, and bases described in Mohanty, et al. (2002a) apply to these analyses. Assumptions, limitations, or bases reported in the subsequent chapters are considered to complement or supercede, when appropriate, those assumptions, limitations, or bases associated with Mohanty, et al. (2002a).

- Analyses presented in this progress report focus on improving the staff understanding of the significance and uncertainties associated with specific areas and should not be viewed as an attempt to address all uncertainties identified in NRC (2004).

- Analyses presented in this report attempt to assist staff in understanding the uncertainties associated with specific features, events, and processes related to postclosure performance of the potential repository system. Where limited information is available, the analyses attempt to likely bound the uncertainties. There may be instances, however, where several processes compete simultaneously. The employed likely conservatism, therefore, may not be readily quantifiable.

- Analyses presented in this report were conducted by independent teams of analysts; therefore, variation in the detail, focus, and format of documentation should be expected.

- The manner in which these analyses were conducted, or the assumptions and approaches used, should not be construed to express the views, preferences, or positions of the NRC staff regarding implementation of regulations at Yucca Mountain, Nevada.

2 ROCKFALL DAMAGE TO WASTE PACKAGE

TASK DESCRIPTION

Evaluate potential waste package mechanical failures caused by accumulated rockfall rubble load.

AUTHORS/CONTRIBUTORS

D. Gute, G. Adams, and L. Howard

2.1 Background and Purpose

In the Risk Insights Baseline Report (NRC, 2004), the risk insight Effects of Accumulated Rockfall on Engineered Barriers identifies potential waste package failure by way of accumulated rockfall rubble loads as having medium significance to waste isolation. Mechanical failure of the waste package by accumulated rockfall rubble adds another potential waste package failure mechanism to the TPA code. Corrosion and juvenile failures of the waste package are considered in the latest version of the TPA code.

The TPA code assesses the mechanical failure of the drip shield; however, it does not evaluate the potential effects of interactions between the drip shield and waste package during sustained accumulated rockfall rubble loads. The TPA code analyses, which use design specifications for the drip shield in CRWMS M&O (2000a)[1], estimate that approximately 70 percent of the drip shields (CRWMS M&O, 2000a) may interact mechanically with the waste package after having failed by buckling or creep within 1,000 years after closure because of accumulated rockfall rubble loads. The bulkheads and support beams of the drip shield provide the structural support of the load. Once the drip shield buckles or fails by creep, the load path changes such that the load is transferred from the bulkhead to the waste package. Therefore, this potential waste package failure mechanism was incorporated into the latest version of the TPA code as an alternative model by implementing the MECHFAIL module (Gute, et al., 2003). The purpose of this task was to evaluate the potential increase in estimated dose resulting from this potential waste package failure mechanism.

The waste package may be breached if accumulated rockfall rubble loads are transferred from the drip shield to the waste package. Because these loads may be transferred to the waste package outer barrier by way of the drip shield bulkhead, localized stresses may exceed the ultimate strength of the Alloy 22 waste package outer barrier. Potential failure of the waste package likely depends on the (i) angle of contact between the drip shield bulkhead and the waste package outer barrier, (ii) magnitude of the accumulated rockfall rubble load, (iii) ultimate strength of the Alloy 22 waste package outer barrier, and (iv) extent of plastic deformation of the Alloy 22 waste package outer barrier needed to reduce the contact stress below the yield stress threshold, which is characterized by the allowable deflection/penetration depth of the bulkhead into the outer barrier.

[1]We understand that the DOE is modifying the drip shield design to a more robust design. However, the new design was not available for these analyses.

An overview of the methodology employed to develop an alternative model that estimates the potential failure of the waste package caused by interactions with the drip shield (CRWMS M&O, 2000a) is delineated in the following section. In addition, the resulting total effective dose equivalent arising from consideration of this potential waste package failure mechanism has been estimated and is presented in subsequent sections.

2.2 Methodology

Potential waste package failures caused by interactions with drip shields (CRWMS M&O, 2000a) that have either buckled or experienced creep failure during sustained accumulated rockfall rubble loads were evaluated. These evaluations were performed with an alternative model based on Gute, et al. (2003) using a modified version of the TPA code. Development of this alternative model abstraction is provided in Appendix A. The mechanical failure code modules in the TPA code were modified to incorporate this alternative waste package failure abstraction and four parameters were added to the TPA code input:

1. ContactAngle[degrees] (distributed normally between 0.0 degrees and 45.0 degrees)

2. DeflectionDepth[m] {a constant value of 4 mm [0.15 in]}

3. BulkheadThickness[m] {a constant value of 0.038 m [1.5 in]}

4. WastePackageOuterBarrierUltimateTensileStrength[MPa] {a constant value of 679.1 MPa [98.5 kpsi]}

Within any grid element of any subarea, if the drip shield (CRWMS M&O, 2000a) fails by either buckling or creep because of accumulated rockfall rubble loads that vary spatially and temporally (Gute, et al., 2003), potential failure of the waste package is evaluated. The number of failed waste packages because of mechanical failure is summarized in the TPA code output. In addition, the estimated total effective dose equivalent is summarized in the TPA code output.

The procedure for estimating failure of the waste package is a multistep calculation. First, the contact area between the drip shield bulkhead and the waste package outer barrier is calculated. This contact area is a function of the contact angle sampled parameter and the assigned allowable deflection/penetration depth. Next, the maximum normal stress for the waste package outer barrier is calculated:

$$\text{maximum normal stress} = \frac{\text{static load acting on the drip shield}}{\text{contact area}} \qquad (2\text{-}1)$$

Afterward, the maximum normal stress is compared with 90 percent of the ultimate tensile strength of the waste package outer barrier per ASME International Boiler & Pressure Vessel Code recommendations for Level D service limits (ASME, 2001, Section III, Division 1, Appendix F), where the ultimate tensile strength is 679.1 MPa [98.5 kpsi]. If the maximum normal stress reaches or exceeds this threshold, the waste package is estimated to have a mechanical failure for that grid element within that subarea. The failure across all grid elements in all subareas is then accumulated for further analysis.

Details of the waste package failure abstraction derivation, which is based on contact angle, allowable deflection/penetration depth, and accumulated rockfall rubble load, are provided in Appendix A.

2.3 Assumptions

In this abstraction, the following assumptions were incorporated to estimate waste package failure by accumulated rockfall rubble load.

- Design specifications for the drip shield are based on CRWMS M&O (2000a).

- Negligible friction exists between the drip shield bulkhead and the waste package outer barrier.

- Contact angle can be represented by a normal distribution between 0 and 45 degrees. The angle with which the bulkhead contacts the outer barrier of the drip shield is assumed to be likely bounded between 0 and 45 degrees. This uncertainty is incorporated into the model and is accounted for in this analysis by sampling the contact angle for 450 realizations.

- Allowable deflection/penetration depth is 4 mm [0.15 in]. This assumption limits the penetration of the drip shield bulkhead into the waste package outer barrier.

The derivation for this waste package failure abstraction is included in Appendix A. The contact angle and allowable deflection/penetration depth are described as part of the derivation.

2.4 Results

The modified TPA code was executed for 450 realizations, and those results compared with basecase TPA code results. An additional sampled parameter (ContactAngle[degrees]) was added and used for both the basecase TPA code runs and the modified code TPA code runs to ensure the same Latin hypercube sample set was obtained. Thus, with this modified input, the test results from the basecase and modified codes could be compared directly.

Two sets of test runs were conducted, each containing three individual scenarios. These separate sets of test runs were performed to estimate the potential number of waste package mechanical failures with and without localized waste package corrosion failures enabled. The first test set was conducted with default input parameters and included localized corrosion failure of the waste package. The second test set was conducted with modified input parameters and eliminated localized waste package corrosion failure. Localized waste package corrosion failure was eliminated by setting ErpInterceptWeld[mVSHE] and OuterOverpackErpIntercept both to high values (1.0×10^{10}).

Three individual scenarios were conducted within each test set to estimate waste package mechanical failure. The first scenario was conducted with the basecase TPA code. The basecase TPA code accounts for drip shield (CRWMS M&O, 2000a) mechanical failure. A second scenario was conducted with the basecase TPA code; however, by modifying input parameters, mechanical failure was eliminated. Mechanical failure was eliminated by setting the drift degradation flag [DriftDegradationScenarioFlag(yes=1, no=0)] and the seismic scenario flag

[SeismicDisruptiveScenarioFlag(yes=1, no=0)] both to zero. In other words, when these flags were set to zero, the mechanical failure of the drip shield was not included as part of the TPA code execution. A third scenario was evaluated with the TPA code modified to incorporate waste package mechanical failure. In this scenario, the basecase TPA code was modified to incorporate waste package mechanical failure.

Figures 2-1 and 2-2 convey the average estimated dose for each timestep calculated from the 450 TPA code realizations performed for each of the three scenarios. Both figures show the highest estimated dose was generated from the modified code that included mechanical failure of the drip shield (CRWMS M&O, 2000a) and waste package. The second highest dose was generated from the basecase TPA code with drip shield (CRWMS M&O, 2000a) mechanical failure using the modified input. And, the lowest dose was generated from the basecase TPA code using the modified input and eliminating mechanical failure of the drip shield (CRWMS M&O, 2000a) and waste package.

As shown in Figure 2-1, results from analysis indicate drip shield (CRWMS M&O, 2000a) and waste package mechanical failures both affect the estimated dose. Mechanical failure of the drip shield (CRWMS M&O, 2000a) results in more than a factor of three increase in the estimated peak mean dose. With the addition of waste package mechanical failure to drip shield (CRWMS M&O, 2000a) mechanical failure, the estimated peak mean dose increases again, but only by 6 percent. Such a small increase may be the result of the large number of localized corrosion failures at early times. Results elsewhere in this progress report (Chapter 3) suggest the estimated number of early waste package failures from localized corrosion may be reduced, thus increasing the relative importance of waste package mechanical failure from impingement of the drip shield (CRWMS M&O, 2000a). This trend is observed in Figure 2-2, in which localized corrosion was eliminated. As shown in this figure, mechanical failure of the drip shield (CRWMS M&O, 2000a) results in a factor of 2.8 increase in the estimated peak mean dose. With the addition of waste package mechanical failure to drip shield (CRWMS M&O, 2000a) mechanical failure, the estimated peak mean dose increases by a factor of 6.9. This increase in the estimated peak mean dose suggests that mechanical failure of the waste package, from impingement of the drip shield (CRWMS M&O, 2000a), could dominate when localized corrosion is eliminated.

Figure 2-3 shows the mean number of estimated waste package failures, from impingement of the drip shield (CRWMS M&O, 2000a), versus time for the first test set, in which localized corrosion of the waste package is occurring. This figure shows the increase in the mean number of estimated waste package failures when mechanical failure, from impingement of the drip shield (CRWMS M&O, 2000a), is compared with an average of 2,233 waste packages estimated to fail by corrosion, which is an average of 280 additional failures. This change represents an increase of 12.5 percent in estimated waste package failures at 1,022 years that can be directly attributed to mechanical failure of the waste package from impingement of the drip shield (CRWMS M&O, 2000a). At 10,000 years, an average of 2,679 waste packages are estimated to fail with the addition of the alternative model accounting for waste package mechanical failure, from impingement of the drip shield (CRWMS M&O, 2000a), compared with an average of 2,407 waste packages estimated to fail by corrosion, an average of 272 additional failures. This change represents an increase of 11.3 percent in estimated waste package failures at 10,000 years that can be attributed directly to mechanical failure of the waste packages from impingement of the drip shield (CRWMS M&O, 2000a).

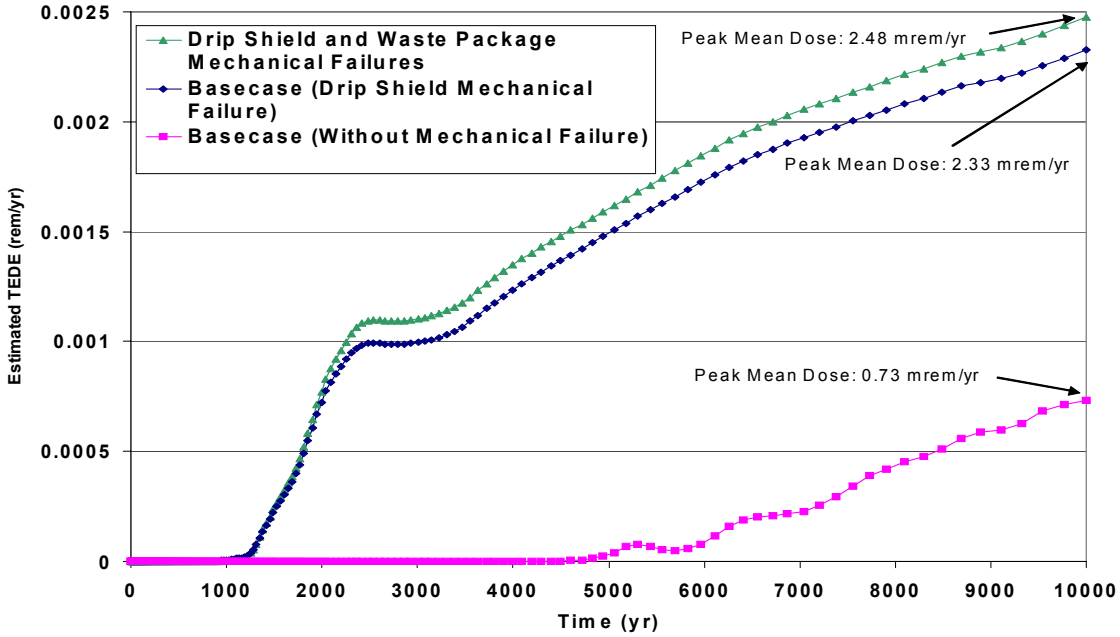

Figure 2-1. Estimated Total Effective Dose Equivalent (TEDE) with Localized Corrosion Averaged Over 450 TPA Code Realizations for the Basecase, Drip Shield (CRWMS M&O, 2000a) Mechanical Failure, and Drip Shield (CRWMS M&O, 2000a) and Waste Package Mechanical Failures

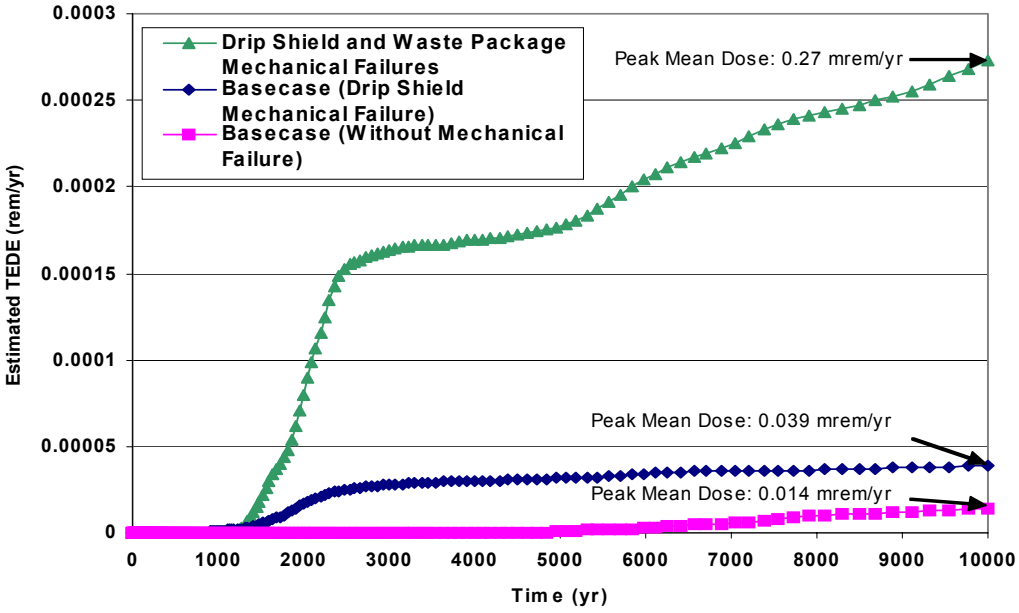

Figure 2-2. Estimated Total Effective Dose Equivalent (TEDE) with Localized Corrosion Eliminated Averaged Over 450 TPA Code Realizations for the Basecase, Drip Shield (CRWMS M&O, 2000a) Mechanical Failure, and Drip Shield (CRWMS M&O, 2000a) and Waste Package Mechanical Failures

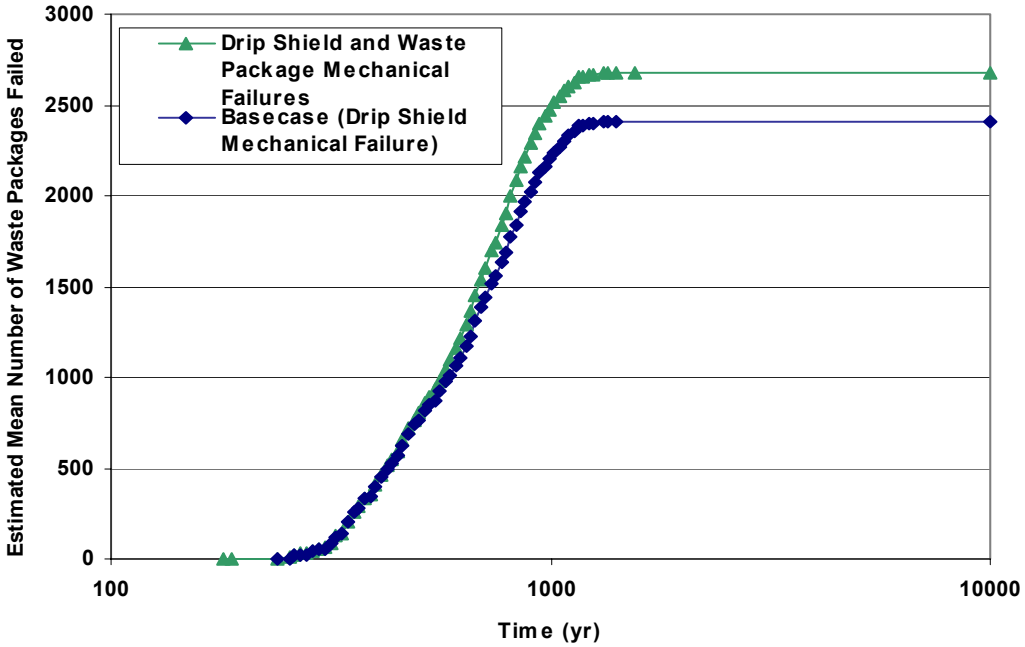

Figure 2-3. Mean Number of Estimated Waste Package Failures with Localized Corrosion Averaged Over 450 Realizations for Drip Shield (CRWMS M&O, 2000a) Mechanical Failure and Drip Shield (CRWMS M&O, 2000a) and Waste Package Mechanical Failures

Figure 2-4 shows the estimated mean number of waste package failures, from impingement of the drip shield (CRWMS M&O, 2000a), versus time for the second test run, in which localized corrosion of the waste package is eliminated. This figure, like Figure 2-3, shows the increase in the mean number of estimated waste package failures, from impingement of the drip shield (CRWMS M&O, 2000a), when mechanical failure of the waste packages is considered; however, in this case, localized corrosion is eliminated. At 1,022 years, results estimate an average of 362 waste package mechanical failures, from impingement of the drip shield (CRWMS M&O, 2000a), with an average of 363 waste package mechanical failures, from impingement of the drip shield (CRWMS M&O, 2000a), at 10,000 years. These results estimate an average of 82 more waste package mechanical failures, from impingement of the drip shield (CRWMS M&O, 2000a), at 1,022 years and 91 more waste package mechanical failures, from impingement of the drip shield (CRWMS M&O, 2000a), at 10,000 years compared to those when localized corrosion also is present.

2.5 Conclusions

An alternative model was developed in this analysis and implemented in the latest version of the TPA code to estimate potential waste package failure caused by drift degradation and subsequent impingement of the drip shield (CRWMS M&O, 2000a) onto the waste package. This waste package mechanical failure abstraction, which relies on a drip shield design from CRWMS M&O (2000a), is likely conservative for estimating the number of waste package failures. As modeled in this analysis and consistent with the abstractions of accumulated rockfall

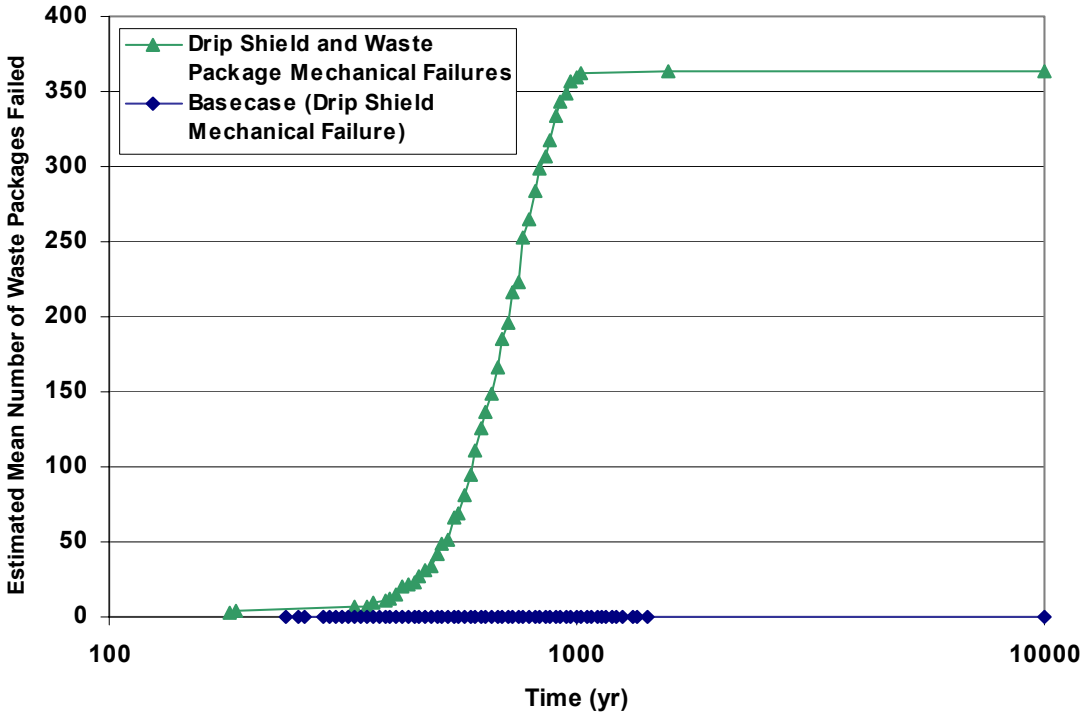

Figure 2-4. Mean Number of Estimated Waste Package Failures with Localized Corrosion Eliminated Averaged Over 450 Realizations for Drip Shield (CRWMS M&O, 2000a) Mechanical Failure and Drip Shield (CRWMS M&O, 2000a) and Waste Package Mechanical Failures

rubble loads developed by Gute, et al. (2003), results estimate that when there is no localized corrosion failure, waste package mechanical failures from impingement of the drip shield (CRWMS M&O, 2000a) may become relatively more important. In this case, an estimated average of 363 waste package failures from impingement of the drip shield (CRWMS M&O, 2000a) results in a factor of nearly seven increase in the estimated peak mean dose. The estimated peak mean dose, however, increases to only 0.27 mrem/yr [0.0027 mSv/yr].

3 WASTE PACKAGE CORROSION AND NEAR-FIELD CHEMISTRY

TASK DESCRIPTION

Integrate waste package corrosion abstraction and near-field chemistry.

AUTHORS/CONTRIBUTORS

O. Pensado, D. Dunn, L. Browning, R. Pabalan, L. Yang, and G. Cragnolino

3.1 Background and Purpose

The Risk Insights Baseline Report (NRC, 2004) deems the persistence of the passive film on the waste package surface to be of high significance to waste isolation. The persistence of a passive film on the surface of the waste package is anticipated to result in extremely low corrosion rates of the waste package. High temperatures and aggressive water chemistry conditions have a potentially detrimental effect on the stability of the passive film and may accelerate corrosion over extended surface areas. Because stability of the passive film and onset of localized corrosion depend on solution compositions, the chemistry of seepage water also is considered of high significance to waste isolation (NRC, 2004). The waste package failure mode has been deemed of medium significance to waste isolation (NRC, 2004). This task develops a refined abstraction in the TPA code that estimates the number of waste packages that may exhibit enhanced corrosion modes as a function of possible solution compositions contacting the waste packages.

The near-field model in the TPA code considers the presence of highly concentrated solutions caused by evaporation and the existence of salt systems of low deliquescence relative humidity. The corrosion potential is likely conservative with respect to experimental data. In this model, localized corrosion could be activated at high temperatures when seepage is not expected.

To investigate the near-field chemistry and waste package corrosion models, the following refinements were explored:

- Delineate the possible environments in contact with the waste package as functions of temperature, relative humidity, and drip shield failure time
- Achieve consistency between corrosion potential computations and experimental data
- Abstract the action of inhibiting oxyanions (nitrate, sulfate, and carbonate) to localized corrosion

With these abstraction refinements, computations outside the TPA code were conducted to estimate the fraction of waste packages exhibiting localized corrosion as a function of solution compositions, employing data in Bechtel SAIC Company, LLC (2003a). This activity supports development of risk insights for near-field aspects (brine deliquescence, dust compositions, and brine compositions) and waste package corrosion aspects (stability of the passive film, loss of passivity, and localized corrosion). The refined abstracted models for near-field chemistry and waste package corrosion have been implemented in the latest version of the TPA code.

3.2 Methodology

The TPA code equations (Mohanty, et al., 1997) for the computation of the corrosion potential, E_{corr}, were modified to achieve consistency between experimental data and computations. In the refined model, the equation for the computation of the partial cathodic current density, i_r^o, in the absence of diffusion control is

$$i_r^o = -\, i_r^{\text{ef}} \frac{C_{\text{O}_2}^{\text{bulk}}(T)}{C_{\text{O}_2}^{\text{bulk}}(T_{\text{ref}})} e^{-\frac{E_a}{RT}} e^{-\frac{Z_r \beta_r F}{RT} E_{\text{corr}}} \left[\frac{\left[H^+\right]}{1\ \text{mol/L}} \right]^{n_H} p\text{O}_2{}^{n_o} \tag{3-1}$$

where (only international units are provided; English system requires a modified equation)

i_r^{ef}	—	reference current density [mol/L]
$C_{\text{O}_2}^{\text{bulk}}$	—	concentration of oxygen in solution as a function of temperature (Mohanty, et al., 1997) [mol/L]
T	—	temperature [K]
T_{ref}	—	reference temperature [K]
E_a	—	activation energy [J/mol]
Z_r	—	number of electrons participating in the reduction reaction (equal to 4) [unitless]
β_r	—	charge transfer coefficient [unitless]
E_{corr}	—	corrosion potential [volts]
n_H	—	reaction order with respect to hydrogen ion concentration [unitless]
n_o	—	reaction order with respect to oxygen partial pressure [unitless]
F	—	Faraday constant [96,486.7 C/mol]
R	—	Ideal gas constant [8.31441 J/mol K]
$\left[H^+\right]$	—	hydrogen ion concentration [mol/L]
pO_2	—	oxygen partial pressure [unitless]

If there is a diffusive layer controlling the transport of oxidizing species, the partial cathodic current density, i_r, is computed as (Mohanty, et al., 1997)

$$i_r = \frac{i_r^o}{1 - \dfrac{i_r^o\, C_{\text{o}_2}^{\text{bulk}}(T_{\text{ref}})}{C_{\text{o}_2}^{\text{bulk}}(T)} \dfrac{\delta}{4 F \phi \tau D_r}} \tag{3-2}$$

where

δ — effective thickness of diffusive layer [m]
ϕ — porosity [unitless]
τ — tortuosity [unitless]
D_r — diffusion coefficient of oxidizing species [m^2/s]

To derive the appropriate decreasing trend of the corrosion potential as a function of temperature, the passive anodic current density, i_a, is assumed to follow an Arrhenius dependence on temperature. From potentiostatic data, an effective activation energy of 44.7 kJ/mol has been estimated (Pensado, et al., 2002). The corrosion potential, E_{corr}, is determined numerically by finding the solution of the equation

$$i_a + i_r = 0 \tag{3-3}$$

Figure 3-1 shows a comparison of the computed corrosion potential as a function of pH and temperature. The parameters i_r^{ef}, β_r, and n_H were determined via least squares curve fitting. Values for all other parameters were consistent with TPA code input data. The refined approach to compute the corrosion potential yields results consistent with experimental trends, since E_{corr} decreases with increasing temperatures and increasing pH. Uncertainty in E_{corr} arises in the TPA code abstraction because of uncertainty in the passive anodic current density, i_a.

The effect of inhibitors on the critical potential, E_{crit}, was modeled as (Dunn, et al., 2004)

$$\Delta E_{\text{crit}} = E^0 \frac{\min(r, r_c)}{r_c} \tag{3-4}$$

where

E^0 — reference maximum increase [800 mV]
r — ratio of effective inhibitor molar concentration to chloride molar concentration [unitless]
r_c — reference ratio (0.1 for mill-annealed Alloy 22 and 0.3 for thermally-aged material) [unitless]

Thus, the critical potential, E_{crit}, was computed as defined in the TPA code, with appropriate parameters for the crevice corrosion repassivation potential for mill-annealed and thermally aged material, and then increased, as a function of the inhibitor concentration, using Eq. (3-4). Localized corrosion is assumed to occur if the corrosion potential is above the critical potential for localized corrosion $(\text{i.e., } E_{\text{corr}} > E_{\text{crit}})$.

For the near-field environment abstraction, the following environments were defined (Browning, et al., 2004).

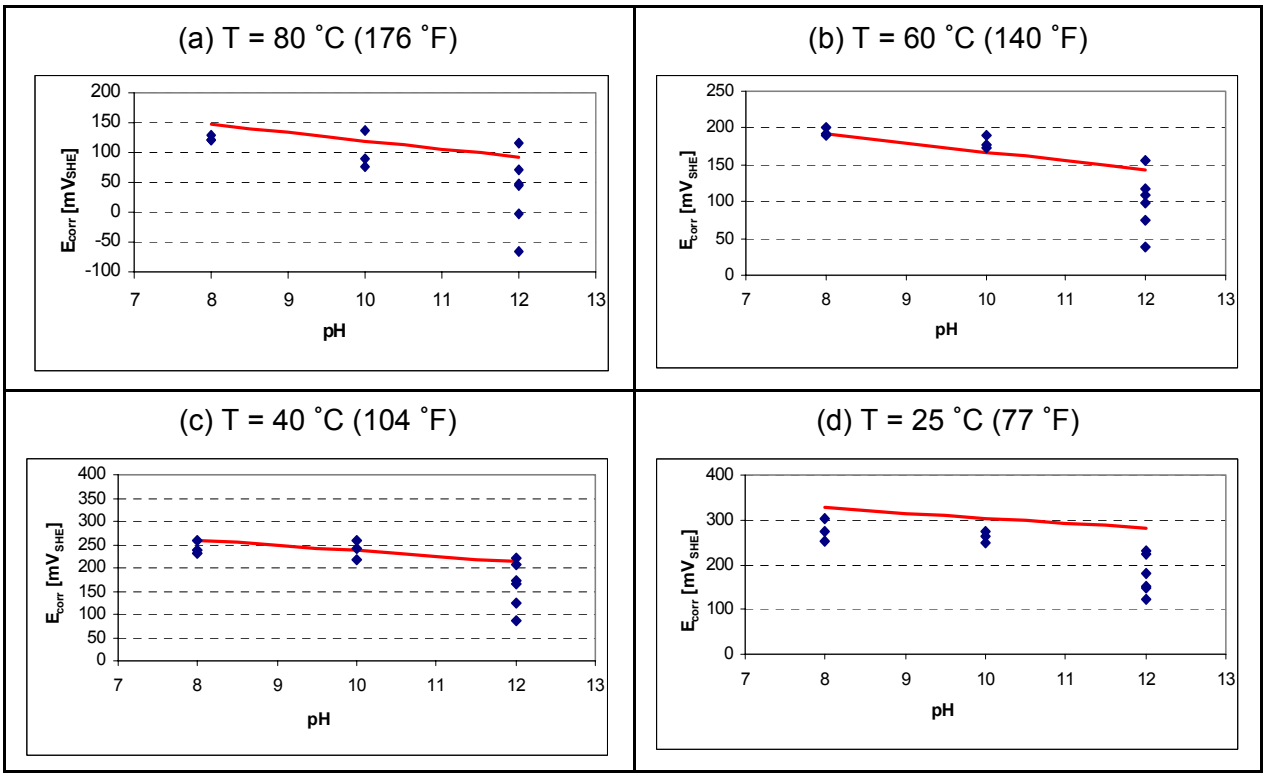

Figure 3-1. Comparison of Computed Corrosion Potential (Continuous Line) As a Function of pH and Temperature to Experimental Data (Diamonds) for (a) 80 °C [176 °F], (b) 60 °C [140 °F], (c) 40 °C [104 °F], and (d) 25 °C [77 °F]. Experimental Corrosion Potentials from Multiple Specimens in 4-M NaCl Solution Were Determined after Approximately 1-Day Exposure.

Environment 1 (no contact of seepage water with waste package, but environment humid enough for salt mixtures to display deliquescence): The DOE analyses suggest that seepage can only occur when the drift wall temperature, T_{dw}, is below a threshold value (Bechtel SAIC Company, LLC, 2003a). The drip shield is intended to avoid contact of seepage with the waste package. If seepage does not contact the waste package, aqueous solutions on the waste package may form by deliquescence of dust particles or mixing dust with condensed water. Analyses by DOE (Bechtel SAIC Company, LLC, 2003a) suggest an abundance of nitrate species in dust, an effective inhibitor to localized corrosion in Alloy 22 (Dunn, et al., 2004). Results suggest that nitrate is abundant and, thus, localized corrosion is unlikely during Environment 1. For the TPA code abstraction, this environment is assumed to prevail for the following conditions for relative humidity, RH, and drift wall temperature

RH > deliquescence and T_{dw} > seepage threshold or time < drip shield failure time (3-5)

Environment 2 (seepage contacting the waste package and evaporating): In the presence of seepage and evaporation, brines may develop on the waste package. Deliquescence of salt mixtures also is possible. Dilution may arise if condensed water on the drift wall or drip shield falls back on brines formed on the waste package surface. As a likely conservative approach,

this dilution process may be neglected in the abstraction. Chemical conditions may induce localized corrosion of Alloy 22. For the TPA code abstraction, Environment 2 is assumed to prevail for the following conditions

$$T_{dw} < \text{seepage threshold and RH} < 95\% \text{ and time} > \text{drip shield failure time} \quad (3\text{-}6)$$

Environment 3 (seepage contacting the waste package without evaporating): In the absence of evaporation, solutions in contact with the waste package may equilibrate in composition with seepage waters. Seepage waters may be diluted and pose no risk to waste package performance. For the TPA code abstraction, Environment 3 is assumed to prevail for the following conditions

$$T_{dw} < \text{seepage threshold and RH} > 95\% \text{ and time} > \text{drip shield failure time} \quad (3\text{-}7)$$

In the TPA code abstraction, not all the waste packages necessarily experience the three environments. For example, if drip shields perform their intended function for an extended period, waste packages may experience only Environments 1 and 3 and are not likely to exhibit localized corrosion. Environment 2 is the most critical environment for localized corrosion.

Cumulative Distribution Functions for Environment 2

Figures 4-9, 4-10, and 4-13 in Bechtel SAIC Company, LLC (2003a) summarize the functional dependence of chloride, nitrate, and pH on temperature {up to 100 °C [212 °F]}, relative humidity, and carbon dioxide partial pressure. Curves are grouped by bin chemistries. Table 4-5 in the same document summarizes time-integrated frequencies (over 20,000 years) of the various bins. The information in the previously mentioned figures and Table 4-5 was used to derive cumulative distribution functions for chloride, nitrate, and pH. In this analysis, only a single representative pH curve for each bin, corresponding to the function yielding the lowest pH values, was employed. The DOE data suggest that chloride concentrations do not strongly depend on temperature or partial pressure variations (Bechtel SAIC Company, LLC, 2003a, Figure 4-10), and nitrate concentrations depend on temperature and pressure variations when the relative humidity is below approximately 70 percent (Bechtel SAIC Company, LLC, 2003a, Figure 4-13).

To derive concentration distributions, the cumulative distribution function for relative humidity on the waste package surface at 100 °C [212 °F] was estimated from 100 Monte Carlo realizations of the TPA code [Figure 3-2(a)]. Chemical bins were sampled at random according to bin frequencies in Table 4-5 (Bechtel SAIC Company, LLC, 2003a). Using the concentration versus relative humidity curves (Bechtel SAIC Company, LLC, 2003a, Figures 4-9, 4-10, and 4-13) and a relative humidity value at 100 °C [212 °F], concentrations of pH, nitrate, and chloride were estimated. From the set of concentration values, cumulative distribution functions for pH, nitrate, and chloride were derived [Figures 3-2(b), 3-2(c), and 3-2(d)]. Table 3-1 includes values of concentrations at a relative humidity equal to 85.8 percent and a waste package temperature of 100 °C [212 °F]. Approximated cumulative distribution functions for the relevant ions also can be derived from values in this table. Table 3-1 also suggests chemistry bins that are likely to induce localized corrosion on welded areas of the waste package at 85.8-percent relative humidity and 100 °C [212 °F] waste package temperature.

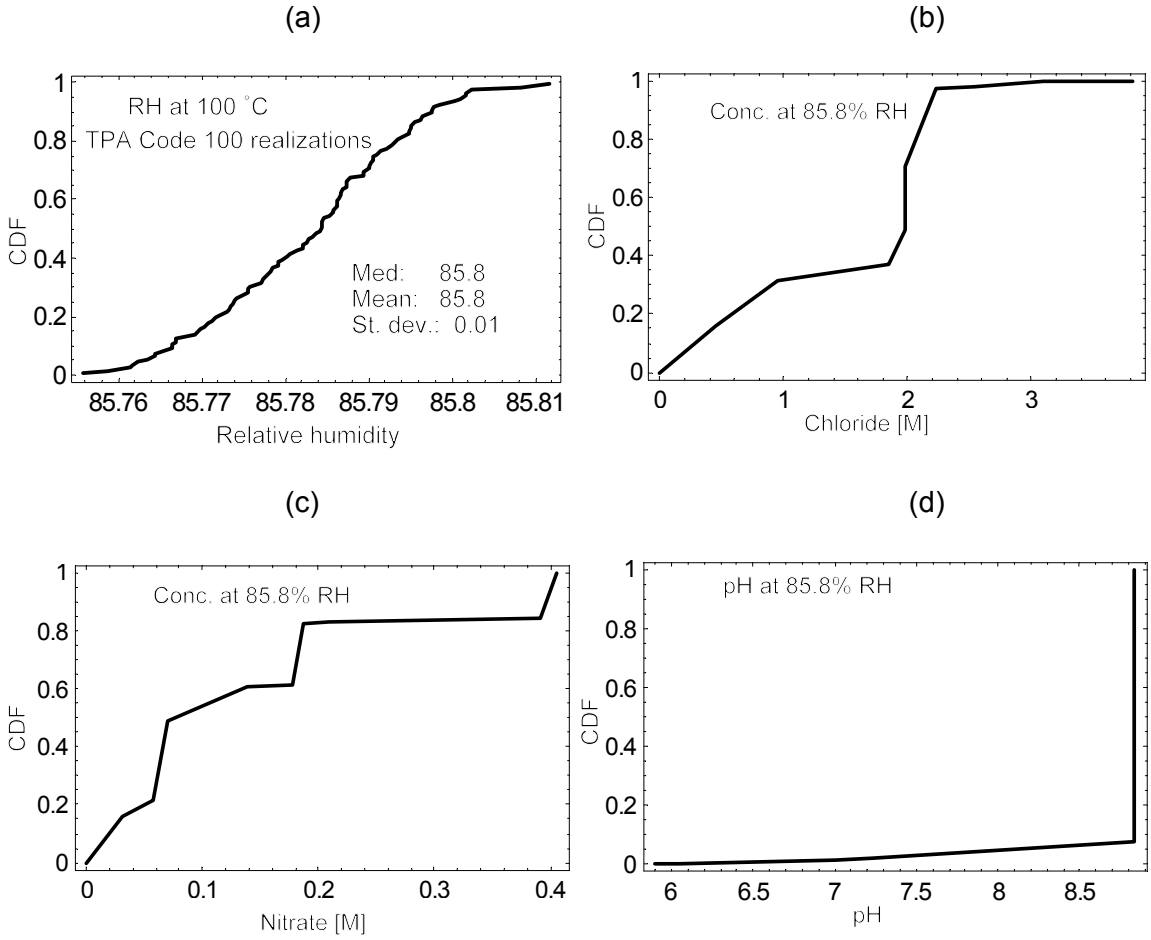

Figure 3-2. Estimated Cumulative Distribution Functions (CDFs) for (a) Relative Humidity at 100 °C [212 °F] Waste Package Temperature, Derived from 100 Realizations of the TPA Code, (b) pH, (c) Nitrate, and (d) Chloride

Table 3-1. Concentrations at 85.8-Percent Relative Humidity and 100 °C [212 °F]. Data Scanned from Figures 4-9, 4-10, and 4-13.*

					Localized Corrosion	
Cl– [M]	**NO_3^- [M]**	**pH**	**Frequency [%]**	**Bin**	**Mill-Annealed**	**Weld**
3.82	0.21	6.05	00.22	3	Unlikely	Likely
3.10	0.39	7.00	01.42	4	Unlikely	Unlikely
2.53	0.18	7.23	00.79	5	Unlikely	Unlikely
1.84	0.06	8.84	05.46	6	Unlikely	Likely
2.23	0.07	8.84	27.15	7	Unlikely	Likely
0.45	0.03	8.84	16.20	8	Unlikely	Unlikely
0.95	0.41	8.84	15.55	9	Unlikely	Unlikely
1.99	0.14	8.84	11.70	10	Unlikely	Unlikely
1.99	0.19	8.84	21.51	11	Unlikely	Unlikely

*Bechtel SAIC Company, LLC. "Technical Basis Document No. 5: In-Drift Chemical Environment." Rev. 1. Las Vegas, Nevada: Bechtel SAIC Company, LLC. 2003.

To estimate the frequency of localized corrosion, the pH, nitrate, and chloride values were independently sampled, by interpolation, from the cumulative distribution functions. For each triplet (Cl^-, NO_3^-, and pH), E_{corr} and E_{crit} were computed. Stochastic parameters for the computation of E_{corr} (e.g., anodic current density at a reference temperature) and E_{crit} (e.g., intercept along the voltage axis) also were sampled. A total of 100 independent waste packages was considered, and the number of waste packages exhibiting $E_{corr} > E_{crit}$ (i.e., the condition for localized corrosion) was estimated. The experiment was repeated 500 times to derive statistics for the number of times localized corrosion was activated.

3.3 Assumptions

The following assumptions were employed in the analyses:

- No drip shield
- No repassivation of localized corrosion (once localized corrosion initiates, it prevails)
- Central subarea location estimates of waste package temperature and relative humidity
- Frequencies of the different bin chemistries defined in Table 4-5 in Bechtel SAIC Company, LLC (2003a)
- Reference waste package temperature of 100 °C [212 °F]

Disregarding drip shield protection is likely conservative. Also, assuming that localized corrosion prevails is likely conservative. In reality, localized corrosion causes the corrosion potential to decrease, possibly repassivating the system. Central subarea locations for estimates of relative humidity were selected for the sake of mathematical convenience, and it is not necessarily a likely conservative selection. A different evolution in time of the relative humidity controls the time at which localized corrosion may occur. Thus, accounting for spatial variability in relative humidity estimates causes a broader distribution of times during which localized corrosion may be exhibited. The frequencies reported in Table 4-5 in Bechtel SAIC Company, LLC (2003a) are time averaged for 20,000 years. The only relevant chemistries, however, are those occurring with Environment 2 conditions. From Figure 4-14 in Bechtel SAIC Company, LLC (2003a), it is noted that the only chemistries prevailing near 1,000 years are Bins 9 and 11. These chemistry bins are relatively benign, given the abundance of localized corrosion inhibitors (Table 3-1). Therefore, use of the 20,000-year average frequencies is likely conservative, because of more aggressive chemistries than Bins 9 and 11. The reference waste package temperature was assumed to be 100 °C [212 °F]. The estimated average relative humidity at this temperature in central subarea locations is 85.8 percent [Figure 3-2(a)]. Figure 4-13 in Bechtel SAIC Company, LLC (2003a) suggests the lowest nitrate concentrations are reached at relative humidities higher than 70 percent. Therefore, the cumulative distribution function derived using 85.8 percent as the reference relative humidity for nitrate concentration is likely conservative. The nitrate concentration in this analysis is likely the most important variable controlling the onset of localized corrosion.

3.4 Results

Ignoring drip shield protection, an estimated average of 0.1 percent (standard deviation = 0.003) of the waste packages under Environment 2 conditions may exhibit localized corrosion. On the other hand, an estimated average of 19 percent (standard deviation = 0.027) of the waste packages under Environment 2 may exhibit localized corrosion on welded areas. Figure 3-3 displays the cumulative distribution function of times from 100 realizations of the TPA code at which the estimated waste package temperature reaches 100 °C [212 °F]. Figure 3-3 may be used to determine the time when localized corrosion may occur for central subarea locations. Because temperature and relative humidity are functions of repository location, Environment 2 conditions may be established at different times. Also, Environment 2 conditions are not established for those waste packages protected against seepage by drip shields.

A second approach, based on sampling the bins (as opposed to directly sampling concentrations) and computing E_{corr} and E_{crit} for each bin, estimated no localized corrosion on mill-annealed areas. Thirteen percent (standard deviation 0.03) of the waste packages in Environment 2, however, exhibited localized corrosion on welded areas. Therefore, it is appropriate and likely conservative in the TPA code abstraction to define cumulative distribution functions for chloride, pH, and inhibiting species and to sample them independently.

Estimating the frequency of localized corrosion depends on the cumulative distribution functions of relevant ions. Independent computations by Pabalan and Yang (2004), using 110 °C [230 °F] as reference temperature, yielded estimated ranges in chloride, nitrate, and pH consistent with those in Figure 3-2.

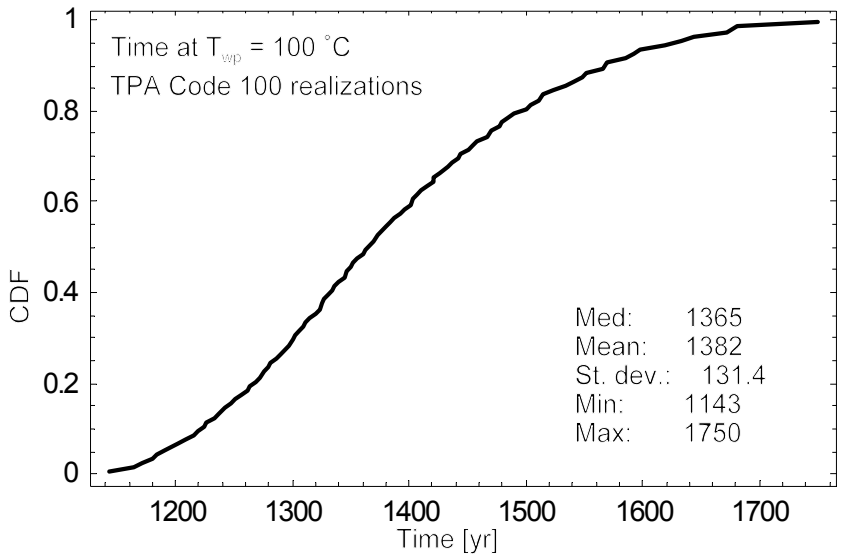

Figure 3-3. Estimated Cumulative Distribution Function (CDF) of Times at Which the Waste Package Temperature Reaches 100 °C [212 °F]

3.5 Conclusions

A refined approach to assess the effects of near-field chemistry and seepage and evaporation conditions in the drift on waste package corrosion was developed and implemented in the latest version of the TPA code. Conclusions from this analysis are

- Dust samples seem abundant in species inhibiting localized corrosion; therefore, localized corrosion is not likely to occur in the absence of seepage water in contact with the waste package (Environment 1).

- Using data reported in Bechtel SAIC Company, LLC (2003a), and ignoring drip shield protection, it was estimated that 0.1 percent of the waste packages under Environment 2 conditions may exhibit localized corrosion on mill-annealed areas, and 19 percent may exhibit localized corrosion on welded areas. These conclusions are dependent on estimates of bin probabilities and cumulative distribution functions for relevant ionic species.

- All waste packages may not necessarily experience Environment 2 conditions. Also, Environment 2 conditions may be established at different times depending on the repository location. Using the TPA code basecase (central subarea locations), selecting 100 °C [212 °F] as the reference waste package temperature, and ignoring drip shield protection, Environment 2 conditions may occur approximately 1,400 years after repository closure.

4 ASH REDISTRIBUTION AND WIND-FIELD VARIABILITY

TASK DESCRIPTION

Evaluate the relative sensitivity of the peak probability-weighted dose to parameters relevant to modeling posteruption ash redistribution.

AUTHORS/CONTRIBUTORS

K. Compton, T. McCartin, and R. Codell

4.1 Background and Purpose

In the Risk Insights Baseline Report (NRC, 2004), both remobilization of contaminated ash and variability of the wind field are rated as medium significance to waste isolation. In the DOE Total System Performance Assessment and the TPA code, the wind direction was fixed toward the location of the reasonably maximally exposed individual to compensate for not modeling the posteruption movement of contaminated ash. Clearly, if the wind direction is allowed to vary and the potential effects of ash remobilization are ignored, the TPA code realizations may not deposit ash at the reasonably maximally exposed individual location. Scoping analyses presented in Hill and Connor (2000), however, indicated that long-term remobilization processes could result in ash deposits that exceed the thickness of primary volcanic deposits when the initial ash deposition is small. Calculations that allow wind direction to vary without accounting for the potentially significant effects of ash remobilization, therefore, provide limited insight about the significance to waste isolation. In the TPA code sensitivity analysis report (Mohanty, et al., 2002b), nine parameters associated with extrusive volcanism were shown to dominate the conditional dose estimates.

In addition to assuming that a potential eruption plume is always directed at the reasonably maximally exposed individual location, current TPA code calculations assume that an airborne mass load above fresh ash deposits, as well as the ash blanket itself, decreases with time after a potential eruption. A relatively straightforward approach to evaluating the potential significance to waste isolation of ash remobilization is to examine the effect of maintaining either or both the airborne particle concentrations or the ash blanket thickness at posteruption values. This effect can be simulated in the TPA code by varying the reduction in the airborne mass load with time (i.e., using larger values for the half-life of this process) or by varying the rate of removal of blanket thickness. Smaller values of the relevant rate constants represent slower decreases in airborne mass loads or blanket thickness from the presumed influx of resuspendible ash through remobilization. If deposited volcanic ash persists longer, or if it is being replenished from remobilization of contaminated ash initially deposited outside the reasonably maximally exposed individual area, the estimated conditional dose curves can persist longer. The convolution equation used to estimate the probability-weighted dose will be sensitive to the tail of the conditional dose distribution, causing the peak mean dose to increase. Therefore, the replenishment of contaminated ash brought into the area around the reasonably maximally exposed individual and the prolongation of the persistence of the elevated airborne mass loading might be important considerations.

The estimated probability-weighted dose from extrusive igneous events is a function of three factors:

- Conditional likelihood of exposure (i.e., the probability that the reasonably maximally exposed individual is exposed to contaminated ash, given that an eruption occurs)
- Conditional magnitude of exposure (i.e., the magnitude of the dose, given that the reasonably maximally exposed individual is exposed to contaminated ash)
- Persistence of the exposure (i.e., the time dependence of the elevated contaminated airborne dust concentrations at the location of the reasonably maximally exposed individual following an eruption)

Different parameters (e.g., wind speed and wind direction) affect the probability-weighted dose by influencing one or more of these three factors. The first two of these factors primarily affect the conditional dose. Given two realizations with the same conditional dose, the realization characterized by a longer persistence would exhibit a higher estimated probability-weighted dose.

4.2 Methodology

The current effort uses sensitivity analyses to examine how factors related to remobilization processes affect the estimated probability-weighted dose. Sensitivity analyses of the conditional dose and the probability-weighted dose to different parameters have been performed using the personal computer version of the TPA code running under Windows™ NT Version 4. Two sets of analyses were conducted. The first set examined the sensitivity of the conditional peak annual dose estimate to variations in selected parameters with all other parameters held constant at their mean values. This analysis was performed to further refine the results of the TPA code sensitivity study and to gain insights into the selection of parameters for a more detailed evaluation. The second analysis set examined sensitivity of the probability-weighted dose to variations in the parameters selected for a more detailed evaluation. For both sets of analyses, modifications to the TPA code input file were used to implement the sensitivity analyses. There was no modification to the TPA source code.

The conditional dose is the average annual dose, $\overline{D}\left(t'|t_e\right)\cdot \mathrm{d}t$, to a person living at time t' given that a volcanic event occurs at time t_e. Risk, however, is a function of both probability and consequence. Because the probability of an eruption occurring within any particular interval in a 10,000-year period is low, these conditional dose curves must be weighted by their probability of occurrence. Assuming that extrusive volcanism has a constant annual probability, p, of occurring in any year, the probability-weighted dose, or risk, $D\left(t'\right)$, to a person living at time t' is the convolution of all possible prior volcanic events multiplied by p

$$D\left(t'\right) = \int_{t_{\min}}^{t'} p \cdot \overline{D}\left(t'|t\right)\cdot \mathrm{d}t \qquad (4\text{-}1)$$

where t_{min} equals the earliest time when volcanism is considered. This convolution procedure yields the probability-weighted dose and can be computed using either a Monte Carlo method or a numerical integration technique. In this report, the numerical integration technique used by Mohanty, et al. (2002b) to perform the convolution is adopted.

The following sections present the methodology used for the two sets of analyses. The methodology for the conditional dose analysis is described in Section 4.2.1 and the methodology for the probability-weighted dose analysis is provided in Section 4.2.2.

4.2.1 Conditional Dose Analysis

The basecase was established by running 100 realizations of a direct-release-only volcanism scenario sampling all the uncertain variables. As a normal part of code execution, the TPA code generates an output file that lists the mean value of all sampled input files. This file was used to define a deterministic basecase input parameter set based on the mean values of each sample parameter.

This basecase parameter set was then modified to allow each selected parameter to be varied through its plausible range, one parameter at a time. Four separate analyses, one for each selected parameter, were conducted by executing a single run consisting of 100 Latin hypercube sampling realizations in which either a uniform or a loguniform distribution (as appropriate) was defined for the selected input parameter. The ranges for the distributions were selected to likely bound the values used in the TPA code input file. In the event the input parameter was defined as a constant in the basecase TPA code input file, reasonable maximum and minimum values were selected to exercise the TPA code through a plausible range. The parameters in Table 4-1 and their associated ranges were evaluated in the TPA code. The mean values derived from the basecase also are given in Table 4-1.

The TPA code output provides estimates of the total ground surface peak dose, the time of peak dose, and the dose from each nuclide at the time of peak dose for each realization. Because the value of each sampled parameter for each vector is listed in the TPA code output, sensitivity of the estimated peak mean dose to the selected parameter for a conditional dose analysis can be examined by generating a scatter plot of the total estimated peak dose plotted against the value of the selected parameter.

4.2.2 Probability-Weighted Dose Analyses

Based on the results of the sensitivity analyses of the estimated peak conditional dose, the parameters in Table 4-2 were selected for detailed evaluation to determine their effects on the peak probability-weighted dose. Analyses were performed using the TPA code to simulate sets of probabilistic runs for the direct-release-only volcanism scenario. For this comparison, calculation of the estimated peak mean dose requires many more runs of the code than the computation of conditional doses described in the previous section. The convolution procedure employed to compute the estimated peak mean dose required calculation of 13 sets of Monte Carlo runs. In each of the 13 runs, time of the event is held constant at a fixed time ranging from 100 to 10,000 years. After estimating the mean dose for each of the fixed event times using 100 runs for each set, the procedure uses convolution to estimate the peak mean dose curve. Although there are approximately 330 sampled parameters, only a relatively small

Table 4-1. Peak Conditional Dose Sensitivity Analysis Parameter Set			
Parameter Name	**Basecase Value**	**Distribution**	**Range**
WindDirection[degrees]	−90	uniform	−180.0, 0
WindSpeed[cm/s]	1.205×10^{3}	loguniform	1×10^{1}, 1×10^{5}
AirborneMassLoadAboveFreshAshBlanket [g/m3]	4.4×10^{-3}	loguniform	1.2×10^{-3}, 1.6×10^{-2}
RateOfReductionOfMassLoading Factor[1/yr]	7×10^{-2}	loguniform	7×10^{-3}, 7×10^{-1}

Table 4-2. Peak Probability-Weighted Dose Sensitivity Analysis Parameter Set		
Parameter Name	**Basecase Value (Distribution)**	**Values Analyzed**
RateOfReductionOfMassLoadingFactor[1/yr]	0.07 (constant)	0.7; 0.07; 0.007; 0.0007; 0.00007
RelativeRateOfBlanketRemoval[1/yr]	0.0007 (constant)	0.7; 0.07; 0.007; 0.0007; 0.00007
WindSpeed[cm/s]	1,205 (exponential with 8.3×10^{-4} recurrence rate)	10; 100; 300; 500; 1,000; 2,000; 3,000; 4,000; 5,000; 10,000
WindDirection[degrees]	−90 (constant)	−30; −50; −70; −80; −90; −100; −110; −130; −150
ConstantRelatingFallTimeToEddyDiffusivity [cm2/s5/2]	400 (constant)	30; 100; 300; 1,000; 3,000

subset of these affect direct-release-only calculations. Therefore, it was determined that 100 realizations were sufficient to obtain an adequate estimate of the direct-release-only dose. Computing a single peak probability-weighted dose, therefore, required 1,300 executions of the TPA code. A set of 5 to 10 values of each selected input parameter was developed and is shown in Table 4-2.

The two parameters that most significantly affect the persistence of exposure {RateOfReductionOfMassLoadingFactor[1/yr] and RelativeRateOfBlanketRemoval[1/yr]} were varied in a systematic fashion. Each parameter ranged from 0.7 $year^{-1}$ (approximately a 1-year half-life) to 0.00007 $year^{-1}$ (approximately a 10,000-year half-life). All possible combinations of the five selected values were evaluated (as listed in Table 4-2) for the parameters representing the persistence of the mass loading and the persistence of the blanket, resulting in a set of 25 analyses. To manage the multiple runs, a set of batch files was written to call the appropriate input files and store the outputs for postprocessing. Parameter values in the input files were checked.

In addition, the sensitivity of the peak probability-weighted dose to several atmospheric transport parameters (wind speed, wind direction, and plume dispersion) was analyzed. The results of the conditional dose analysis suggested that the sensitivity of the results to the wind speed was not a smooth function, but was characterized by two distinct regions, one in which

wind velocities are apparently too low to transport ash to the reasonably maximally exposed individual location and one in which ash deposition occurs at the reasonably maximally exposed individual location. Because the system-level sensitivity analysis (Mohanty, et al., 2002b) showed results were highly sensitive to this parameter and because it was not known whether these results carried through to the probability-weighted dose, the sensitivity of the probability-weighted dose to variations in the wind speed at the time of the eruption was considered. A similar analysis was performed to estimate the impact of wind direction on the peak probability-weighted dose.

Evaluation of plume dispersion was limited by the conceptual model employed in the TPA code, which assumes constant wind speed and wind direction. During an eruption, wind speed and wind direction are unlikely to be constant and spatially uniform. The winds to which an eruption column is exposed may vary with height and time, possibly changing significantly during the course of an eruption lasting many days. In addition, the wind field seen by the particles may vary with time and location after the particles leave the eruption column. In contrast to the single-lobed dispersion pattern generated by the one-dimensional wind field used by ASHPLUME, variations of wind speed and wind direction are likely to produce a deposition pattern with multiple lobes corresponding to differences in wind direction and wind speed at different times during the eruption. The net effect of these variations likely produces a deposition pattern somewhat more dispersed and multilobate relative to the pattern expected from a constant, one-dimensional wind field, as was observed in the 1994 Cerro Negro eruption (Hill, et al., 1998). There is no straightforward way to evaluate such a deposition pattern using the TPA code, given the one-dimensional wind field assumed by the conceptual model underlying ASHPLUME (Jarzemba, 1997). Varying the parameter used to determine the turbulent dispersion of the airborne ash (ConstantRelatingFallTimeToEddyDiffusivity[cm2/s5/2]), however, allows the introduction of a more or less turbulent dispersion into the model. This variation can serve as a qualitative surrogate for temporal heterogeneity in the wind field.

This analysis is not a rigorous accounting for the effect of a wind field that is temporally and spatially variable during an eruption. The approach provides a qualitative surrogate, not an approximation method, for which likely bounding analyses can be performed.

Without explicitly modeling a spatially and temporally variable wind field, it is not possible to make a direct comparison that would indicate the extent to which this approach approximates a more complex wind field.

4.3 Assumptions

The assumptions made in the two sets of analyses are presented in this section. First, the assumptions for the conditional dose analysis are given in Section 4.3.1. The assumptions for the analysis involving the probability-weighted dose are described in Section 4.3.2.

4.3.1 Conditional Dose Analysis

The conditional dose analysis is exploratory in nature. No major assumptions were necessary to conduct this analysis other than those implicit within the TPA code.

4.3.2 Probability-Weighted Dose Analysis

For the probability-weighted dose analysis, there are two major assumptions. Both assumptions relate to the choice of parameters used to simulate processes not included in the TPA code.

The first key assumption is that variation of the decay rate of both the blanket and the mass load above the fresh ash blanket provides a reasonable approach to simulating the effect of redistribution. These processes are modeled as a first-order decay process in the TPA code. A more realistic effect of remobilization on supporting elevated mass loads is likely to show a nonmonotonic evolution of airborne mass loading at the reasonably maximally exposed individual location. Therefore, it is not possible to make a direct evaluation of the extent to which a particular parameter value can be used to simulate a particular remobilization scenario. Because of the convolution procedure used, however, it is expected the peak probability-weighted dose would be closely related to the area under the curve, representing the evolution of the airborne mass load through time. Based on that expectation, approximate comparisons (e.g., mass loads elevated for timescales of decades, centuries, or millennia) are likely valid. For long times, the estimated peak doses may be affected significantly by the decay of Am-241, with a half-life of 432 years, and hence, the values, in which essentially no decay in the mass loads occurs, likely bound the results.

The second key assumption is that insight into the behavior of a temporally variable wind field can be gained by variation of the constant relating fall time to eddy diffusivity. For the reasons provided previously, it is assumed this approach produces results qualitatively similar to an explicit evaluation of a temporally variable, heterogenous wind field.

4.4 Results

This section discusses results from the two analyses described in the methodology section. Results for the conditional dose analysis are provided in Section 4.4.1, and the probability-weighted dose results are presented in Section 4.4.2.

4.4.1 Conditional Dose Results

Parameters related to the deposit (i.e., mass loadings) appear to affect primarily the magnitude of exposure by way of affecting the total dust inhaled (i.e., for a constant ventilation rate, the exposure increases with increasing airborne mass loading). Sensitivity of the dose to mass loads is linear when inhalation is the dominant exposure pathway, as is the case when the basecase values are used. Persistence of the airborne mass loading, as expected, has no impact on the estimated peak conditional dose, given the direct deposition of ash occurs at the reasonably maximally exposed individual location. These results are illustrated in Figure 4-1.

Wind speed and wind direction appear to affect the estimated peak conditional dose primarily through the probability of exposure. There are essentially two regions of effectively constant dose: scenarios in which the reasonably maximally exposed individual is exposed to contaminated ash and scenarios in which no (or limited) exposure occurs. Wind speeds below a few meters per second appear to result in deposition of the majority of the tephra within 20 km [12.4 mi] of the vent. Winds more than approximately 20 degrees away from the

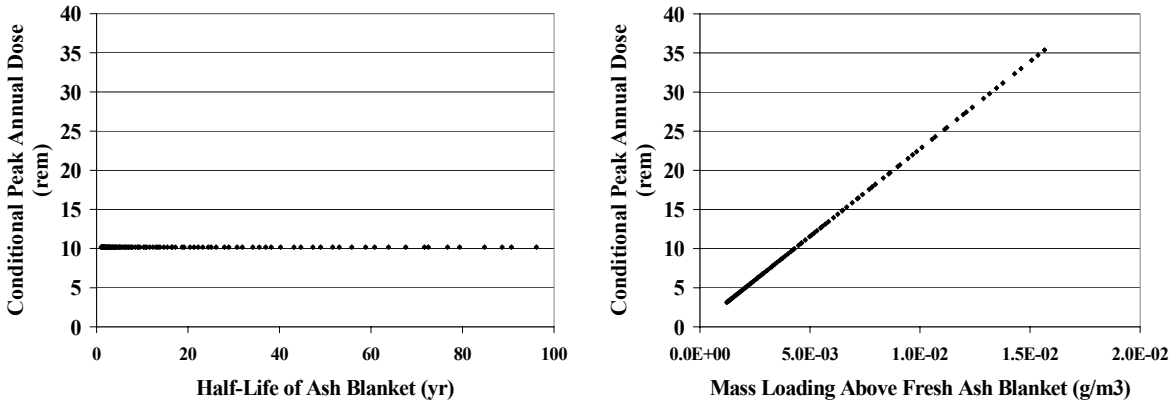

Figure 4-1. Sensitivity of Estimated Peak Conditional Dose to Initial Level and Persistence of Mass Loading about Ash Blanket[1]

reasonably maximally exposed individual location appear to avoid direct deposition of significant amounts of tephra at the reasonably maximally exposed individual location. A relatively flat plateau in both sensitivity curves in Figure 4-2 suggests the estimated peak conditional dose is not particularly sensitive to the thickness of the ash blanket, once some critical thickness is reached. This behavior is consistent with a dose dominated by inhalation, in which the inhalation dose is mainly a function of the airborne ash mass loading, the specific activity of the airborne ash, the inhalation rate, and the dose conversion factor for inhalation. For this model, blanket thickness would affect the estimated dose only indirectly, in that resuspension from a thin ash blanket would be more likely to contain a higher percentage of uncontaminated soil and, therefore, a lower concentration of radionuclides in the airborne dust. Note the instability in Figure 4-2 results at wind speeds of approximately 400 cm/s [13 ft/s]. The cause of this instability appears to be unrelated to the wind speed, but its exact nature is uncertain.

Parameters related to the eruption, on the other hand, appear to affect primarily the magnitude of exposure by way of affecting concentration of the radionuclides in the contaminated ash blanket and, therefore, the specific activity of the inhaled ash. For example, the combination of event power and event duration determines the total volume of erupted tephra. The conduit diameter (using the geometric model for waste package entrainment) affects the estimated number of waste packages intercepted. The specific activity in the ash and, therefore, the estimated conditional dose can be increased by either reducing the volume of erupted tephra or increasing the number of entrained waste packages. The variation in conditional dose with these parameters is consistent with this hypothesis.

---

[1]The half-life of the ash blanket is, t_h, computed from the removal constant using a first-order expression in which $t_h = \frac{\ln(2)}{\lambda}$, where the rate constant, λ, is the annual rate of removal.

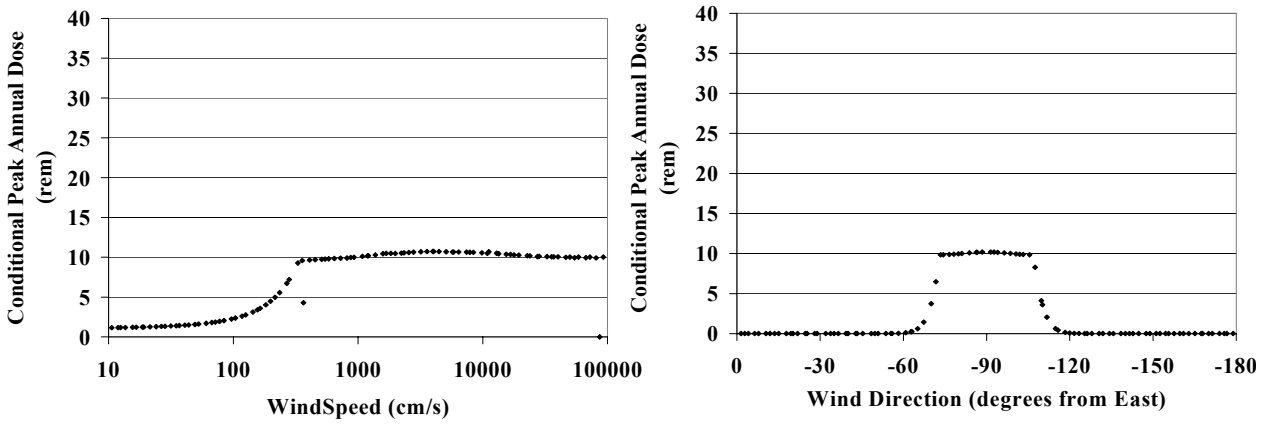

Figure 4-2. Sensitivity of Estimated Peak Conditional Dose to Wind Speed and Wind Direction

Estimates from these analyses suggest the peak probability-weighted dose from extrusive igneous events is a function of the conditional likelihood of exposure, the conditional magnitude of exposure, and the persistence of the exposure. Parameters demonstrating a binary-type response, such as wind speed and wind direction, appear to affect the conditional likelihood of exposure. Parameters that demonstrate a linear or inverse response, such as event power and duration or conduit diameter, appear to affect the conditional magnitude of exposure. Parameters to which the estimated dose is known to be sensitive, but that do not affect the peak conditional dose, may affect the peak probability-weighted dose by their impact on the tail of the conditional dose distribution. These parameters will be discussed in the next section.

4.4.2 Probability-Weighted Dose Results

The TPA code feature most suitable for evaluating the effect of the redistribution of contaminated ash is the persistence of the ash blanket. Although the estimated peak conditional dose is unaffected by the persistence of the ash blanket, persistent tails can have a significant effect on the probability-weighted dose, as indicated in Figure 4-3. This figure shows sensitivity of the estimated peak probability-weighted dose within the 10,000-year period to the persistence of mass loading and to the persistence of the ash blanket. The persistence is expressed as a half-life, t_h, determined from the selected removal rate constant by the relation $t_h = \frac{ln(2)}{\lambda}$, where λ is the removal rate constant. Examination of the results for a limited persistence of mass loading (t_h = 10 years) suggests the impact of a longer lived blanket is not highly significant if the airborne mass load is not sustained. This limited persistence of mass loading is most likely because there is a large disparity in the default values of the rate of decay of the airborne mass load (7 percent per year) in comparison with the default removal rate of the ash blanket (0.07 percent per year).

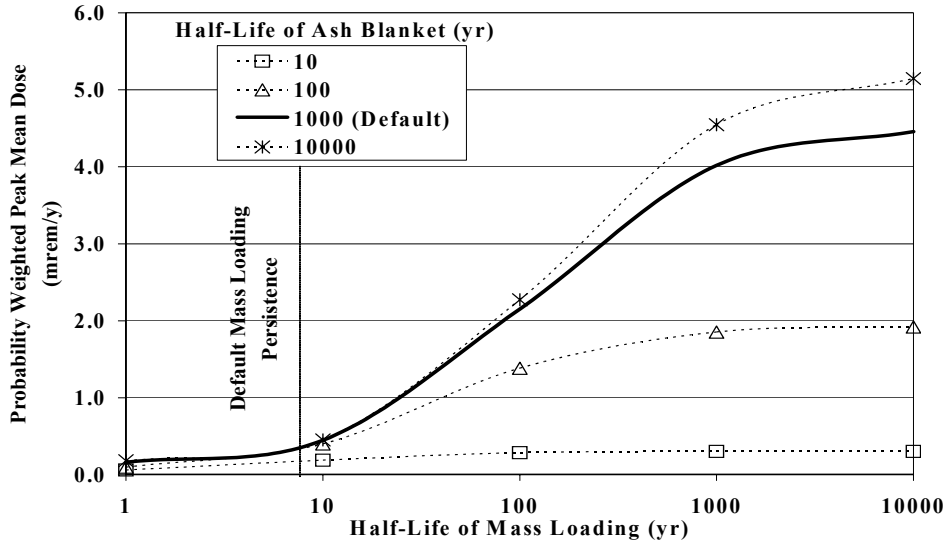

Figure 4-3. Sensitivity of Estimated Peak Probability-Weighted Dose to Persistence of Ash Deposits and Mass Loadings[2]

Increasing the persistence of the mass loading by one order of magnitude (t_h = 100 years) results in approximately a fivefold increase in the estimated peak probability-weighted dose. The effect, however, appears to be likely asymptotically bounded as the persistence increases of both the ash blanket and the elevated mass loading with a maximum increase in the estimated peak probability-weighted dose of approximately one order of magnitude. Most of the increase is associated with increasing the persistence of the mass loading. Increasing the persistence of the ash blanket without increasing the mass loading has a much smaller effect.

As mentioned, three analyses were performed to evaluate the effect of the wind field on the estimated probability-weighted dose. These analyses comprised evaluations of sensitivities of the probability-weighted dose to the wind speed, the wind direction, and the dispersion of the plume. Figure 4-4 shows the effect of wind speed at the time of the eruption on the estimated probability-weighted dose.

Examination of Figure 4-4 shows the effect of the wind speed on the estimated probability-weighted dose is considerably more gradual than on the conditional dose. This additional effect suggests that wind speed also influences persistence of the ash blanket. A potential mechanism for this effect is that lower wind speeds would result in thinner ash blankets at the reasonably maximally exposed individual location, giving rise to a shorter-lived ash blanket. A similar effect is shown in Figure 4-5 in the difference between estimates of the conditional dose and the probability-weighted dose for the wind direction, with a much narrower plateau of constant

---

[2]The half-life of the ash blanket, t_h, is computed from the removal constant using a first-order expression in which $t_h = \frac{ln(2)}{\lambda}$, where the rate constant, λ, is the annual rate of removal.

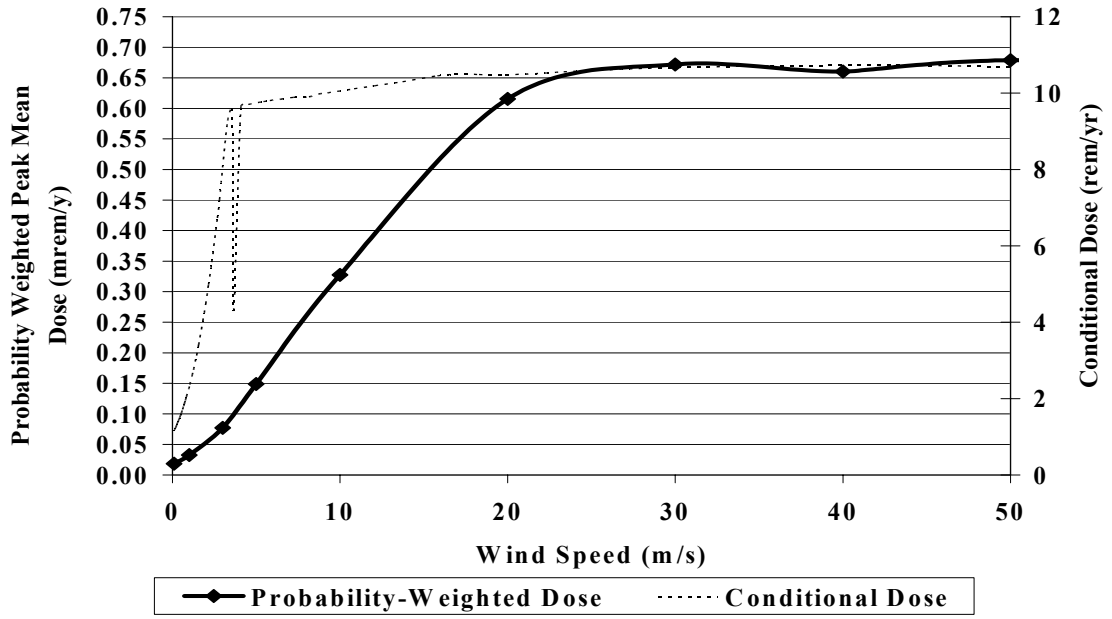

Figure 4-4. Sensitivity of Estimated Peak Probability-Weighted Dose and Conditional Dose to Wind Speed

dose levels. Note the instability in Figure 4-4 results at wind speeds approximately 400 cm/s [13 ft/s]. As with the Figure 4-2 results, the cause of this instability appears to be unrelated to the wind speed, but its exact nature is uncertain.

Dispersion of the deposited ash associated with a temporally and spatially heterogeneous wind field does not appear to affect the estimated risk significantly. In the absence of remobilization mechanisms, a more dispersed plume is associated with a slightly lower estimated risk, as seen in Figure 4-6.

These results also may arise from a potentially decreased blanket thickness associated with a more dispersed deposit. The most significant effect of a variable wind field would be to cause the deposited ash from the volcanic plume to miss the reasonably maximally exposed individual location, or to miss an area that could contribute ash to the reasonably maximally exposed individual location by redistribution, completely. This might occur, for example, if the wind was blowing to the north or west at the time of the eruption.

4.5 Conclusions

The two sets of analyses described in this chapter yielded the three conclusions presented in this section.

Conclusion 1: The rate of decay of the mass loading of fresh ash appears to have a significant effect on the estimated peak probability-weighted dose. The current TPA code approach does not couple persistence of the airborne mass loading to remobilization of ash from the receptor site. Results of the sensitivity analysis show the estimated peak probability-weighted

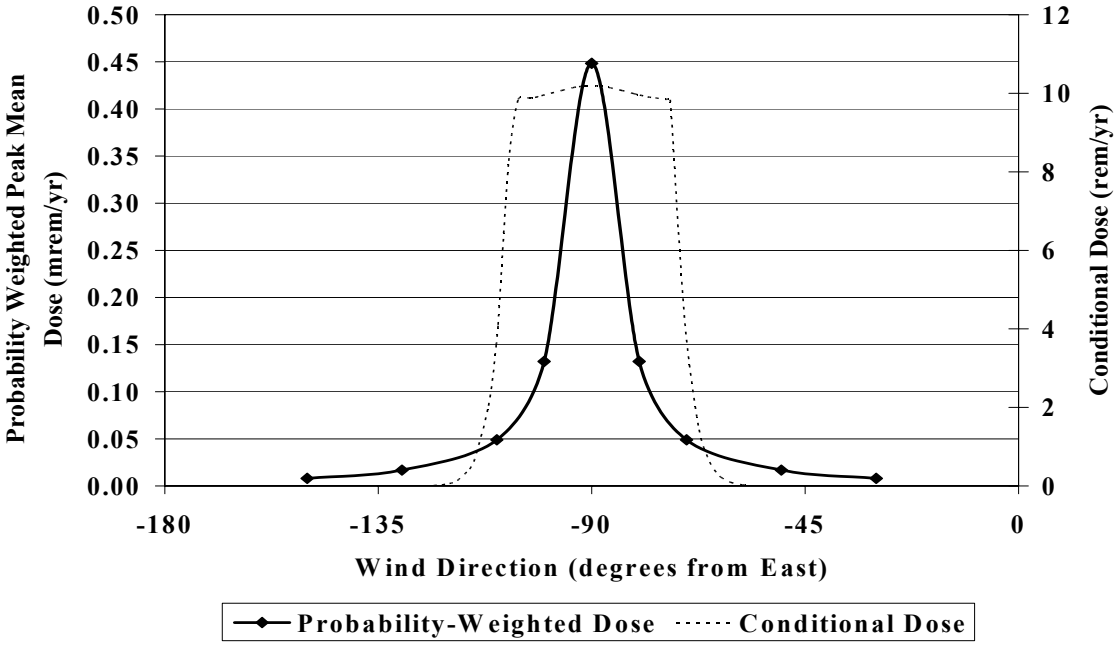

Figure 4-5. Sensitivity of Estimated Peak Probability-Weighted Dose and Conditional Dose to Wind Direction

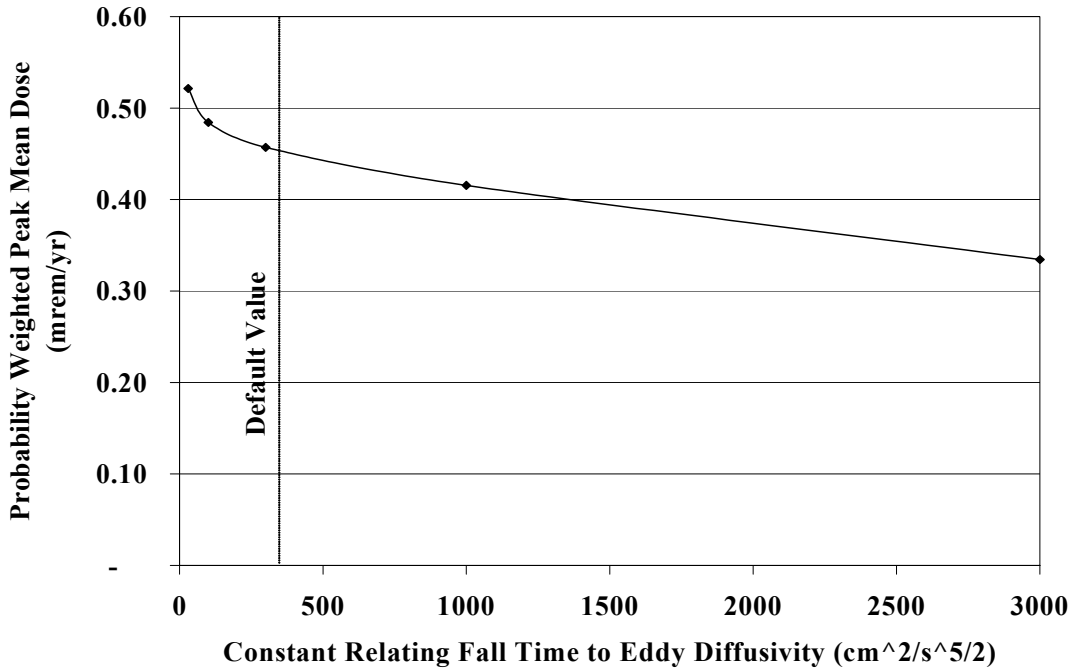

Figure 4-6. Sensitivity of Estimated Peak Probability-Weighted Dose to Dispersion of Ash Deposition

dose is sensitive to the rate at which airborne dust levels decrease. More generally, in the current TPA code model, reduction in the estimated probability-weighted dose appears to be most influenced by two rate constants with the faster rate constant controlling. In this case, because the rate constant for mass loading decay is so much larger than that for removal of the ash blanket, the reduction in mass loading may dominate. If the opposite was true (if the removal rate of the blanket was faster than the mass load decay rate), the persistence of the ash blanket may control.

Conclusion 2: Redistribution of contaminated ash appears unlikely to increase significantly the estimated peak dose arising from a volcanic eruption over the case in which the ash is directly deposited at the reasonably maximally exposed individual location. Although not a likely bounding approach, fixing the wind direction to the south appears reasonable to account for the effect of remobilization of the contaminated ash.

Redistribution of contaminated ash may affect the estimated peak mean dose from extrusive volcanism in two ways. Redistribution may either supply or replenish the contaminated ash at the reasonably maximally exposed individual location, resulting in an increased persistence of elevated airborne mass loads of respirable contaminated ash that may extend during periods of time to a century or more. In the event the initial ash deposit did not include the reasonably maximally exposed individual location, the likelihood of exposure to contaminated ash may be increased. Fixing the wind direction to the south affects only the likelihood of exposure. Because it may not simultaneously account for an increased persistence of the exposure, fixing the wind direction may not be considered a likely bounding assumption. The effect of persistence of exposure alone is unlikely to increase the estimated dose significantly. A likely bounding evaluation estimates the maximum effect is approximately one order of magnitude more than the basecase TPA code expected dose, which is associated with an assumption of more persistent elevated mass loadings. However, when other likely conservatisms are considered (e.g., dilution of contaminated ash with unaffected sediments, less than 100-percent likelihood that the contaminated ash will be remobilized to the reasonably maximally exposed individual area, and the relative improbability of mass load decay times on the order of centuries to millennia), the likely conservatism of a preferential wind direction (i.e., assuming that any eruption would result in exposure of the reasonably maximally exposed individual) appears to offset substantially the likely nonconservatism associated with the lack of an explicit remobilization model that could increase the persistence of mass loading at the reasonably maximally exposed individual location. To produce estimated doses significantly higher than those obtained by fixing the wind direction, remobilization would have to produce mass loadings at the reasonably maximally exposed individual location from tephra initially deposited elsewhere, which are similar in magnitude and duration to mass loadings from tephra directly deposited at the reasonably maximally exposed individual location, and elevated mass loads would have to persist on the order of centuries or longer rather than decades. In other words, remobilization would have to increase both likelihood and duration of exposure simultaneously.

Conclusion 3: Overall, results suggest variability in the wind field does not significantly alter the estimated peak dose at the reasonably maximally exposed individual location. Fixing the wind direction to the south appears a reasonably conservative approach to account for the effect of a variable wind field.

Spatial and temporal heterogeneities in the wind field during an eruption may result in a more dispersed ash blanket. This ash blanket may cover a larger area, and may be generally thinner. The probability of ash deposition may increase, but the persistence may be somewhat less

because of the thinner ash blanket. Fixing the wind direction to the south appears to be a reasonable approach because the wind direction bounds the effect on the probability of exposure, and the other major effect of a variable wind field (increased dispersion) is likely to decrease the estimated peak probability-weighted dose.

5 RESUSPENSION OF VOLCANIC ASH

TASK DESCRIPTION

Verify assumptions regarding the amount of fine ash particles resuspended in the air and the influence on estimated dose.

AUTHORS/CONTRIBUTORS

T. McCartin, P. LaPlante, R. Benke, R. Codell, K. Compton, B. Hill, D. Hooper, J. Rubenstone, and J. Trapp

5.1 Background and Purpose

If an extrusive volcanic event occurs through the repository footprint, it is likely that waste packages contacted by ascending magma will be damaged, and spent nuclear fuel may become entrained. During a volcanic event, spent nuclear fuel, entrained in magma, may be transported within airborne tephra resulting in volcanic ash and spent nuclear fuel particle deposition on the surface of the Earth. Once deposited on the ground surface, small particles of spent nuclear fuel and ash may be resuspended into the air, and particles may be inhaled causing radiation exposure.

The process of resuspension is represented in numerous exposure assessment models, including in the TPA code, by a mass loading model. Mass loading is the airborne concentration (e.g., g/m^3) of particles suspended in air. Prior sensitivity analyses discussed in the Risk Insights Baseline Report (NRC, 2004) identified the airborne mass load parameter (i.e., the airborne particle concentration) as an influential parameter for the extrusive volcanism dose estimation. The risk insight, Inhalation of Resuspended Volcanic Ash, is rated a high significance to waste isolation in NRC (2004).

The sensitivity analyses were based on a previous TPA code inhalation model that included two volcanic ash mass loading values (one value representing conditions soon after the occurrence of an eruptive event, termed fresh ash, and the other value representing long-term conditions after the ash has become part of the soil, termed soil), breathing rate, and exposure duration representing all activities. A modification to the TPA code refined the inhalation model to more precisely account for different levels of surface-disturbing human activities, related exposure durations, and associated mass loads (e.g., 0.10 fraction of the day spent outside doing high surface-disturbing activities). Given the high significance to waste isolation of the inhalation dose calculation, this task evaluates and verifies the assumptions for mass loading parameters used in the TPA code and evaluates the impacts on dose estimations. This chapter summarizes the bases, assumptions, and derivations of the mass loading and related inhalation model parameters and their potential effects on consequence analyses for a postulated extrusive volcanism scenario.

5.2 Methodology

As implemented in the TPA code, the mass loading parameters provide the average airborne particle concentrations in air for use in calculations (involving breathing rate and exposure duration parameters) to estimate the inhalation dose. Some or all these parameters are defined by the exposure scenario at 10 CFR Part 63, are temporally and spatially variable, and are interdependent. For example, the amount of dust in the air varies temporally and spatially and is influenced by a number of variables including the types of human activities and local characteristics assumed for the exposure scenario. In turn, the types of human activities determine the amount of time spent outdoors, the activity level, and, subsequently, the breathing rate. Although such variables normally are measured on short timescales (seconds and hours) and can include transient extremes, an estimate of annual dose should include parameter values representative of average annual exposure conditions experienced by the dose receptor.

The inhalation dose estimate is based on how much mass is inhaled per day. In this analysis, staff evaluates breathing rates; types of human activities and activity levels (such as time spent outdoors and time spent performing surface-disturbing activities); mass loading data applicable to surface-disturbing activities, including light work (e.g., walking) and hard work (e.g., gardening and digging); and dust levels that might develop shortly after an igneous event. These evaluations are used to derive those parameters needed to estimate the mass load inhaled per day for comparison with values from previous assumptions and parameters.

Breathing rates vary according to types of activities, which is important because higher breathing rates may occur during periods when the mass loading may be higher because of surface-disturbing activities (e.g., gardening may raise mass loading and the breathing rate compared with sleeping when the breathing rate and mass loading may be low). Table 5-1 provides breathing rates and daily exposure times for indoor and outdoor activities used to estimate the total mass inhaled per day. Breathing rates are based on physiologic data while exposure times were estimated by staff as reasonable assumptions.

The value for mass loading is likely to be strongly influenced by the occurrence of an igneous event due to the dispersal of ash particles in the region. Selecting appropriate values for mass loading for fresh ash is based on consideration of measurements and observations of mass loading for volcanic eruptions at Cerro Negro, Nicaragua, and Montserrat, West Indies. Although much available mass loading information applicable to volcanic ash is based on 24-hour measurements not directly applicable to short-term exposure calculations, these two data sources include shorter duration mass loading measurements associated with specific types of surface-disturbing activities.

Measurements of mass loading at Cerro Negro (Hill and Connor, 2000), collected for airborne dust particles less than 100 μm [0.004 in] in diameter using both fixed and personal breathing zone samplers, varied from approximately 1 to 10 mg/m^3 [6.24×10^{-8} to 6.24×10^{-7} lbm/ft^3] for conditions indicative of light disturbance (walking) to heavy disturbance (behind a moving automobile). At Montserrat (Searl, et al., 2002), measured mass loading due to 10-μm [0.0004-in] diameter particles (i.e., PM_{10}) was as high as 2.5 mg/m^3 [1.56×10^{-7} lbm/ft^3] for short time periods of high disturbance and was generally at much lower levels most of the time {i.e., average mass

Table 5-1. Activity-Specific Breathing Rates, Times, and Daily Inhaled Volumes					
		Outdoors		Indoors	
Activity	Breathing Rate* (m^3/hr)	Time/day (hours)	Inhaled Volume (m^3)	Time/day (hours)	Inhaled Volume (m^3)
Sleeping	0.4	—	—	8.00	3.20
Sedentary	0.5	—	—	3.00	1.50
Light work	0.6	2.00	1.20	3.00	1.80
Moderate work	1.7	2.75	4.68	2.00	3.40
Hard work	2.5	0.25	0.62	0.50	1.25
Offsite	0.6	1.25	0.75	1.25	0.75
Total	—	6.25	7.25	17.75	11.90

*Based on information in Kennedy, W.E. and D.L. Strenge. NUREG/CR–5512. "Residual Radioactive Contamination from Decommissioning: Technical Basis for Translating Contamination Levels to Annual Total Effective Dose Equivalent." Vol. 1. Table 6.23. Washington, DC: NRC. 1992.

loading less than 0.25 mg/m^3 [1.56×10^{-8} lbm/ft^3]}. The Montserrat mass loadings were reported at different locations, both indoors and outdoors, for a 14-hour period. Although many mass loading measurements reported in the scientific literature are not directly comparable, because of the potential differences in objectives and methodologies, values such as 0.02 mg/m^3 [1.25×10^{-9} lbm/ft^3] for clean air, 0.22 mg/m^3 [1.37×10^{-8} lbm/ft^3] for high-end urban particulate, and 110 mg/m^3 [6.87×10^{-6} lbm/ft^3] as barely tolerable for breathing (Kennedy and Strenge, 1992) provide a general frame of reference for the values being considered. The airborne particulate concentrations reported for volcanic ash, as expected, are generally higher than more commonly measured values reported in air pollution or dust research. Staff was unable to identify studies reporting airborne particulate concentrations for resuspended ash from surface-disturbing activities that were higher than those concentrations reported for Cerro Negro.

As previously mentioned, time-dependent data reported at Montserrat showed high mass loadings of short duration over time. Measured values of mass loading versus time typically showed transient peaks 5 to 10 times higher than most values and were well more than 10 times shorter in duration. To account for the observation that peaks are of short duration, composite mass loading values were estimated by applying time weighting to the values of the reported range {i.e., 1 to 10 mg/m^3 [6.24×10^{-8} to 6.24×10^{-7} lbm/ft^3]}. Composite mass loading values were estimated for different levels of surface-disturbing activities including light, moderate, and heavy work. Within each level of surface-disturbing activity, low, medium, and high composite mass loads were estimated. Specifically, the composite mass loading is the sum of the products of each reported range end value (upper and lower) and the respective time weights. The time weights were based on the reported time series of measured mass loads (Searl, et al., 2002) and included the

percentage of time the mass loading was expected to be at the upper end of the range. The remainder of the time, the mass loading was assumed to be at the low end of the range.

Because disturbance of surficial deposits is likely greatest during hard work activities, the time weights considered for estimating a composite mass loading for outdoor hard work activity are the largest at 5, 25, and 50 percent (i.e., the percentage of time the measured upper peak mass load value applies to low, medium, and high composite mass loads). Comparable time weights for the outdoor moderate work activity, for which surface disturbance is expected to be less, are reduced by a factor of five from the outdoor hard work activity values (i.e., 1, 5, and 10 percent of the time the upper peak value applies) and further reduced by another factor of five for light work activities (i.e., 0.2, 1, and 2 percent of the time the upper peak value applies). Table 5-2 presents the estimated composite mass loadings for fresh ash based on this approach. Table 5-2 uses a mass load range of 1 to 10 mg/m^3 [6.24×10^{-8} to 6.24×10^{-7} lbm/ft^3] to estimate the composite value. As described previously, the values measured at Cerro Negro varied between 1 and 10 mg/m^3 [6.24×10^{-8} and 6.24×10^{-7} lbm/ft^3] for particle sizes to 100 microns [0.004 in], while the mass loading values reported for Montserrat were as high as 2.5 mg/m^3 [1.56×10^{-7} lbm/ft^3] for particle sizes to 10 microns [0.0004 in]. Assuming particles to 100 microns [0.004 in] in diameter can be inhaled, the range measured at Cerro Negro was used for the current approach (it can be expected that values measured at Montserrat would have been higher if larger particle sizes were included in the measurements).

Indoor values for mass loading are likely less than the outdoor values. For various activity levels of housework, the indoor mass load is assumed half the outdoor work mass loading. The assumption that the mass loading indoors is half the outdoor values for similar levels of activity (e.g., moderate work activities) may be likely overly conservative when the mass loading values are especially high (i.e., high work activities). Indoor activities that involve little to no dust-increasing motion (i.e., sleeping and sedentary activities) are assumed to generate mass loads half the indoor light work value. Table 5-3 provides estimated indoor composite mass loadings for fresh ash conditions based on the time weighting approach previously discussed.

A similar approach can be used to estimate composite mass loading values for the background conditions (i.e., soil) that might be representative of mass loading once the effects of volcanic ash on the mass loading have substantially dissipated. This dissipation is estimated to take hundreds of years, however, the longevity of the ash blanket is subject to impacts from redistribution of regional ash deposits to the receptor location (as analyzed in Chapters 4 and 6 of this report). Estimated composite mass loading results for soil are presented in Tables 5-4 and 5-5.

5.3 Assumptions

Estimation of the mass loading is dependent on the types of surface-disturbing activities assumed for a potentially exposed individual. Estimates of the amount of material inhaled are dependent on assumptions regarding the time spent outdoors, where mass loading is likely to be highest, and the time spent doing moderate to hard work activities, which tend to raise mass loading because of surface disturbance. It was assumed the individual spent a significant portion of time outdoors (five hours per day) at the compliance location, and the presence of ash does not affect the activities of the exposure scenario after the ash had been deposited. Additionally, the potentially exposed individual was assumed to spend a significant amount of time performing moderate to

Table 5-2. Estimated Composite Values of Mass Loading for Outdoor Activities Assuming Fresh Ash Conditions				
Activity	**Mass Load Range (mg/m^3)**	**Low Composite Mass Load (mg/m^3)**	**Medium Composite Mass Load (mg/m^3)**	**High Composite Mass Load (mg/m^3)**
Light work	1–10	1.02 (0.2% high value)	1.09 (1% high value)	1.18 (2% high value)
Moderate work	1–10	1.09 (1% high value)	1.45 (5% high value)	1.90 (10% high value)
Hard work	1–10	1.45 (5% high value)	3.25 (25% high value)	5.50 (50% high value)

Table 5-3. Estimated Composite Values of Mass Loading for Indoor Activities Assuming Fresh Ash Conditions				
Activity	**Mass Load Range (mg/m^3)**	**Low Composite Mass Load (mg/m^3)**	**Medium Composite Mass Load (mg/m^3)**	**High Composite Mass Load (mg/m^3)**
Sleeping	0.25–2.5	0.25 (0.1% high value)	0.26 (0.5% high value)	0.27 (1% high value)
Sedentary	0.25–2.5	0.25 (0.1% high value)	0.26 (0.5% high value)	0.27 (1% high value)
Light work	0.50–5.0	0.51 (0.2% high value)	0.54 (1% high value)	0.59 (2% high value)
Moderate work	0.50–5.0	0.54 (1% high value)	0.72 (5% high value)	0.95 (10% high value)
Hard work	0.50–5.0	0.72 (5% high value)	1.62 (25% high value)	2.75 (50% high value)

hard work indoors (2.5 hours per day) and outdoors (3 hours per day) or approximately 40 hours per week performing moderate to hard work activities.

Estimation of daily mass of volcanic ash inhaled involves other assumptions. Many of these assumptions already have been discussed in the methods section and are summarized here for transparency.

Table 5-4. Estimated Composite Values of Mass Loading for Outdoor Activities Assuming Soil Conditions				
Activity	**Mass Load* Range (mg/m^3)**	**Low Composite Mass Load (mg/m^3)**	**Medium Composite Mass Load (mg/m^3)**	**High Composite Mass Load (mg/m^3)**
Light work	0.1–0.7	0.10 (0.2% high value)	0.11 (1% high value)	0.11 (2% high value)
Moderate work	0.1–0.7	0.11 (1% high value)	0.13 (5% high value)	0.16 (10% high value)
Hard work	0.1–0.7	0.13 (5% high value)	0.25 (25% high value)	0.40 (50% high value)
*Based on information in Kennedy, W.E. and D.L. Strenge. NUREG/CR–5512. "Residual Radioactive Contamination from Decommissioning: Technical Basis for Translating Contamination Levels to Annual Total Effective Dose Equivalent." Vol. 1. Table 6.23. Washington, DC: NRC. 1992.				

Table 5-5. Estimated Composite Values of Mass Loading for Indoor Activities Assuming Soil Conditions				
Activity	**Mass Load Range (mg/m^3)**	**Low Composite Mass Load (mg/m^3)**	**Medium Composite Mass Load (mg/m^3)**	**High Composite Mass Load (mg/m^3)**
Sleeping	0.025–0.18	0.025 (0.1% high value)	0.026 (0.5% high value)	0.026 (1% high value)
Sedentary	0.025–0.18	0.025 (0.1% high value)	0.026 (0.5% high value)	0.026 (1% high value)
Light work	0.050–0.35	0.051 (0.2% high value)	0.053 (1% high value)	0.056 (2% high value)
Moderate work	0.050–0.35	0.053 (1% high value)	0.065 (5% high value)	0.080 (10% high value)
Hard work	0.050–0.35	0.065 (5% high value)	0.120 (25% high value)	0.200 (50% high value)

- Ash particle diameters less than 100 μm [0.004 in] may be resuspended by wind or human disturbances and may be inhaled into the body, although only those less than 10 μm [0.0004 in] may enter the deep lung.

- Mass loading measurements from eruptions at Cerro Negro, Nicaragua, and Montserrat, West Indies, are likely representative of potential ash deposit and disturbance conditions for a postulated eruption event in the Yucca Mountain region.

- Average receptor activity characteristics are assumed (not worst case).

- Applicable surface-disturbing activities include gardening, walking, and riding in a truck.

- Heavy outdoor or indoor work generates high mass loading for a percentage of time that is five times greater than that for moderate work, and the percentage for moderate work is five times greater than light work.

- Sleeping and sedentary activities generate high mass loading for a percentage of time that is half the percentage applicable to light work activities.

- Mass loading indoors is half the outdoor mass loading.

- Indoor mass loading for nondisturbance activities (e.g., sleeping) is half the indoor light work value.

5.4 Results

Daily values for estimated inhaled mass from fresh ash, calculated as the product of the associated breathing rates, activity duration times, and composite mass loadings are presented in Tables 5-6 through 5-8. Results are stratified by low, medium, and high estimated composite mass loadings.

The estimated amounts of mass inhaled on a daily basis assuming low, medium, and high composite mass loadings from fresh ash conditions are 12.1, 16.8, and 22.8 mg [2.67×10^{-5}, 3.70×10^{-5}, and 5.03×10^{-5} lbm] {assuming an average breathing rate of 15 m^3/day [530 ft^3/day], an average daily mass inhaled for the three composite mass loading values would be 0.8, 1.1, and 1.5 mg/m^3 [5.0×10^{-8}, 6.9×10^{-8}, and 9.4×10^{-8} lbm/ft^3]}. By way of comparison, the previous values used in the TPA code analyses result in an average estimated mass load of ash inhaled of approximately 40 mg/day [8.8×10^{-5} lbm/day] from all activities, or approximately two to three times greater than the values provided in Tables 5-6 through 5-8. Because the estimated mass loading of fresh ash has a primarily linear effect on dose, it is likely the estimated dose is approximately two to three times less than the previous dose estimates if the values in Tables 5-6 through 5-8 are used.

Table 5-6. Estimated Daily Mass Inhaled from Outdoor and Indoor Exposures to Fresh Ash Conditions Assuming a Low Composite Mass Loading			
Activity	**Outdoor Mass Inhaled (mg)**	**Indoor Mass Inhaled (mg)**	**Total Mass Inhaled (mg)**
Sleeping	Not applicable	0.81	0.81
Sedentary	Not applicable	0.38	0.38
Light work	1.22	0.92	2.14
Moderate work	5.09	1.85	6.94
Hard work	0.91	0.91	1.82
All activities	7.22	4.87	12.09

Table 5-7. Estimated Daily Mass Inhaled from Outdoor and Indoor Exposures to Fresh Ash Conditions Assuming a Medium Composite Mass Loading			
Activity	**Outdoor Mass Inhaled (mg)**	**Indoor Mass Inhaled (mg)**	**Total Mass Inhaled (mg)**
Sleeping	Not applicable	0.84	0.84
Sedentary	Not applicable	0.39	0.39
Light work	1.31	0.98	2.29
Moderate work	6.78	2.46	9.24
Hard work	2.03	2.03	4.06
All activities	10.12	6.70	16.82

The estimated daily amount of mass inhaled was similarly calculated for soil conditions and is presented in Tables 5-9 through 5-11. The amount of mass inhaled on a daily basis assuming low, medium, and high composite mass loadings from soil conditions is estimated to be 1.17, 1.50, and 1.87 mg [2.58×10^{-6}, 3.31×10^{-6}, and 4.12×10^{-6} lbm]. Assuming an average breathing rate of 15 m^3/day [530 ft^3/day], an estimate of the average daily mass inhaled for the three composite mass loading values would be 0.08, 0.1, and 0.12 mg/m^3 [5.0×10^{-9}, 6.2×10^{-9}, and 7.5×10^{-9} lbm/ft^3]. By way of comparison, the TPA code input values estimate an average mass for soil inhaled of approximately 1.1 mg/day [2.4×10^{-6} lbm/day] from all activities or approximately 60–95 percent of the values provided in Tables 5-9 through 5-11.

Table 5-8. Estimated Daily Mass Inhaled from Outdoor and Indoor Exposures to Fresh Ash Conditions Assuming a High Composite Mass Loading			
Activity	**Outdoor Mass Inhaled (mg)**	**Indoor Mass Inhaled (mg)**	**Total Mass Inhaled (mg)**
Sleeping	Not applicable	0.87	0.87
Sedentary	Not applicable	0.41	0.41
Light work	1.42	1.06	2.48
Moderate work	8.88	3.23	12.11
Hard work	3.44	3.44	6.88
All activities	13.74	9.01	22.75

Table 5-9. Estimated Daily Mass Inhaled from Outdoor and Indoor Exposures to Soil Conditions Assuming a Low Composite Mass Loading			
Activity	**Outdoor Mass Inhaled (mg)**	**Indoor Mass Inhaled (mg)**	**Total Mass Inhaled (mg)**
Sleeping	Not applicable	0.08	0.08
Sedentary	Not applicable	0.04	0.04
Light work	0.12	0.09	0.21
Moderate work	0.50	0.18	0.68
Hard work	0.08	0.08	0.16
All activities	0.70	0.47	1.17

The mass loading from fresh ash has a far greater effect on inhalation dose than the mass loading from ash that has become a part of the soil (termed soil conditions) owing to the greater mass loading estimated for fresh ash conditions.

5.5 Conclusions

Analysis estimates composite daily mass loading varies by approximately a factor of two for a wide range of duration for the peak values (i.e., 5 to 50 percent of the time). Using the medium value for the composite mass loading for fresh ash conditions {i.e., 1.12 mg/m^3 [7.0 × 10^{-8} lbm/ft^3]} and soil conditions {i.e., 0.1 mg/m^3 [6.2 × 10^{-9} lbm/ft^3]} in the TPA code resulted in approximately a factor of two reduction in the overall dose estimate. The results from this analysis were considered in developing mass loading parameters in the latest version of the TPA code.

Table 5-10. Estimated Daily Mass Inhaled from Outdoor and Indoor Exposures to Soil Conditions Assuming a Medium Composite Mass Loading			
Activity	**Outdoor Mass Inhaled (mg)**	**Indoor Mass Inhaled (mg)**	**Total Mass Inhaled (mg)**
Sleeping	Not applicable	0.08	0.08
Sedentary	Not applicable	0.04	0.04
Light work	0.13	0.10	0.23
Moderate work	0.61	0.22	0.83
Hard work	0.16	0.16	0.32
All activities	0.90	0.60	1.50

Table 5-11. Estimated Daily Mass Inhaled from Outdoor and Indoor Exposures to Soil Conditions Assuming a High Composite Mass Loading			
Activity	**Outdoor Mass Inhaled (mg)**	**Indoor Mass Inhaled (mg)**	**Total Mass Inhaled (mg)**
Sleeping	Not applicable	0.08	0.08
Sedentary	Not applicable	0.04	0.04
Light work	0.13	0.10	0.23
Moderate work	0.75	0.27	1.02
Hard work	0.25	0.25	0.50
All activities	1.13	0.74	1.87

This approach for estimating composite values for mass loading provides the basis for input values to computer models for easy comparison with other estimates of mass loading based on the daily mass inhaled. The discussion in Chapter 4 of this report provides further information regarding mass loading. Furthermore, the results from this analysis supported the development of the alternative ash remobilization model and associated data and input parameters in Chapter 6.

6 ASH REMOBILIZATION MODELING FOR EXTRUSIVE VOLCANISM

TASK DESCRIPTION

Develop an alternative model to estimate the risk of extrusive volcanism, taking into account ash remobilization and assumptions of wind speed and direction.

AUTHORS/CONTRIBUTORS

R. Benke, D. Hooper, B. Hill, R. Nes, and B. Winfrey

6.1 Background and Purpose

An extrusive volcanic event may occur if a volcanic eruption intersects the potential repository at Yucca Mountain and releases high-level waste directly into the atmosphere as trace contamination of volcanic tephra (i.e., ash). The surface transport of ash following the initial deposition from a volcanic eruption plume is referred to as ash remobilization. The transport of ash by surficial water drainage in Fortymile Wash (referred to as fluvial remobilization) and by wind (referred to as eolian remobilization) is addressed in this chapter.

Resuspension of ash particles produces airborne concentrations (also referred to as the airborne mass load) of ash and high-level waste. The estimated total dose for extrusive volcanism, which is dominated by the inhalation of resuspended volcanic ash, is significantly influenced by the amount of fine ash particles in the air (NRC, 2004). Ash remobilization processes may considerably affect the thickness of the deposited ash layer near the receptor and the extent of potential mixing of the ash with the underlying soil, which both factor into the proportion of ash in the airborne particle load. The reasonably maximally exposed individual (i.e., receptor) may be exposed to airborne contamination from the resuspension of (i) the initial ash deposit at the receptor location, (ii) fluvially remobilized ash in Fortymile Wash, and (iii) ash deposited in the Yucca Mountain region and remobilized by eolian processes. This analysis accounts for these three source terms for airborne concentration of high-level waste at the receptor location through time. Chapter 5 of this progress report focuses on the airborne particle mass load (above a fresh ash deposit and soil) but does not address explicitly the time evolution of the airborne concentration of ash and high-level waste at the receptor location from initial deposit, fluvial remobilization of ash, and eolian remobilization of ash.

An alternative model was developed and implemented in the latest version of the TPA code with the intention of gaining fundamental insights into ash remobilization and risk to the reasonably maximally exposed individual, that may be used to capture the main effects of surficial transport processes on the airborne concentration of high-level waste at the receptor location as a function of time after an eruption. A description is provided of the alternative model, which can account for wind-field variations along the height of the tephra column that affect the initial deposition of ash and the first-order processes affecting fluvial and eolian remobilization of ash. Intermediate results from the conceptual model development and detailed analyses (Hooper, 2004) factored into developing the alternative model. The output of the alternative model is the temporal evolution of the airborne concentration of high-level waste at the receptor location following a volcanic eruption that intersects the potential repository at Yucca Mountain. The alternative model uses a lookup table, which contains parameter values determined from detailed analyses, to estimate time

evolutions of the airborne concentration of high-level waste at the receptor location from the initial deposit and fluvial and eolian remobilization of ash. Detailed analyses calculate the three-dimensional deposition of ash with a stratified wind field and provide data for the lookup table and the values for other input parameters used in the alternative model.

This task directly relates to the four risk insights presented in the Risk Insights Baseline Report (NRC, 2004). These four risk insights and their associated significance to waste isolation are

- Inhalation of Resuspended Volcanic Ash (high significance to waste isolation)
- Remobilization of Ash Deposits (medium significance to waste isolation)
- Wind Vectors During an Eruption (medium significance to waste isolation)
- Volume of Ash Produced by an Eruption (medium significance to waste isolation)

6.2 Methodology

This task consists of two subtask. The first subtask relates to development of an alternative model for the TPA code that captures the first-order effects of ash remobilization on the airborne concentration of high-level waste at the receptor location. The second subtask relates to the conceptual model development and detailed analyses to provide input data for the alternative TPA code model and obtain fundamental insights about remobilization and risk to the reasonably maximally exposed individual. These two subtask are detailed next.

6.2.1 Subtask 1—Alternative Model

The ASHPLUMO module for the TPA code calculates the initial areal deposition of ash and high-level waste at the receptor location by invoking the ASHPLUME code. To account for the variation in the mass of ash at the receptor location with time, the TPA code uses a compartment abstraction. An alternative approach is to implement more flexibility in representing the time dependence of airborne concentrations of high-level waste. Implementing the alternative model required coding changes in the ASHRMOVO and DCAGS modules and modifications to the TPA code input file. There were no modifications to the ASHPLUME code (within the TPA code) or the ASHPLUMO module.

The TPA code was modified to enable the user to select one of two modes for calculating the evolution of airborne mass load at the receptor location following a volcanic eruption. The first mode is consistent with the current TPA code model; the second mode invokes the alternative model presented in this chapter.

The parameter AshEvolutionMode in the TPA code input file represents the mode for calculating the airborne mass load with allowed values of either 0, to fix the wind direction toward the receptor and neglect the effects of ash remobilization, or 1, to account for a stratified wind field and estimate the effects of ash remobilization.

When AshEvolutionMode is set to 0, the DCAGS module uses simple exponential decay functions to account for the erosion of the initial ash deposit and an assumed reduction of airborne particle loading with time after an eruption. These relationships are used in the current TPA code. The alternative model described in this chapter is not used for this mode of calculating the evolution of ash.

When AshEvolutionMode is set to 1, the TPA code accounts for three components of the airborne concentration of high-level waste through time at the receptor location. The first component is the contribution from ash initially deposited at the reasonably maximally exposed individual location. The second component is the contribution from the fluvial remobilization of ash. The third component is the contribution from the eolian remobilization of ash. The airborne concentration of high-level waste through time at the receptor location is determined as the sum of these three contributions. Figure 6-1 presents a schematic representation of the three components and the sum for an example eruption that deposits ash in each of the three source regions. Because modeled eruptions may not always deposit ash in all three source regions, there may be some TPA code realizations in which at least one of the three contributions is zero. The remainder of this section focuses on this alternative mode for calculating the evolution of ash at the receptor location (i.e., AshEvolutionMode set to 1). For this mode, the ASHPLUMO module is not used in the TPA code calculations. The alternative model is used to calculate the inhalation doses only.

To account for the effect of a stratified wind field on ash dispersion during modeled eruptions, the alternative model uses a lookup table. The lookup table is used to apply the suite of results computed from detailed analyses using the parallelized version of the TEPHRA code, as described in Section 6.2.2, into the alternative model. The lookup table approach is implemented for the alternative model because this approach, performing ASHPLUME calculations for an initial ash deposit in three dimensions (i.e., variable thicknesses over a two-dimensional grid) and tracking the remobilization of ash through time, would be extremely computationally intensive. Because of the large computational requirements for this detailed modeling for the time evolution of the three dimensional distribution of ash, the detailed analyses (Section 6.2.2) using a parallelized version of the TEPHRA code was performed outside the TPA code. This external code produces results that populate the lookup table for the alternative model. Table 6-1 shows the format for the lookup table.

The output from the alternative remobilization model to the DCAGS module is a time history of the airborne concentration of high-level waste at the receptor location. The alternative remobilization model accounts for the inhalation of resuspended radioactive material both outdoors and indoors. The presentation of the mathematical relationships used in the alternative model is focused on the outdoor airborne concentration of high-level waste. Calculations of the indoor airborne mass load use the same proportions from each of three contributions (i.e., initial deposit at the receptor location, fluvial remobilization, and eolian remobilization) for the total outdoor airborne particle concentration to which the receptor is exposed. In other words, the proportion of the airborne mass load from the three components is the same indoors and outdoors. The outdoor airborne concentration of high-level waste [g/m^3] at the receptor location weighted by the outdoor occupancy fractions during heavy and light disturbance, $H_{\mathrm{RMEI,outdoor}}(t)$, is calculated as

$$H_{\mathrm{RMEI,outdoor}}(t) = f_{\mathrm{out}-H}\, H_{i-H}(t) + f_{\mathrm{out}-L}\, H_{i-L}(t) + \left(f_{\mathrm{out}-H} + f_{\mathrm{out}-L}\right) H_f(t) + \left(f_{\mathrm{out}-H} + f_{\mathrm{out}-L}\right) H_e(t) \quad (6\text{-}1)$$

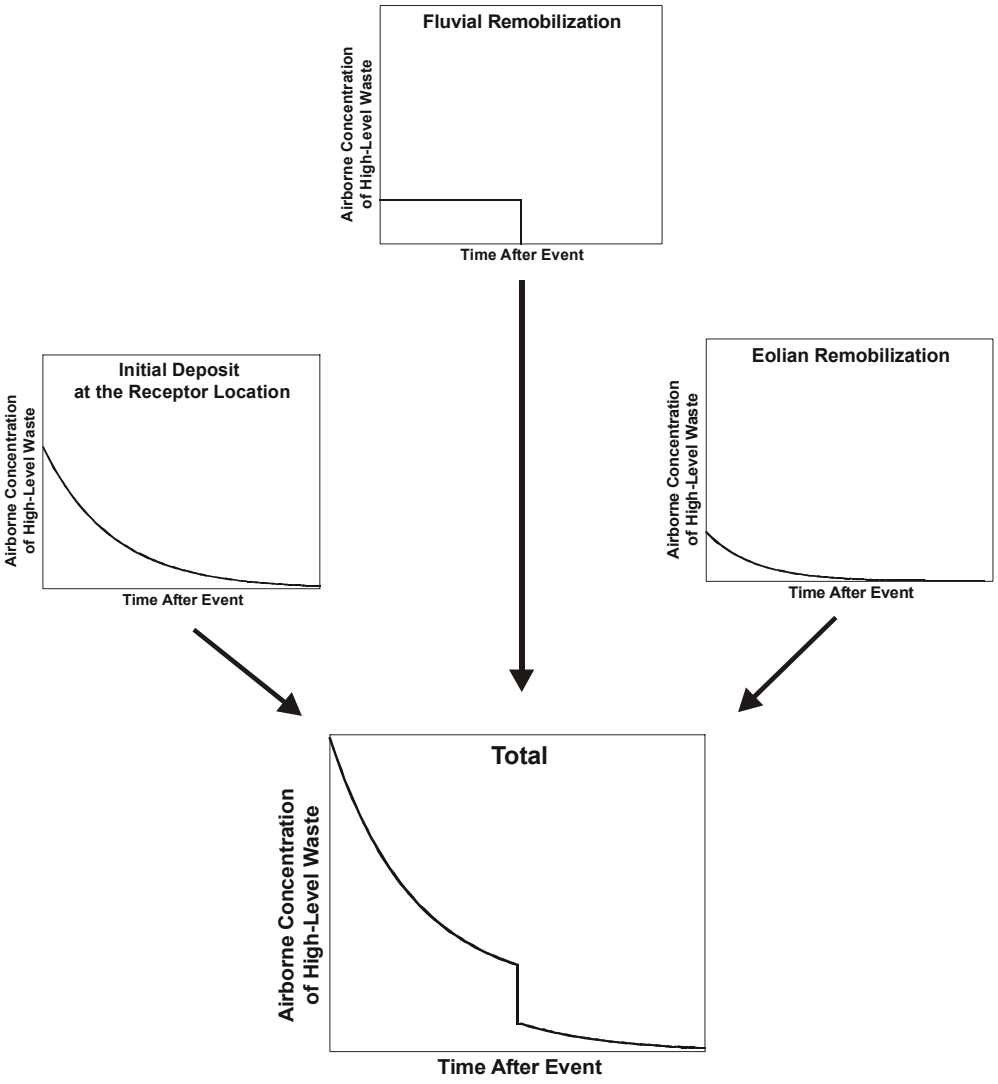

Figure 6-1. Schematic Representation of the Time Evolution of the Total Airborne Concentration of High-Level Waste at the Receptor Location Resulting from Contributions from the Initial Deposit at the Receptor Location, Fluvial Remobilization, and Eolian Remobilization for an Example Eruption that Deposits Ash in Each of the Three Source Regions

Table 6-1. Format for the Lookup Table Consisting of *n* Realizations of the TEPHRA Code*

$c_{HLW,i,1}$	$c_{ash,i,1}$	$m_{HLW,f,1}$	$m_{ash,f,1}$	$a_{ash,f,1}$	$m_{HLW,e,1}$	$m_{ash,e,1}$	$a_{ash,e,1}$
$c_{HLW,i,2}$	$c_{ash,i,2}$	$m_{HLW,f,2}$	$m_{ash,f,2}$	$a_{ash,f,2}$	$m_{HLW,e,2}$	$m_{ash,e,2}$	$a_{ash,e,2}$
.	.	.	.	.	.	.	.
.	.	.	.	.	.	.	.
.	.	.	.	.	.	.	.
.	.	.	.	.	.	.	.
.	.	.	.	.	.	.	.
.	.	.	.	.	.	.	.
.	.	.	.	.	.	.	.
$c_{HLW,i,n}$	$c_{ash,i,n}$	$m_{HLW,f,n}$	$m_{ash,f,n}$	$a_{ash,f,n}$	$m_{HLW,e,n}$	$m_{ash,e,n}$	$a_{ash,e,n}$

*A description of the parameters is provided in Table 6-2 of the Risk Analysis for Risk Insights Progress Report. Each row corresponds to the results from a single realization of the TEPHRA code, denoted by the indices (1, 2, ..., n).

where

$H_{i\text{-}H}(t)$ — contribution to the airborne concentration of high-level waste from the initial ash deposit at the receptor location during heavy distrubance [g/m^3]

$H_{i-L}(t)$ — contribution to the airborne concentration of high-level waste from the initial ash deposit at the receptor location during light disturbance [g/m^3]

$H_f(t)$ — contribution to the airborne concentration of high-level waste from the fluvial remobilization of ash [g/m^3]

$H_e(t)$ — contribution to the airborne concentration of high-level waste from the eolian remobilization of ash [g/m^3]

f_{out-H} — fraction of time receptor spends outdoors with heavy disturbance [unitless] {OccupancyFractionOutsideHeavyDisturbance[-]}

f_{out-L} — fraction of time receptor spends outdoors with light disturbance [unitless] {OccupancyFractionOutsideLightDisturbance[-]}

t — time following volcanic eruption [yr]

A discussion on each of the calculations follows separately for each contribution.

Table 6-2. Summary Table of the Input Parameters for the Alternative RemobilizationModel		
Parameter	**Description**	**Source**
w_i	Weighting factor for the contribution of the airborne mass load above the initial deposit to the total airborne particle concentration at the receptor location [unitless]	TPA code input file
$c_{\mathrm{HLW},i}$	Mass of high-level waste for the initial deposit at the receptor location per unit area [g/m^2]	Lookup table
$c_{\mathrm{ash},i}$	Mass of ash for the initial deposit at the receptor location per unit area [g/m^2]	Lookup table
$S_{\mathrm{ash,out}-H}$	Outdoor mass load above fresh ash with heavy disturbance [g/m^3]	TPA code input file
$S_{\mathrm{ash,out}-L}$	Outdoor mass load above fresh ash with light disturbance [g/m^3]	TPA code input file
$f_{\mathrm{out}-H}$	Fraction of time receptor spends outdoors with heavy disturbance [unitless]	TPA code input file
$f_{\mathrm{out}-L}$	Fraction of time receptor spends outdoors with light disturbance [unitless]	TPA code input file
λ_r	Rate of reduction of airborne mass load [1/yr]	TPA code input file
w_f	Weighting factor for the contribution of the airborne mass load above the sediment deposit from fluvial remobilization to the total airborne particle concentration at the receptor location [unitless]	TPA code input file
$m_{\mathrm{HLW},f}$	Mass of high-level waste deposited in the Fortymile Wash catchment basin from the eruption [g]	Lookup table
$m_{\mathrm{ash},f}$	Mass of ash deposited in the Fortymile Wash catchment basin from the eruption [g]	Lookup table
$a_{\mathrm{ash},f}$	Area of the Fortymile Wash catchment basin with an ash deposit from the eruption [m^2]	Lookup table
$\rho_{\mathrm{ash},f}$	Density of proximal ash deposit [g/m^3]	TPA code input file
$Y_{\mathrm{sediment},f}$	Preeruption sediment volume from the drainage basin that discharges through Fortymile Wash per unit area per discharge event [m/event]	TPA code input file
$A_{\mathrm{basin},f}$	Total area of the drainage basin that discharges through Fortymile Wash [m^2]	TPA code input file

Table 6-2. Summary Table of the Input Parameters for the Abstracted Model (continued)		
Parameter	**Description**	**Source**
T_f	Average time between significant flow events [yr/event]	TPA code input file
$Y_{ash,f}$	Posteruption volume of fluvial remobilized ash at the Fortymile Wash depositional region per unit area per discharge event [m/event]	TPA code input file
w_e	Weighting factor for the contribution of the particle mass load above the initial ash deposit in the eolian source area to the total airborne particle concentration at the receptor location [unitless]	TPA code input file
$m_{HLW,e}$	Mass of high-level waste deposited in the eolian source region from the eruption [g]	Lookup table
$m_{ash,e}$	Mass of ash deposited in the eolian source region from the eruption [g]	Lookup table
$a_{ash,e}$	Area of the eolian source region with an initial ash deposit from the eruption [m^2]	Lookup table
$\rho_{ash,e}$	Density of the distal ash deposit [g/m^3]	TPA code input file
A_{eolian}	Total area of the eolian source region [m^2]	TPA code input file

6.2.1.1 Contribution from the Initial Deposit at the Receptor Location

The contribution from the initial deposit addresses airborne concentrations for heavy and light disturbances separately. The contribution from the initial deposit during heavy disturbance is calculated as

$$H_{i\text{-}H}(t) = c_i \times S_{ash,out\text{-}H} \times f_R(t) \times \exp(-\lambda_r t) \quad (6\text{-}2)$$

where

c_i — concentration factor for high-level waste in ash for the initial deposit at the receptor location (grams of high-level waste per unit area/grams of ash per unit area) [g_{HLW}/g_{ash}]

$S_{ash,out\text{-}H}$ — outdoor mass load above fresh ash with heavy distrubance [g/m^3] {AirborneMassLoadAboveFreshAshBlanketHeavyDisturbance[g/m3]}

$f_R(t)$ — time-dependent fraction of resuspended mass emanated from contaminated volcanic layer [unitless]

λ_r — rate of reduction of airborne mass load [1/yr]
{RateOfReductionOfMassLoadingFactor[1/yr]}

The contribution from the initial deposit during light disturbance is calculated as

$$H_{i-L}(t) = w_i \times c_i \times S_{\text{ash,out}-L} \times f_R(t) \times \exp(-\lambda_r t) \quad (6\text{-}3)$$

where

w_i — weighting factor for the contribution of the airborne mass load above the initial deposit to the total airborne particle concentration at the receptor location [unitless]

$S_{\text{ash,out}-L}$ — outdoor mass load above fresh ash with light disturbance [g/m^3]
{AirborneMassLoadAboveFreshAshBlanketLightDisturbance[g/m3]}

The weighting factor, W_i, is a TPA code input parameter. Heavy disturbance conditions tend to result from human-induced activities and are assumed to occur only on the initial deposit at the receptor location. Large-scale heavy disturbance conditions in the fluvial and eolian source regions, such as sand storms, are neglected because those conditions are not likely to significantly affect annual dose estimates due to a low probability of occurrence and short duration of exposure relative to the annual time frame. Small-scale heavy disturbance conditions in those regions, due to plowing fields, for example, are neglected because the surface area affected by increased surface-disturbing activities, at any given time, is likely a small fraction of the total surface area for the source region. Additionally, localized increases in surface-disturbing activities on the fluvial and eolian source regions are expected to have a small effect on the annual-average airborne mass load at the receptor location because (i) the airborne concentration reduces due to dispersion as the plume migrates downwind and (ii) the wind blows the plume from the localized surface-disturbing activities directly toward the receptor only part of the time.

In other words, heavy disturbance activities and outdoor mass loads during heavy disturbances do not apply to the contributions from fluvial and eolian remobilization. For these reasons, a weighting factor is not included in Eq. (6-2). The concentration factor, c_i, is a value calculated from the lookup table (Table 6-1) in the following manner

$$c_i = \frac{c_{\text{HLW},i}}{c_{\text{ash},i}} \quad (6\text{-}4)$$

where

$c_{\text{HLW},i}$ — mass of high-level waste per unit area for the initial deposit at the receptor location [g/m^2]

$c_{\text{ash},i}$ — mass of ash per unit area for the initial deposit at the receptor location [g/m^2]

For thin ash deposits, the time-dependent resuspension factor, $f_R(t)$, accounts for the dilution of resuspended contaminated ash with noncontaminated soil. If the ash deposit is thicker than or equal to the resuspendible layer thickness {DepthOfResuspendibleLayer[cm] hereinafter referred to as d_r}, $f_R(t)$ equals unity. If the ash deposit is thinner than the resuspendible layer thickness, $f_R(t)$ equals the ratio of the ash deposit thickness to the thickness of the resuspendible layer (<1).

6.2.1.2 Contribution from Fluvial Remobilization

The fluvial remobilization contribution to the airborne concentration of high-level waste at the receptor location is calculated as

$$H_f(t) = w_f \times c_f \times d_f \times S_f(t) \tag{6-5}$$

where

w_f — weighting factor for the contribution of the airborne mass load above the sediment deposit from fluvial remobilization to the total airborne particle concentration at the receptor location [unitless]

c_f — concentration factor for high-level waste in the sediment [$g_{HLW}/g_{sediment}$]

d_f — dilution factor for mixing noncontaminated and contaminated sediments during fluvial remobilization [unitless]

$S_f(t)$ — airborne mass load above the sediment deposit [g/m^3]

Although ash remains in the Fortymile Wash catchment basin, the airborne mass load above the sediment deposit, $S_f(t)$, is set equal to the value of the TPA code input parameter for the outdoor airborne mass load of ash above a fresh deposit for light disturbance {AirborneMassLoadAboveFreshAshBlanketLightDisturbance[g/m3]}. After the ash has been depleted from the Fortymile Wash catchment basin, $S_f(t)$ is set equal to zero (refer to additional discussion in Section 6.3, Assumptions).

The weighting factor, w_f, is a parameter specified in the TPA code input. The concentration factor, c_f, is a value calculated from the lookup table (Table 6-1) in the following manner

$$c_f = \frac{m_{\mathrm{HLW},f}}{m_{\mathrm{ash},f}} \tag{6-6}$$

where

$m_{HLW,f}$ — mass of high-level waste deposited in the Fortymile Wash catchment basin from the eruption [g]

$m_{ash,f}$ — mass of ash deposited in the Fortymile Wash catchment basin from the eruption [g]

The dilution factor, d_f, is calculated as

$$d_f = \frac{v_{ash,f}}{v_{sediment,f} + v_{ash,f}} \quad (6\text{-}7)$$

where

$v_{ash,f}$ — total volume of ash deposited in the Fortymile Wash catchment basin [m^3]

$v_{sediment,f}$ — total volume of noncontaminated sediment yielded by the Fortymile Wash drainage system during the time period of fluvial ash remobilization [m^3]

The ash volume is calculated from parameters in the lookup table and TPA code input file as

$$V_{ash,f} = \frac{m_{ash,f}}{\rho_{ash,f}} \quad (6\text{-}8)$$

where $\rho_{ash,f}$ represents the density of ash [g/m^3] and equals the value for the TPA code ash density parameter AshBulkDensity[g/cm3] multiplied by a unit conversion factor of 1,000,000 cm^3/m^3.

The sediment volume, $V_{sediment,f}$, also is calculated from parameters in the lookup table and TPA code input file as

$$v_{sediment,f} = Y_{sediment,f}\left(A_{basin,f} - a_{ash,f}\right)n_{deplete} \quad (6\text{-}9)$$

where

$Y_{sediment,f}$ — Preeruption sediment volume from the drainage basin that discharges through Fortymile Wash per unit area per discharge event [m/event]

$A_{basin,f}$ — Total area of the drainage basin that discharges through Fortymile Wash [m^2]

$a_{ash,f}$ — area of the Fortymile Wash catchment basin with an ash deposit from the eruption [m^2]

$n_{deplete}$ — number of significant flow events required to deplete the Fortymile Wash catchment basin of ash [unitless]

The number of significant flow events required to deplete the Fortymile Wash catchment basin of ash is determined from the following relationship

$$n_{deplete} = \frac{v_{ash,f}}{Y_{ash,f} a_{ash,f}} \quad (6\text{-}10)$$

where $Y_{ash,f}$ represents the posteruption volume of fluvial remobilized ash yielded from the Fortymile Wash catchment basin per unit area per discharge event [m/event].

The duration of fluvial remobilization component, $t_{duration,f}$, depends on the timing of the fluvial remobilization events and is computed as

$$t_{duration,f} = n_{deplete} T_f \quad (6\text{-}11)$$

where T_f represents the average time between significant flow events [yr/event].

6.2.1.3 Contribution from Eolian Remobilization

The eolian remobilization contribution to the airborne concentration of high-level waste at the receptor location is calculated as

$$H_e(t) = w_e \times c_e \times d_e \times S_e(t) \quad (6\text{-}12)$$

where

w_e — weighting factor for the contribution of the airborne mass load above the initial ash deposit in the eolian source area to the total airborne particle concentration at the receptor location [unitless]

c_e — concentration factor for high-level waste in the eolian ash deposit [g_{HLW} /g_{ash}]

d_e — dilution factor for the eolian sediments [unitless]

$S_e(t)$ — airborne mass load above the eolian deposit [g/m^3]

Initially, $S_e(t)$ is set equal to the value of the TPA code input parameter for the outdoor airborne mass load of ash above a fresh deposit for light disturbance {AirborneMassLoadAboveFreshAshBlanketLightDisturbance[g/m3]}. The reduction in the airborne particle mass load above the eolian deposit with time is modeled with an exponential

decay function dependent on the value of the TPA code input parameter {RateOfReductionOfMassLoadingFactor[1/yr]}, which is the same approach used to model the reduction in the airborne particle mass load above the initial deposit at the receptor location.

The weighting factor, w_e, is a TPA code input parameter. The concentration factor, c_e, is a value calculated from the lookup table (Table 6-1) in the following manner

$$c_e = \frac{m_{\mathrm{HLW},e}}{m_{\mathrm{ash},e}} \tag{6-13}$$

where

$m_{\mathrm{HLW},e}$ — mass of high-level waste deposited in the eolian source region from the eruption [g]

$m_{\mathrm{ash},e}$ — mass of ash deposited in the eolian source region from the eruption [g]

The dilution factor, d_e, is calculated from values in the lookup table and the TPA code input parameters as

$$d_e = \begin{cases} \dfrac{a_{\mathrm{ash},e}}{A_{\mathrm{eolian}}} & \text{if} \quad \dfrac{m_{\mathrm{ash},e}\left(100\,\frac{\mathrm{cm}}{\mathrm{m}}\right)}{a_{\mathrm{ash},e}\,\rho_{\mathrm{ash},e}} > d_r \\ \dfrac{m_{\mathrm{ash},e}}{a_{\mathrm{ash},e}\,\rho_{\mathrm{ash},e}} \cdot \dfrac{a_{\mathrm{ash},e}}{A_{\mathrm{eolian}}} \cdot \dfrac{100\,\frac{\mathrm{cm}}{\mathrm{m}}}{d_r} & \text{if} \quad \dfrac{m_{\mathrm{ash},e}\left(100\,\frac{\mathrm{cm}}{\mathrm{m}}\right)}{a_{\mathrm{ash},e}\,\rho_{\mathrm{ash},e}} \le d_r \end{cases} \tag{6-14}$$

where

$a_{\mathrm{ash},e}$ — area of the eolian source region with an initial ash deposit from the eruption [m^2]

d_r — resuspendible layer thickness [cm] {DepthOfResuspendibleLayer[cm]}

$\rho_{\mathrm{ash},e}$ — density of the distal ash deposit [g/m^3]

A_{eolian} — total area of the eolian source region [m^2]

6.2.1.4 Execution of the Modified TPA Code

On execution of the modified TPA code, when the alternative model is activated (i.e., when the AshEvolutionMode flag is set to a value of 1), each realization of the TPA code selects a set of parameter values from the lookup table (Table 6-1). The lookup table contains parameter sets (approximately 1,024 sets) that are large compared with the typical number of realizations used in a TPA code simulation. Thus, the selection is performed without replacement (i.e., the same set of input parameter values is not selected twice within the same TPA code simulation). This condition may be relaxed if the number of TPA code realizations exceeds the number of parameter sets in the lookup table. Using the values for the selected set of parameter values, the alternative model calculations presented in the previous equations estimate the airborne concentration of high-level waste through time at the receptor location. This approach replaces

calculations performed by the ASHPLUMO, ASHRMOVO, and DCAGS modules. The radionuclide dose conversion factor calculations in the DCAGS module were modified to accept the airborne concentration of high-level waste directly from the alternative model. Table 6-2 provides a summary of the input parameters used by the alternative model. To accommodate the alternative model, the TPA code input file was modified. Table 6-3 presents the current and modified values of the TPA code igneous activity parameters.

6.2.2 Subtask 2—Detailed Analyses for Generating Data for the Alternative Model and Obtaining Risk Insights

The objectives for this subtask are to generate data for the alternative model (i.e., parameter values for use in the lookup table and other input parameter values as described in Section 6.2.1) and to yield fundamental insights about remobilization and risk to the reasonably maximally exposed individual. Further discussion of this subtask follows in the remaining paragraphs of this section.

A parallelized version of the TEPHRA code that includes modifications for a stratified wind field was developed by the staff to generate three-dimensional plots of the ash deposit. The TEPHRA code also was modified to account for high-level waste incorporation.

The staff investigated remobilization processes, developed the first-order conceptual model for fluvial remobilization that is abstracted for the alternative model in this chapter, and conducted detailed analyses. A conceptual model was formulated to address the potential remobilization and redistribution of contaminated tephra (i.e., ash) in the Fortymile Wash drainage system (Hooper, 2004). Although sediment erosion, transport, and deposition rates in arid regions such as Yucca Mountain are not well constrained, a sediment budget was constructed to account for long-term redistribution processes in the Fortymile Wash drainage system (Hooper, 2004). Following a potential volcanic eruption, a submillimeter-to-meter thick deposit of tephra may be deposited on the hillslopes around Yucca Mountain, which are part of the Fortymile Wash watershed. Surface processes subsequently may remobilize and redistribute the tephra deposit. The significance to waste isolation of these processes is that, through time, potentially significant amounts of resuspendible particles containing high-level waste may be transported to the general area of the reasonably maximally exposed individual. Simple mass-balance scoping calculations (Hill and Connor, 2000; Hooper, 2004) indicate the accumulation rate of remobilized tephra likely exceeds the decay rate in airborne mass load from the initial volcanic deposit at the receptor location. Thus, remobilization of tephra deposits may sustain estimated airborne mass loads and associated inhalation doses for longer periods of time than suggested by simple decay relationships for the initial volcanic deposits (e.g., Bechtel SAIC Company, LLC, 2003b,c). Generally speaking, the risk from a volcanic eruption increases when estimated inhalation doses persist for longer times after the eruption (NRC, 2004, Figure 4.3.11-2).

Modeling estimates that account for these remobilization and redistribution processes suggest that sediment yield is initially much higher than preeruption rates in the first few years following a potential eruption (Hooper, 2004). After one decade or a few decades, sediment yield may return to the preeruption rate in studied climatic settings, but remobilized tephra in an arid climate may likely account for the bulk of the transported sediment in the drainage system; only

Table 6-3. Modifications to Igneous Activity Parameters in the TPA Code Input File. All Parameters Are Constants by Default, Except AshEvolutionMode Is an Integer Constant.

Parameter Name	Current TPA Code Value	Modified Value
AshEvolutionMode*	n/a	0
RateOfReductionOfMassLoadingFactor[1/yr]	0.07†	0.07‡
RelativeRateOfBlanketRemoval[1/yr]	0.0007§	0.0007‡
FractionOfQuicklyRedistributableAshMobilizedEachYear	0.01	n/a‖
FractionOfModeratelyRedistributableAshMobilizedEachYear	0.001	n/a‖
FractionOfSlowlyRedistributableAshMobilizedEachYear	0.0003	n/a‖
ConcentrationFactorOfRadionuclidesDuringFluvialTransport	1	n/a‖
WindErosionRateUndisturbedLand[g/m2/yr]	224.36	n/a‖
TotalAreaOfAshInFortymileWashCatchmentBasin[m2]	1.5×10^8	n/a‖
FractionOfAshInFortymileWashCatchmentQuicklyRedist	0.4	n/a‖
FractionOfAshInFortymileWashCatchmentModRedist	0.35	n/a‖
FractionOfAshInFortymileWashCatchmentSlowlyRedist	0.25	n/a‖
DepositionFractionOfWindblownAshAtReceptorLocation	0.1	n/a‖
WindErosionRateDisturbed[g/m2/yr]	4262.9	n/a‖
FluvialErosionRateDisturbed[g/m2/yr]	44.87	n/a‖
FluvialErosionSoilDepth[m]	0.01	n/a‖
WindErosionSoilDepthDisturbed[m]	0.15	n/a‖
WindErosionSoilDepthUndisturbed[m]	0.01	n/a‖
RemobilizedAshVolume[m3]	1.48×10^8	n/a‖
FluvialDepositFractionAtReceptorLocation	0.3	n/a‖
DepositionRateOfSoilFromLongRangeSources[g/m2/yr]	10	n/a‖

n/a not applicable

*AshEvolutionMode is a TPA code input parameter that allows the user to select the mode for calculating evolution of ash at the receptor location. Two values are allowed, either 0 for the wind direction fixed toward the receptor without ash remobilization or 1 for sampling the wind direction and accounting for the effects of ash remobilization.

†The TPA code uses a simple exponential decay function to account for the reduction of mass load with time after an eruption. The RateOfReductionOfMassLoadingFactor[1/yr] input parameter controls the degree to which the ash increases the airborne mass load. The default value listed for this parameter does not account for the effects of remobilization, because the wind is directed toward the reasonably maximally exposed individual. As a first-order estimate for the effects of remobilization, the RateOfReductionOfMassLoadingFactor[1/yr] parameter value can be decreased. Figure 4.3.11-2 of the Risk Insights Baseline Report (NRC. "Risk Insights Baseline Report." ML0405601620. Washington, DC: NRC. April 2004. <www.nrc.gov/waste/hlw-disposal/reg-initiatives/resolve-key-tech-issues.html>) shows the sensitivity to the reduction rate of airborne mass load with time after an eruption.

‡These parameters are used in the calculations when AshEvolutionMode is set to 0, but are not used when AshEvolutionMode is set to 1.

§This parameter is listed in the TPA code input file but no longer used in calculations.

‖ This input parameter is removed from the TPA code.

minor to negligible amounts of tephra dilution likely may occur in the first decades following a potential eruption. This model appears most sensitive to the erosion rate, thickness, and volume of dispersed tephra in the watershed. Model results, however, estimate the flux of redistributed tephra in Fortymile Wash near the reasonably maximally exposed individual location is significantly higher than fluxes implied in Bechtel SAIC Company, LLC (2003b,c).

6.3 Assumptions

The alternative model accounts for the inhalation pathway. There are no calculations for other pathways (such as groundshine). The other main assumptions in this analysis are related to three contributions to the airborne concentration of high-level waste at the receptor location.

For the contribution from the initial deposit at the receptor location, it is assumed that inhalation doses following the volcanic event are dominated by the airborne mass load from ash (i.e., the effects on the airborne concentration of high-level waste from the resuspension of contaminated soil are neglected). Heavy disturbance activities during a portion of each year are assumed to occur on the initial deposit at the receptor location only and not on the source regions for fluvial and eolian remobilization.

For the fluvial remobilization contribution, data suggest that fluvial remobilization events are frequent enough to replenish the deposition region of Fortymile Wash with fresh sediment to roughly offset the reduction in airborne mass load with time for an aged deposit. Although ash remains in the Fortymile Wash catchment basin, these offsetting factors may result in an estimated mass load approximately constant with time. Thus, the airborne mass load at the deposition region of Fortymile Wash is assumed constant between the time of the eruption and the time, $t_{\text{duration},f}$, for fluvial remobilization to deplete the ash from the Fortymile Wash catchment basin [Eq. (6-11)]. Uniform mixing of remobilized ash and clean sediment is assumed. At times greater than $t_{\text{duration},f}$, it is assumed further fluvial remobilization in Fortymile Wash results in the deposition of noncontaminated sediment over the older contaminated sediment deposit. The clean sediment deposit is assumed to have a thickness greater than the resuspendible layer thickness. For times greater than $t_{\text{duration},f}$, the airborne particle load is thus set to zero to represent no contribution from fluvial remobilization to the airborne concentration of high-level waste at the receptor location.

For the eolian remobilization contribution, a factor equal to the fraction of the eolian source region covered by the initial deposit is used to account for dilution by noncontaminated sediment originating from areas without an initial ash deposit. The reduction with time in the particle mass load over the source deposit for eolian remobilization is assumed to be similar to the reduction associated with the initial deposit at the receptor location. A simple exponential decay function is used to model the reduction in the particle mass load with time for both the initial deposit at the receptor location and the averaged deposit for eolian remobilization.

Specific assumptions for the first-order conceptual model for fluvial remobilization of ash are presented in Hooper (2004).

6.4 Results

The focus of this analysis was to develop (i) an alternative model that captures the main effects of ash transport processes on the airborne mass load as a function of time after an eruption and (ii) detailed models and analyses to provide the TPA code input data. The alternative model and the associated input data developed in this analysis were implemented in the latest version of the TPA code.

6.5 Conclusions

To support the analyses described in Chapter 4 of this report, an alternative model was developed and implemented in the latest version of the TPA code with modifications made to the ASHRMOVO and DCAGS modules and to the TPA code input data. This alternative model calculates the initial deposit of ash at the receptor location by accounting for variations in the wind speed and wind direction along the height of the tephra column. The alternative model also accounts for subsequent first-order processes affecting fluvial and eolian remobilization of ash and thereby computes a time history of airborne concentrations of high-level waste at the receptor location. Results for ash remobilization from detailed analytical work with the TEPHRA code are assimilated into the TPA code as an input data file (i.e., lookup table) and as TPA code input parameter values.

7 CREDIT ATTRIBUTED TO ALLUVIUM

TASK DESCRIPTION

Reassess the credit attributed to the alluvium unit in delaying movement of sorbing radionuclides.

AUTHORS/CONTRIBUTORS

M. Smith and P. Bertetti

7.1 Background and Purpose

The sensitivity analysis in Mohanty, et al. (2002b) indicates the saturated alluvium length and radionuclide sorption coefficients ranked among the top 10 influential parameters, and NRC (2004) concludes the saturated zone transport distance has medium significance to waste isolation, and retardation in the saturated alluvium has high significance to waste isolation. The radionuclide sorption coefficients provide an indication of the magnitude of retardation that may occur. The saturated zone transport time for important nuclides, such as Np-237, was sensitive to the range of retardation factor values used in the TPA code and in the DOE site recommendation (CRWMS M&O, 2000b,c). The saturated alluvium length is important because the alluvium has a large capacity to retard many radionuclides. The uncertainty remaining in the saturated alluvium length, however, does not have a significant effect on overall system performance because the minimum length used in current performance assessments, when coupled with the range of retardation factor used, provides significant retardation for most radionuclides. Radionuclide sorption coefficients and the length of saturated alluvium also are shown to be important by DOE in CRWMS M&O (2000b,c) and Bechtel SAIC Company, LLC (2003d, 2002, 2001).

Modeling retardation in the saturated alluvium is performed by the DOE and NRC staffs using the distribution coefficients (K_d) approach. The K_d approach is favored in regulatory environments for its computational efficiency that permits probabilistic analyses and the ease of measuring K_d values with batch and column tests (Zhu, 2003). The K_d approach, however, also may be appropriate for cases of dynamic chemical evolution and long-term modeling (Reardon, 1981; Zhu, 2003). The use of a constant, linear K_d approach in modeling, even though the K_ds may be neither linear nor constant, may be acceptable given the range of chemistry is constrained, and the concentration range of important nuclides is limited. Flow-through laboratory experiments or field experiments may be used to gain confidence in the K_d approach for the varied mineralogical and chemical environments in the saturated alluvium.

This study reassesses the credit attributed to the saturated alluvium unit in delaying movement of radionuclides (e.g., Np-237, Am-241, and Pu-240) that tend to sorb onto mineral surfaces. This reassessment was accomplished with an alternative surface complexation model by estimating the effect of a modified implementation on parameters used by the TPA code to determine radionuclide retardation factors. Parameter range modifications were based on analyses of samples of saturated alluvium within Fortymile Wash. These analyses focused on Np-237, because the variation of its retardation factor has a high significance to waste isolation (NRC, 2004).

7.2 Methodology

Reassessing the credit attributed to the alluvium included two subtask (i) estimate the effect of modifications made to the implementation of the TPA code data file used to calculate the effective surface area normalized distribution coefficient (Ka′) values and (ii) verify the TPA code parameter ranges used to determine the neptunium retardation factors for saturated alluvium. Staff verified application of models and parameters used to represent sorption values for saturated alluvium in the TPA code and conducted TPA code runs to test the distribution ranges for hydraulic and chemical parameters. Analyses of field data, specifically from the Nye County Early Warning Drilling Program, and the effect on dose estimates were evaluated.

7.2.1 Subtask 1—Evaluate the Effect of Modifications Made to the Implementation of the TPA Code Data File Used to Calculate the Effective Surface Area Normalized Distribution Coefficient (Ka′) Values

The TPA code determines neptunium retardation factors through a series of calculations to account for the alluvium surface area, bulk density, and chemistry of the saturated zone groundwater. External to the TPA code, a surface complexation modeling approach was used to develop a series of model curves to estimate actinide Ka′ values for varying pH and partial pressure of CO_2. Curve-fitting techniques were then used to develop an equation and a corresponding set of coefficients to represent the estimated Ka′ curves. The TPA code samples values of pH and partial pressure of CO_2 and calculates Ka′ values using the equation and its associated coefficients, which are contained in the TPA code data file.

During assessment of radionuclide retardation credit attributed to the alluvium, differences were discovered between the neptunium Ka′ values generated by the coefficients in the TPA code data file and the values estimated by the surface complexation model curves. The differences were caused by residuals in the curve fits for neptunium, particularly at low partial pressures of CO_2. To make the calculated Ka′ values consistent, a curve-fitting exercise was conducted in which the range of pH values for the surface complexation model curves was made consistent with the range sampled by the TPA code. Modified curve fit coefficients were determined and implemented in the TPA code data file.

An evaluation was performed by analyzing the partial pressure of CO_2, pH, and alluvium retardation factor values produced by the TPA code and comparing those to published DOE values. The range of neptunium distribution coefficients (K_ds) for the saturated alluvium produced by the TPA code also was compared with the range of measured neptunium K_ds for alluvium published by DOE in Bechtel SAIC Company, LLC (2003d). Dose estimates for neptunium produced by the TPA code before and after implementation of the model modifications in the TPA code data file were compared to investigate the potential significance to waste isolation of the modifications.

7.2.2 Subtask 2—Verify Modified TPA Code Parameter Ranges Used to Determine the Neptunium Retardation Factors for Saturated Alluvium Produce Reasonable Results

7.2.2.1 Mineral Content

Well cuttings from Nye County Early Warning Drilling Program Wells NC–EWDP–2D and NC–Washburn–1X were analyzed using semiquantitative x-ray diffraction techniques to determine the mineralogy of the alluvium. Results of the analyses suggest the minerals studied in experiments used to develop the surface complexation model approach that provides the basis for the neptunium Ka′ values in the TPA code are present in the alluvium. Also, mineralogical analyses of samples from the sonic core collected at Nye County Early Warning Drilling Program Well NC–EWDP–19PB suggested the sonic core samples had the same basic mineral composition as the well cuttings.

7.2.2.2 Water Chemistry

Water chemistry data from Nye County Early Warning Drilling Program wells located within the estimated saturated zone flow paths suggest the ranges of pH and partial pressure of CO_2 along the estimated flow paths may be different than the ranges used in the TPA code. Analyses suggest the ranges of pH and partial pressure of CO_2 are more restricted within the saturated alluvium. Based on these data, both the pH and CO_2 sampled distribution ranges were modified in the TPA code. The pH parameter pH_AllUZ_SZLayers[StandardUnits] was modified to range from 6.7 to 9.0 rather than the basecase range 6.3 to 9.6. The partial pressure of CO_2 parameter LogCO2PartialPressure_AllUZ_SZLayers[atm] was modified to range from −4.0 to −0.77 atm rather than the basecase range −5.08 to −0.77 atm.

7.2.2.3 Specific Surface Area

Although appropriate for consolidated igneous rocks, such as the volcanic tuffs that make up Yucca Mountain, the method of estimating specific surface area in the TPA code may have limited application to the porous saturated alluvium. The primary limitation is that the pore size distribution is difficult to establish for the alluvium. Sampling a range of measured effective alluvium surface areas may address this issue.

Measured surface areas from sonic core samples are significantly different from previous well cuttings samples (higher by a factor of two). The measured surface area for well cuttings ranges from approximately 5 to 40 m^2/g [2.4×10^4 to 2.0×10^5 ft^2/lbm] with an average value of nearly 16 m^2/g [7.8×10^4 ft^2/lbm]. The sonic core sample surface areas range from approximately 20 to 40 m^2/g [1.0×10^5 to 2.0×10^5 ft^2/lbm] with an average of nearly 29 m^2/g [1.4×10^5 ft^2/lbm]. The increase in measured surface area observed in the sonic core samples is attributable to the greater clay fraction in those samples, and it is likely that the clay-sized fraction of well cuttings was lost during drilling and sample collection. Adding 10- to 15-percent clay to the well cuttings (the difference between what was observed in the sonic core results and the well cuttings) increases the estimated surface areas of the cuttings approximately 10 to 15 m^2/g [4.9×10^4 to 7.3×10^4 ft^2/lbm], which results in equivalent average measured surface areas for both sample groups.

Results from the experimental and modeling approach suggest actinide sorption by minerals is proportional to the effective surface area. The estimate for the effective surface areas for clays and zeolites is 10 percent of the measured (N_2-BET) surface area. These specific surface areas may be scaled by a factor to account for the clay and zeolite fraction within the samples. For the sonic core samples, applying this factor may produce an estimated specific surface area range from 3 to 9 m^2/g [1.5×10^5 to 4.4×10^5 ft^2/lbm]. These results are consistent with the DOE-measured specific surface area values for alluvium (Bechtel SAIC Company, LLC, 2003d).

The TPA code results suggest the effective porosity of alluvium is the parameter having the next largest influence on the retardation factor, after the sampled Ka′ value. Sampled Ka′ values are converted first to K_d values (multiplying by a specific surface area) and then to retardation factor values for use in NEFTRAN. Effective porosity also may affect transport because it is used in calculating linear velocity. Thus, the range of values for alluvium effective porosity is used in the TPA code calculations for the flow and retardation factors. Note that a likely conservative assumption for the flow factor (low effective porosity) is not necessarily conservative for the retardation factor (i.e., low porosity increases the retardation factor, while high porosity decreases the retardation factor).

For this study, an increased range for porosity was used as a surrogate for changing the range of the alluvium-specific surface area. The AlluviumMatrixPorosity_SAV parameter was modified to range from 0.1 to 0.35 rather than the default range 0.1 to 0.15. It is recognized that changing porosity also may affect the nonsorbing tracer transport times in the saturated zone.

7.3 Assumptions

Few assumptions are made in the analyses, other than those implicit within the TPA code. The TPA code input parameter values for partial pressure of CO_2, pH, and alluvium porosity were modified to the ranges discussed in Sections 7.2.2.2 and 7.2.2.3.

7.4 Results

This section presents results from the analysis described in this chapter. The TPA code results computed with modifications to data used to determine effective surface area normalized distribution coefficient values are presented in Section 7.4.1. Results from modified TPA code parameter ranges for neptunium retardation factors are provided in Section 7.4.2.

7.4.1 Subtask 1—Evaluate the Effect of Modifications Made to the Implementation of the TPA Code Data File Used to Calculate the Effective Surface Area Normalized Distribution Coefficient (Ka′) Values

An analysis of results from the TPA code with the modified TPA code data file suggests the independently developed surface complexation model approach produced neptunium K_d values consistent with the range of measured values published by DOE in Bechtel SAIC Company, LLC (2003d). The DOE range is from 3 to 13 ml/g [0.36 to 1.6 gal/lbm], while the TPA code produced a range approximately 0.4 to 18 ml/g [0.05 to 2.2 gal/lbm]. Analysis and review of the TPA code output of values for pH, partial pressure of CO_2, and Np-237 retardation factor for

alluvium for the modified case suggested these values were within their expected ranges, and all had appropriate distribution shapes and correlation.

Using the modified TPA code data file, the estimated Np-237 retardation factor distribution has lower mean and median values than the basecase file. The estimated peak mean Np-237 groundwater doses in 10,000 years decreased by less than a factor of two relative to the basecase, as shown in Figure 7-1. Without modifications, the TPA code does not estimate Ka′ values supported by the surface complexation model results, so these data file modifications were incorporated in the latest version of the TPA code. All subsequent analyses of the effects of parameter distribution modifications conducted in Subtask 2 include the modified version of the TPA code data file.

7.4.2 Subtask 2—Verify Modified TPA Code Parameter Ranges Used to Determine the Neptunium Retardation Factors for Saturated Alluvium Produce Reasonable Results

7.4.2.1 Mineral Content

Results of mineral content analyses suggest the minerals of primary importance in the saturated alluvium are the minerals used to develop the surface complexation model approach for the TPA code. Analysis of the results from Nye County Early Warning Drilling Program Well NC–EWDP–19PB suggests the sonic core samples have the same bulk and clay mineralogies observed in well cuttings. The sonic core samples have a higher clay content, but also tend to have a grain-size distribution skewed toward the sizes of gravel and cobble. Differences in both the clay content and grain-size arise from the manner in which the sonic core samples were collected compared with the collection of well cuttings samples. The sonic core samples are more representative of the true grain size and mineral distribution present in the alluvium. Because these results support the present approach used in the TPA code, there is no effect on results.

7.4.2.2 Water Chemistry

Application of the modified chemistry ranges for pH and partial pressure of CO_2 in the TPA code decreased the estimated peak mean Np-237 groundwater dose in 10,000 years by nearly one order of magnitude, as shown in Figure 7-2.

The modified ranges of pH and partial pressure of CO_2 support the significant capacity of the saturated alluvium to retard Np-237 during the 10,000-year period. Relative to the ranges of pH and partial pressure of CO_2 in the basecase TPA code, the modified ranges are more representative of groundwater chemistry in the saturated alluvium. These ranges may not, however, account for potential temporal variations in chemistry. Moreover, sorption coefficient values for some actinides, uranium in particular, may be more affected by adjusting the range of sampled chemistry than is neptunium.

7.4.2.3 Specific Surface Area

As shown in Figure 7-3, the range of nonsorbing tracer transport times in the saturated zone was extended slightly with the change in the sampled range of alluvium porosity. Increasing the range of alluvium effective porosity by increasing the maximum sampled value may lower the

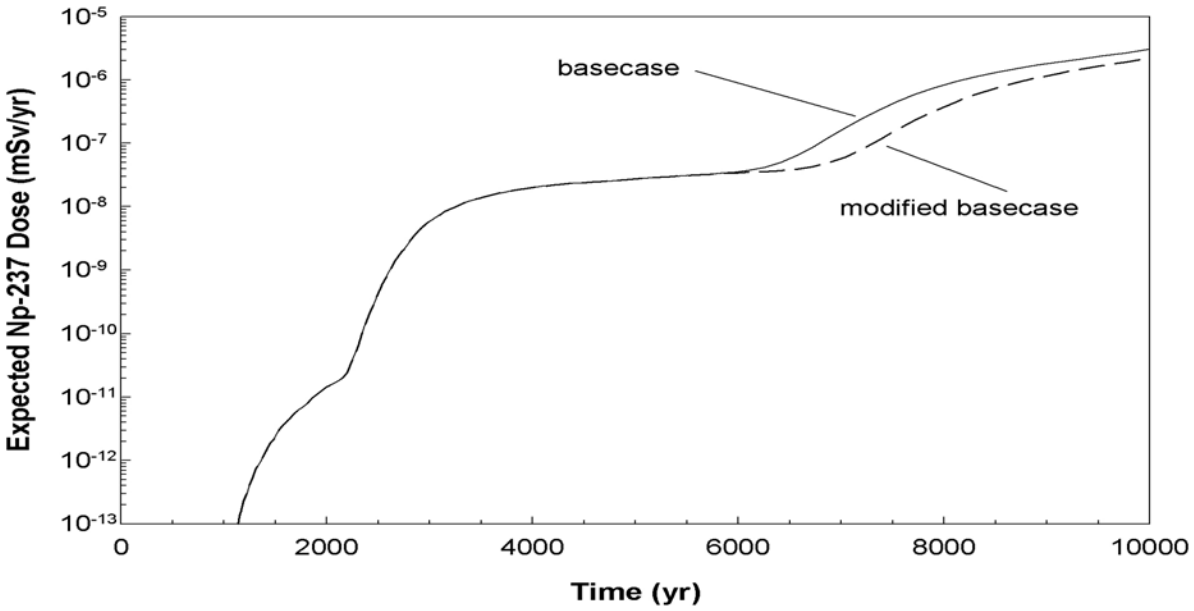

Figure 7-1. Estimated Np-237 Total Effective Dose Equivalent for Original Basecase and Modified Basecase (Modified Np-237 Ka′ Curve Fit Coefficients) Using the TPA Code

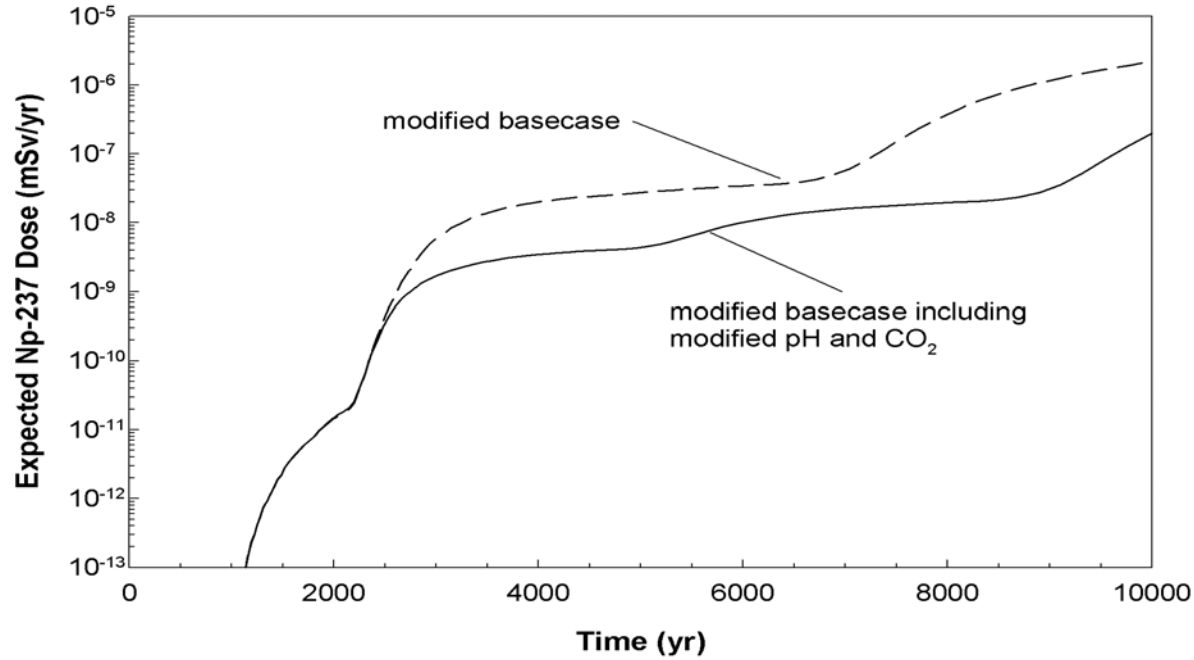

Figure 7-2. Estimated Np-237 Total Effective Dose Equivalent for Modified Basecase Including Modified pH and CO_2 and Modified Basecase (Modified Np-237 Ka′ Curve Fit Coefficients) Using the TPA Code

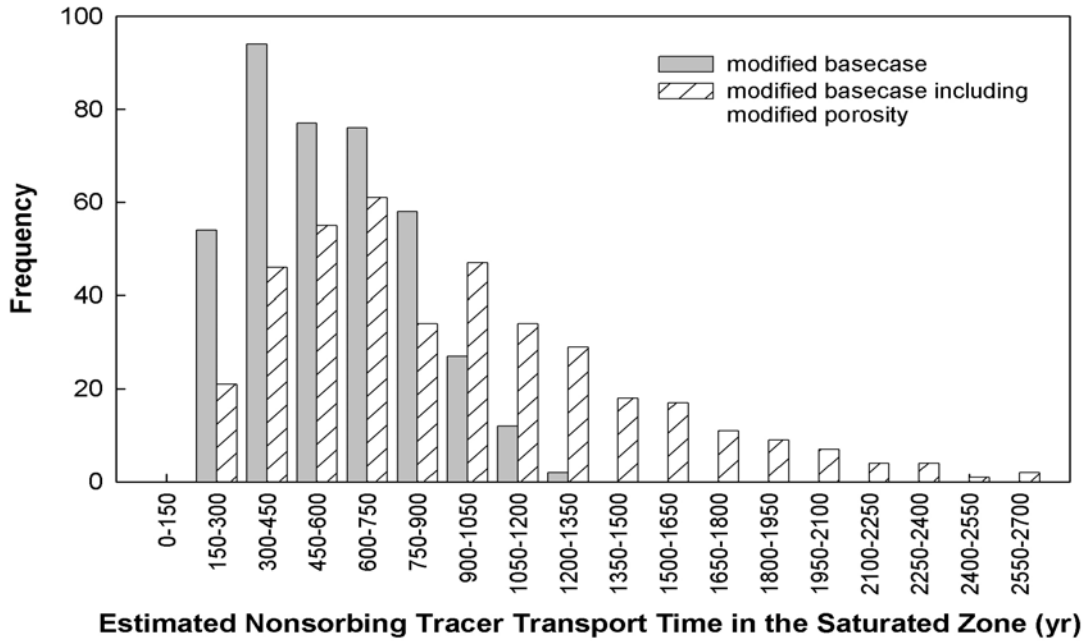

Figure 7-3. Histogram of Estimated Nonsorbing Tracer Transport Times in the Saturated Zone for Modified Basecase Including Modified Porosity Range and Modified Basecase (Modified Np-237 Ka′ Curve Fit Coefficients) Using the TPA Code

calculated specific discharge of the alluvium, producing longer nonsorbing tracer transport times in the saturated zone alluvium. It is important to note, however, that the changes in nonsorbing tracer transport times in the saturated zone may be small relative to the effects of porosity changes on the Np-237 retardation factor. For example, the mean saturated zone travel time increases from 572 to 923 years for the basecase and porosity modification, but as shown in Figure 7-4, the effects of porosity modification on the Np-237 retardation factors may produce delays on the order of 5,000–10,000 years. Figure 7-4 shows the change in porosity decreased the estimated peak mean Np-237 groundwater dose in 10,000 years by nearly two orders of magnitude. Figure 7-5 shows that the composite effect of all changes (pH, partial pressure of CO_2, and porosity) reduced the estimated peak mean Np-237 groundwater dose in 10,000 years by nearly two orders of magnitude.

7.5 Conclusions

This section summarizes significant results from the analysis.

- An alternative surface complexation model with a modified implementation of the TPA code data file used to calculate the effective surface area normalized distribution coefficient (Ka′) values decreased the estimated peak mean Np-237 groundwater dose in 10,000 years by nearly a factor of two. These modifications were incorporated in the latest version of the TPA code.

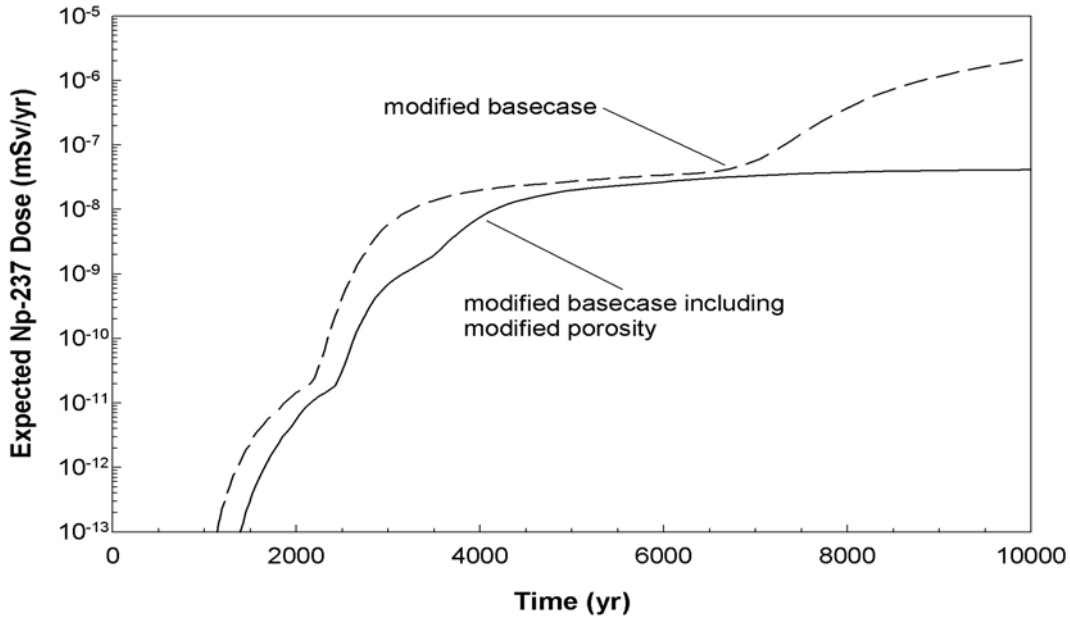

Figure 7-4. Estimated Np-237 Total Effective Dose Equivalent for Modified Basecase Including Modified Porosity Range and Modified Basecase (Modified Np-237 Ka′ Curve Fit Coefficients) Using the TPA Code

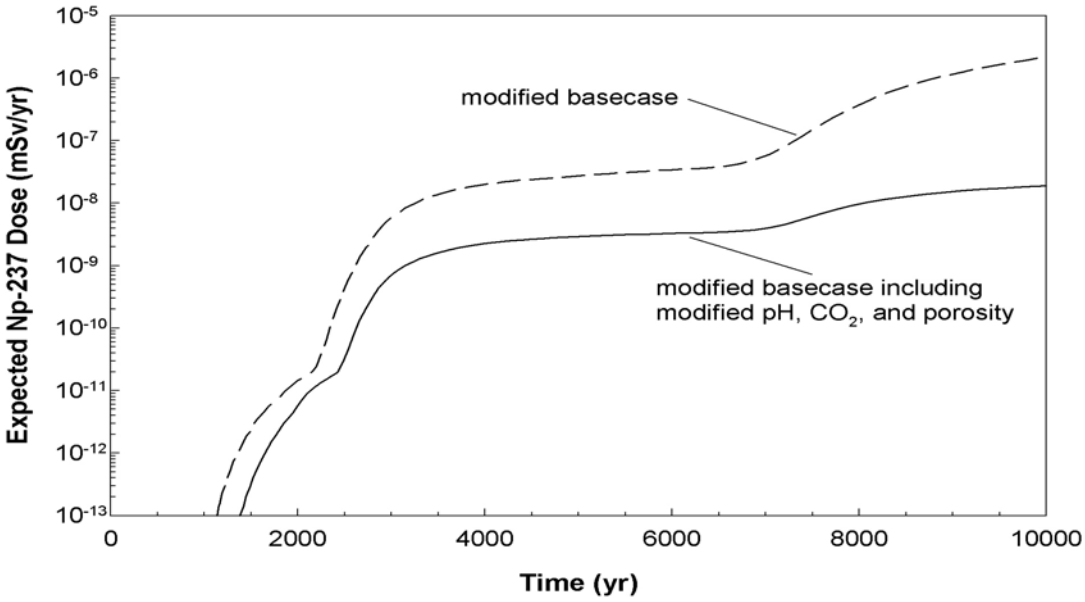

Figure 7-5. Estimated Np-237 Total Effective Dose Equivalent for Modified Basecase Including All Parameter Changes (pH, CO_2, and Porosity) and Modified Basecase (Modified Np-237 Ka′ Curve Fit Coefficients) Using the TPA Code. The Majority of the Observed Effects from the Modified Parameters Is Attributable to Porosity.

- Results of mineral content analyses suggest the minerals of primary importance in saturated alluvium are the same minerals used to develop the surface complexation model approach for the TPA code. These results support the present approach used in the TPA code.

- Application of modified chemistry ranges for pH and partial pressure of CO_2 in the TPA code decreased the estimated peak mean Np-237 groundwater dose in 10,000 years by nearly one order of magnitude. These modifications were incorporated in the latest version of the TPA code.

- The specific surface area calculation for saturated alluvium used by the TPA code is applicable for consolidated rock-like tuffs, but may not be applicable for alluvium. For this analysis, an increased range for porosity was used as a surrogate to estimate the importance of specific surface area on overall system performance, because porosity affects the calculation of specific surface areas. The results estimate a decrease in the peak mean Np-237 groundwater dose in 10,000 years caused by the increase in alluvium surface area.

8 FUEL INCORPORATION AND INITIAL PLUME VELOCITY

TASK DESCRIPTION

Evaluate sensitivity of the ASHPLUME model assumptions for spent nuclear fuel incorporation into tephra and initial plume velocity on dose estimates.

AUTHOR

R. Codell

8.1 Background and Purpose

Factors affecting the releases to the environment from extrusive volcanism have a high or medium significance to waste isolation in NRC (2004). For example, the risk insight Volume of Ash Produced by an Eruption is identified with medium significance to waste isolation. This analysis has two parts and examines the effects of several model assumptions on the estimated dose from extrusive volcanic events at Yucca Mountain.

8.1.1 Part 1—Alternative Model for Incorporation of Spent Nuclear Fuel into Tephra

If an extrusive volcanic event occurs at Yucca Mountain, buried waste may become entrained in the rising magma, becoming part of the eruptive plume that may be transported as falling tephra downwind of the potential repository. Models of the entrainment of buried waste make many assumptions that may be reasonable, but are difficult to validate. This analysis evaluates an equally credible alternative model for waste entrainment and compares the results for estimated peak dose to the reasonably maximally exposed individual to results from the current model.

8.1.2 Part 2—Alternative Model for Initial Plume Velocity

The initial plume velocity in the present ASHPLUME model is calculated by dividing the rate of magma expulsion from the volcanic vent by the vent area and density of the molten rock. This approach may underestimate plume velocities, because the volcanic column leaving the vent is mostly gas by volume and much less dense than molten rock alone. This analysis, with an alternative model for initial plume velocity, compares the results to the original data from the Cerro Negro (Nicaragua) volcano by areal deposition of tephra and to doses estimated from the transport of contaminated tephra to the exposed population.

8.2 Methodology

The alternative model for incorporation of spent nuclear fuel into tephra uses a modified version of the ASHPLUME FORTRAN code. The alternative model for vent velocity uses an approximation for column density from Woods (1988). Modifications made for both alternative models are described in this section. Both models were run in the context of the TPA code. The methodology used in the two parts of this analysis is described next.

8.2.1 Part 1—Alternative Model for Incorporation of Spent Nuclear Fuel into Tephra

The volcanic scenario has three main components: (i) interaction of intruding magma with the engineered materials and structures, (ii) transport of the radionuclides in the contaminated tephra to the biosphere, and (iii) exposure of the individual or group from the contaminated tephra. There are few known direct examples useful for formulating a model for the first component, interaction of magma with engineered materials and structures. Useful information may be drawn from real and simulated nuclear reactor accidents and from experiments with the spent nuclear fuel wasteform, but these are far from ideal analogies to the volcanic case.

The current TPA code model of this phenomenon assumes all waste packages contacted by magma are destroyed and waste mixes with magma to become part of the tephra plume released at the surface of the Earth. The current mixing model is based on a relationship between tephra particle size and fuel particle size. The analysis presented in this chapter attempts to determine if an alternative model of this interaction materially affects the estimated dose consequences.

8.2.1.1 Current Source Term Model

The current TPA code model assumes that spent UO_2 fuel and tephra mix according to an incorporation ratio, ρ_c, which stipulates that a tephra particle of diameter D_a can incorporate fuel particles with a diameter $10^{-\rho_c} D_a$ or smaller. One of the desirable features of the current incorporation model is that it allows treatment of the tephra/fuel mixing as a direct analytical function that is easily incorporated into the Suzuki model (1983) for tephra transport. The Suzuki model depicts the transport of tephra particles from a volcanic plume into a steady wind field

$$X(x,y) = \int_{\rho^a_{min}}^{\rho^a_{max}} \int_{z=0}^{H} \frac{5QP(z)f(\rho^a)}{8\pi C(t+t_s)^{5/2}} \exp\left\{ -\frac{5\left[(x-ut)^2 + y^2\right]}{8C(t+t_s)^{5/2}} \right\} d\rho dz \qquad (8\text{-}1)$$

where

$X(x,y)$	—	mass of tephra per unit area accumulated at location *(x*, y) [g/cm^2]
ρ^a	—	common logarithm of tephra particle diameter [cm]
ρ^a_{min}	—	minimum value of ρ^a particle diameter [cm]
ρ^a_{max}	—	maximum value of ρ^a particle diameter [cm]
z	—	vertical distance from ground surface [km]
H	—	height of eruption column above vent [km]
Q	—	total quantity of erupted material [g]

$P(z)$	—	distribution function for particle diffusion out of the vertical column [unitless]
$f(\rho^a)$	—	distribution density function of tephra particle log diameters [unitless]
C	—	constant related to eddy diffusivity and fall time of particles [$cm^2/s^{5/2}$]
t	—	particle fall time [s]
t_s	—	particle diffusion time in eruption column [s]
u	—	wind speed [cm/s]

The distribution function, $P(z)$, is discussed in Section 8.2.2 [Eq. (8-8)] of this chapter. Particle fall time, t, is derived in Suzuki and presented in Jarzemba (1997). The important point is that the distribution function is a function of terminal velocities of the particles, which, in turn, depend on the specific gravity of the particles.

Jarzemba (1997) modified the Suzuki model to estimate the fuel fraction as a function of particle size, $FF\ (\rho^a)$, to yield

$$FF(\rho^a) = \frac{U}{Q} \int_{\rho=-\infty}^{\rho=\rho^a} \frac{m(\rho-\rho_c)}{1-F(\rho)}\, d\rho \qquad (8\text{-}2)$$

where

U	—	total mass of fuel ejected [g]
$m(\rho - \rho_c)$	—	normalized probability distribution of fuel mass with $(\rho-\rho_c)$ [unitless]
$F(\rho)$	—	cumulative distribution of the tephra mass [unitless]

Development of Eq. (8-2) used a direct relationship between tephra particle size and fuel concentration that was single valued.

8.2.1.2 Alternative Conceptual Source Term Model

It is likely that mixing between tephra and fuel would be highly heterogeneous, leading to a wide range of fuel-to-tephra ratios for a given tephra particle size. Because fuel is so dense compared with the tephra, it is also likely that a fraction of the tephra particles would be of high density and have settling rates higher than lighter tephra particles of the same diameter.

An alternative fuel incorporation model was developed that examines the possibility of heterogeneous mixing of fuel and tephra in the volcanic scenario. The alternative model is based on parsimony (also known as Occam's Razor). That is, because the actual process of fuel incorporation is uncertain, the minimum number of assumptions is made. For this model, the main assumption is the fraction of mass of fuel incorporated into the tephra is proportional to the mass of the tephra. For this analysis, the total mass of tephra and the number of tephra particles greatly exceed the fuel mass and the number of fuel particles, and the size range of tephra particles is much greater than the corresponding size range for fuel particles. The two distributions for coarse fuel and fine fuel particle diameters used in the current analysis and a

typical value for the tephra particle diameter (i.e., median tephra) are shown in Figure 8-1. These distributions for coarse fuel and fine fuel were successfully used with the current TPA code incorporation model, although current model implementation of the model relies on smooth distributions of tephra and fuel particle sizes.

The alternative model was implemented with a direct simulation approach, which used a relatively small number of representative fuel and tephra particles in discrete size ranges. This alternative model used the Suzuki model (1983) for tephra transport [Eq. (8-1)], but replaced the outer integral by a summation of discrete particle sizes

$$X(x,y)=\sum_{L=1}^{\mathrm{NI}}\Delta m_L\int_{z=0}^{H}\frac{5QP(z)\rho_L^a}{8\pi C(t+t_s)^{5/2}}\exp\left\{-\frac{5\left[(x-ut)^2+y^2\right]}{8C(t+t_s)^{5/2}}\right\}dz \qquad (8\text{-}3)$$

where

ρ_L^a	—	common logarithm of the diameter of the L^{th} tephra particle bin [cm]
Δm_L	—	mass of tephra/fuel particles associated with the L^{th} indicator particle [g]
NI	—	number of indicator particles [unitless]

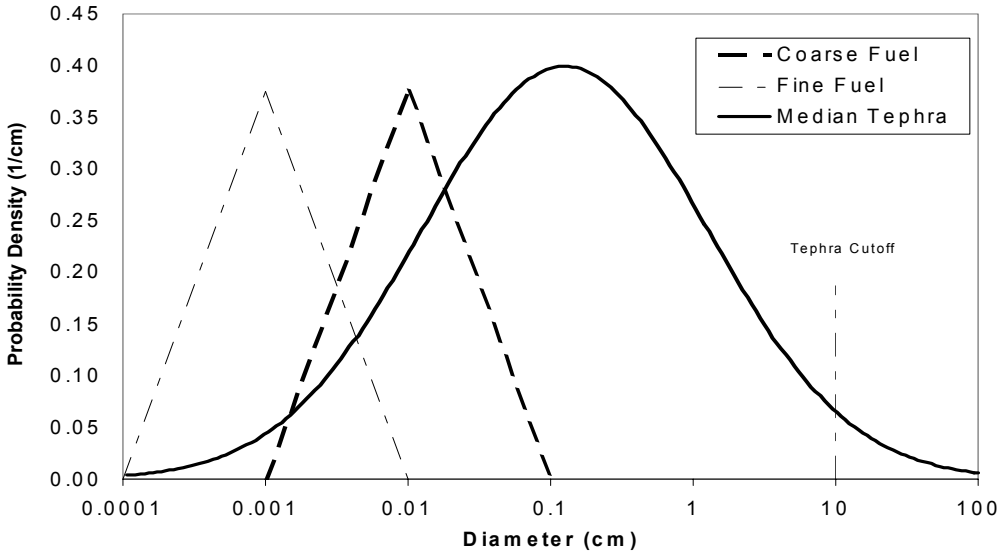

Figure 8-1. Probability Density Functions for Median Tephra and Course and Fine Fuel Particle Diameters. Tephra Cutoff is Maximum Tephra Particle Size Used in Calculations of Particle Transport.

Although the summation in Eq. (8-3) is for a different range than the integral in Eq. (8-1), both accomplish approximately the same effect by capturing the contribution to $X(x,y)$ for the range of tephra particles.

Because there was often more than a five order of magnitude difference between the total number of tephra and fuel particles, in a direct binning approach to mixing the two distributions, there would have to be more than 10^5 bins to account for all the possible combinations of tephra and fuel particles. The use of such a large number of bins is computationally demanding, both in computer storage and runtime, because the overall model is a small part of the TPA code (Mohanty, et al., 2002a).

A more computationally efficient approach was to consider three classes of tephra/fuel combinations in which the discriminant was the ratio of the number of fuel particles per tephra particle. First, the distributions of the fuel mass and tephra mass were discretized into 100 bins, each bin representing a range of fuel or tephra sizes. The bins were determined by dividing, on a logarithmic scale, the log of the diameter into 100 equal divisions. The mass and true number of particles in each bin were then calculated.

Next, there is a large number (approximately 20,000) of indicator particles defined to represent the tephra particles. The number of these indicator particles was apportioned to each of the 100 tephra bins according to the relative mass in each tephra bin. Each of the indicator particles represents initially an approximately equal mass of tephra. The indicator particles also represent the mass of a tephra particle, its fuel content after mixing, and the number of actual tephra particles.

The probability of a fuel particle of size j being incorporated into a tephra particle of size i is equal to the fraction of the overall tephra mass contained in tephra bin i. The number of fuel particles per tephra particle is distributed according to a Poisson distribution.

Because each indicator particle represents an approximately equal quantity (mass) of tephra, there is a varying number of indicator particles in each tephra bin. For each tephra bin, all the fuel bins are cycled through to determine the ratio, μ (which also is the parameter of the Poisson distribution), that equals the number of fuel particles of size j to number of tehpra particles of size i. If μ is large (i.e., μ >20), there would be a nearly uniform number of fuel particles per tephra particle. In this case, all the indicator particles in the tephra bin receive an equal number of fuel particles of size j.

For smaller μ (i.e., 0.1 > μ >20), there would be a variable number of fuel particles per tephra particle determined from a Poisson distribution with parameter μ. The indicator particles in the i^{th} tephra bin are sampled to determine how many fuel particles of size j would be added; some getting few or none, and some getting multiple additions of fuel. The algorithm is as follows:

1. For each tephra bin i, calculate the probability, Pr, from the Poisson distribution

$$Pr = \frac{e^{-\mu}\mu^{p}}{p!} \tag{8-4}$$

where p is the number of fuel particles of size j to be added, ranging from 1 to 50

2. The number of fuel particles of size j added to tephra bin i, $Np_{i,j}$ would be the number of indicator particles in that tephra bin times the probability

3. Randomly sample each indicator particle in the tephra bin without replacement to determine whether it gets p fuel particles until all $Np_{i,j}$ fuel particles are gone

4. Repeat for p up to 50 fuel particles per tephra particle

For small μ (i.e., μ < 0.1), there would be no more than one fuel particle per tephra particle. In this case, there would be a second category of indicator particles (small μ indicator particles) that stand apart from the regular indicator particles. These contain exactly a single fuel particle attached to each tephra particle. The small μ indicator particles represent a quantity of tephra particles equal to the number of fuel particles of size j, apportioned from the total fuel by the mass fraction of tephra of size i. An equal number of tephra particles is subtracted from the other indicator tephra particles in each bin to maintain an overall mass balance of tephra.

The algorithm is repeated for all combinations of tephra and fuel particle sizes. The particle sizes, densities, and fuel contents represented by all indicator particles are then used with Eq. (8-3) to estimate the tephra-layer thickness and fuel concentration at the downwind location.

The mixing of fuel with tephra is likely determined by complex mechanical, thermal, and chemical processes. These relationships have been inferred from observations of analogous data and are uncertain. Therefore, in this approach calculations were performed, assuming all fuel in the affected waste packages would be incorporated into magma, for two different size ranges of the spent nuclear fuel particles differing by a factor of 10, with the expectation that uncertainties in the mixing rules and other factors would be encompassed by the two sets of results.

8.2.2 Part 2—Alternative Model for Initial Plume Velocity

The initial plume velocity in the current ASHPLUME model is estimated by dividing the rate of magma expulsion from the volcanic vent by the vent area and density of the magma. The alternative analysis compares the results to the original data from the Cerro Negro volcano using the areal deposition of tephra and to doses estimated from the transport of contaminated tephra in the current model.

For the nominal case in the current model, the vent velocity, W_0, was calculated from Eq. (4-5) in Jarzemba (1997)

$$W_0 = \frac{q}{\psi_p \pi r^2} \tag{8-5}$$

where

q — the eruption rate [g/sec]
ψ_p — particle density {2.6 g/cm^3 [162 lbm/ft^3]}
r — vent radius [cm]

The vent radius from Eq. (4-6) in Jarzemba (1997) was 309 cm [10.1 ft]

$$\log_{10}(r) = -0.069 + 2\log_{10}(\psi_p) + 0.274\log_{10}(Q) \tag{8-6}$$

The vent velocity, W_0, is 12.83 cm/s [0.42 ft/s].

For the alternative conceptual model, the vent velocity accounts for the fact that the volcanic column is mostly gas, which was accomplished by changing the column density to that used in the jet model of Woods (1988). The density also is called β, but is not related to the beta in the Suzuki model. For clarity in this report, the density is called B. The column density is computed using

$$\frac{1}{B} = \frac{nR_g\theta}{P} + \frac{1-n}{\sigma} \tag{8-7}$$

where

n — gas mass fraction, estimated to be 0.03 [unitless]
θ — bulk temperature in column {1,300 K [1,880 °F]}
R_g — gas constant for dusty gas {285 m^3-Pa/(kg-K) [2.50 × 10^{-2} ft^3-atm/(lbm-°R)]}
P — atmospheric pressure {1.0 × 10^5 Pa [14.5 psi]}
σ — density of solid particles 2,600 kg/m^3 [162 lbm/ft^3]

Using these values and converting units in Eq. (8-7) yields a column density at the vent of B = 0.00897 gm/cm^3 [0.56 lbm/ft^3]. Substituting for the 2.6 gm/cm^3 [162 lbm/ft^3] in Eq. (8-5), the vent velocity is 3,720 cm/s [122 ft/s].

Vent velocity appears only in Eq. (2-2) for the probability density distribution, $P(z)$, in the current model (Jarzemba, 1997)

$$P(z) = \frac{\beta W_0 Y \exp(-Y)}{V_0 H\left[1-(1+Y_0)\exp(-Y_0)\right]} \tag{8-8}$$

where

Y — $\frac{\beta W(z)}{V_0}$ [unitless]

$W(z)$ — particle velocity as a function of height [cm/s]

Y_o — $\frac{\beta W_0}{V_0}$ [unitless]

β — constant controlling the diffusion of particles out of the eruption column [unitless]

W_0 — volcanic eruption velocity at vent exit [cm/s]

V_0 — particle terminal velocity at sea level [cm/s]

The maximum height H [km] that the plume attains is based on an empirical correlation

$$H = 0.0082 P_w^{0.25} \tag{8-9}$$

where P_w is eruptive power [W].

The plume is assumed to reach a specified height irrespective of vent velocity, and the particle velocities are assumed to be linearly interpolated from the velocity at the vent to zero at the top of the plume

$$W(z) = W_0 \left[1 - \frac{z}{H} \right] \tag{8-10}$$

The result of the alternative vent velocity model is compared with the nominal Cerro Negro experimental data when converted to an areal density gm/cm^2 from a thickness using the average density of 1.2 g/cm^3 [75 lbm/ft^3] for tephra.

8.3 Assumptions

The assumptions made in Part 1 and Part 2 of this analysis are presented in this section. First, the assumptions for the analysis of the alternative model for the spent nuclear fuel incorporation into tephra are described in Section 8.3.1. Then, the assumptions for the analysis of the alternative model for the initial plume velocity are described in Section 8.3.2.

8.3.1 Part 1—Alternative Model for Incorporation of Spent Nuclear Fuel into Tephra

The model uses all the assumptions in the current model ASHPLUME (Jarzemba, 1997) as employed in the TPA code, except for the following condition. The fraction of fuel incorporated into the tephra is proportional to the mass of the tephra particle. This rule is incorporated into the model by sorting the tephra and the fuel, each into 100 respective bins representing a range of fuel or tephra diameters. The bins were determined by dividing the log of the diameters into

100 equal divisions. The number of fuel particles per tephra particle was determined for this rule to be a Poisson distribution. This mixing rule allowed a distributed density for each diameter of a tephra particle, whereas the original model used a fixed density for a given tephra particle size.

8.3.2 Part 2—Alternative Model for Initial Plume Velocity

The model uses an increased plume velocity at the volcanic vent, based on the fact that the volcanic column is mostly gas. The density of the column was based on the model of Woods (1988), which assumed the column contained condensed (solid and liquid) rock and 3-percent water vapor by mass and had a temperature of 1,300 K [1,880 °F] and an atmospheric pressure of 1.0×10^5 Pa [14.5 psi]. Model parameters are shown in Table 8-1.

8.4 Results

Results from Part 1 and Part 2 of the analysis are presented in this section. Results for the analysis of the alternative model for the spent nuclear fuel incorporation into tephra are described in Section 8.4.1. Two separate discussions of results for the analysis of the alternative model for the initial plume velocity are described for tephra deposition on the ground surface in Section 8.4.2.1 and for estimated peak dose in Section 8.4.2.2.

8.4.1 Part 1—Alternative Model for Incorporation of Spent Nuclear Fuel into Tephra

Results from alternative model were compared with the current model for a set of 100 random vectors chosen by Latin hypercube sampling from distributions typical of the recent NRC performance assessment (Mohanty, et al., 2002b). A constant 100 waste packages are assumed to be involved in the event, which is toward the high end of the likely range. Table 8-2 shows the input parameters to the TPA code relevant to the volcanism source term model. The comparison consisted of a presentation of the estimated peak dose, vector by vector, for the two models, assuming the volcanic event occurred at 1,000 years after repository closure. The actual estimation of risk from the TPA code considers the low probability of volcanic events, averaging dose over the realizations, and a convolution of events through time to generate an estimated mean dose curve. The figures presented are for estimated peak doses from a single event time, not weighted by event probability.

Figure 8-2 shows the particle density versus tephra particle diameter for the median dose vector (from the 100 Monte Carlo samples) and the coarse fuel distribution estimated for the current and alternative models. Each part of this figure depicts a representative density of particles in the bins for the tephra/fuel mixing. The alternative model estimated a wide range of particle densities, whereas the current model estimated a single particle density for a given tephra particle size (dark line near the bottom of Figure 8-2). This figure shows the range of particle densities, but not the quantity. Histograms of particle mass for the two models would be nearly indistinguishable because of the overwhelming mass of tephra compared with fuel. Nevertheless, it is interesting to note in Table 8-3 that, in many cases, the alternative model estimated a significant portion of the fuel would exist in dense particles, defined here as particles with densities greater than 2.0 g/cm^3 [124 lbm/ft^3]. The current model does not estimate any

Table 8-1. Parameters for Vent Velocity Model		
Parameters	**Value**	**Unit**
Volcanic Event Duration	3.46×10^5	s
Volcanic Event Power	7.338×10^9	W
Tephra Mass	3.46×10^{12}	g
Wind Speed	900	cm/s
Beta	10	unitless
Diffusivity Constant	400	$cm^2/s^{5/2}$
Air Viscosity	0.00018	g/(cm-s)
Air Density	0.00129	g/cm^3
Water Content by Mass	0.03	unitless
Particle Shape Parameter	0.5	unitless
Column Height	2.4	km
Mean Particle Diameter	0.07	cm
Particle Log_{10} Standard Deviation	1.0	unitless
Column Temperature	1300	K
Condensed Matter Density	2.6	g/cm^3
Atmospheric Pressure	1.0×10^5	Pa

dense particles. The implication of results from the alternative model is that dense particles may be transported in the volcanic plume differently because they would have a higher settling velocity than their lighter counterparts in the current model.

Figure 8-3 shows the model comparison for the 100 estimated peak doses using the default, fine fuel particle-size distribution. The alternative model consistently estimates a smaller peak dose. The average of the estimated peak doses was 74 percent higher for the current TPA code model.

Figure 8-4 shows the model comparison for the coarse fuel-size distribution, which increased the particle sizes by a factor of 10. Interestingly, some of the alternative runs estimated higher peak doses than the current model, although the average peak doses for the current model were still higher (by 18 percent) than the alternative model. Also, the estimated mean dose for the alternative model increases for the coarser fuel distribution, whereas the estimated mean dose decreases for the current model. These results suggest a denser particle with a higher

Table 8-2. Volcanic Parameters and Probability Distributions Relevant to Source Term Models		
Parameter	**Distribution/Value**	**Unit**
Number of Waste Packages Impacted	100	unitless
Volcanic Event Duration	uniform ($1.8 \times 10^5 – 1.3 \times 10^6$)	s
Volcanic Event Power	uniform ($3.5 \times 10^9 – 5.3 \times 10^{11}$)	W
Maximum Raw Tephra Density	1.6	g/cm^3
Minimum Raw Tephra Density	0.8	g/cm^3
Mean Tephra Particle Size	logtriangular (0.01, 0.1, 1.0)	cm
Tephra Particle Size Log_{10} Standard Deviation	1.0	unitless
Fuel Particle Size, Fine	logtriangular (0.0001, 0.001, 0.01)	cm
Fuel Particle Size, Coarse	logtriangular (0.001, 0.01, 0.1)	cm
Wind Speed	exponential (0.0083)	cm/s
Wind Direction	directly toward exposed population	unitless
Location of Receptor	20 km directly down wind of source	—

settling velocity does not necessarily lead to a result of a smaller estimated peak dose. For certain conditions, particles that might have passed over the location because they did not settle fast enough now land in the target area, contributing to a higher estimated peak dose.

8.4.2 Part 2—Alternative Model for Initial Plume Velocity

This section presents two separate discussions of results from Part 2 of the analysis for the alternative model of initial plume velocity. The discussions of results are for tephra deposition on the ground surface in Section 8.4.2.1 and for peak dose in Section 8.4.2.2.

8.4.2.1 Tephra Deposition on Ground Surface

The tephra deposition estimated by the models was compared with the observed Cerro Negro tephra thicknesses presented in Hill, et al. (1998). For the nominal case with the current vent

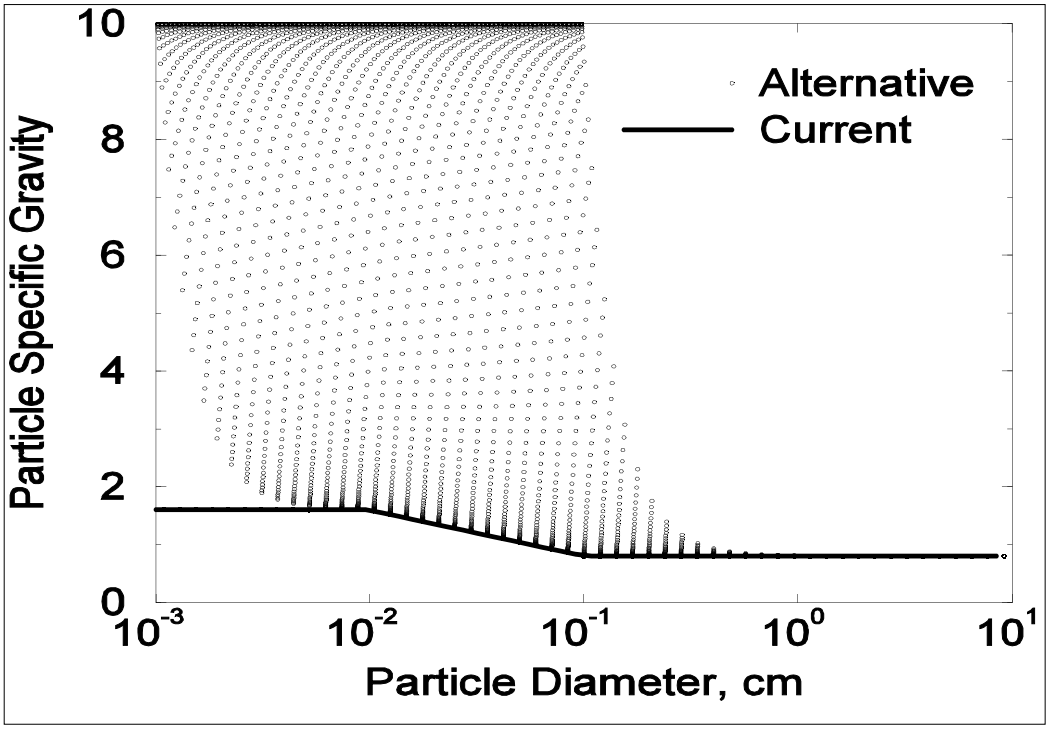

Figure 8-2. Estimated Particle Density Distribution for Median Dose Vector and Coarse Fuel Distribution for the Current TPA Code Model and the Alternative Model

velocity model, Figure 8-5 shows the ASHPLUME model results compared with the data. The match is reasonable, however, the data fall somewhat below the ASHPLUME model estimates. For the modified case with the alternative vent velocity model, Figure 8-5 displays results with the nominal value for β equal to 10 and also for a decreased value for β equal to 1. The results for the two values of beta are mostly similar, which suggest the relative insensitivity to β. Note the instability in the model results at *x* equal to 12 km [7.5 mi] and β equal to 10. The cause of this stability appears to be unrelated to the change in vent velocity, but the exact nature is uncertain.

Table 8-3. Estimated Fraction of Fuel in Dense Tephra Particles from Alternative Model

	Fine Fuel Distribution	Coarse Fuel Distribution
Minimum	0.013	0.09
Mean	0.088	0.29
Maximum	0.270	0.60

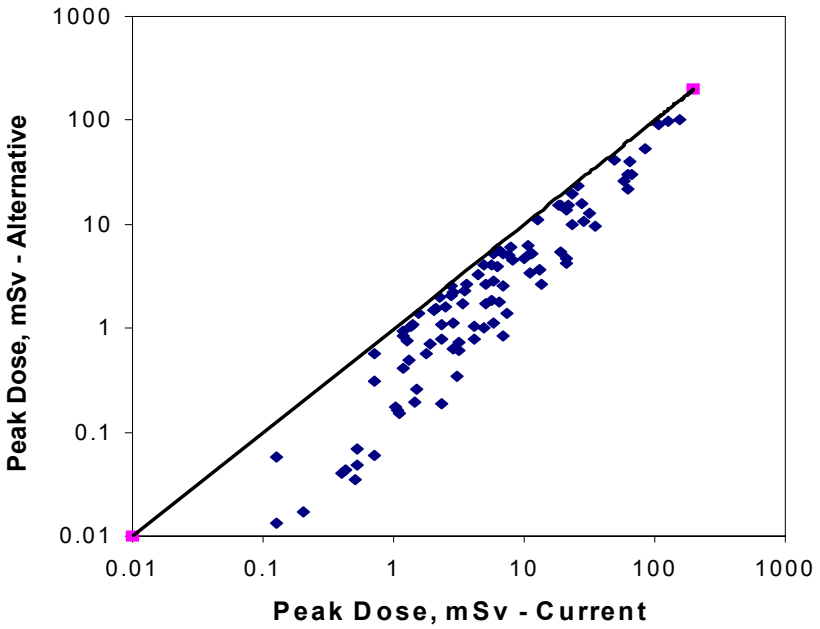

Figure 8-3. Estimated Peak Dose for 100 Vectors from the Alternative Model and the Current TPA Code Model for Fine Fuel Particle-Size Distribution. Diagonal Line Indicates Equal Dose for Either Model.

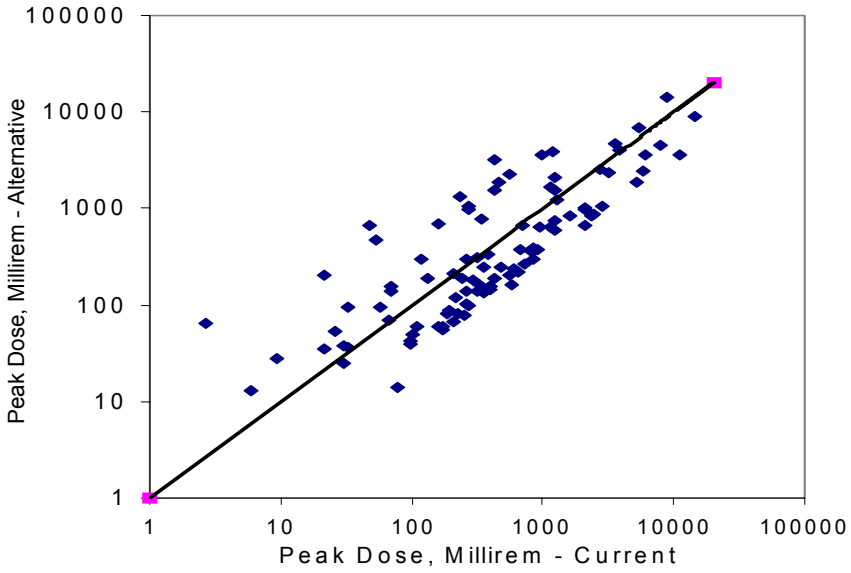

Figure 8-4. Estimated Peak Dose for 100 Vectors from the Alternative Model and the Current TPA Code Model for Coarse Fuel-Size Distribution. Diagonal Line Indicates Equal Dose for Either Model.

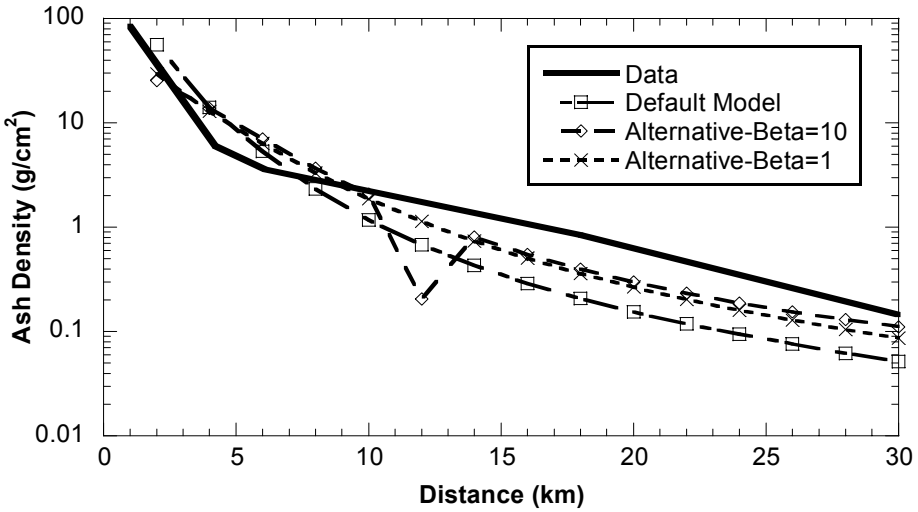

Figure 8-5. ASHPLUME Results and Cerro Negro Tephra Thickness Data for Tephra Density As a Function of Distance along the Centerline of Tephra Plume. Note the Model Instability for Alternative Model with β = 10.

Figure 8-6 shows results for the alternative vent velocity model for areal deposition of tephra. The plume is symmetrical, so Figure 8-6 shows only one-half the actual plume. The results are quantitatively similar to those calculated for the original validation and presented in Hill, et al. (1998). Note the model instability near *x* equal to 15 km [9.3 mi] and *y* equal to 0.

8.4.2.2 Estimated Peak Dose

When the alternative vent velocity was substituted directly into the TPA code for one set of conditions, the estimated peak dose appeared to decrease. Figure 8-7 compares the estimated peak doses from both models for each realization assuming the volcanic event occurred at 1,000 years. The majority of the estimated peak doses are smaller for the alternative model. Figure 8-8 shows the estimated peak mean dose for both models computed using a convolution procedure for a range of volcanic event times from 100 to 10,000 years. This result shows a modest decrease in the estimated dose for the alternative model.

8.5 Conclusions

This section presents conclusions from Part 1, the alternative spent nuclear fuel incorporation model, and Part 2, the alternative plume velocity model, of the analysis. Conclusions for the analysis of the alternative model for the spent nuclear fuel incorporation into tephra are described in Section 8.5.1. Conclusions for the analysis of the alternative model for the initial plume velocity are described in Section 8.5.2.

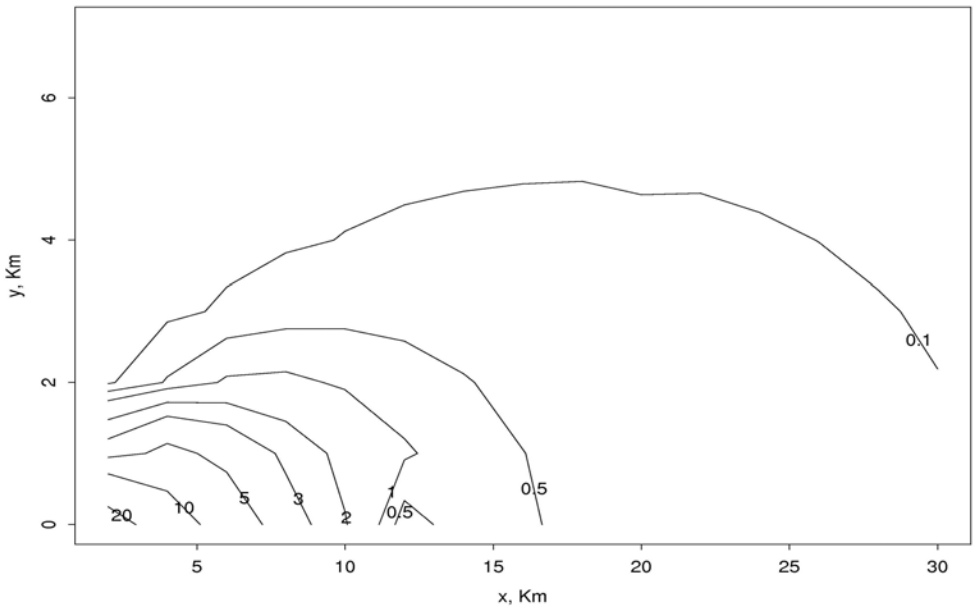

Figure 8-6. Areal Distribution of the Ash Thickness Computed By ASHPLUME, Using the Alternative Vent Velocity Model and $\beta = 10$. Note the Instability at $\times$ = 12 km [7.5 mi]. Because of Symmetry, One-Half the Areal Distribution Is Shown.

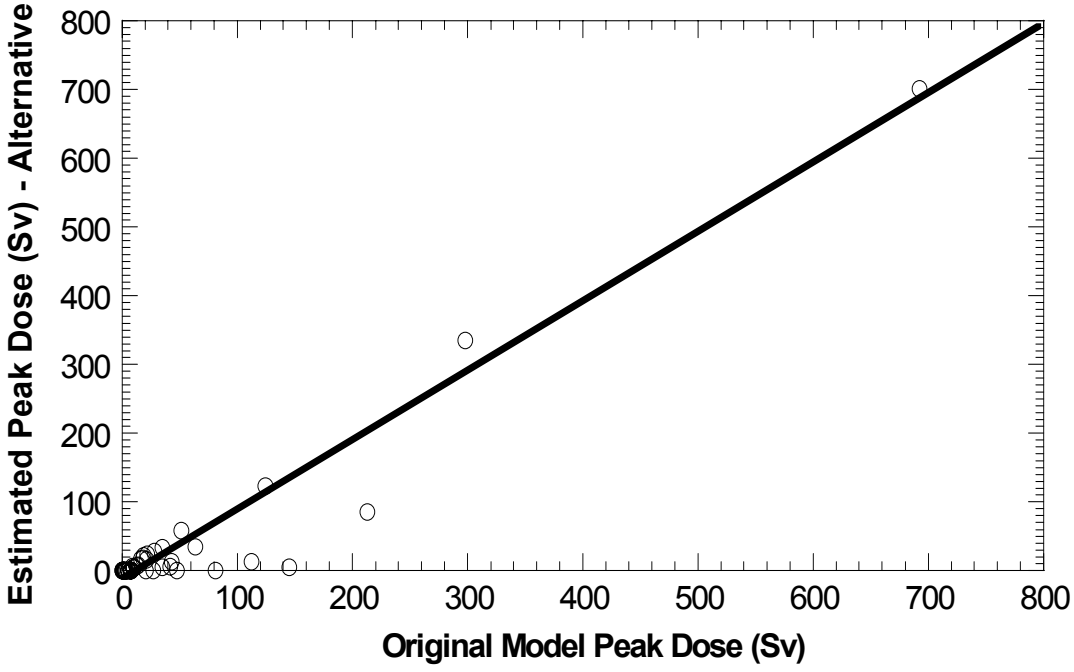

Figure 8-7. Estimated Peak Volcanic Dose for 50 Vectors Computed Using the Alternative and Current TPA Code Vent Velocity Models

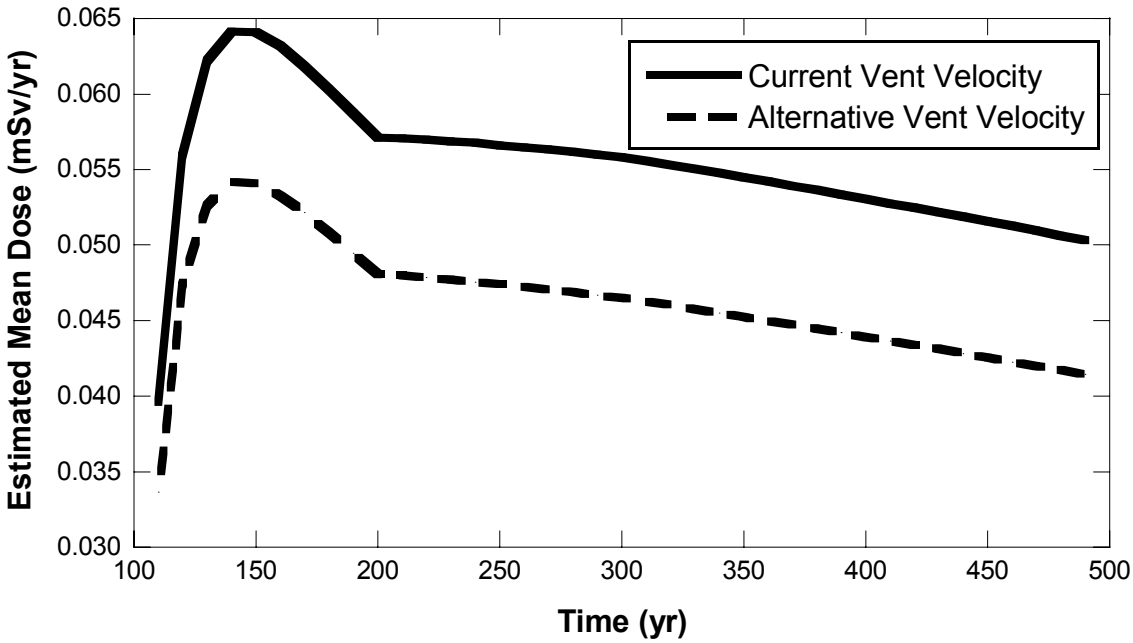

Figure 8-8. Estimated Mean Doses for 500 Years from ASHPLUME Computed Using the Alternative and Current TPA Code Vent Velocity Models

8.5.1 Part 1—Alternative Model for Incorporation of Spent Nuclear Fuel into Tephra

Results for the alternative conceptual model for fuel incorporation into tephra estimate that a significant fraction of spent nuclear fuel may be incorporated into dense particles, however, most of the fuel may be incorporated into the bulk of the tephra and have essentially the same density as virgin tephra. The fraction of spent nuclear fuel in dense particles is sensitive to the size distribution of the spent nuclear fuel. Most dense tephra/fuel particles may be at the small end of the particle-size range.

Analogous data exist to determine magma and wasteform interactions for volcanism in general and nuclear reactor research and accidents. Mixing tephra and spent nuclear fuel may be sensitive to mechanical, chemical, and thermal conditions involving the interaction of magma and the engineered wasteform. These factors influence the way in which the fuel may be incorporated in the tephra and its degree of heterogeneity. The current TPA code model is not sensitive to considerations of mixing fuel and tephra, however, the alternative model is sensitive. The alternative model shows a significant difference in results when the fuel-size distribution is changed by a factor of 10. Nevertheless, differences between the current TPA code model and the alternative model are not large (on average, less than a factor of two difference in dose estimates) compared with the many other uncertainties in the modeling of volcanism, lending credibility to the fuel incorporation model in the current TPA code.

The dissolution of spent nuclear fuel into magma has not been taken into account mechanisticallly, but it is possible that particles at the small end of the size spectrum may be more affected than larger particles. Spent nuclear fuel may be soluble in molten basalt to 40 percent (Westrich, 1982). Fuel dissolved directly into the magma may be somewhat uniformly

dispersed into the tephra, probably independent of the tephra particle size. If this were the outcome, dissolution may likely drive the results closer to the current TPA code incorporation ratio model, which tends to give a more uniform concentration of spent nuclear fuel in tephra than does the alternative model. Therefore, the conclusion that the differences between the current TPA code model and the alternative model are not large is still likely to hold.

8.5.2 Part 2—Alternative Model for Initial Plume Velocity

Both the current and modified models for vent velocity give reasonable results compared with the Cerro Negro data. The alternative vent velocity model estimates a modest decrease in the peak dose compared with the current TPA code model.

From these results, using either the current TPA code models or the alternative models for spent nuclear fuel incorporation and plume velocity does not make an overwhelming difference in dose estimates, and, in either case, the current TPA code model is likely conservative.

9 HIGH BURNUP SPENT NUCLEAR FUEL

TASK DESCRIPTION

Evaluate the disposal of spent nuclear fuel with a wide variation in the degree of burnup, and compare peak expected dose with estimates from the use of an average representative inventory.

AUTHOR

L. Howard

9.1 Background and Purpose

Commercial nuclear power plants use a variety of fuels and fuel configurations in the reactor core to generate power. Each fuel assembly, depending on the reactor configuration, initial fuel enrichment, burnup, and age of the waste may have a unique isotopic composition. Approximately 97 percent of the 1998 commercial spent nuclear fuel inventory in the United States is classified as low burnup with less than 45 GWd/MTU (Jain, et al., 2004). Current industry trends show an increasing degree of burnup. The amount of high burnup spent nuclear fuel with greater than 45 GWd/MTU is likely to increase in the coming years and may account for as much as 30 percent of the total projected inventory to be placed at the potential high-level waste repository at Yucca Mountain. This analysis is intended to evaluate the disposal of high burnup spent nuclear fuel and compare the estimated peak dose with the estimated dose from a representative inventory.

The DOE source term calculations can be reviewed in two primary references, DOE (2002) for the preclosure source term and DOE (2001a) for the postclosure source term. Both references calculate the source term using a weighted average method in which the pressurized water reactor and boiling water reactor commercial spent nuclear fuel waste inventories are determined using weighted averages of the reported enrichments, burnup, and ages from the reactor. The weighting terms are provided based on the number of fuel assemblies with a given value of each characteristic in the waste stream. Characteristics of the likely bounding pressurized water reactor and boiling water reactor wasteforms are the maximum reported burnup, maximum reported enrichment, and the minimum reported age in the waste stream for each fuel type (DOE, 2001a). DOE presents the radionuclide inventory in a curies per fuel assembly basis compared with curies per metric ton of uranium presented in this chapter and used in the TPA code inventory abstraction.

High burnup fuel is likely to increase the uncertainties associated with cladding failure (NRC, 2004). Performance assessments suggest a high correlation between dose and fraction of failed cladding because cladding failure may lead to increased radionuclide release rates. When compared with low burnup fuel, a more significant range of uncertainties is likely for high burnup fuel. NRC (2004) identifies the risk insight Cladding Degradation with a medium significance to waste isolation.

The analysis that follows studies the significance to waste isolation of high burnup fuels by estimating the inventory and thermal output of spent nuclear fuel waste in comparison to the

values used in the TPA code. This comparison is made to the values of the data files, as well as comparison to the estimated peak dose of a high burnup fuel inventory, and to those values of the representative inventory provided by the TPA code. The use of only high burnup fuel is considered to likely bound the inventory.

9.2 Methodology

Radionuclide inventories for high burnup fuels were estimated using the ORIGEN-ARP code Version 2.00 (Bowman and Leal, 2000). The ORIGEN-ARP code Version 2.00 performs burnup calculations using libraries with files of radionuclide characteristics, such as decay parameters and neutron cross sections, defined for different types of assemblies and uranium enrichments. The library for the 15 × 15 pressurized water reactor assembly was used because the relative increase in radionuclide inventory with burnup does not change significantly with fuel design. Because the principal purposes of this study were to estimate the effects of the increase in radionuclide inventory and the impact on the source term for postclosure, the 15 × 15 pressurized water reactor library was used for a 5.0-wt % enriched U-235 fuel at 65-GWd/MTU burnup. The estimates were compared with a 15 × 15 pressurized water reactor with a 4.0-wt % enriched U-235 fuel at 45-GWd/MTU burnup, literature values, and the TPA code inventory values. Cross sections used in the calculations were obtained by interpolation between the cross sections in the libraries for various fuel exposures.

Pressurized water reactor fuel was analyzed because it has a higher inventory of most radionuclides and generally may have a higher range of burnup than boiling water reactor fuel. The radionuclide inventories were estimated based on a typical three-depletion case (irradiation) in the reactor with a 10,000-year decay case in which the cooling time is assumed to be 10 years prior to emplacement in the potential repository. This calculation estimates radionuclide inventories for direct comparison with the inventory used in the TPA code in curies per metric ton uranium at 10 years from the reactor and important radionuclide concentrations as the waste decays during the 10,000-year period.

The ORIGEN-ARP code Version 2.00 estimated source term was compared to a number of source term analyses in the literature to verify the calculations. These calculations include those used in this analysis, such as Ramsdell, et al. (2001) and Sanders and Gauld (2003). Significant benchmarking and validating have been accomplished for the ORIGEN-ARP code Version 2.00 code calculations against isotopic analyses of high burnup fuels, such as by Sanders and Gauld (2003), and numerous references included in Bowman and Leal (2000). Although most radionuclide concentrations important to estimated dose increase with increasing burnup, as shown in Figure 9-1 and Table 9-1 for the 65-GWd/MTU case inventory, increase in the source term is likely not large in magnitude when comparing inventories in Table 9-1 from the low end of the high burnup fuel range (45 GWd/MTU) with those at the high end of the high burnup fuel range (65 GWd/MTU). For the source term, the likely bounding performance assessment inventory may be made entirely of high burnup spent nuclear fuel. As previously discussed, the potential repository inventory may be as much as 30-percent high burnup spent nuclear fuel, significantly less than the 100-percent high burnup inventory used in this analysis.

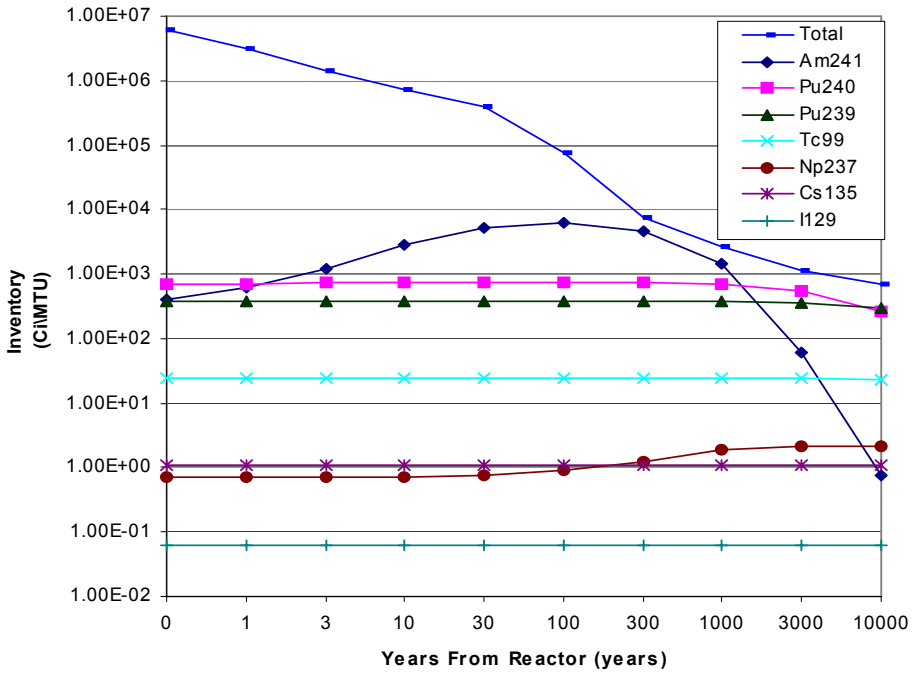

Figure 9-1. ORIGEN-ARP Code Version 2.00 Radionuclide Inventory Showing Decay of 65-GWd/MTU Fuel Throughout 10,000 Years from Reactor

To analyze the effects of a wide variation in high burnup fuel on estimated dose, the inventory of the 43 radionuclides tracked in the TPA code was changed to the high burnup 65-GWd/MTU fuel inventory estimated using ORIGEN-ARP code Version 2.00. This change of the initial radionuclide inventory values provides a likely bounding calculation of the source term effects on the estimated dose of the TPA code by assuming 100 percent of the inventory of the potential repository commercial spent nuclear fuel is a high burnup fuel inventory. Results from TPA code basecase runs (i.e., no extrusive volcanism) were used to compare the change in estimated dose as a result of the change in inventory by holding sampled parameters at constant mean values.

The activities of short-lived fission products tend to remain constant or decrease slightly with increasing burnup, while activities of activation products and actinides tend to increase with increasing burnup. High burnup fuel also may increase uncertainties associated with other fuel attributes such as cladding failure, surface area, rim effect, and segregation of volatile radionuclides (instant release fraction). Detail is provided about these additional spent nuclear fuel attributes in a review report on disposal issues associated with high burnup spent nuclear fuel (Jain, et al., 2004).

Table 9-1. Comparison of Calculated High Burnup Inventory to TPA Code Inventory for Nuclides Important to Long-Term Performance					
Nuclide	**ORIGEN-ARP* 65-GWd/MTU Inventory at 10 Years Decay (Ci/MTU)**	**TPA Code Initial at 10 Years Inventory (Ci/MTU)**	**Difference to TPA Code Inventory (%)**	**ORIGEN-ARP* 45-GWd/MTU Inventory at 10 Years Decay (Ci/MTU)**	**Difference to TPA Code Inventory (%)**
Am-241	2.88×10^{3}	2.08×10^{3}	40	2.35×10^{3}	14
Pu-240	7.32×10^{2}	5.44×10^{2}	35	6.11×10^{2}	12
Pu-239	3.84×10^{2}	3.69×10^{2}	4	3.57×10^{2}	−3
Tc-99	2.42×10^{1}	1.45×10^{1}	67	1.78×10^{1}	23
Np-237	7.28×10^{-1}	4.34×10^{-1}	68	4.69×10^{-1}	8
Cs-135	1.10×10^{0}	5.36×10^{-1}	105	6.91×10^{-1}	29
I-129	6.13×10^{-2}	3.57×10^{-2}	72	4.30×10^{-2}	20
Total: 43 Nuclides in the TPA code	4.23×10^{5}	2.57×10^{5}	65	—	—
*code Version 2.00					

9.3 Assumptions

The following assumptions were incorporated in this analysis.

- The ORIGEN-ARP code Version 2.00 inventory calculation uses a typical 15 × 15 pressurized water reactor fuel assembly with a 5-wt % enriched U-235 fuel irradiated at 65-GWd/MTU burnup.

- The high burnup fuel inventory estimated using the ORIGEN-ARP code Version 2.00 provides a likely bounding repository inventory because approximately 70 percent of the potential repository inventory may be low burnup spent nuclear fuel.

- Decay heat values provided in the TPA code data file provide representative decay heat values for the life of the potential repository.

9.4 Results

Table 9-1 provides a comparison between selected long-lived radionuclides in the source term estimated for the 65-GWd/MTU high burnup fuel, the 45-GWd/MTU burnup fuel, and the representative repository inventory used in the TPA code. Using mean values (single-realization TPA code run to highlight the change in estimated groundwater dose caused by the source term change), the estimated peak dose at 10,000 years increased from 0.162 to 0.297 mrem/yr [0.00162 to 0.00297 mSv/yr], which is a factor of 1.8 increase. The results suggest a low sensitivity of the estimated peak dose to the radionuclide inventory.

The decay heat load for the two spent nuclear fuel burnup cases discussed previously was estimated to analyze the impact of higher burnup fuel. The 45 and 65 GWd/MTU cases are compared with literature values from Ramsdell, et al. (2001) in Figure 9-2. The literature values from Ramsdell, et al. (2001) encompass 1–30 years decay. The basecase TPA code pressurized water reactor decay heat profile used in this analysis for pressurized water reactor spent nuclear fuel is also presented in Figure 9-2 for comparison. This is the basecase profile for the TPA code, and it uses an average burnup fuel profile of 48 GWd/MTU.

The range of thermal output from the various burnup levels presented here is relatively small and supports the calculated profiles for this analysis. Because approximately 70 percent of the potential repository spent nuclear fuel is estimated to have been irradiated at burnups of less than 45 GWd/MTU and, thus, have lower magnitude decay heat profiles than those burnups presented in Figure 9-2, the repository decay heat load as a whole is likely bounded in the basecase TPA code. The thermal output used in the TPA code is a weighted average of the pressurized water reactor and boiling water reactor waste packages with weighted average fuel enrichment and burnup values taken from the literature. As can be seen from this analysis, the percentage of waste packages in the potential repository at higher burnup may increase the thermal output, assuming the same decay time. The potential repository, however, is likely to have waste packages at lower thermal outputs because of lower enrichments and burnup and longer decay times from the reactor prior to emplacement in the potential repository. Thus, the analysis is considered to be likely bounding.

9.5 Conclusions

Literature review and analysis suggest increasing fuel burnup changes the radionuclide inventory in spent nuclear fuels. The activities of short-lived fission products tend to remain constant or decrease slightly, while activities of activation products and actinides tend to increase with increasing burnup, thus also increasing the amount of decay heat the waste generates at a given point in time from the reactor. For use in the TPA code calculations, the source term and thermal load values are weighted averages used to model the potential repository inventory as a whole.

This analysis estimated the effect of a change in inventory on peak dose. An inventory consisting of a nonweighted, 100-percent, 65-GWd/MTU high burnup fuel inventory was used in the TPA code to estimate peak dose, and those results were compared with basecase TPA code results. The estimated peak dose increased by a factor of less than two when compared with the basecase estimated peak dose for the nominal scenario (i.e., no extrusive volcanism).

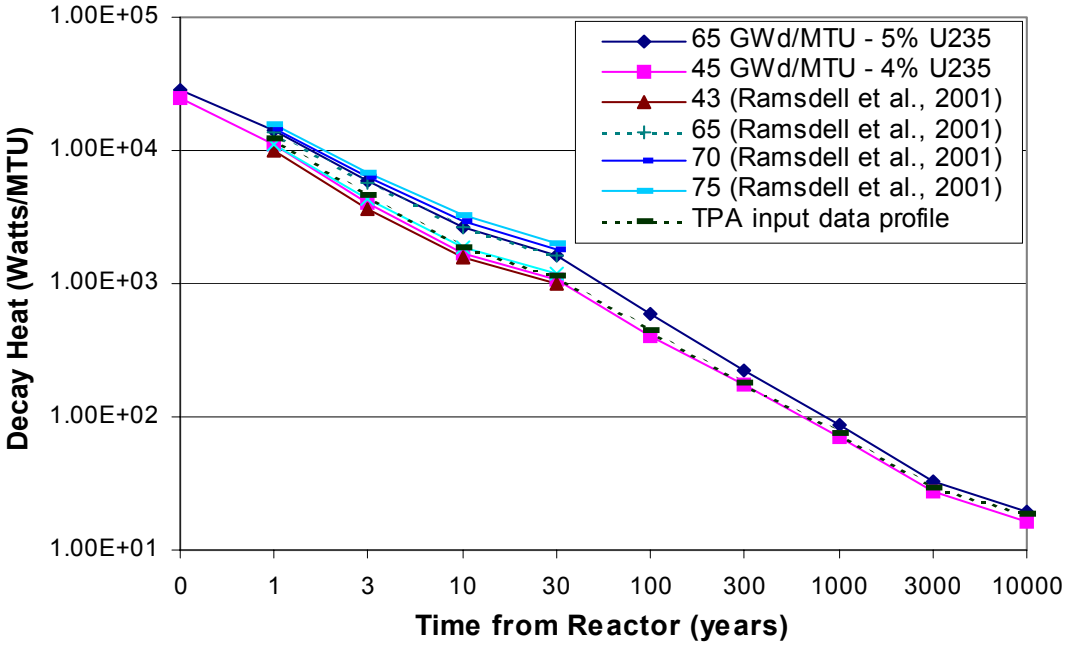

Figure 9-2. High Burnup Fuel Decay Heat Comparison—ORIGEN-ARP Code Version 2.00-Calculated Values, TPA Code Profile, and Data Extracted from NUREG/CR–6703 (Ramsdell, et al., 2001)

10 NATURAL BACKFILL AND IGNEOUS CONSEQUENCES

TASK DESCRIPTION

Evaluate the effects of natural backfill on igneous consequences.

AUTHORS/CONTRIBUTORS

R. Benke, G. Adams, B. Hill, G. Ofoegbu, and D. Gute

10.1 Background and Purpose

This task evaluates the effect of natural backfill on igneous consequences using an alternative model. Igneous consequences may be divided into two parts, consequences from a volcanic eruption and consequences from an igneous intrusion. In a volcanic eruption, flowing magma may disrupt emplaced waste packages, and high-level waste may be released directly to the atmosphere as contaminated ash. In an igneous intrusion, flowing magma may disrupt emplaced waste packages and lead to the contamination of groundwater. Because the Number of Waste Packages Affected by Eruption has been determined to be of high significance to waste isolation (NRC, 2004) compared to medium significance for the Number of Waste Packages Damaged by Intrusion, this task focused only on how natural backfill affects the consequences from a volcanic eruption.

Natural backfilling relates to the degradation of the drifts through time whereby rock masses may fall from the drift ceiling and fill the original drift openings with rock rubble. The size of the drift opening (or void area) may be reduced during time because degraded rock may occupy more volume as fallen rubble compared with the original volume occupied as part of one drift ceiling. Bulking factors may be used to account for this change in rock density and occupied volume. Significant natural backfilling may bury the drip shield and waste package, prevent the flow of magma along a drift, and limit the number of waste packages contributing to the direct release of high-level waste into the atmosphere from a volcanic eruption. Although natural backfill may limit the flow of magma along a drift, the upward flow of magma in the volcanic conduit is unaffected by natural backfill. In other words, waste packages intersected by the primarily vertical conduit may still contribute to the direct release source term even if the drifts are completely backfilled. The basecase eruptive source-term model in the TPA code estimates the number of affected waste packages as the number of waste packages contained within the volcanic conduit. An alternative model accounts for the dog-leg flow of magma down a drift. In the alternative model, magma flows down a drift and contacts waste packages, and the inventory of these affected waste packages is available for direct release. For this reason, the natural backfill only affects the consequences from the alternative model. Although natural backfilling also may affect the integrity of the drip shield and waste package, the models for a volcanic eruption are insensitive to the integrity of the drip shields and waste packages contacted by flowing magma.

The natural backfilling processes addressed in this analysis are not the result of a seismic event. Seismic events may induce drift degradation (referred to as seismic rockfall). Because of the small probabilities for seismic rockfall and volcanic eruption events individually, the probability for a scenario involving seismic rockfall followed by a volcanic eruption is likely to fall below the 10^{-8} annual probability of occurrence threshold specified by 10 CFR Part 63 and, therefore, is not considered. In addition, it is unlikely that ground motions associated with a volcanic eruption may exceed the estimated threshold for minor drift damage of 0.2 g (Gute, et al., 2003, Figure 4-15).

10.2 Methodology

The approach to evaluating the effects of natural backfill on the consequences from an igneous eruption is divided into two parts. In the first part, the fraction of waste packages buried by natural backfill is estimated as a function of time using an approach developed for this analysis. In the second part, the TPA code was used to estimate the consequences from a volcanic eruption for the basecase source-term model and the alternative model. The results from the TPA code are combined with the results from the first part to estimate igneous risk curves (as functions of time) with and without the effects of natural backfill.

10.2.1 Estimate of the Fraction of Waste Packages Buried by Natural Backfill

Based on the MECHFAIL module (Gute, et al., 2003), a numerical model was created using Mathematica® Version 4.1.0.0 to estimate the fraction of waste packages buried by drift degradation debris at various postclosure times. The analyses used fractions of lithophysal (85 percent) and nonlithophysal (15 percent) rock that are consistent with recent DOE information (Bechtel SAIC Company, LLC, 2003e).

Each realization of the numerical model sampled a backfill time (Gute, et al., 2003, Figure 4-10) and bulking factors consistent with those used in the TPA code (Table 10-1). Using the MECHFAIL module relationship between bulking factor and the maximum degradation zone height (Gute, et al., 2003, Figure 4-6), the degradation rates for the two rock types were estimated in each realization (Section 10.3.1, Assumption 1). Multiplying the degradation rates by postclosure time determined the degraded height of the drift at that time. The height of rock debris was estimated from the amount of fallen natural backfill rock and the bulking factor.

The steps of the numerical model for drift degradation are described next.

1. Sample time for complete natural backfill.

2. Sample a bulking factor for lithophysal rock. Interpolate the maximum degradation zone height in lithophysal rock from the sampled value for the lithophysal bulking factor.

3. Sample a bulking factor for nonlithophysal rock. Interpolate the maximum degradation zone height in nonlithophysal rock from the sampled value for the nonlithophysal bulking factor.

Table 10-1. Input Parameters Used in the Mathematica® Simulations for Natural Backfill	
Parameter Name	**Distribution/Value**
Number of Realizations [unitless]	10,000
Fraction of Drifts in Lithophysal Rock [unitless]	0.85
Fraction of Drifts in Nonlithophysal Rock [unitless]	0.15
Drift Radius [m]	2.75
Minimum Cross-Sectional Area of Rock Debris to Fill the Sides of the Drip Shield [m^2] (Figure 10-1)	6.58
Time Required for Complete Natural Backfill of the Drift [yr]	Beta Distribution Minimum = 250 Maximum = 1,000 Alpha shape parameter = 3.25842 Beta shape parameter = 1.82124
Bulking Factor for Lithophysal Rock [unitless]	Uniform Distribution Minimum = 1.15 Maximum = 1.50
Bulking Factor for Nonlithophysal Rock [unitless]	Uniform Distribution Minimum = 1.35 Maximum = 1.50
Maximum Drift Degradation Zone Height [m] As a Function of the Bulking Factor [unitless] for the Elliptical Drift Degradation Geometry [Gute, et al., 2003, Figure 4-6]*	Data Pairs Bulking Factor, Maximum Drift Degradation Zone Height (1.1, 40) (1.2, 21.5) (1.3, 15.5) (1.4, 12) (1.5, 10)

*Gute, G.D., G. Ofoegbu, F. Thomassy, S. Hsiung, G. Adams, A. Ghosh, B. Dasgupta, A.H. Chowdhury, and S. Mohanty. "MECHFAIL: A Total-system Performance Assessment Code Module for Evaluating Engineered Barrier Performance under Mechanical Loading Conditions." CNWRA 2003-06. San Antonio, Texas: CNWRA. 2003.

4. Estimate degradation rates for lithophysal and nonlithophysal rock per the MECHFAIL report [Gute, et al., 2003, Eq. (4-10)]

$$\text{Degradation Rate}\left[\text{m/yr}\right] = \frac{\text{Maximum Degradation Zone Height}\left[\text{m}\right] - \text{Drift Radius}\left[\text{m}\right]}{\text{Time for Complete Natural Backfill}\left[\text{yr}\right]} \quad (10\text{-}1)$$

where the maximum degradation zone heights are determined by interpolation from the sampled bulking factors (see data pairs in Table 10-1).

The following calculations are performed for a specific postclosure time. For a single realization, steps 5–9 are repeated for each specific postclosure time.

5. Estimate the cross-sectional area covered by rubble debris for lithophysal and nonlithophysal rock

$$\text{Lithophysal Rubble Debris Area}\left[\text{m}^2\right] = \frac{\pi}{2}\left(\text{Drift Radius}\left[\text{m}\right]\right)\left(\text{Lithophysal Bulking Factor [unitless]}\right) \times \left(\text{Lithophysal Degradation Rate}\left[\text{m/yr}\right]\right)\left(\text{Time}\left[\text{yr}\right]\right) \quad (10\text{-}2)$$

$$\text{Nonlithophysal Rubble Debris Area}\left[\text{m}^2\right] = \frac{\pi}{2}\left(\text{Drift Radius}\left[\text{m}\right]\right)\left(\text{Nonlithophysal Bulking Factor}\left[\text{unitless}\right]\right) \times \left(\text{Nonlithophysal Degradation Rate}\left[\text{m/yr}\right]\right)\left(\text{Time}\left[\text{yr}\right]\right) \quad (10\text{-}3)$$

6. If the rubble debris area for lithophysal rock exceeds the minimum area (Figure 10-1), the debris height above the crown of the drip shield is estimated based on an elliptical rubble geometry (Assumption 2 in Section 10.3.2)

$$\text{Lithophysal Rubble Debris Height}\left[\text{m}\right] = \frac{2}{\pi}\frac{\left(\text{Lithophysal Rubble Debris Area}\left[\text{m}^2\right] - \text{Minimum Area of Rock Debris}\left[\text{m}^2\right]\right)}{\text{Drift Radius}\left[\text{m}\right]} \quad (10\text{-}4)$$

If the rubble debris area for lithophysal rock does not exceed the minimum area (Figure 10-1), the debris height above the crown of the drip shield equals zero.

7. If the rubble debris area for nonlithophysal rock exceeds the minimum area (Figure 10-1), the debris height above the crown of the drip shield is estimated based on an elliptical rubble geometry (Section 10.3.2, Assumption 2)

$$\text{Nonlithophysal Rubble Debris Height } [\text{m}] = \frac{2}{\pi}\frac{\left(\text{Nonlithophysal Rubble Debris Area } [\text{m}^2] - \text{Minimum Area of Rock Debris } [\text{m}^2]\right)}{\text{Drift Radius } [\text{m}]} \quad (10\text{-}5)$$

If the rubble debris area for nonlithophysal rock does not exceed the minimum area (Figure 10-1), the debris height above the crown of the drip shield equals zero.

8. When the distance between the lithophysal rock debris height (above the crown of the drip shield) and the degraded height of the drift ceiling is less than 1 m [3.28 ft] (Section 10.3.3, Assumption 3), the waste packages below the lithophysal rock are assumed to be effectively buried from flowing magma, and the source term for the alternative model is reduced by the fraction of the repository in lithophysal rock.

9. When the distance between the nonlithophysal rock debris height above the crown of the drip shield and the degraded height of the drift ceiling is less than 1 m [3.28 ft] (Section 10.3.3, Assumption 3), the waste packages below the nonlithophysal rock are assumed to be effectively buried, and the source term for the alternative model is reduced by the fraction of the repository in nonlithophysal rock.

10. Steps 1–9 are repeated for each realization of the Mathematica® Version 4.1.0.0 simulation. The average source term for the alternative model (i.e., fraction of waste

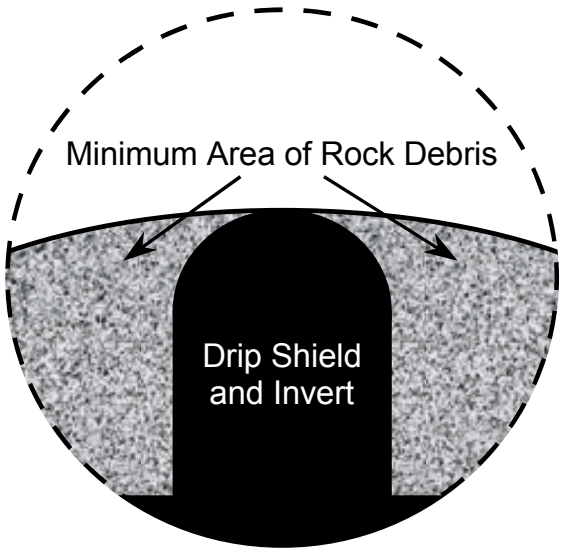

Figure 10-1. Cross-Sectional View of the Emplacement Drift Showing the Minimum Area of Rock Debris Required to Fill the Voids on the Sides of the Drip Shield for an Elliptical Drift Degradation Geometry. The Degraded Drift Ceiling Is Not Shown.

packages not buried under natural backfill) is estimated at each of the postclosure times. The alternative model estimates the number of waste packages contributing to the source term based on an open drift geometry (i.e., buried fraction is zero) by sampling from a probability distribution function. Ultimately, the results of the Mathematica® Version 4.1.0.0 simulation (i.e., fraction of waste packages not buried under natural backfill as a function of postclosure time) are used to scale the consequences from the alternative model. Because the consequences of a volcanic eruption are proportional to the number of waste packages contributing to the source term, this scaling on the consequences produces the same effect if each sampled value for the number of waste packages was scaled by the Mathematica® Version 4.1.0.0 simulation results.

10.2.2 Estimate Igneous Risk Curves With and Without the Effects of Natural Backfill

The algorithms employed in Mohanty, et al. (2002b) to estimate total dose weighted by an annual probability for igneous events [e.g., Figure 3-45(b)] were used with an annual event probability of 10^{-7} to estimate risk curves from the TPA code outputs. For estimating the direct release of high-level waste into the atmosphere resulting from a volcanic eruption, the TPA code was executed for both the source-term models. The first set of calculations used the basecase source term for a volcanic eruption [i.e., VolcanoModel set to 1 (Geometric) in the TPA code input file] where the number of waste packages affected is estimated as the number intersected by upward flowing magma within the volcanic conduit. The second set of calculations used the alternative model [i.e., VolcanoModel set to 2 (Distribution) in the TPA code input file] accounts for the dog-leg flow of magma down a drift. Each set is composed of 13 separate TPA code simulations with 400 realizations for eruption times at 100; 200; 300; 400; 500; 700; 1,000; 1,500; 2,500; 4,000; 6,000; 8,000; and 10,000 years. Table 10-2 highlights those changes (compared with the basecase source term values for a volcanic eruption) made to the parameter values and flag settings in the TPA code input file.

10.3 Assumptions

This analysis is based on three major assumptions, which are described next.

10.3.1 Assumption 1—Degradation Rates

As described in the MECHFAIL report (Gute, et al., 2003, pages 4–14), the ground support system is likely to remain effective on the order of tens of years, to as long as 100 years after permanent closure (after cessation of maintenance). As a result, the ground support system is not likely to be effective after 100 years. This work adopts those degradation rates for estimating the effects of natural backfill.

10.3.2 Assumption 2—Elliptical Drift Degradation Geometry

The elliptical drift degradation geometry is assumed for this work (Gute, et al., 2003, Figures 4-2 and 4-3). Initial rockfall is assumed to collect at the sides of the drip shield. A minimum amount of rockfall (minimum cross-sectional area of rock debris) is required to fill the drift voids along the sides of the drip shield. Beyond this minimum amount of rockfall, the elliptical drift

Table 10-2. TPA Code Input Parameter Values for the Two Calculational Sets. The First Set Used the Basecase Source Term Model for a Volcanic Eruption. The Second Set Used the Alternative Model. Each Set Contained 13 TPA Code Simulations for the Different Values for the AgeOfWaste[yr] Parameter.

Parameter Name	Basecase Value	Set 1 Value	Set 2 Value
VolcanismDisruptiveScenarioFlag(yes=1,no=0)	0	1	1
DirectReleaseOnlyFlag(yes=1,no=0)	0	1	1
NumberOfRealizations	1	400	400
MaximumTime[yr]	100,000	10,000	10,000
VolcanoModel(1=Geometric,2=Distribution)	1	1	2
TimeOfNextVolcanicEventinRegionOfInterest[yr]	Finite Exponential Distribution Min. = 100.0; Max. = 10,000.0; and Recurrence Rate = 1×10^{-7}	Constant* 100	Constant* 100
FractionOfTimeVolcanicEventIsExtrusive	0.999	1	1
AgeOfWaste[yr]	26	Set to one of the following values*: 26; 126; 226; 326; 426; 626; 926; 1,426; 2,426; 3,926; 5,926; 7,926; or 9,926	Set to one of the following values*: 26; 126; 226; 326; 426; 626; 926; 1,426; 2,426; 3,926; 5,926; 7,926; or 9,926

*The algorithm for generating igneous risk curves requires the time of the volcanic event be fixed at 100 years and the age of waste to be varied to account for radioactive decay. The values for the age of waste shown are chosen so the algorithm can estimate risk curves based on eruptions at 100; 200; 300; 400; 500; 700; 1,000; 1,500; 2,500; 4,000; 6,000; 8,000; and 10,000 years.

degradation geometry is used to estimate the height of rockfall debris above the drip shield crown. The minimum area of rock debris was estimated based on the DOE dimensions (CRWMS M&O, 2001, Figure 5-3) with a maximum invert thickness of 0.576 m [1.89 ft] to the base of the drift, instead of the 0.606 m [1.99 ft] shown in the DOE figure.

10.3.3 Assumption 3—1-m [3.28-ft] Minimum Degraded Void Height

A minimum degraded void height of 1 m [3.28 ft] was used to estimate the eruptive source term for the alternative model with a degraded drift geometry. Flowing magma may entrain loose rubble during the course of an eruption because of pressure fluctuations in the conduit. When the gap between the degraded drift ceiling and the rock rubble was at least 1 m [3.28 ft], waste packages were assumed available for entrainment in flowing magma. As a first-order approximation, the magma is assumed to be blocked from flowing down a degraded drift when the gap between the height of the rock debris is less than 1 m [3.28 ft] from the height of the degraded drift. For such a condition, waste packages along the drift (outside the conduit-drift intersection) may be treated as buried, with their waste sequestered from entrainment into flowing magma and erupting tephra. Although magma flow down a drift with natural backfill is not explicitly analyzed in Bechtel SAIC Company, LLC (2003f), magma interaction with the end of the drift is discussed.

10.4 Results

Figure 10-2 shows estimated unburied fractions of waste packages in the repository at various postclosure times. These results are relevant only to the alternative model for igneous consequences. These results were combined with the TPA code outputs to estimate risk curves for volcanic eruptions that account for the effect of natural backfill.

When the effect of natural backfill is neglected, Figure 10-3 shows the contributions for the two eruptive source-term models. The estimated curve shown in Figure 10-3(a) for the basecase model compares well to other curves presented for volcanic eruptions using the TPA code (Mohanty, et al., 2002b, Section 3.7). Figure 10-3(b) shows the estimated contributions for the two eruption models accounting for the effect of natural backfill. Natural backfilling has no effect on the basecase source-term model. For times less than approximately 400 years, natural backfilling is estimated to have a negligible effect on the risk contribution from the alternative model. For times between approximately 400 and 600 years, natural backfilling reduces the estimated contribution from the alternative model by less than a factor of two. For times greater than approximately 600 years, natural backfilling is estimated to significantly reduce the contribution from dog-leg flow. For times greater than 800 years, natural backfill has buried all waste packages and the estimated contribution from dog-leg flow is reduced to zero.

Figure 10-4 shows the total estimated risk from the alternative model, where the two contributions in Figure 10-3(a) are summed for the case neglecting natural backfill, and the two contributions in Figure 10-3(b) are summed for the case accounting for natural backfill. For times less than nearly 400 years, natural backfilling is estimated to have a negligible effect on the risk. For times beyond 600 years, natural backfilling is estimated to reduce the risk from the alternative model by more than a factor of two. At times greater than approximately 750 years, the estimated alternative model risk is reduced by more than a factor of 10. Within the 10,000-year period, the estimated peak risk from a volcanic eruption occurs at almost

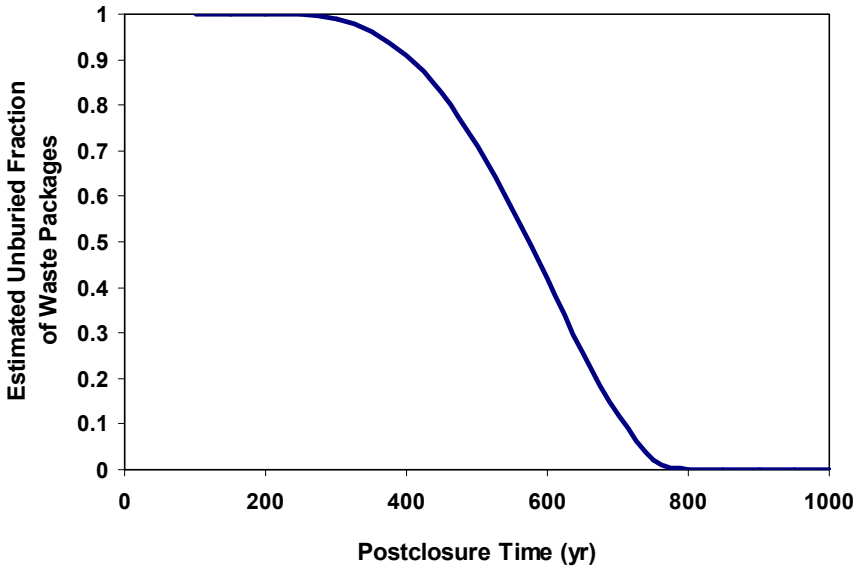

Figure 10-2. Unburied Fraction of Waste Packages As Estimated by the Numerical Model for Drift Degradation. Waste Packages Are Unburied When the Height of the Degraded Drift Opening Above the Waste Package and Drip Shield Exceeds 1 m [3.28 ft].

200 years. Natural backfilling has no effect on the estimated peak risk from a volcanic eruption for both source-term models used in the TPA code.

10.5 Conclusions

This section presents the conclusions of this analysis and provides a discussion for each of the three major assumptions.

1. Natural backfilling is estimated to have no effect on the risk from a volcanic eruption for the basecase source-term model used in the TPA code.

2. Natural backfilling is estimated to have no effect on the peak risk within the 10,000-year period for the alternative model, which accounts for the dog-leg flow of magma down a drift during a volcanic eruption.

For Assumption 1, design changes to the ground support system and to preclosure ventilation may delay significant drift degradation and also may delay the effects of natural backfill compared with the natural backfill effects estimated in this analysis. This potential delay has no effect on the three conclusions stated previously. The potential delay may increase the time specified (i.e., delay the time beyond 750 years stated in Section 10.4) at which the natural backfilling has a significant effect on the estimated risk from the alternative model. The net effect of completely backfilled drifts, however, may not change. In other words, completely backfilled drifts are still likely to reduce the estimated risk from the alternative model by more

(a)

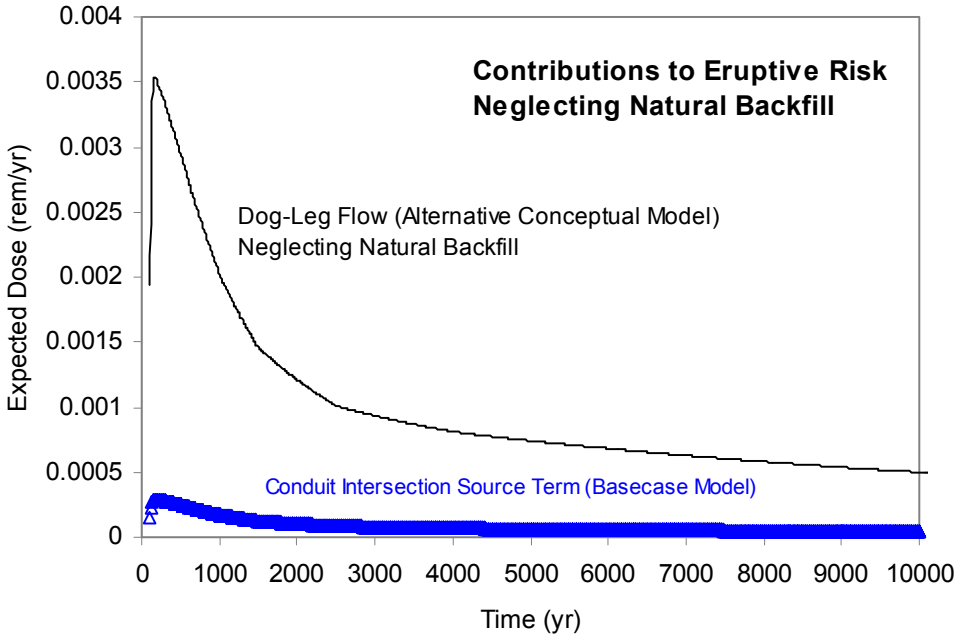

(b)

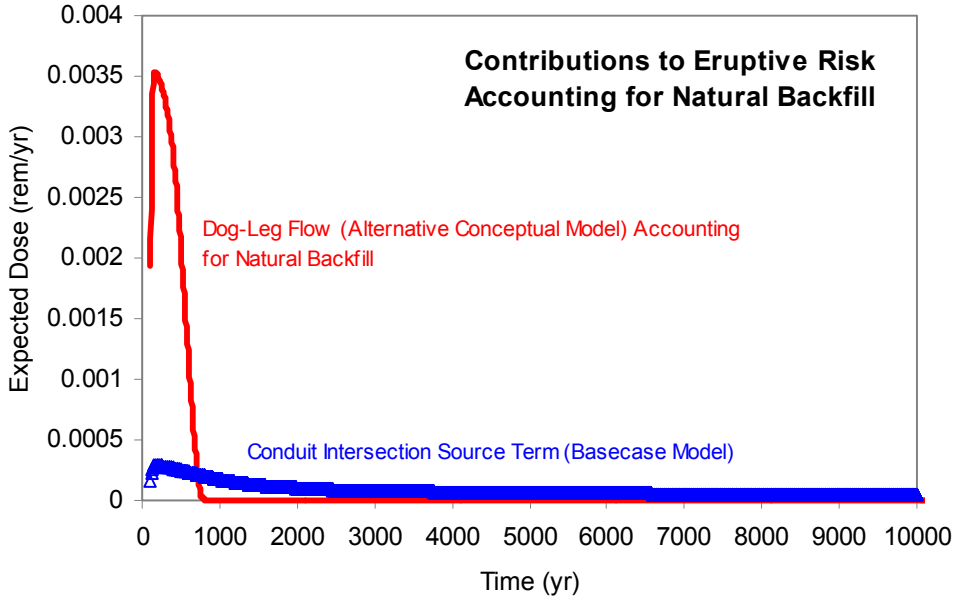

Figure 10-3. Estimated Contributions to Eruptive Risk with an Annual Volcanic Probability of 10^{-7} (a) Neglecting Natural Backfill and (b) Accounting for Natural Backfill

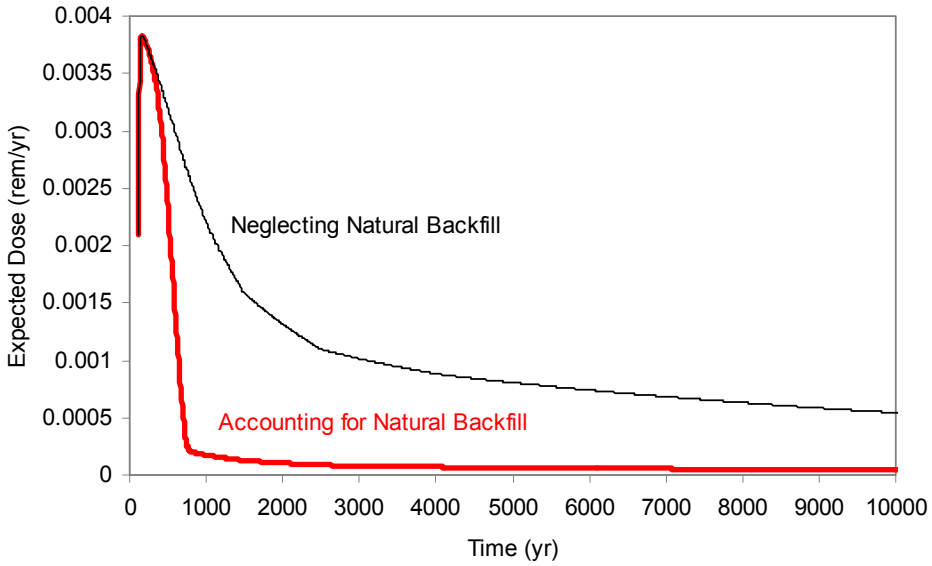

Figure 10-4. Estimated Effect of Natural Backfill on the Eruptive Risk With an Annual Volcanic Probability of 10^{-7} for the Alternative Model with Dog-Leg Flow

than a factor of 10, albeit delayed from the 750 years specified previously, if design changes delay significant drift degradation.

Assumption 2 relates to the elliptical drift degradation geometry for calculating the minimum amount of rock debris to fill the sides of the drip shield. Only significant differences in the drift degradation geometry or drift dimensions may affect the time at which natural backfill may effectively stop the flow of magma down a drift, which is based on the size of the void between the rubble pile and the degraded drift ceiling.

Assumption 3 specifies the minimum void height of 1 m [3.28 ft] for allowing magma flow in a degraded drift. Varying the value of this assumed quantity by a factor of two {i.e., values of 0.5 m [1.64 ft] or 2 m [6.56 ft]} shifts the time at which natural backfilling significantly reduces the estimated risk from the alternative model by a couple hundred years. In comparison to the estimated time of 750 years stated in Section 10.4, alternative minimum void heights of 0.5 m [1.64 ft] or 2 m [6.56 ft] may delay or accelerate the natural backfill effect. The three conclusions are not affected by the two alternative values.

11 NEAR-FIELD TEMPERATURE AND NATURAL BACKFILL

TASK DESCRIPTION

Evaluate the dose consequence of increased waste package and drip shield temperatures resulting from natural backfilling by drift degradation.

AUTHORS/CONTRIBUTORS

S. Mohanty and G. Adams

11.1 Background and Purpose

Current NRC and CNWRA calculations of the degradation of mined openings suggest that as much as 100 percent of the drifts may degrade during the first 1,000 years after repository closure (Gute, et al., 2003). The natural drift material dislodged from the drift roof, henceforth referred to as rockfall rubble or natural backfill, is likely to accumulate on the drift floor and surround the drip shield. The insulating effects of the natural backfill material are likely to increase drip shield, waste package, and wasteform temperatures. High temperatures may adversely affect the load-bearing capacity of the drip shield and the waste package, thus increasing their failure potential during the period of high temperatures. The increased temperature also may accelerate drip shield and waste package corrosion and wasteform dissolution if water seepage into the drift occurs. The increase in the near-field temperature from rockfall is discussed in the risk insight Effects of Accumulated Rockfall on Engineered Barriers in the Risk Insights Baseline Report (NRC, 2004). This risk insight has a rating of medium significance to waste isolation.

The DOE calculations with engineered backfill at repository closure, which can be viewed as a surrogate for natural backfilling with rockfall rubble, suggest the estimated peak waste package temperature may increase from nearly 165 to 315 °C [329 to 599 °F] (DOE, 2000), and temperatures of other components of the engineered system may increase correspondingly. The NRC independent analyses also estimate a similar increase in temperature at the waste package surface. For example, making a conduction-only assumption for heat transfer through the backfill material, Fedors, et al. (2003) estimated a peak temperature of approximately 351 °C [664 °F]. Using selected values for a hypothetical backfill surrounding the drip shield and making a similar conduction-only heat transfer assumption, Mohanty, et al. (2004) also estimated similar temperatures as high as 351 °C [664 °F]. These three calculations suggest the estimated peak temperature at the waste package could be nearly 185 °C [333 °F] higher in the presence of backfill material compared with the no-backfill case.

The temperatures estimated by DOE and NRC are based on several key assumptions. Key assumptions are the engineered backfill is representative of natural backfill and the assumptions for the engineered backfill are applicable to the heat transfer estimate for natural backfill. The effective thermal conductivity used in computing temperatures of an engineered backfill system is 0.27 W/(m-K) [0.156 BTU/(hr-ft-°F)], but may not be representative of the natural backfill system. Intuitively, the presence of any backfill may decrease convective and radiative heat transfer and may increase the conductive heat transfer from the engineered system.

Constraining the heat transfer assumption for the backfill material to conduction-only implies the backfill layer may behave as a thermal blanket at all temperatures. It may be argued that analyses with high temperatures likely bound the adverse effects of temperature on water chemistry, rock stability, and drip shield/waste package corrosion rates. It may be argued, however, that such analyses are not likely bounding because of the beneficial effect of high temperatures that keep water from contacting the waste package for a prolonged period. Consequently, this analysis develops an alternative thermal model to estimate the effect of drift degradation on near-field temperature evolution.

This task also estimates the impact on waste package temperature of current TPA code assumptions for the representation of natural backfilling because of drift degradation and determines the potential impact of natural backfilling on dose estimates.

11.2 Methodology

The methodology developed for this analysis directly links heat transfer to backfill characteristics. Because the temperatures are estimated as a function of heat transfer regimes, with the conduction and convection regimes determined explicitly, the approach eliminates the assumption that heat transfer in the natural backfill is from conduction-only. The heat transfer regimes are determined from the flow characteristics of the natural backfill medium, which are derived from the particle size distribution.

This section describes estimations of the (i) heat transfer regime; (ii) natural backfill permeability, which is used in determining flow characteristics; (iii) significance of the convection regime; and (iv) temperature based on appropriate flow regimes.

11.2.1 Determination of the Heat Transfer Regime

When there is no backfill between the drip shield and the drift wall, radiation and convection heat transfer are likely to occur. When the backfill material is present, generally radiation heat transfer may be neglected at temperatures below 400 °C [752 °F]. Depending on the nature of natural backfilling, however, convective heat transfer may occur because of buoyant forces from heated air contained in the pore spaces near the waste package. The Rayleigh number, which expresses the ratio of transport of energy by free convection to the transport by conduction, may be used to establish the condition for the onset of free convection. Convection currents may develop when the temperature gradient exceeds a critical value, but the temperature that establishes natural convection in air may not be sufficient to establish natural convection in air in a porous medium, largely because the viscous drag of the solids on the fluid may lead to small apparent velocities (Burmeister, 1993).

The approach used in this analysis is a physics-based model. For this model, convective heat transfer in the region with backfill is based on porous media petrophysical characteristics that relate radial heat transfer to natural convection in an annular region. The onset of natural convection and the heat transfer rates are related to the permeability of the natural backfill material. The permeability is estimated from porosity and particle size distribution of the natural backfill material.

Convection in the annular region between two horizontally emplaced concentric cylinders, with the inner cylinder temperature being higher, may be characterized by

$$\mathrm{Ra} = \frac{g\beta\left(T_{\mathrm{do}} - T_{\mathrm{bfo}}\right)r_i^3}{\nu\alpha_m} \tag{11-1}$$

where

Ra — Rayleigh number [unitless]
g — Acceleration caused by gravity [m/s^2]
β — Volume of thermal expansion [1/K]
r_i — Backfill inner radius [m]
ν — Kinematic viscosity [m^2/s]
α_m — Thermal diffusivity [m^2/s]
T_{bfo} — Lower temperature at the backfill outer surface [K]
T_{do} — Higher temperature at the backfill inner surface [K]

If the space between the outer and inner cylinders is filled with a porous medium, the Rayleigh number may be expressed by

$$\mathrm{Ra}_{r_i} = g\beta K r_i \frac{T_{\mathrm{do}} - T_{\mathrm{bfo}}}{\nu\alpha_m} \tag{11-2}$$

where K is the permeability [m^2] of the porous medium. The onset of free convection in porous media may occur at or above Rayleigh numbers of the order of $4\pi^2$ (i.e., $\mathrm{Ra}_c > 39.5$) (Lapwood, 1948). This criterion is based on horizontal layers filled with nonmoving fluid and upper and lower boundaries that may be both impermeable to flow and isothermal.

In this equation, K and α_m are functions of the characteristics and the accumulation pattern of the backfill material. The parameter K for the natural backfill may be determined from bulk physical properties (i.e., textural quantities such as grain size, sorting, packing, and particle size distribution).

11.2.2 Estimation of Natural Backfill Permeability

A physics-based model is used in this analysis to estimate the permeability of the accumulated natural backfill. This model estimates permeability from particle size distribution statistics and other properties (e.g., porosity and tortuosity) in the Carman-Kozeny equation.

Permeability of a medium, *K*, which is an assembly of a distribution of spherical particle sizes, may be represented by (Panda and Lake, 1994).

$$K = \frac{\overline{D}_p^2 \phi^3}{72\tau\left(1-\phi\right)^2}\left[\frac{\left(\gamma C_{D_p}^3 + 3C_{D_p}^2 + 1\right)^2}{\left(1+C_{D_p}^2\right)^2}\right] \tag{11-3}$$

where

C_{D_p} — Coefficient of variation of the particle size distribution $\left(\text{equal to } \sigma_{Dp}/\overline{D}_p\right)$ [unitless]

σ_{D_p} — Standard deviation of a particle size distribution [m]

ϕ — Bulk porosity [unitless]

$\overline{D}_p$ — Mean particle diameter [m]

τ — Tortuosity of the bulk medium [unitless]

γ — Skewness of a particle size distribution [unitless]

This equation is valid for any particle size distribution type. When $C_{D_p} = 0$, the terms in the square bracket vanish, and Eq. (11-3) reduces to the Carman-Kozeny equation, an equation that estimates the permeability of an assembly of single-size spheres of diameter D_p.

Parameters $\overline{D}_p$ and C_{D_p} in Eq. (11-3) may be derived from measurements. But measured data typically are reported as median grain size, $D_{p_{\text{med}}}$ (instead of $\overline{D}_p$), and Trask sorting coefficient, S_0 (instead of C_{D_p}). The experiments are typically based on a weight statistic that is usually determined from a sieve analysis, in comparison to the equations based on number statistics (Krumbein and Monk, 1942; Krumbein, 1936). Sieve analysis results use the Φ - distribution. In this approach, the particle size distribution is described through Φ classes, and each Φ class is described by the weight fraction. Here, $\Phi = -\log_2 D_p$, which represents the Φ - distribution and its attributes

$$\overline{D}_p = \exp\left\{-\left[\overline{\Phi}\left(ln\,2\right) + 2.5\sigma_\Phi^2\left(ln\,2\right)^2\right]\right\} \tag{11-4}$$

where $\overline{\Phi} = -\log_2 D_{P_{\text{med}}}$ for a Φ normal distribution and $D_{P_{\text{med}}}$ is in millimeters.

$$\sigma_{D_p}^2 = \exp\left\{-\left[2\overline{\Phi}\left(ln\,2\right) + 4\sigma_\Phi^2\left(ln\,2\right)^2\right]\right\} \tag{11-5}$$

where

$$\sigma_{\Phi} = \frac{\overline{\Phi} S_0^2 - \overline{\Phi}}{0.675 + 0.675\, S_0^2} \tag{11-6}$$

and S_0 is the Trask sorting coefficient (Krumbein, 1936), which is defined as

$$S_0 = \sqrt{F_{\Phi\ 25\%} / F_{\Phi\ 75\%}} \tag{11-7}$$

where *F* represents the weight fraction. Equations (11-4) through (11-6) assume that the particle size distribution is statistically isotropic and homogeneous. As these equations show, C_{D_p} is a function of S_0 and the median grain size. C_{D_p} increases with S_0 for a given $\overline{D}_p$. This increase is slow if the particle sizes are poorly sorted. In the limit of extremely poor sorting, C_{D_p} appears to be independent of sorting.

11.2.3 Determining the Significance of the Convection Regime

For a horizontal layer of porous medium of thickness *L* and width *h* heated from below when Ra exceeds the critical value $\mathrm{Ra}_c \approx 39.5,$ the Nusselt number is given by

$$\mathrm{Nu}_L = \frac{hL}{K} = \frac{\mathrm{Ra}_L}{40} \text{ when } \mathrm{Ra}_L \geq 40, \text{ else } = 1 \tag{11-8}$$

The Nusselt number of a horizontally emplaced annulus of porous medium with a heat source located at the inner surface of the annulus may be represented by the following correlation

$$\mathrm{Nu} \cong 0.44\, \mathrm{Ra}_{r_i}^{1/2} \frac{ln(r_o / r_i)}{1 + 0.916(r_i / r_o)^{1/2}} \tag{11-9}$$

where r_o and r_i are the radii of the outer and inner annulus surface.

The correlation (Bejan, 1984, p. 194) was obtained from experiments by Caltagirone (1976) and is appropriate for $1.19 \leq \frac{r_o}{r_i} \leq 4$. The correlation is valid for Nu >>1. The outer surface of the natural backfill material may be viewed as the outer wall of the annulus, and the drip shield outer wall may be considered as the inner wall of the annulus.

11.2.4 Temperature Calculation

Temperature calculations use the same basic formalism presented in Mohanty, et al. (2004) except for a few modifications, as shown next. The steady-state temperature drop in the drift is estimated from the rock wall temperature

$$T_{\text{wp}} - T_{\text{rw}} = \frac{q}{2\pi \text{wpl}} \left[\frac{ln\left(\frac{r_{\text{rw}}}{r_{\text{bfo}}}\right)}{k_{cv2} + k_{\text{r2}}} + \frac{ln\left(\frac{r_{\text{bfo}}}{r_{\text{dso}}}\right)}{k_{\text{bf}}} + \frac{ln\left(\frac{r_{\text{dso}}}{r_{\text{dsi}}}\right)}{k_{\text{ds}}} + \frac{ln\left(\frac{r_{\text{dsi}}}{r_{\text{wp}}}\right)}{k_{cv1} + k_{\text{r1}}} \right] \tag{11-10}$$

where

k	—	Equivalent thermal conductivity [W/(m-K)]
T	—	Surface temperature [K]
q	—	Heat flux above the waste package [W]
wpl	—	Waste package spacing [m]

Numerical notations 1 and 2 in the subscripts represent region 1 (region between the waste package and the drip shield) and region 2 (region between the drip shield and the rock wall). Character notations wp, rw, bf, bfo, ds, dsi, dso, cv, and r refer to waste package, rock wall, backfill, backfill external surface, drip shield, drip shield internal surface, drip shield external surface, convection, and radiation, respectively. Equations used to estimate the equivalent conductivities, k_{cv1}, k_{rl}, k_{cv2}, k_{r2}, and k_{bf}, are presented next.

The convective heat transfer from natural convection in the unbackfilled region is represented explicitly, which is based on temperature, diameter (D), Prandtl number (Pr), acceleration because of gravity, and volume of thermal expansion (Incropera and DeWitt, 1995; Manteufel, 1997). This model replaces the previously assumed equivalent thermal conductivity for convective heat transfer, a fixed value that is 30 times the air thermal conductivity (k_{air})

$$k_{\text{cv1}} = 0.386 k_{\text{air}} \left(\frac{\text{Pr}}{0.861 + \text{Pr}} \right)^{1/4} \left[\frac{\left(ln \frac{D_{\text{dsi}}}{D_{\text{wp}}} \right)^4 \; g \beta \left(T_{\text{wp}} - T_{\text{dsi}} \right)}{\nu \alpha \left(D_{\text{wp}}^{-3/5} + D_{\text{dsi}}^{-3/5} \right)^5} \right]^{1/4} \tag{11-11}$$

The radiative heat transfer may be represented by

$$k_{r1} = \frac{ln\left(\frac{r_{dsi}}{r_{wp}}\right)\sigma r_{wp}\left(T_{wp}^2 + T_{dsi}^2\right)\left(T_{wp} + T_{dsi}\right)}{\frac{1}{\in_{wp}} + \frac{1-\in_{dsi}}{\in_{dsi}}\left(\frac{r_{wp}}{r_{dsi}}\right)} \tag{11-12}$$

where

σ — Stefen-Boltzman constant {5.67×10^{-8} W/(m^2-K^4) [1.71×10^{-9} BTU/(hr-ft^2-°R^4)]}

$\in$ — emissitivity [unitless]

$$k_{cv2} = 0.386 k_{air}\left(\frac{Pr}{0.861+Pr}\right)^{1/4}\left[\frac{\left(ln\frac{D_{rw}}{D_{bfo}}\right)^4 g\beta\left(T_{bfo} - T_{rw}\right)}{\nu\alpha\left(D_{bfo}^{-3/5} + D_{rw}^{-3/5}\right)^5}\right]^{1/4} \tag{11-13}$$

$$k_{r2} = \frac{ln\left(\frac{r_{rw}}{r_{bfo}}\right)\sigma r_{bfo}\left(T_{bfo}^2 + T_{rw}^2\right)\left(T_{bfo} + T_{rw}\right)}{\frac{1}{\in_{bfo}} + \frac{1-\in_{rw}}{\in_{rw}}\left(\frac{r_{bfo}}{r_{rw}}\right)} \tag{11-14}$$

$$k_{bf} = \frac{q'}{2\pi}\frac{ln\left(\frac{r_o}{r_i}\right)}{T_{do} - T_{bfo}} \tag{11-15}$$

where

$$q' = Nu \cdot q_c \tag{11-16}$$

and

$$q_c = 2\pi k_m \frac{T_{do} - T_{bfo}}{ln\left(\frac{r_o}{r_i}\right)} \tag{11-17}$$

where k_m is the thermal conductivity of the backfill [W/(m-K)].

Parameters such as k_{r2}, k_{bf}, k_{cv1}, and k_{r1} on the right-hand side of Eq. (11-10) are functions of temperature for which this equation is solved. Although this equation may be simplified for obtaining a solution explicitly, obtaining such a solution is rather cumbersome (involving a fourth-order equation). Therefore, an iterative solution was used to solve Eq. (11-10) to obtain waste package temperature.

11.2.5 Implementation in the TPA Code

The alternative model presented in the previous section was implemented in the latest version of the TPA code. The implementation involved three key changes to the TPA code: (i) implementation of Eqs. (11-1) through (11-17) for computing flow-regime-based heat transfer, (ii) implementation of the Brent method (Press, et al., 1992) to iteratively solve Eq. (11-10) for the waste package temperature, and (iii) modifications to the TPA code to account for time-dependent backfill thickness.

The current version of the TPA code approximates the conductances as shown in Eq. (11-10) and does not account for convection. The iterative solution of the Brent method permits explicit incorporation of the temperature dependency of convection. Therefore, heat transfer can be computed as a function of the heat transfer regime.

The time-dependent backfill thickness is supplied to the TPA code in the form of tabular data (Manepally, et al., 2003; Fedors, et al., 2003) using an externally generated file that provides information on the change in drift diameter and backfill thickness as a function of time. The backfill thickness is not allowed to exceed the gap between the undegraded drift and the drip shield (horizontal lines in Figure 11-1). In the TPA code, the backfill thickness is specified as constant with time in the TPA code input file. To represent time-dependent drift degradation, the backfill thickness in the modified TPA code was varied as a function of time, as implemented in Manepally, et al. (2003).

11.3 Assumptions

The following assumptions were incorporated into the model pertaining to (i) heat transfer calculations, (ii) geometric simplifications before and during drift degradation, and (iii) natural backfill characteristics. Additional assumptions may be found in Chapter 5 of Mohanty, et al. (2002a). The simplifications used in the model did not always lead to likely conservative dose estimates.

11.3.1 Heat Transfer Assumptions

- Heat transfer through various engineered components in the drift (e.g., waste package, invert, backfill, and drip shield) is quasi-steady state.

- Heat transfer along the drift is negligible. This assumption is an artifact of the use of an entire line of waste packages in a drift as a line source. This assumption implies limited variation at the waste package scale.

11.3.2 Geometric Simplifications

- The engineered components inside the drift are idealized assuming the waste package is coaxial with the drift, the invert is a wedge occupying 25 percent of the drift volume, and the drip shield is circular and coaxial with the drift.

- The natural backfill material around the drip shield may be idealized as a concentric annular region coaxial with the waste package and drip shield limited in thickness (horizontal lines in Figure 11-1) to the original distance between the drift wall and the outer

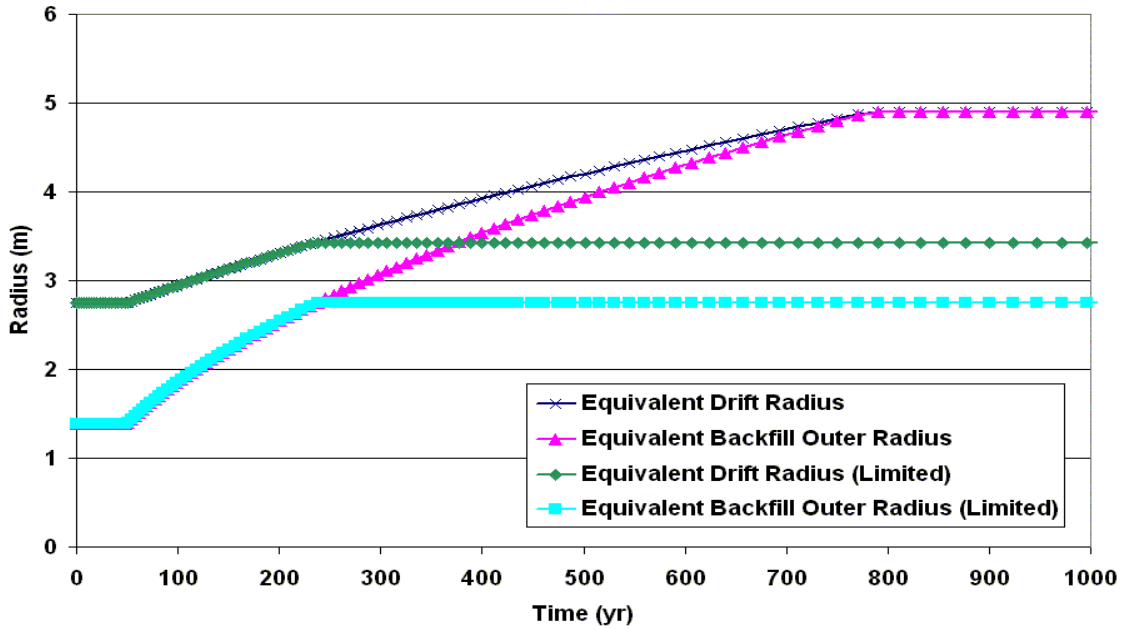

Figure 11-1. Equivalent Drift Radius and Backfill Radius As a Result of Drift Degradation and Natural Backfilling of the Drift (Manepally, et al., 2003)

surface of the drip shield. This assumption implies that drift degradation is relatively homogeneous. It is likely that certain portions of the drift may have no rubble accumulation, whereas, other sections may be filled with rubble.

- The fallen material is sufficient to fill the drift and the void created as a result of drift degradation. Figure 11-2 illustrates drift degradation for a partially degraded drift with the fallen material surrounding the drip shield.

11.3.3 Backfill Material Assumptions

- The natural backfill material may remain unconsolidated during the entire simulation period. Consolidation may decrease convective heat transfer and may increase conductive heat transfer. The net result is a likely increase in waste package temperature compared to the unconsolidated backfill case.

- The permeability of the natural backfill material is greater than 1 darcy (~ 1×10^{-12} m^2). The permeability model in Eq. (11-3) generally not applicable for permeability less than 1 darcy (Panda and Lake, 1994).

- Particles are spherical, and particles with a range of diameters are present in the system. Though the model is based on spherical particles, the effect of nonspherical particles may be captured by varying porosity because the nonsphericity and spheroid eccentricity may have the greatest impact on porosity (Lake, 1989).

- The particle assembly satisfies statistical homogeneity.

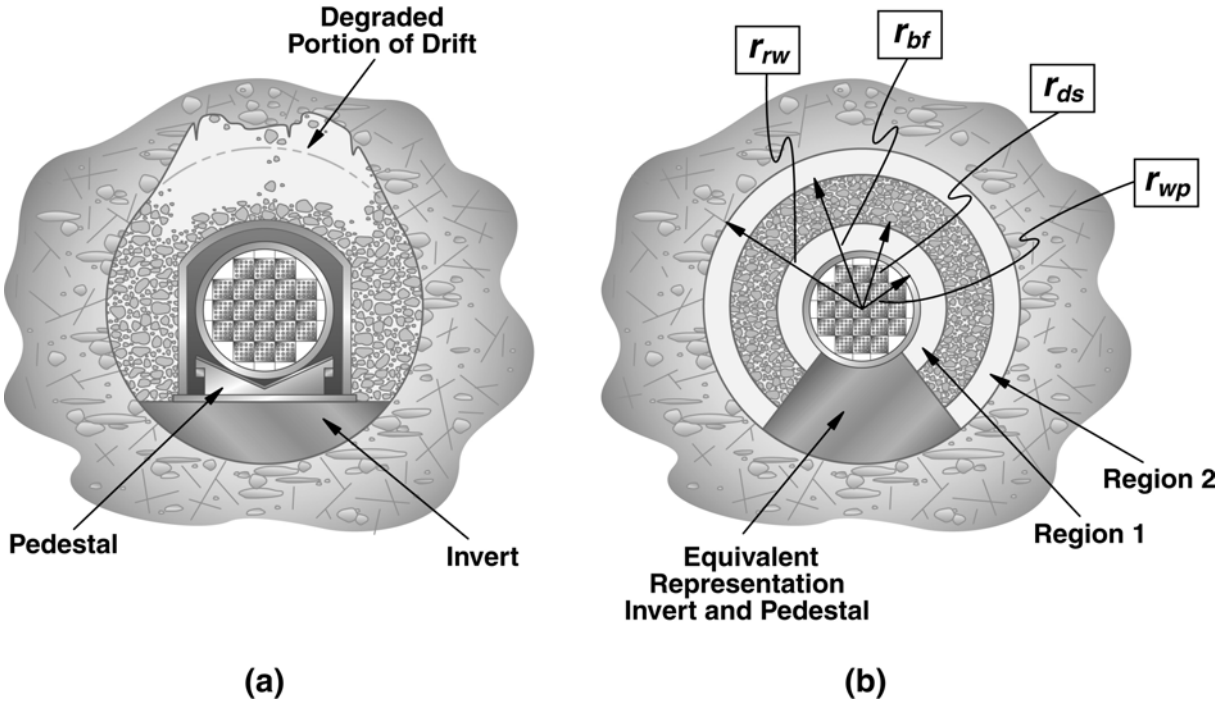

Figure 11-2. Schematic Showing (a) Natural Backfilling from Drift Degradation and (b) Idealization of Natural Backfilling for Computing Heat Transfer

11.4 Results

To estimate the dose consequence of natural backfilling by drift degradation, first the temperature at the waste package was computed. The temperature behavior was investigated for various arbitrarily chosen natural backfilling conditions (e.g., time of backfill and volume of backfill). Nominal values used in these calculations are presented in Table 11-1. Most of these values are either identical or similar to values in the TPA code.[1] Because an important aspect of this study was to determine if natural (free) convection in the natural backfill influences the estimated waste package temperature, the flow characteristics of the natural backfill material were investigated as a function of mean particle size, $\overline{D}_p$; porosity, ϕ; tortuosity, τ; coefficient of variation, c_{D_p}; and skewness of the distribution, γ, characterizing the particle size distribution.

11.4.1 Air Flow Characteristics of the Natural Backfill Material

Estimates of permeability were first performed without any distributional assumptions for the natural backfill material particle sizes. The permeability was then estimated assuming a phi

[1]These values are used only to show the trend in the temperature.

Table 11-1. Input Parameter Names and Values			
Symbol	**Parameter Description**	**Parameter Value**	**Unit**
wpl	Waste package spacing	6.14	m
k_{ds}	Drip shield thermal conductivity	20.77	W/(m-K)
bth	Backfill thickness	0–1.36	m
D_{rw}	Drift diameter	5.5	m
D_{wp}	Waste package diameter	1.579	m
D_{dsi}	Drip shield internal diameter	2.75	m
D_{dso}	Drip shield outer diameter	2.78	m
D_{bfi}	Backfill internal diameter	D_{dso}	m
D_{bfo}	Backfill outer diameter	D_{dso} + 2 × bth	m
σ	Stefan-Boltzman constant	5.67×10^{-8}	$W/(m^2\text{-}K^4)$
ϵ_{wp}	Emissivity of waste package surface	0.87	unitless
ϵ_{bfo}	Emissivity of backfill outer surface	0.8	unitless
ϵ_{rw}	Emissivity of drift wall	0.8	unitless
ϵ_{dsi}	Emissivity of drip shield internal surface	0.63	unitless
T_{rw}	Drift wall temperature	427.3	K
L	Waste package length	5.275	m
β	Volume of thermal expansion	0.00285	1/K
K	Permeability	1×10^{-12} (~ 1 darcy)	m^2
ν	Kinematic viscosity	3.239×10^{-5}	m^2/s
g	Acceleration caused by gravity	9.81	m/s^2

Table 11-1. Input Parameter Names and Values (continued)			
Symbol	**Parameter Description**	**Value**	**Unit**
γ	Skewness of a particle size distribution	0–1.5	unitless
τ	Tortuosity of the bulk medium	1.25–3.0	unitless
C_{D_p}	Coefficient of variation of the particle size distribution	0.1–0.6	unitless
k_{air}	Thermal conductivity of air	0.0373	W/(m-K)
S_o	Trask sorting coefficient	2.0	unitless
α_m	Thermal diffusivity	3.417×10^{-4}	m^2/s
T_{do}	Temperature at the backfill inner surface	458.5	K
T_{bfo}	Temperature at the backfill outer surface	429.4	K
k_m	Thermal conductivity of the backfill	0.27	W/(m-K)
Pr	Prandtl number	0.7	unitless
ϕ	Bulk porosity	0.3	unitless
$\overline{D}_p$	Average diameter of backfill particle	0.1	m

(i.e., Φ)-normal distribution for the particle sizes. Following are the key observations using Eq. (11-3):

- Permeability, K, increased with an increase in $\overline{D}_p$. $\overline{D}_p$ was varied between 100 and 500 mm [0.33 and 1.64 ft] at various ϕ values (0.1 and 0.6), while keeping other parameters fixed $\left\{\tau = 2.5,\ \lambda = 0.25, \text{ and } \sigma_{D_p} = 60\,\text{mm}\left[0.2\,\text{ft}\right]\right\}$. σ_{D_p} was adjusted in such a manner that C_{D_p} could be maintained at 0.6. Parameters $\overline{D}_p$ and ϕ contributed most to the increase in the estimated permeability.

- Permeability increased with an increase in C_{D_p}. C_{D_p} was varied between 0.1 and 0.6 at various ϕ values. Other parameters were fixed $\left\{\tau = 2.5,\ \lambda = 0.25, \text{ and } \overline{D}_p = 100\,\text{mm}\left[0.33\,\text{ft}\right]\right\}$.

σ_{D_p} was varied in such a manner that the desired C_{D_p} values were obtained. Permeability increased with C_{D_p}, but not as dramatically as with $\overline{D}_p$ and porosity.

- Permeability increased with an increase in γ. γ was varied between 0 and 1.5 at various ϕ (0.1 and 0.6). Other parameters were fixed $\left\{\tau = 2.5,\ \overline{D}_p = 100\,\text{mm}\ [0.33\,\text{ft}],\ \text{and}\ \sigma_{D_p} = 60\,\text{mm}\ [0.2\,\text{ft}]\right\}$. Permeability increased with γ, but not as dramatically as with $\overline{D}_p$, ϕ, and C_{D_p}.

- Results from the Φ-normal distribution example: $D_{p_{\text{med}}}$ was specified at 1,000 mm [3.28 ft], and the sorting coefficient, S_0, was varied between 1 and 1.25. $\overline{D}_p$ and σ_{D_p} were obtained from $D_{p_{\text{med}}}$ and S_0 as shown in Eqs. (11-4) through (11-6). When the particles were well sorted (i.e., $S_0 = 1$), a permeability value of 255.1 mm^2 (2.58×10^8 darcy) was obtained. But as S_0 was increased, the permeability value rapidly decreased. At $S_0 = 1.25$, the estimated permeability was 6.93×10^{-7} mm^2 (0.702 darcy). Similar calculations were performed at higher S_0 and D_p values. The effect of ϕ, S_0, and $\overline{D}_p$ were studied using $\phi = 0.5$, $S_0 = 2$, and $D_{p\,\text{med}} = 5{,}000\,\text{mm}\left[16.4\,\text{ft}\right]$. τ has only a moderate influence on the estimated *K*.

A high *K* leads to a high Ra [Eq. (11-2)]. Previous analyses suggest the permeability may be high enough in many cases to give rise to high Ra and Nusselt numbers, implying likely substantial heat transfer by natural convection.

11.4.2 Temperature Calculations

Because the characteristics of the natural backfill material are uncertain, several likely bounding and representative calculations were performed to understand the trend in temperature evolution as a function of time.

Figures 11-3 and 11-4 show the effects of mean particle diameter, $\overline{D}_p$, and porosity, ϕ, on estimated waste package temperature. The abrupt rise in temperature at 50 years pertains to the beginning of the postclosure period, which is associated with the end of the ventilation period. The mean particle diameter was varied between 0.1 and 0.5 m [0.33 and 1.64 ft] (Figure 11-3). The porosity was varied between 0.1 and 0.6 (Figure 11-4). Other parameters in the modified TPA code were set to their mean values. Of the two parameters, porosity had a greater effect on estimated waste package temperature than did the mean particle diameter. Analyses also were performed in which skewness, tortuosity, and the coefficient of variation of the particle size distribution were varied. These three parameters had a much smaller effect on estimated waste package temperature.

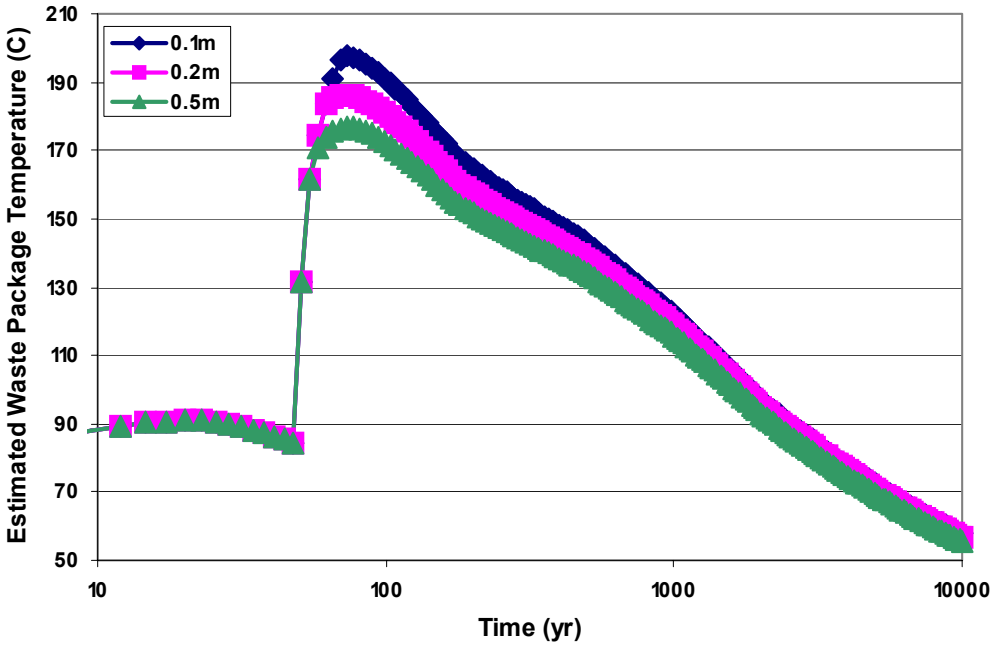

Figure 11-3. Estimated Variation in Waste Package Surface Temperature at Different Mean Particle Diameters of the Natural Backfill from Mean Value TPA Code Simulations

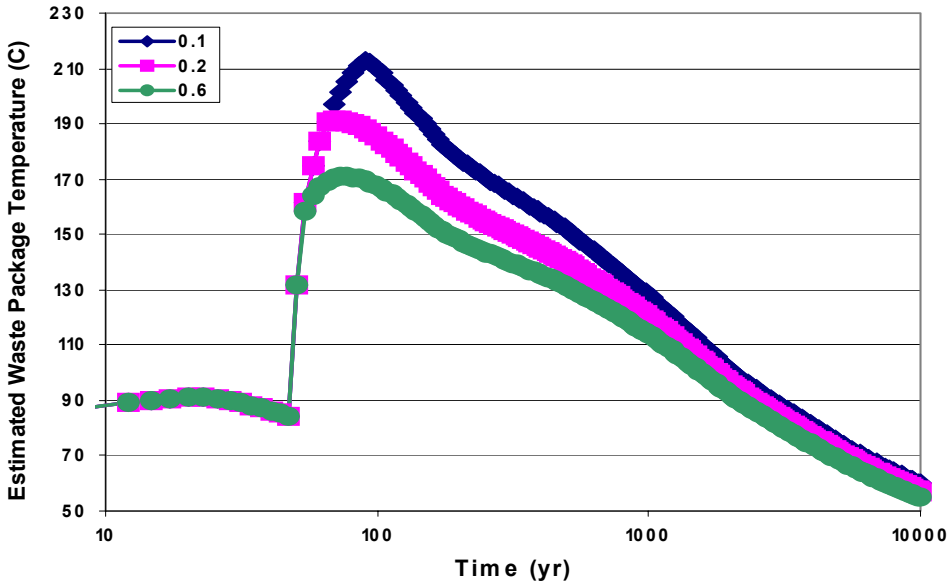

Figure 11-4. Estimated Variation in Waste Package Surface Temperature at Different Porosities of the Natural Backfill from Mean Value TPA Code Simulations

Figures 11-5 and 11-6 show the estimated temperature evolution using 450-realization Monte Carlo runs in which various parameters were sampled from assigned ranges: particle diameter {0.1–0.5 m [0.33–1.64 ft]}, porosity (0.1–0.6), tortuosity (1.25–3.0), skewness (0.0–1.5), and coefficient of variation 0.1–0.6. For these parameters, uniform distributions were used. Figure 11-5 shows the average waste package temperature from 450 realizations for three cases: conduction only, convection and conduction, and no backfill.[2] Similar to the previous two figures, the abrupt rise in estimated temperature at 50 years corresponds to the end of the ventilation period. As shown in this figure, the estimated peak mean temperature for the combined convection and conduction heat transfer mode is 195 °C [383 °F] and occurs at 73 years (i.e., 23 years after repository closure). The estimated peak mean temperature for conduction only is 217 °C [423 °F] and occurs at 118 years (i.e., 68 years after repository closure). These estimated peak mean temperatures are within 22 °C [40 °F] of each other, with the combined mode having the lower estimated peak mean temperature. Figure 11-5 also shows that, as convection occurs, the estimated peak mean waste package temperature shifts to earlier times. The estimated peak mean temperature for the combined mode occurs 45 years earlier than when conduction alone is assumed. Figure 11-6 shows the range of estimated waste package temperatures for variation in input parameters using 450 Monte Carlo realizations. The lowest estimated peak temperature is 182 °C [360 °F], while the highest is 213 °C [415 °F]. This difference represents a 31 °C [55 °F] increase in the estimated peak temperature over the parameter ranges specified.

These analyses suggest the estimated waste package temperature can be sensitive to the heat transfer characteristics of natural backfill material. As Figures 11-3 and 11-4 suggest, the two key parameters anticipated to govern heat transfer in the backfill are mean particle diameter and porosity.

Heat transfer calculations suggest the estimated waste package temperature may be in between the value obtained from the no-backfill condition and the case with the conduction-only heat transfer in the natural backfill.

11.4.3 Dose Consequence Calculations

To estimate the dose consequences of potentially higher waste package and drip shield temperatures, the iterative calculations used in the standalone code module were integrated as an alternative model into the latest version of the TPA code. Figure 11-7 compares estimates of the expected dose curves for three heat transfer cases: no backfill, conduction-only, and conduction and convection. The expected dose curves were estimated from 450 Monte Carlo realizations. The random sampling sequence was preserved in all these cases for a comparison among the cases.

Prior to approximately 2,700 years, Case 1 (no backfill heat transfer) gives the highest estimate of the expected dose, and Case 2 (conduction-only heat transfer) gives the lowest estimate of the expected dose. The estimated mean dose curve for Case 3 (convection and conduction heat transfer), which represents the alternative model developed in this chapter, lies in between

[2]Only the mean values are shown in these figures because the goal was to estimate the trends associated with the various heat transfer modes in the presence and absence of the backfill.

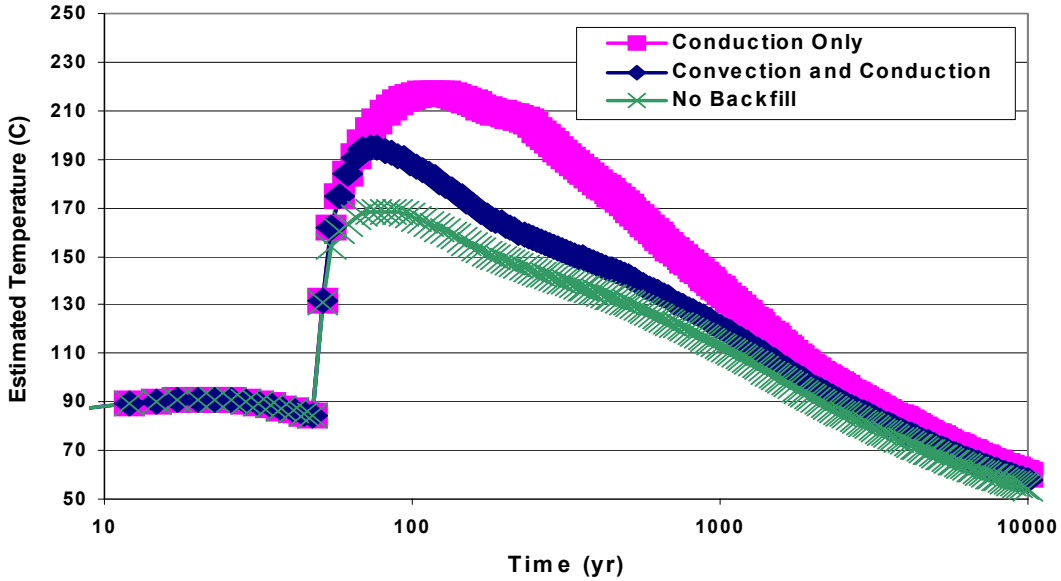

Figure 11-5. Estimated Evolution of Waste Package Temperature for Subarea 1 As a Function of Various Assumptions Regarding Heat Transfer in the Natural Backfill with Each Curve Representing the Average Temperature from 450 Monte Carlo Realizations

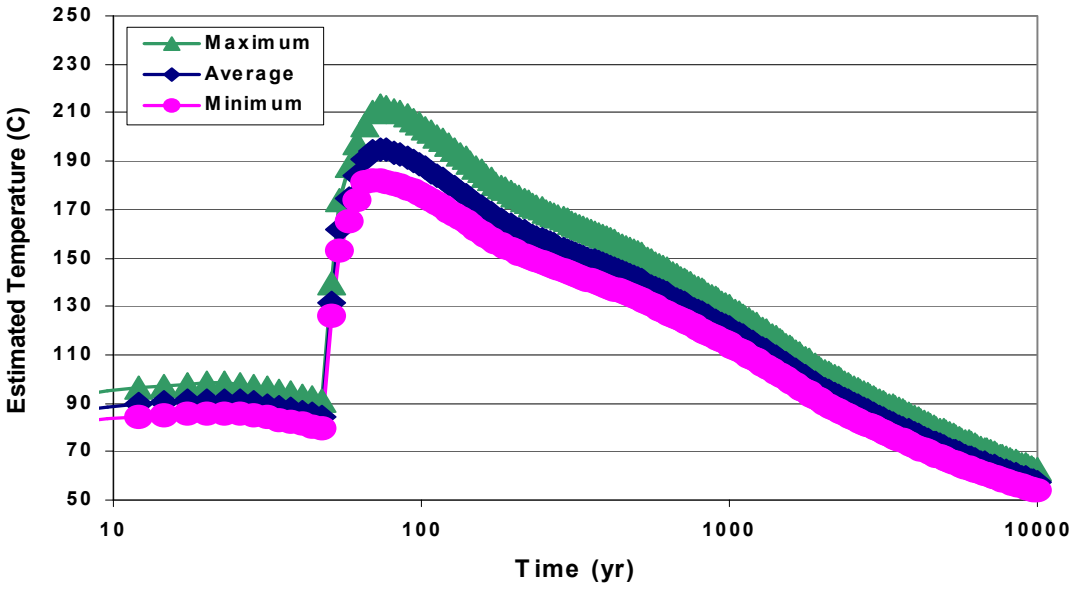

Figure 11-6. Estimated Average, Minimum, and Maximum Waste Package Surface Temperatures for Subarea 1 from 450 Monte Carlo Realizations

the Case 1 and Case 2 dose estimates, which is intuitive. After approximately 2,700 years, the opposite is observed in Figure 11-7. In addition, at times prior to approximately 2,700 years, the percentage difference in total effective dose equivalent is much greater than it is after 2,700 years. For example, at 2,044 years, the conduction-only total effective dose equivalent is 47 percent lower than the convection and conduction total effective dose equivalent. At 5,434 years, the conduction-only total effective dose equivalent is 11 percent higher than that for the convection and conduction effective dose equivalent. The crossover of the estimated dose curves from the three cases can be explained as follows: lower overall temperature for the no backfill case may lead to early release, which may result in a higher early dose estimate. Water may enter the failed waste package early at lower temperatures. Lower temperatures also may lead to lower wasteform dissolution, resulting in lower rates of release of radionuclides and lower dose estimates at later times. Conversely, a higher overall temperature for the conduction-only case may result in a lower early release and dose estimate. In addition, higher temperatures may lead to greater wasteform dissolution and higher rates of release and a higher dose estimate at later times.

11.5 Conclusions

The drifts excavated into the Yucca Mountain geologic system may degrade throughout the potential repository. One way in which drift degradation may affect repository performance is by increasing the repository temperature including the drip shield, waste package, and wasteform temperatures. The increased temperature also may accelerate drip shield and waste package

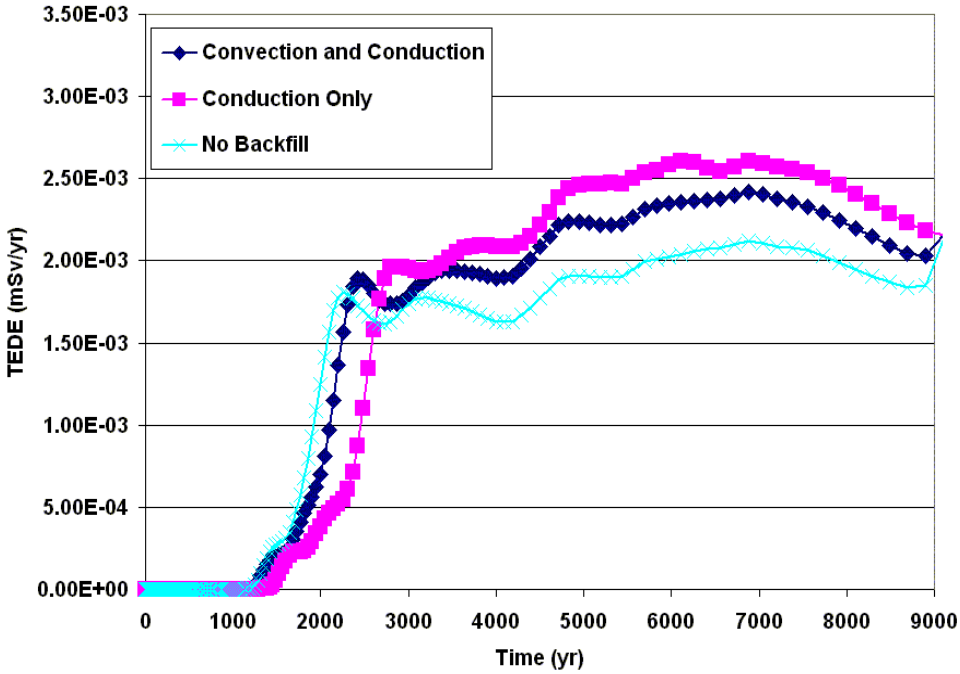

Figure 11-7. Estimated Expected Groundwater Dose As a Function of Time for Various Heat Transfer Assumptions in the Natural Backfill Averaged Over the 450 Monte Carlo Realizations

corrosion and wasteform dissolution if seepage waters contact these engineered features. High temperatures may adversely affect the load-bearing capacity of the drip shield and the waste package, thus increasing the failure potential during the period of high temperatures.

Ad hoc analyses using an engineered backfill as a surrogate for natural backfill estimated there may be a substantial increase {from 165 to 351 °C [329 to 664 °F]} in the peak waste package temperature, thus prompting the need for a closer look at, and treatment of, the heat transfer characteristics of the natural backfill. This task estimates waste package temperature using a representation of natural backfilling because of drift degradation and the potential impact on dose estimates.

The natural backfill material is likely to have a large variation in rock/particle sizes, potentially varying from 1 m [3.28 ft] in diameter to a few microns. The particle sizes and shapes determine the regime over which convective heat transfer may be the dominant heat transfer mechanism, and uncertainties in the particle size distribution may result in the heat transfer ranging from pure conduction-dominated heat transfer to convection-dominated heat transfer. The waste package temperature, computed using selected parameter ranges, suggests sensitivity to the presence or absence of a hypothetical backfill. For the parameter ranges used in this calculation, an estimated peak mean temperature difference of 48 °C [86 °F] was estimated between the peak conduction-only temperature {217 °C [423 °F]} and the peak no backfill temperature {169 °C [336 °F]}. Estimated doses computed in this analysis using assumptions of no backfill, conduction-only, and convection and conduction are different by less than one order of magnitude. The alternative model developed in this analysis to account for the effects of natural backfill on waste package temperature was implemented in the latest version of the TPA code.

12 NEAR-FIELD THERMAL, HYDROLOGICAL, AND CHEMICAL INTEGRATION

TASK DESCRIPTION

Evaluate the integration of the thermal, hydrological, and chemical abstraction models for physical consistency.

AUTHORS/CONTRIBUTORS

D. Esh, O. Pensado, S. Mohanty, R. Fedors, L. Browning, R. Codell, and B. Leslie

12.1 Background and Purpose

The TPA code has used different abstracted models to represent the thermal, hydrological, and chemical responses within the emplacement drifts (Mohanty, et al., 2002a,b). When different submodels are used to represent environmental variable responses, integration may be manually evaluated. The main objective of the analysis was to evaluate integration of the thermal, hydrological, and chemical abstraction models for physical consistency. There are three elements evaluated in this analysis.

- The chemical environment for corrosion should not be applicable unless temperatures of the waste package surface are below 150 °C [302 °F].
- There should not be liquid water flowing around or through the waste packages if the drift surface temperature is at or significantly above boiling.
- The integration between liquid flow and chemical environment abstraction should be evaluated for appropriateness.

The significance to waste isolation of the analysis is derived from the importance of the environmental variables with respect to the onset of localized corrosion of the waste package engineered barrier. The Risk Insights Baseline Report (NRC, 2004) identifies two risk insights: Persistence of a Passive Film and Chemistry of Seepage Water as having high significance to waste isolation. The link between these two risk insights arises primarily from localized corrosion and transpassive dissolution of waste package materials, which both are sensitive to the temperature at which aggressive chemistries may be present on the surface of the waste package. This analysis was designed to ensure the responses of the environmental variables are physically consistent such that formation and persistence of aggressive environments for the waste package barrier may not be significantly under or overestimated. Analysis in this chapter supports development of the refined model for waste package corrosion and near-field chemistry presented in Chapter 3.

12.2 Methodology

In investigating localized corrosion of the waste package, the elements of this task encompass and evaluate the consistency between thermal, hydrological, and chemical conditions in the near field. The following results from the TPA code were analyzed. One necessary condition

for localized corrosion is the establishment of an aqueous environment, which is assumed to occur when the relative humidity exceeds the critical relative humidity for localized corrosion. In the implementation in the TPA code, it is assumed that concentrated solutions (aggressive chemistry conditions) prevail in these high-temperature environments. During this time, waste package temperature is estimated from the TPA code computations. The time at which the aggressive chemistry conditions end is estimated in the TPA code as the time at which the waste package temperature falls below a temperature called the in-drift evaporation temperature. This temperature is assumed to represent conditions of limited evaporation in the drift. For limited evaporation conditions, water in contact with the waste package tends to be in equilibrium with seepage water, becoming diluted and unable to sustain localized corrosion. The time at which flowing water rewets the waste package after the initial thermal pulse and the waste package temperature at this rewetting time are extracted from the TPA code results. The basic analysis approach was to produce the response of the variable of interest (e.g., relative humidity, temperature, and water flow) with the TPA code. The next step was to extract the temporal responses into Microsoft® Excel 97 to visually evaluate the TPA code output. From the visual output, the information was interpreted to summarize the environmental variable response to some simple concepts.

In the TPA code computations, flags were enabled to store all intermediate outputs of the basecase. There were no changes to the TPA code or the input data, aside from enabling flags to generate intermediate output.

12.3 Assumptions

Assumptions or likely conservatisms implicit within the TPA code apply to this analysis. The code and its default input data were not modified for this task. Only results for Subarea 1 were analyzed. It is assumed that results for Subarea 1 are representative of other subareas in the integration of environmental variables. In addition, 25 realizations do not suffice to produce correlated samples of input parameters (the implemented Latin hypercube sampling algorithm in the TPA code needs one more realization than the sampled parameters to produce correlations). Given that none of the environmental variables of interest depends on correlated input parameters, selection of only 25 realizations does not change the results and conclusions from this analysis.

12.4 Results

Figure 12-1 is a plot of environmental variable responses for Realization 1 and illustrates the TPA code thermal, hydrological, and chemical results evaluated for integration and consistency in this chapter. Figure 12-1 is used to explain some of the variables and the basic thermal, hydrological, and chemical responses generated in the TPA code. The figure shows the TPA code estimates of the relative humidity and temperature at the waste package surface, the flow of water to the waste package, and the concentration of chloride at the waste package surface. The variables displayed in Figure 12-1 are qm3hit/yr/wp/sa (the volume of water flow in cubic meters per year hitting a waste package per subarea), relhumwp (the relative humidity at the waste package surface), clwp (the molar chloride concentration at the waste package surface), and tempwp (the temperature at the surface of the waste package).

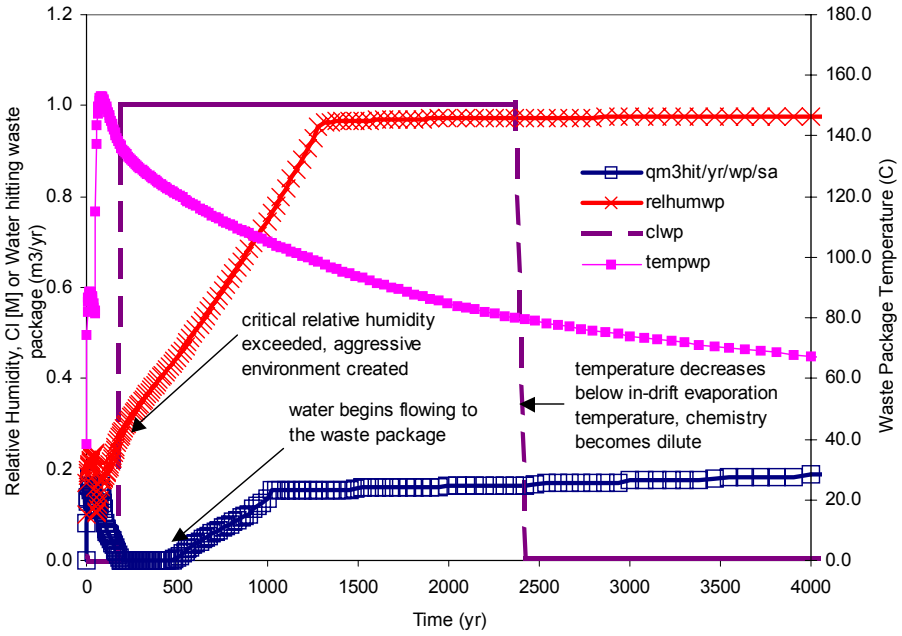

Figure 12-1. Selected Environmental Variable Responses (Realization 1)

Values used in this analysis for Subarea 1 of the potential repository are presented in Table 12-1. The relative humidity at increase in the first row of the Variable column of Table 12-1 presents sampled values of the critical relative humidity for aqueous corrosion. The first time the relative humidity exceeds this critical relative humidity is listed in the second row as time of increase, and the corresponding waste package temperature at that time is listed in the third row as temperature at increase. Information in these three rows represents onset of the establishment of aggressive solutions potentially leading to localized corrosion. The end of the aggressive chemistry period is provided in the fourth row as time of decrease and represents the time when the waste package temperature is below the in-drift evaporation temperature, specified as a constant equal to 80 °C [176 °F] in TPA code input. This conceptualization assumes water chemistry becomes diluted when seepage water contacts the package, and these solutions are unable to promote localized corrosion. The waste package temperature corresponding to the onset of rewetting of the waste package is presented in the fifth row as waste package temperature at rewetting. The time when water rewets the waste package following the initial thermal pulse is provided in the sixth row as the rewetting time. This time corresponds to returning to the nonzero flow rate of water hitting the waste package. The last row in Table 12-1 is the difference between rows 4 and 6. This value represents the time when water flow contacts the waste package to the time aggressive chemistry conditions no longer exist. The persistence of aggressive solutions may be overestimated because, when seepage water contacts the waste package in the absence of significant evaporation, solutions in contact with the waste package may tend to become dilute.

For the realizations evaluated, the deliquescence relative humidity was selected so that the onset of corrosion processes did not begin until the temperature was below 150 °C [302 °F].

Table 12-1. Summary of Environmental Variable Responses for the Basecase TPA Code

Variable	Realization Number									
	1	2	3	4	5	6	7	8	9	10
*RH at increase	0.27	0.49	0.38	0.37	0.25	0.35	0.42	0.54	0.46	0.31
Time of increase (yr)	181	770	640	461	366	544	501	923	750	306
Temp at increase (°C) [°F]	137 [278.6]	118 [244.4]	126 [258.8]	127 [260.6]	140 [284]	128 [262.4]	123 [253.4]	115 [239]	120 [248]	133 [271.4]
Time of decrease (yr)	2,420	2,930	3,230	2,730	3,470	3,150	2,540	3,080	3,080	2,660
Waste package temp at rewetting (°C) [°F]	121 [249.8]	113 [235.4]	117 [242.6]	131 [267.8]	131 [267.8]	124 [255.2]	111 [231.8]	115 [239]	†CF	†CF
Rewetting time (yr)	488	923	900	366	559	640	833	900	†CF	†CF
Potential overestimate of aggressive chemistry (yr)	1,932	2,007	2,330	2,364	2,911	2,510	1,707	2,180	2,330	2,354

*RH—Relative humidity
†CF—Continuous flow of water to the waste package

Thus, the first element evaluated in this analysis was satisfied. In the TPA code input, the deliquescence relative humidity is CriticalRelativeHumidityAqueousCorrosion, Uniform [0.242,0.56], where CriticalRelativeHumidityAqueousCorrosion is the TPA code parameter name, Uniform is the probability distribution type, and [0.242,0.56] identifies the distribution range.

As suggested by the analysis of Realizations 9 and 10, instances may exist where liquid water is flowing to the waste package even though the waste package is at 160 °C [320 °F] or more. Table 12-1 does not show the estimated peak waste package temperatures that exceeded 160 °C [320 °F] in Realizations 9 and 10. There may be penetration of water through an above-boiling region above the drift because of condensation in fractures. There may be a temperature difference between the drift wall (farther from the decay heat source) and the waste package. It is unlikely for the water penetration to persist through a 65-°C [117-°F] temperature difference between the boiling point of water and the waste package temperature. The refined model developed in Chapter 3 addresses flow conditions at these temperatures as stated in Element 2 of Section 12.1.

Comparison of the temporal response of the flow of water to the waste package and the chemical environments given in Table 12-1 suggests a difference between the moisture

response and the chemical environments. The parameter IndriftEvaporationTemperature[C] set at 80 °C [176 °F] in the basecase TPA code input determines when the aggressive chemistries associated with boiling and evaporation return to more dilute values.

Whereas moisture flow returns to the waste package anywhere from approximately 400 to 900 years in the realizations examined, the aggressive chemistry persists to approximately 2,400–3,500 years. A second TPA code simulation and subsequent analysis were performed where the TPA code input parameter IndriftEvaporationTemperature[C] was set to 100 °C [212 °F]. The analysis methodology was otherwise identical to that presented previously. Much of the model response was identical to the first TPA code simulation discussed in detail previously. There was, however, a significant decrease in the difference in the timing between moisture flow and aggressive chemistry persistence. Yet, the average timing difference was still more than 1,000 years.

The significance of the results is that the length of time aggressive chemical conditions are applied for localized corrosion of the waste package may be overestimated. Also, because in some realizations liquid water is available to the waste package at high temperatures, advective release of radionuclides may be overestimated.

12.5 Conclusions

This analysis evaluates the three elements in Section 12.1 related to the integration of the thermal, hydrological, and chemical model abstractions. The analysis suggests moisture may flow continually to the waste package, even at high temperatures, and there may be an overestimation of the number of waste packages impacted by localized corrosion and radionuclide release rates. Therefore, by better integration of the thermal, hydrological, and chemical model abstractions, there may be a reduction in waste package localized corrosion failure and radionuclide release rates.

This analysis also supports the analysis described in Chapter 3. The near-field chemistry and waste package corrosion model was refined in Chapter 3 to address integration of the thermal, hydrological, and chemical environments.

13 DRIP SHIELD AND FLUORIDE

TASK DESCRIPTION

Evaluate the potential for failure of the drip shield within 10,000 years by general corrosion caused by fluoride in infiltrating water.

AUTHORS/CONTRIBUTORS

R. Codell, T. Ahn, and B. Leslie

13.1 Background and Purpose

The effects of fluoride concentration on the drip shield corrosion rate are identified as an uncertainty associated with the risk insight Drip Shield Integrity in the Risk Insights Baseline Report (NRC, 2004). This risk insight has a rating of medium significance to waste isolation. The drip shield will be constructed from titanium alloys resistant to localized corrosion in chloride solutions for a wide temperature range. The uniform corrosion rate of titanium alloys, however, may be dependent on the fluoride concentration. Faster corrosion rates and shorter failure times may occur on drip shield sections exposed to solutions with fluoride concentrations greater than 10^{-4} molar [M] (Brossia, et al., 2001; Lin, et al., 2003). This analysis estimates the effects of fluoride in infiltrating water on the corrosion rate and potential failure of the drip shield.

The current TPA code conceptual model for general corrosion of the drip shield assumes that fluoride ions attack the titanium and are consumed in the process. The likely number of moles of fluoride consumed by a mole of titanium (the ligand number) is between one and six. Experiments on the formation of fluoride and titanium complexes conducted at high temperatures {up to 450 °C [842 °F]} using weak alkaline fluoride solutions (pH 8–9), suggest the dominant ratio is two moles fluoride to one mole titanium (Barsukova, et al., 1980). Experiments conducted by Knauss, et al. (2000) at lower temperatures {100 to 300 °C [212 to 572 °F]} suggest a trend of decreasing ligand number with decreasing temperature, tending toward a one-to-one ratio of fluoride to titanium at likely repository temperatures.

Fluoride may reach the drip shield dissolved in dripping water. The concentration of fluoride in this water is estimated to be approximately 5×10^{-5} mol/L, although there are factors that may increase this value. Water within the pores of the tuff rock may be significantly more concentrated with fluoride. Pore water is not likely representative of dripping water, however. Pore water extracted from rock may be out of equilibrium with infiltrating water, which moves mostly in the rock fractures. That average J–13 Well water contains approximately 1.15×10^{-4} mol/L fluoride (Harrar, et al., 1990) suggests the infiltrating water recharging the water table may have a fluoride concentration lower than that of pore water and closer to the concentration of infiltrating water. The amount of fluoride in pore water within a few meters of the drift may not pose a threat to the drip shield. It is unlikely that fluoride in the pore water is released from the pores to the drift. The thermal pulse, while capable of releasing water by boiling it from the rock, may leave most of the fluoride behind in the rock pores because fluoride is nonvolatile. It may not be ruled out that water containing fluoride infiltrating from the Earth surface may become concentrated as it evaporates close to the hot drift. The concentration of fluoride may depend on complicated processes that determine which minerals precipitate

earliest at evaporation. If fluoride was limited by the solubility of fluorite (CaF_2), it may attain a concentration at 25 °C [77 °F] of approximately 3.16×10^{-4} mol/L (Bechtel SAIC Company, LLC, 2003a). Knauss, et al. (2000) note that EQ3/EQ6 simulations of the evaporation of J–13 Well water show that the free fluoride concentration increases more than one thousandfold from 1.1×10^{-4} to 0.18 mol/L before becoming limited by fluorite precipitation, probably because calcite ($CaCO_3$) precipitates first and removes calcium from the system. Experiments gave similar results. DOE developed an analysis of likely types of pore waters that may enter the drifts and classified these into 11 bins (Bechtel SAIC Company, LLC, 2003a). These binned water types reflect the reconcentration of ambient pore waters and the precipitation of a host of minerals, including calcite and fluorite. The highest fluoride concentration was 0.00138 mol/L, with concentrations greater than 0.001 mol/L estimated to be in nearly 48 percent of the concentrated waters. The average fluoride concentration of binned water inputs was approximately 0.001 mol/L.

Although high fluoride concentrations may form, the volume of those infiltrating streams may be greatly diminished, reducing the probability that dripping water aligns with proper-sized dents. To take the possible reconcentration of fluoride into account with the simultaneous reduction in the water dripping rate, an analysis is presented in which the maximum fluoride concentration is allowed to increase to 0.18 mol/L, the highest likely fluoride concentration for evaporating J–13 Well water.

Lin, et al. (2003) describe the limiting factors for drip shield corrosion by fluoride as supply limits of fluoride, transport limits like diffusion through thin films, and reaction rate limits between fluoride and titanium. The paper concludes that drip shield failure by fluoride corrosion is not likely because one or more factors limit the contact or reaction with titanium to rates too small to affect integrity within 10,000 years.

The most severe corrosion rate model in Lin, et al. (2003) was optimized so the highest possible concentrations are always present by adjusting the surface area so evaporation equals the dripping rate. This nonmechanistic model maximizes the supply or reaction rate to the titanium surface and may be nonphysical in many situations, but likely conservative (e.g., area greater than physically possible). Kuntz (2003) also presented an analysis for dripping into a concave dent on the top of the drip shield. The denting model is based on a situation that has a reasonable, physical mechanism for capturing fluoride in dripping water. Kuntz did not give sufficient details, however, and it is unclear how factors such as reflux, evaporation, and chemical reaction rates were incorporated.

This analysis develops an alternative model that accounts for fluoride-enhanced corrosion of the waste package. The alternative model estimates corrosion in water collected in dents on the waste package surface. Results from the alternative model also are presented.

13.2 Methodology

The methodology used in the alternative model to analyze corrosion in a dent is described in this section. The dent conceptual model is a mechanistic model for the reaction between fluoride and titanium. This model explicitly accounts for dripping, evaporation, and chemical reaction rates.

Following Kuntz (2003), the dent in the drip shield is assumed to be cone-shaped. That is, the dent is on the crest of the drip shield and is in the shape of a right circular cone of radius r_0 and depth h_0 as shown in Figure 13-1. Dripping water may fall into the cone at a rate proportional to the time-dependent reflux plus infiltration. A fraction of the total infiltration and reflux in the drift may fall into the cone. Water may evaporate from the surface of (the water in) the dent, balancing the inflow or spilling over, if the dent is full.

Initially, the dent was modeled as a transient mixed system (i.e., a stirred-tank reactor) with the following phenomena: (i) influx of dripping water, (ii) evaporation of water from the surface, (iii) change in water level, (iv) overflow of water from a full dent, (v) change in concentration of fluoride in the dent, and (xi) reaction between fluoride and titanium.

The initial approach was abandoned, however, because the short transients in the system required timesteps in the numerical solution that were small fractions of a year and also necessitated large expenditures of computer and programming time. Instead, a quasi-steady-state approximation was applied that avoids dealing with the time derivatives of water level and concentration. The quasi-steady-state approximation still allows the concentrations and water levels to change, but the rates of change with time are not important. This approach allows the substitution of nonlinear algebraic equations for differential equations and eliminates the problem of stiff-transient numerical solutions.

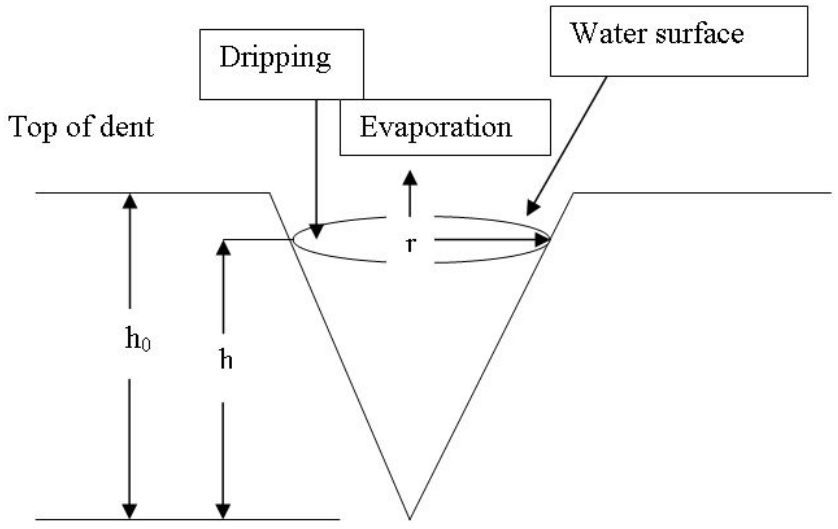

Figure 13-1. Schematic Showing a Dent on the Crest of the Drip Shield

13.2.1 Water Mass Balance

The alternative model balances the water flowing into the dent with the water leaving the dent by evaporation and overflow. Estimated evaporation rates expressed as cubic meters per year (m^3/yr) per drift segment are shown in Figure 13-2 and are derived from the Supplemental Science and Performance Analyses thermal hydrological simulations (DOE, 2001b). The estimated inflow to the drift is shown in Figure 13-3 as m^3/yr per drift segment. The inflow plus reflux is derived approximately from the Supplemental Science and Performance Analyses estimates, which give a weighted average flow per drift segment of 0.37 m^3/yr [13 ft^3/yr]. A numerical experiment, shown later, in which the inflow plus reflux and evaporation rates are doubled, suggests relatively minor effects on the results.

For a right circular cone, the surface area of exposed water A_{ws} [m^2] is determined to be

$$A_{ws} = \pi r^2 \tag{13-1}$$

where r is the radius of the cone [m] at the water level h [m]. If the radius of the top of the dent is r_0 [m], the exposed water surface area of the full dent, A_{ws0} [m^2], is

$$A_{ws0} = \pi r_0^2 \tag{13-2}$$

The exposed area of the water surface is estimated by equating the evaporation from the dent to the inflow; that is,

$$A_{ws} = Q_r(t) F_{drip} / E(t) \tag{13-3}$$

where $Q_r(t)$ is the time-dependent inflow plus reflux rate for each drip shield [m^3/yr] from Figure 13-3, and F_{drip} [unitless] is the fraction of the reflux that drips into the dent. The specific evaporation rate $E(t)$ [m/yr] is estimated by dividing the evaporation rate per drift segment from Figure 13-2 (m^3/yr) by the effective surface area of the drip shield A_{ds} [m^2].

If the area of the water surface exceeds the maximum surface area of the dent, the excess water spills out of the dent at a rate q_{out} [m^3/yr]

$$q_{out} = Q_r(t) F_{drip} - A_{ws0} E(t), \text{ if } A_{ws} > A_{ws0} \tag{13-4}$$

13.2.2 Fluoride Mass Balance

Fluoride flux, F_{in} [mol/yr], is assumed transported into the dent by dripping at the rate

$$F_{in} = Q_r(t) F_{drip} C_{in} \times 1{,}000 \tag{13-5}$$

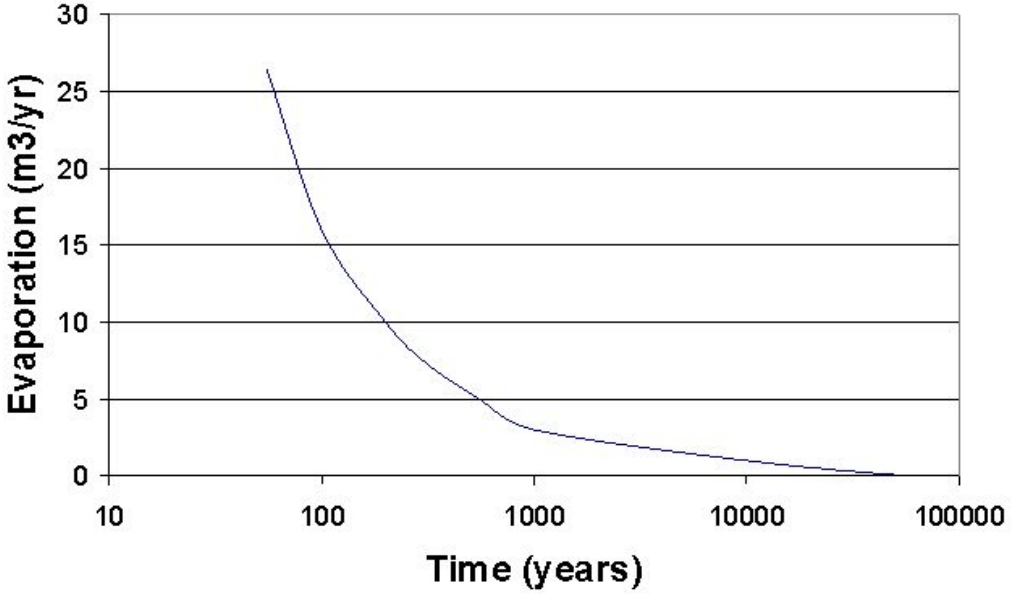

Figure 13-2. Evaporation Rates of Water from a Drip Shield Dent in 10,000 Years (DOE, 2001b)

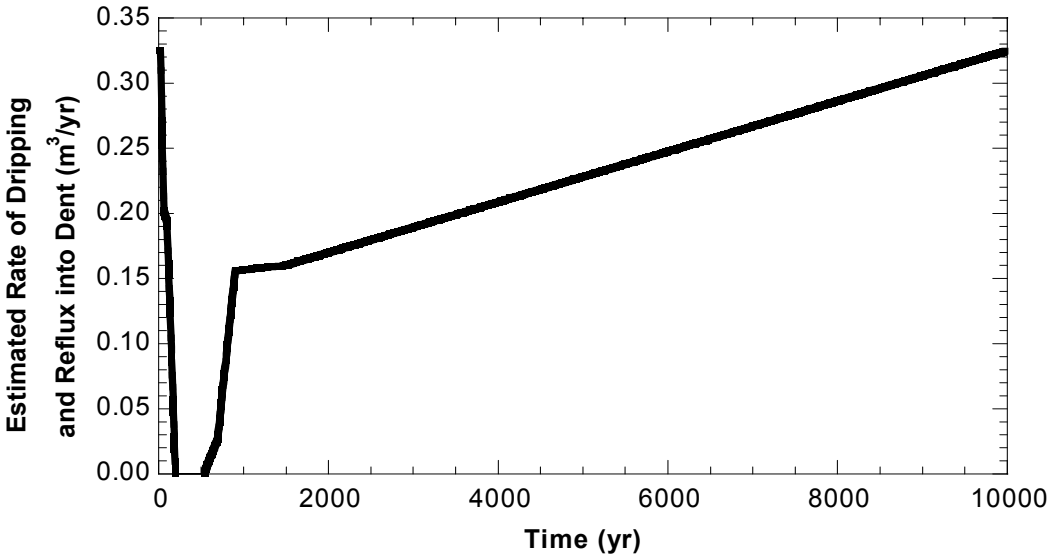

Figure 13-3. Estimated Infiltration and Reflux Rate of Water to a Drip Shield Dent in 10,000 Years

where C_{in} [mol/L] represents the concentration of fluoride, and 1,000 is used to convert from cubic meters to liters.

If water overflows the dent, it may carry fluoride out at the concentration C [mol/L] in the dent (the dent is assumed to be well-mixed) at a flux F_{out} [mol/yr]

$$F_{out} = q_{out}\ C \times 1{,}000 \tag{13-6}$$

Fluoride also may be consumed by reaction with the exposed titanium in the dent. This wetted area, A_{Ti} [m^2], is determined by the water level in the dent

$$A_{Ti} = \pi r \sqrt{r^2 + h^2} \tag{13-7}$$

where

$$r = \sqrt{A_{ws} \ / \ \pi} \tag{13-8}$$

and

$$h = r h_0 \ / \ r_0 \tag{13-9}$$

The removal rate of fluoride by reaction with titanium, F_{react} [mol/yr], is

$$F_{react} = A_{Ti} K(C) N \times 4.5 \ / \ 47.9 \tag{13-10}$$

where $K(C)$ represents the reaction rate $[\mu m / yr]$ of titanium as a function of fluoride concentration as determined by Brossia, et al. (2001) shown in Figure 13-4 and N [unitless] represents the ligand number, which is the number of moles of fluoride consumed per mole of titanium. The density of titanium is 4.5 g/cm^3 and the atomic weight of titanium is 47.9 g/mole.

13.2.3 Solution Algorithm

For a given input of the dent dimensions r_0 and h_0, the dripping fraction F_{drip}, the input concentration C_0, the surface area of the drip shield A_{ds}, and the fluoride and titanium ratio (also called ligand number N), step through time in 5-year increments solving for the water height and concentration of fluoride in the dent. The evaporation rate and the reflux plus infiltration rate are estimated by the graphical relationships shown in Figures 13-2 and 13-3. Concentration of fluoride in the dent is estimated implicitly by the nonlinear algebraic equation

$$F_{in} - F_{out} - F_{react} = 0 \tag{13-11}$$

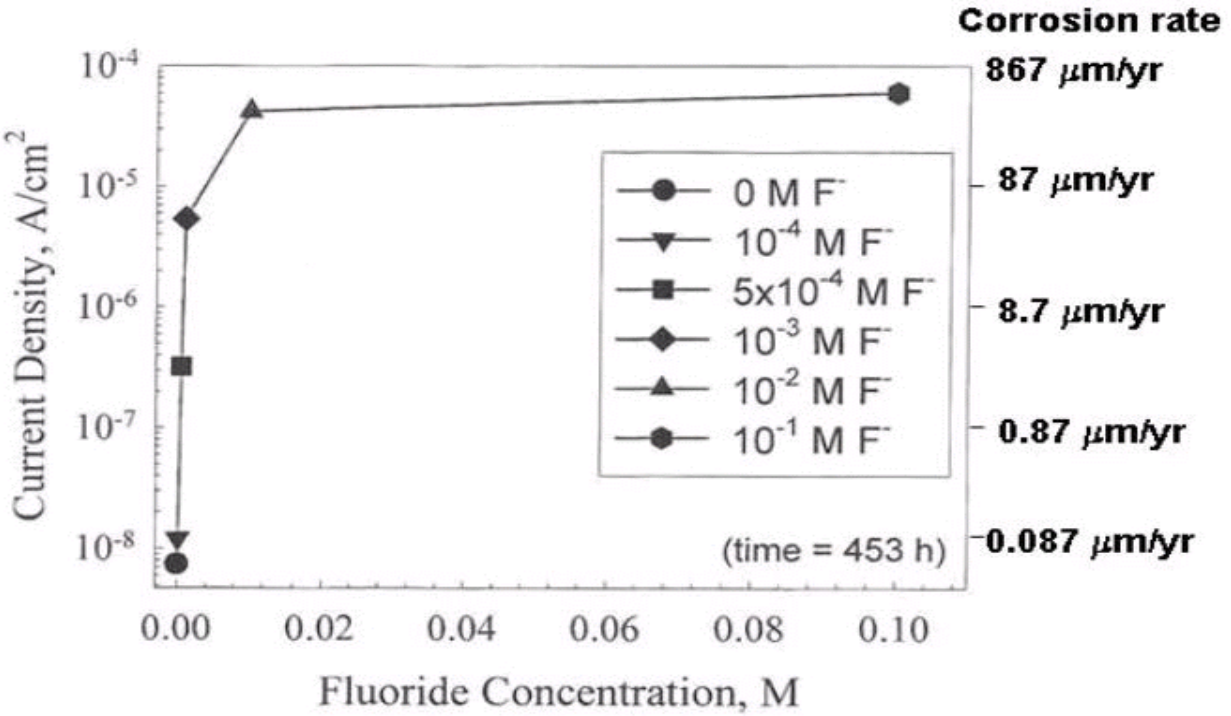

Figure 13-4. Drip Shield Corrosion Rate As a Function of Fluoride Concentration (after Brossia, et al., 2001)

Because F_{react} is a nonlinear function of concentration, Eq. (13-11) is solved using the Brent algorithm for functional minimization (Press, et al., 1992). Once C is estimated, the corrosion rate $K(C)$ is determined from the Brossia, et al. (2001) relationship in Figure 13-4. The maximum corrosion thickness T [cm/yr] within the dent is the integral of $K(C)$ for 10,000 years

$$T = 10{,}000 \int_0^{10{,}000} K(C)\,dt \qquad (13\text{-}12)$$

where 10,000 is used to convert from microns to centimeters.

13.3 Assumptions

This section presents the assumptions made in modeling corrosion of the drip shield by fluoride. The key assumptions include

- The model considers only the corrosion caused by reaction of the titanium with fluoride. Corrosion because of oxidation of titanium and dissolution of the passive titanium dioxide layer are not considered in this model.

- Fluoride is consumed in the reaction with titanium and cannot reenter the system once consumed or act as a catalyst to enhance corrosion.

- One mole of fluoride reacts irreversibly with one mole of titanium. The actual stoichiometric ratio for the reaction of fluoride with titanium may range from 1/1 to 6/1, but the ratio chosen is likely conservative and favored by some experimental evidence.

- Infiltrating water may evaporate as it drains vertically toward the drift, thereby concentrating its fluoride content in proportion to the amount of evaporation. Experimental and computed geochemical evidence suggests that calcite ($CaCO_3$) precipitates first, consuming much of the available calcium, thereby limiting the precipitation of fluorite (CaF_2).

- The concentration of fluoride is determined only by infiltrating water and not by water driven off from the rock pores. This assumption is likely conservative. Water that enters the drifts may come from a variety of sources, including infiltration and condensation of water vapor driven out of the rock by the heat. Although pore water may contain more fluoride than infiltrating water, the two water sources may be out of equilibrium because of the lack of close contact. Furthermore, heat may mobilize only water vapor because fluoride is not volatile.

- Dents capable of storing dripping water are assumed to form on the drip shield. This requires heavy rocks falling on the drip shield to cause it to dent. Furthermore, dents that form off the centerline of the drip shield may drain easier than dents forming exactly on the centerline.

- Dents are in the shape of a right circular cone.

- Water is assumed to evaporate from the surface at a rate determined by the temperature and humidity in the drift. The model takes no account for reduced evaporation caused by the buildup of strong electrolytes. Slower evaporation may reduce concentrations in the dent.

- The rate of change in the fluoride concentration and water level in the dent is ignored. This model simplification for computational expediency is based on the assumption that short transients in the dent because of the small volumes are not likely to have a material effect on the outcome.

13.4 Results

The results presented next consider four example cases:

Example 1. A detailed analysis for a single case to illustrate the changes to water level, fluoride concentration, and corrosion rate during the thermal pulse

Example 2. A Monte Carlo simulation to show the corrosion rate for the nominal case for a range of input parameters

Example 3. A Monte Carlo simulation, as above, but for the case of higher evaporation rate and reflux and infiltration rate, as might be present in parts of the repository

Example 4. A Monte Carlo simulation, as noted previously, to allow the infiltrating water to reach fluoride concentrations as high as 0.18 mol/L

13.4.1 Example 1—Detailed Results

The following example demonstrates processes in detail for a single set of parameters.

The dent has a radius of 0.05 m [0.16 ft] and a depth of 0.025 m [0.08 ft]. Ten percent of the reflux plus infiltration drips into the dent (F_{drip} = 0.1). The inflowing concentration is 0.0001 mol/L fluoride, and 1 mole of fluoride corrodes 1 mole of titanium. The effective area of the drip shield for evaporation is 20 m^2 [215 ft^2]. The evaporation rate is as depicted in Figure 13-2.

Figure 13-3 shows the input rate of infiltrating and recirculating water entering the dent. Figure 13-5 shows the water surface area as a function of time. Figure 13-6 shows the concentration of fluoride in the dent as a function of time. The water level drops and the concentration rises during the period when evaporation is larger than the inflow. Figure 13-7 shows that the reaction rate increases during this period, however, both concentration and reaction rate are limited by the consumption of fluoride, and the corrosion process is limited by the supply of fluoride. Most of the time, the corrosion rate is small because the fluoride concentration does not change much from its input level due to fluoride being consumed at a rate about the same as the supply rate. The sharp increases and decreases in these figures are artifacts of the model, most likely caused by linear interpolation of the evaporation rate table and the corrosion rate relationship and are not likely to affect the result.

13.4.2 Example 2—Monte Carlo Analysis for a Range of Input Parameters

Table 13-1 shows the input parameters randomly sampled using a uniform distribution between the given ranges. This exercise varies the model for a range of possible conditions to estimate parameter sensitivities and is not necessarily representative of the actual uncertainties for these parameters.

For 500 realizations, the parameter having the largest effect on the estimated corroded thickness T for 10,000 years is C_{in}, with a positive correlation coefficient of 0.845. Figure 13-8 shows this relationship. For the likely range of C_{in}, which is below 0.0001 mol/L, no failures by fluoride corrosion alone are likely.

Corrosion thickness in 10,000 years is less strongly correlated to two other parameters: maximum dent radius r (correlation coefficient −0.237) and F_{drip} (correlation coefficient

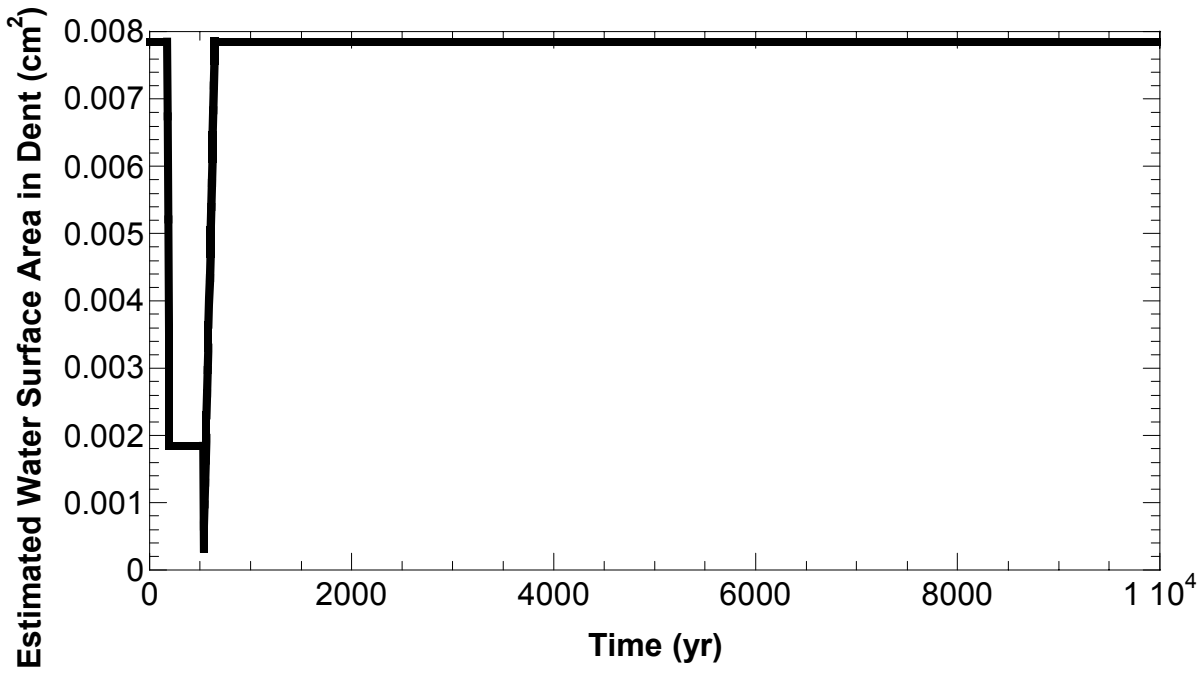

Figure 13-5. Estimated Water Surface Area of a Drip Shield Dent in 10,000 Years

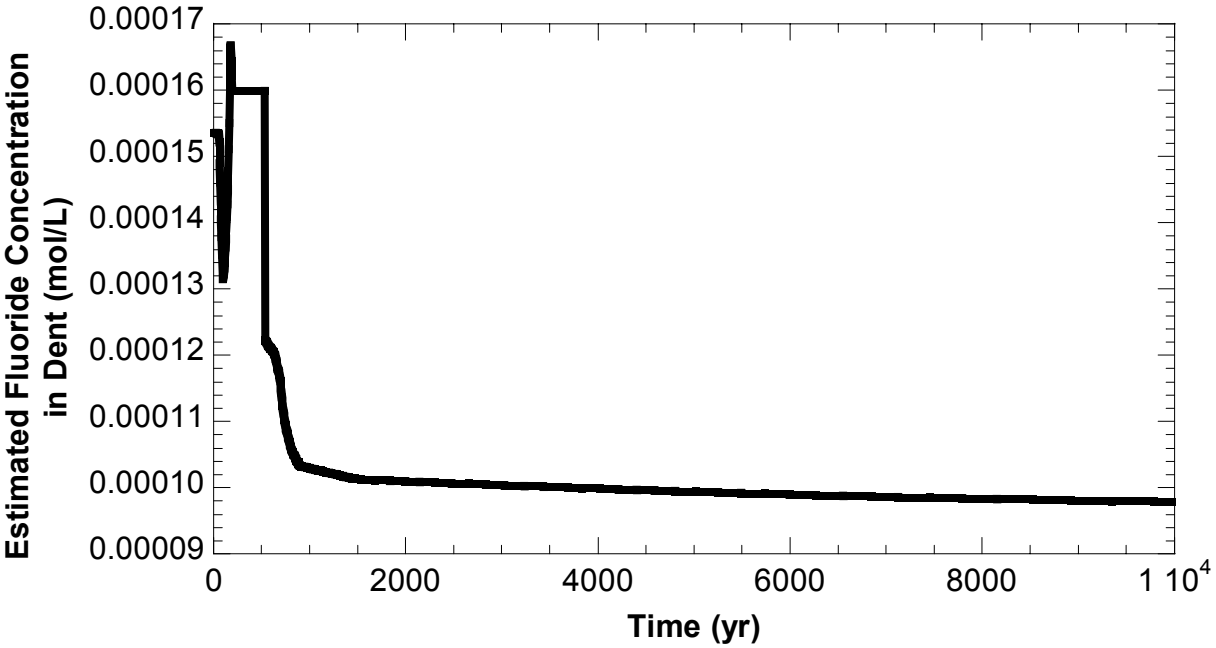

Figure 13-6. Estimated Fluoride Concentration in a Drip Shield Dent in 10,000 Years

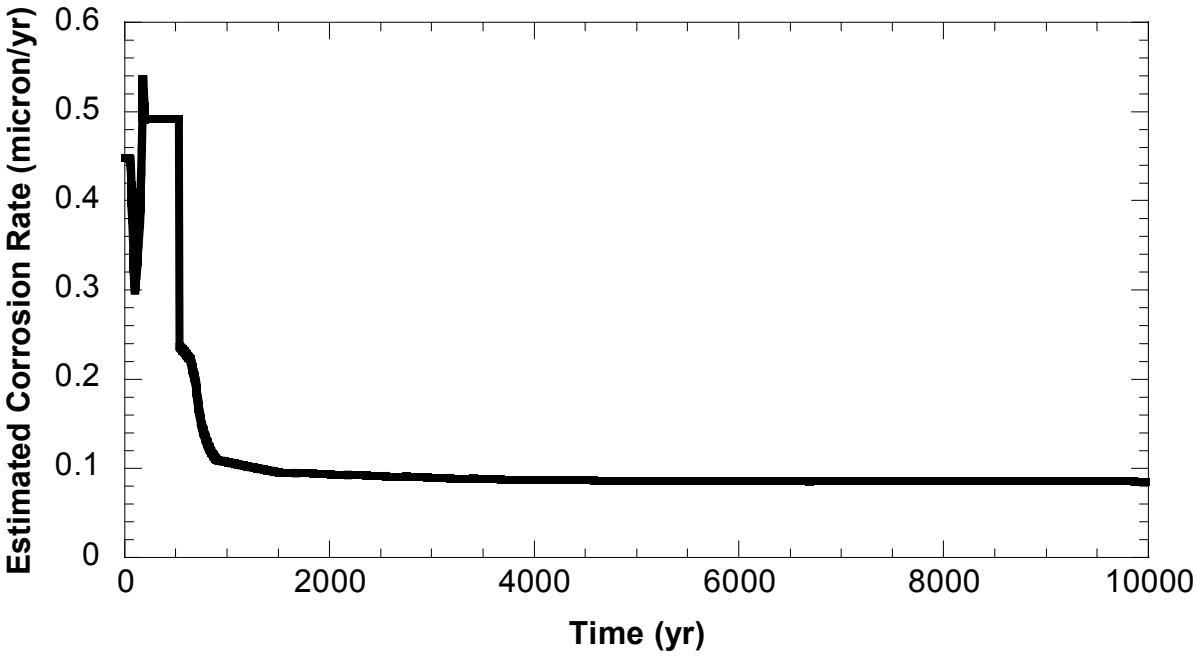

Figure 13-7. Estimated Drip Shield Corrosion Rate from Fluoride in 10,000 Years

Table 13-1. Input Ranges for Monte Carlo Runs with All Distributions Uniform			
Parameter	**Definition**	**Minimum**	**Maximum**
C_{in}	Input concentration of dripping water into dent [mol/L]	0.0	0.001
r_0	Radius of right circular cone-shaped dent at surface of drip shield [m]	0.01	0.2
h	Depth of right circular dent at middle [m]	0.002	0.2
A_{ds}	Effective area of drip shield over which evaporation from Figure 13-2 would be spread [m^2]	10.0	30.0
F_{drip}	Fraction of water entering drift that falls into the dent [unitless]	0.005	0.5

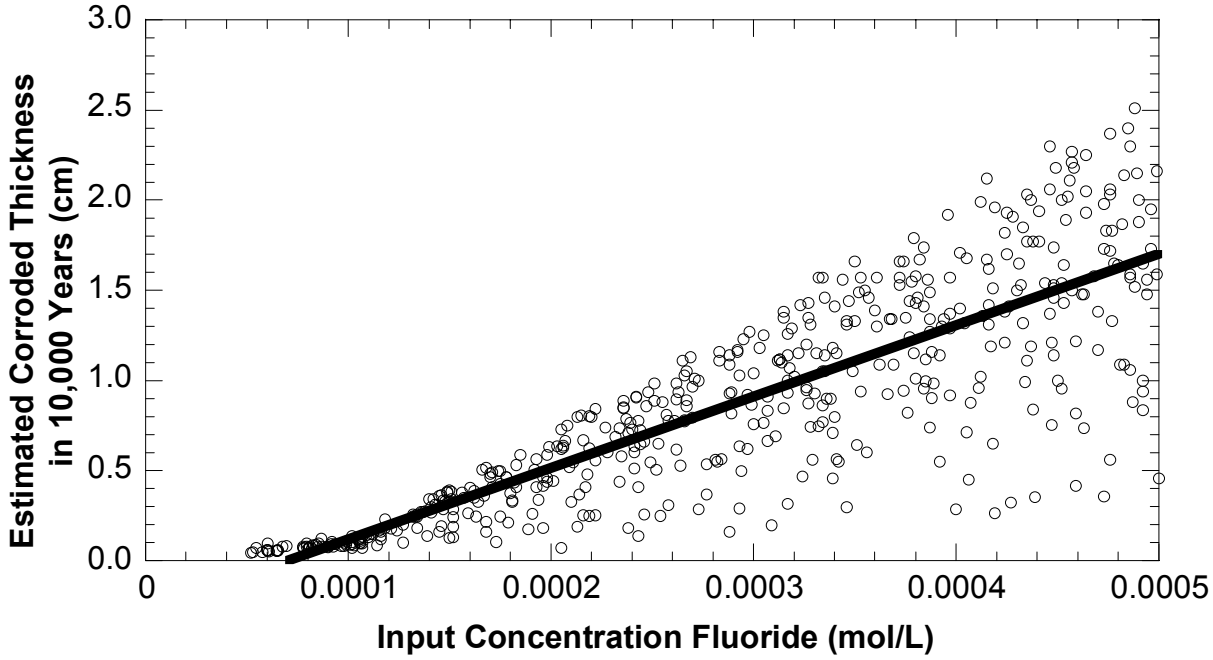

Figure 13-8. Estimated Corroded Thickness of the Drip Shield in 10,000 Years As a Function of Input Concentration of Fluoride with No Reconcentration of Infiltrating Water. Linear Regression Is Shown. Input Concentrations of Fluoride Are Not Expected to Exceed Approximately 0.0001 mol/L.

0.28). Therefore, the greatest corrosion may take place for small dents with large fractions of water dripping into the dents and large input concentrations.

13.4.3 Example 3—Higher Evaporation and Reflux Plus Infiltration

Figure 13-9 shows estimates for a more severe case, in which the infiltration and evaporation rates are increased by a factor of two more than the values shown in Figures 13-2 and 13-3. This increase leads to a slightly increased estimate of total corrosion for 10,000 years. Also shown in this figure is the linear regression of 10,000-year corrosion versus time. The corroded thickness for 10,000 years is well below 1.5 cm [0.6 in] for the likely input concentration of less than 0.0001 mol/L of fluoride.

13.4.4 Example 4—Maximum Fluoride Concentration Allowed to Reach 0.18 mol/L

Figure 13-10 shows the case where infiltrating water evaporates and attains higher fluoride concentrations up to a limit of 0.18 mol/L. Estimates of titanium corroded in 10,000 years are considerably higher than for Examples 2 and 3, but still well below the total drip shield thicknesses for likely concentrations of infiltrating water less than 0.0001 mol/L.

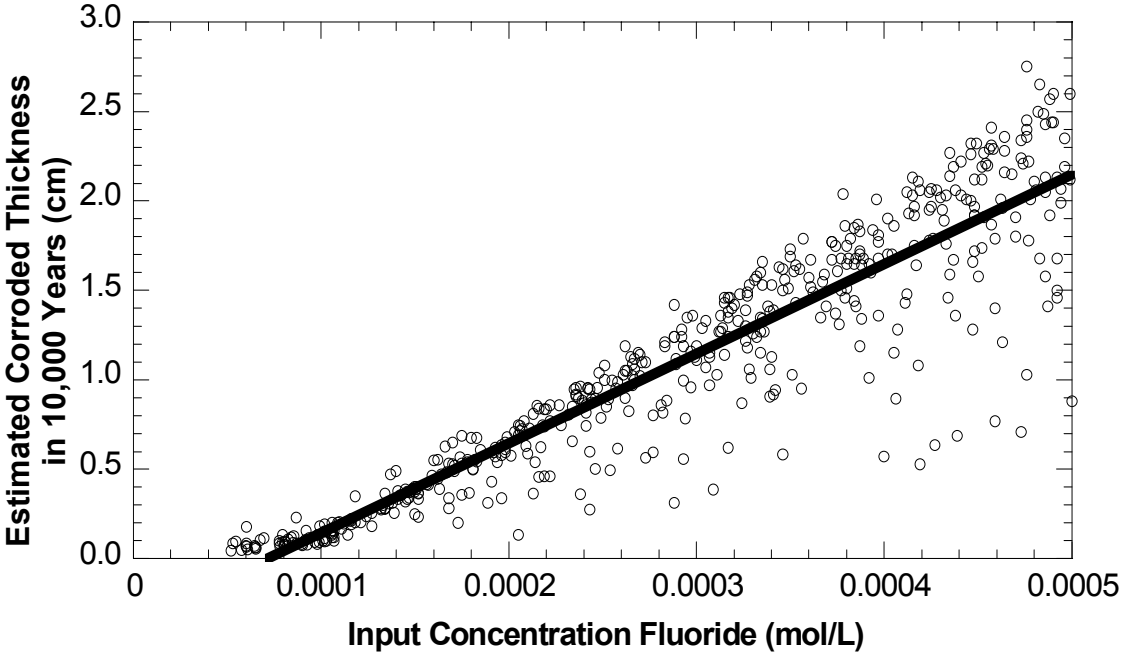

Figure 13-9. Estimated Corroded Thickness of the Drip Shield in 10,000 Years As a Function of Input Concentrations of Fluoride with High Evaporation and Reflux. Linear Regression Is Shown. Input Concentrations of Fluoride Are Not Expected to Exceed Approximately 0.0001 mol/L.

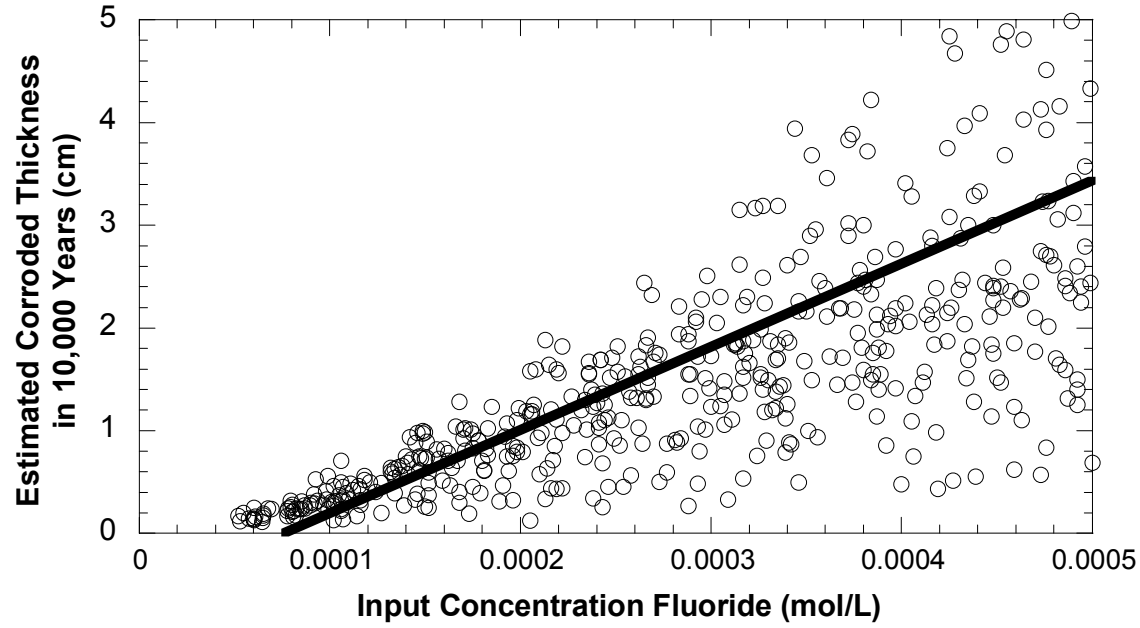

Figure 13-10. Estimated Drip Shield Corrosion Thickness in 10,000 Years for an Upper Internal Fluoride Concentration Limit of 0.18 Molar. Linear Regression Is Shown. Input Concentrations of Fluoride Are Not Expected to Exceed Approximately 0.0001 mol/L.

13.5 Conclusions

Using an alternative model, this analysis estimates the total corroded thickness of the drip shield in 10,000 years. The alternative model takes into account dripping water collecting in dents on the crown of the drip shield, the evaporation of water from the dent, the overflow of water from the dent, and the reaction rate between fluoride and titanium.

Failure of the drip shield by fluoride corrosion alone during 10,000 years is considered unlikely for the following reasons:

- For likely concentrations of fluoride in input water below 0.0001 mol/L, it is estimated there would be no failure by fluoride corrosion alone. Except during the relatively short period when evaporation is estimated to be much higher than the infiltration and reflux rates, the reaction rate between fluoride and titanium may be dominated by fluoride concentration in the infiltrating water. The 10,000-year corrosion thickness is likely only mildly sensitive to the rates of infiltration and reflux.

- Calculations were performed assuming the most pessimistic ligand number, $N = 1$; that is, 1 mole of fluoride corrodes 1 mole of titanium. Considering that aqueous fluoride and titanium complexes may form with N ranging from 1 to 6, it is possible the stoichiometric ratio is higher than 1/1, and each mole of titanium may consume more than 1 mole of fluoride.

- Water infiltrating the drifts is likely to be dilute during most of the 10,000 years. Although reconcentration of fluoride in infiltrating water is possible, concentration may be limited eventually by precipitation of minerals like fluorite. It is likely that much of the water and dissolved minerals driven away by the thermal pulse may be lost by the process of shedding condensed water around the drifts. Therefore, the thermal pulse may represent a net loss of fluoride from the system that may otherwise contact the drip shield.

- For the unlikely case of reconcentration of fluoride to high levels, the flow rate of the dripping water may be diminished greatly. The dripping water stream may have to coincide with the location of a dent on the waste package crest or may be lost by runoff from the curved surface. These considerations may further reduce the likelihood of corrosion through the drip shield.

The denting scenario may be a more realistic circumstance for the collection of water onto the drip shield surface and may be given more credence compared to the dripping scenario without denting considered in Lin, et al. (2003). Results from the alternative model presented in this chapter suggest drip shield failure by fluoride corrosion is unlikely in 10,000 years.

14 CONCLUSIONS

This progress report describes a series of analyses conducted to enhance risk insights about the performance of the potential repository at Yucca Mountain. These analyses by the NRC staff and their technical support contractor, CNWRA, improve understanding of the potential repository system at Yucca Mountain and help refine the risk insights. The analyses can be used by the staff in risk-informing activities during prelicensing interactions with stakeholders and in reviewing any DOE license application. Each task corresponds to at least one of the risk insights in NRC (2004).

A task by task summary of the key results is presented next. Chapter numbers and titles are shown for easy reference.

- An alternative model, which uses drip shield design from CRWMS M&O (2000a)[1], was developed and incorporated into the latest version of the TPA code to account for the effect of drift degradation, via impingement of the drip shield onto the waste package, on waste package failure. Analysis suggests that when localized corrosion is eliminated, waste package mechanical failures from impingement of the drip shield (CRWMS M&O, 2000a) onto the waste package may dominate. There are an average of 363 waste package mechanical failures from impingement of the drip shield (CRWMS M&O, 2000a) onto the waste package and a factor of nearly seven increase in the estimated peak mean dose compared with the basecase results (Chapter 2, Rockfall Damage to Waste Package).

- The TPA code model for near-field chemistry and waste package corrosion that accounts for seepage and evaporation conditions in the drift was refined. Without seepage into the drift, localized corrosion may not occur. With seepage and evaporation, brines may develop (referred to as Environment II) and localized corrosion may occur on the waste packages if the drip shield is not present. For example, using the DOE estimates of solution concentrations at 100 °C [212 °F] and chemistry bin frequencies and ignoring drip shield protection, it was estimated that 0.1 percent of the waste packages for Environment II may be affected by localized corrosion on mill-annealed areas and 19 percent on welded areas. All waste packages may not experience Environment II, and Environment II may occur at different times depending on the repository location. For seepage without significant evaporation, seepage waters likely pose no added risk to waste package performance. The refined model was implemented in the latest version of the TPA code (Chapter 3, Waste Package Corrosion and Near-Field Chemistry).

- The effects of ash redistribution and wind-field direction assumptions on dose estimates were evaluated using the current TPA code model and parameters. The current approach fixes the wind direction to the south in the direct release calculations and appears reasonable to account for the effects of remobilization. The increased probability-weighted dose associated with more persistent mass loads is estimated to be approximately one order of magnitude above the current basecase. A more variable treatment of the wind field during the eruption is likely to reduce the estimated peak

[1]We understand that the DOE is modifying the drip shield design to a more robust design. However, the new design was not available for these anlayses.

probability-weighted dose by allowing the possibility of both a more dispersed tephra blanket and a reduced chance that tephra is directly deposited at the location of the reasonably maximally exposed individual. Although the likely conservatism of the current approach cannot be precisely quantified, it provides a significant degree of compensation for any effect of a more persistent mass load arising from remobilization (Chapter 4, Ash Redistribution and Wind-Field Variability).

- To refine the bases for volcanic ash inhalation exposure-related parameters, an alternative approach was developed to estimate composite mass loading parameters. The approach incorporated varying levels of surface disturbance and accounted for the transience in measured peak mass loads. Adjusting the duration of transient peak mass loading for a wide range of values changed estimated mass loadings by a factor of approximately two. Using inhaled mass based on the medium mass loads, the estimated dose decreased by a factor of two. Results from this analysis were considered in developing the alternative ash remobilization model and mass loading parameters in Chapter 6 (Chapter 5, Resuspension of Volcanic Ash).

- To support the analyses described in Chapter 4, an alternative ash remobilization model and associated data and input parameters were developed and implemented in the latest version of the TPA code. This alternative model calculates the initial deposit at the receptor location by accounting for variations in wind speed and wind direction along the height of the tephra column. Subsequent fluvial and eolian remobilization of ash are accounted for in this alternative model to determine a time history of airborne concentrations at the receptor location. Results for ash remobilization from detailed analytical work with the TEPHRA code provided data for a lookup table and the TPA code input parameters (Chapter 6, Ash Remobilization Modeling for Extrusive Volcanism).

- Assumptions and model results related to the saturated zone alluvium length and radionuclide sorption coefficients were investigated with an alternative surface complexation model by modifying implementation of the TPA code data. Analysis suggests that neptunium retardation factor values decreased the estimated peak Np-237 dose in 10,000 years by nearly a factor of two. Investigations of chemistry ranges for pH and partial pressure of CO_2 suggest a decrease in the Np-237 dose in 10,000 years by nearly one order of magnitude. The modified implementation of the TPA code data was incorporated into the latest version of the TPA code (Chapter 7, Credit Attributed to Alluvium).

- Two alternative models for fuel incorporation into ash and vent velocity were analyzed. First, results from an alternative model of fuel incorporation into ash that allows for a range of fuel concentrations for a given ash particle diameter were compared with the results from a fuel-incorporation model in the ASHPLUME module of the TPA code, which uses a fixed fuel concentration. Results of estimated peak doses to the receptor suggest that the differences between the two models are not large; therefore, the analysis supports assumptions associated with the current TPA code. Second, using an alternative model that calculates the effects of volatile components of the magma on the density (and, therefore, the initial velocity) in the vent yields a small difference in the estimated dose when compared with the current model, in which volatile components are ignored. Based on these results, neither alternative model has a large effect on dose estimates, and, in

both cases, the current TPA code model is likely conservative (Chapter 8, Fuel Incorporation and Initial Plume Velocity).

- The effects of spent nuclear fuel burnup on inventory and dose estimates were evaluated. Results from the ORIGEN calculations suggest that a change in the fuel burnup leads to differences in the radionuclide inventory used in the TPA code. Dose estimates for the nominal scenario (i.e., no extrusive volcanism) increase by a factor of nearly two for an inventory based on a burnup of 100 percent 65 GWd/MTU when compared with the basecase inventory, which has a weighted-average burnup of 38.5 GWd/MTU (Chapter 9, High Burnup Spent Nuclear Fuel).

- The effect of rockfall rubble on the entrainment of spent nuclear fuel in magma flowing in a drift was estimated using an alternative model that accounts for the dog-leg flow of magma to compute the number of entrained waste packages. For volcanic eruption, natural backfill has no effect on the estimated risk computed using the current basecase vertical conduit source term model in the TPA code. Natural backfill has no effect on the peak eruptive risk (occurs approximately at 250 years) estimated using the alternative model. At times greater than 750 years, however, accounting for natural backfill with the alternative model reduces the estimated eruptive risk by more than a factor of 10, compared with estimates of the eruptive risk for the alternative model if natural backfill is excluded (Chapter 10, Natural Backfill and Igneous Consequences).

- An alternative thermal model was developed and implemented in the latest version of the TPA code to account for heat transfer through the natural backfill material resulting from drift degradation. Depending on the natural backfill material characteristics, convection through the backfill around the drip shield may play a significant role in determining the waste package surface temperature. When convection plays a role in addition to conduction, the estimated waste package temperature can be considerably lower than the previously reported peak waste package temperature of 351 °C [664 °F], which is twice the estimated peak temperature of the no-backfill case. In either case, the estimated dose does not appear to be substantially affected (Chapter 11, Near-Field Temperature and Natural Backfill).

- Integration of the thermal, hydrological, and chemical model abstractions was investigated in the near-field conceptual model of the TPA code. Analysis suggests better integration of these models may reduce both the number of waste packages impacted by localized corrosion and radionuclide release rates. The refined model presented in Chapter 3 for waste package corrosion and chemistry of water contacting the waste package addresses integration of the near-field environments. This investigation supports the analysis described in Chapter 3 (Chapter 12, Near-Field Thermal, Hydrological, and Chemical Integration).

- The effects of fluoride in dripping water on drip shield corrosion were modeled using an alternative model to take into account the balance between the supply and the consumption of fluoride. In the alternative model, the most probable scenario for fluoride-enhanced corrosion was water collecting in dents on the top surface of the drip shield. Failure of the drip shield by fluoride-enhanced corrosion in the 10,000-year period was estimated to be unlikely (Chapter 13, Drip Shield and Fluoride).

15 REFERENCES

ASME. *ASME International Boiler and Pressure Vessel Code*. New York City, New York: ASME. 2001.

Barsukova, M.L., V.A. Juzenetsov, V.A. Dorofeyeva, and L.I. Khodakovskii. "Measurements of the Solubility of Rutile TiO_2 in Fluoride Solutions at Elevated Temperatures." *Geochem. Internat.* Vol. 7. pp. 41–49. 1980.

Bechtel SAIC Company, LLC. "Technical Basis Document No. 5: In-Drift Chemical Environment." Rev. 1. Las Vegas, Nevada: Bechtel SAIC Company, LLC. 2003a.

———. "Technical Basis Document No. 13: Volcanic Events." Rev. 2. Las Vegas, Nevada: Bechtel SAIC Company, LLC. 2003b.

———. "Characterize Eruptive Processes at Yucca Mountain, Nevada." ANL–MGR–GS–00002. Rev. 1. Las Vegas, Nevada: Bechtel SAIC Company, LLC. 2003c.

———. "Technical Basis Document No. 11: Saturated Zone Flow and Transport." Rev. 2. Las Vegas, Nevada: Bechtel SAIC Company, LLC. 2003d.

———. "Mechanical Drift Degradation Analysis." Presented to the Advisory Committee on Nuclear Waste, November 19, 2003. Las Vegas, Nevada: Bechtel SAIC Company, LLC. 2003e.

———. "Dike/Drift Interactions." MDL–MGR–GS–000005. Rev. 00. Las Vegas, Nevada: Bechtel SAIC Company, LLC. 2003f.

———. "Risk Information to Support Prioritization of Performance Assessment Models." TDR–WIS–PA–000009. Rev. 01. Las Vegas, Nevada: Bechtel SAIC Company, LLC. 2002.

———. "FY01 Supplemental Science and Performance Analyses, Volume 1: Scientific Bases and Analyses." TDR–MGR–MD–000007. Rev. 00. Las Vegas, Nevada: Bechtel SAIC Company, LLC. 2001.

Bejan, A. "Convection Heat Transfer." New York, New York: John Wiley and Sons. 1984.

Bowman, S.M. and L.C. Leal. NUREG/CR–0200, ORNL/NUREG/CSD–2/V1/R6, "ORIGEN-ARP: Automatic Rapid Process for Spent Fuel Depletion, Decay, and Source Term Analysis." Oak Ridge, Tennessee: Oak Ridge National Laboratory. March 2000.

Brossia, C.S., L. Browning, D.S. Dunn, O.C. Moghissi, O. Pensado, and L. Yang. "Effect of Environment on the Corrosion of Waste Package and Drip Shield Materials." CNWRA 2001–03. San Antonio Texas: CNWRA. 2001.

Browning, L.B., R. Fedors, L. Yang, O. Pensado, R. Pabalan, C. Manepally, and B. Leslie. "Estimated Effects of Temperature—Relative Humidity Variations on the Composition of In-Drift Water in the Potential Nuclear Waste Repository at Yucca Mountain, Nevada." Abstracts of the Scientific Basis for Nuclear Waste Management XXVIII, San Francisco, California, April 13–16, 2004. Paper CC7.11.1. J.M. Hanchar, S. Stroes-Gascoyne, and L. Browning, eds. Warrendale, Pennsylvania: Materials Research Society. 2004.

Burmeister, L.C. "Convective Heat Transfer, Second Edition." New York, New York: John Wiley and Sons. 1993.

Caltagirone, J.P. "Thermo-Convective Instabilities in a Porous Medium Bounded by Two Concentric Horizontal Cylinders." *Journal of Fluid Mechanics*. Vol. 76. pp. 337–362. 1976.

Codell, R.B., N. Eisenberg, D. Fehringer, W. Ford, T. Margulies, T. McCartin, J. Park, and J. Randall. NUREG–1327, "Initial Demonstration of the NRC's Capability to Conduct a Performance Assessment for a High-Level Waste Repository." Washington, DC: NRC. May 1992.

CRWMS M&O. "Multiscale Thermohydrologic Model." ANL–EBS–MD–00001. Rev. 00 ICN 02. Las Vegas, Nevada: CRWMS M&O. 2001.

———. "Design Analysis for the Ex-Container Components." ANL–XCS–ME–000001. Rev 00. Las Vegas, Nevada: CRWMS M&O. 2000a.

———. "Total System Performance Assessment (TSPA) for the Site Recommendation." TDR–WIS–PA–000001. Rev. 00 ICN 01. Las Vegas, Nevada: CRWMS M&O. 2000b.

———. "Total System Performance Assessment Model for Site Recommendation." MDL–WIS–PA–000002. Rev. 00. Las Vegas, Nevada: CRWMS M&O. 2000c.

DOE. TDR–MGR–RL–00000, "Preclosure Safety Analysis Guide." Rev. 00. Las Vegas, Nevada: Yucca Mountain Site Characterization Office. 2002.

———. ANL–WIS–MD–000006, "Inventory Abstraction." Rev. 00 ICN 02. Washington, DC: Office of Civilian Radioactive Waste Management. 2001a.

———. DOE/RW–0540, "Yucca Mountain Preliminary Site Suitability Evaluation." Las Vegas, Nevada: DOE, Office of Civilian Radioactive Waste Management. 2001b.

———. "Abstraction of NFE Drift Thermodynamic Environment and Percolation Flux." ANL–EBS–HS–000003. Rev. 00 ICN 01. Las Vegas, Nevada: DOE. 2000.

Dunn, D.S., L. Yang, C. Wu, and G.A. Cragnolino. "Effect of Inhibiting Oxyanions on the Localized Corrosion Susceptibility of Waste Package Container Materials." Symposium CC: Scientific Basis for Nuclear Waste Management XXVIII Spring Meeting, San Francisco, California, April 12–16, 2004. J.M. Hanchar, S. Stroes-Gascoyne, and L. Browning, eds. Vol. 824, Abstract CC1.7. Warrandale, Pennsylvania: Materials Research Society. pp. 33–38. 2004.

Fedors, R.W., G.R. Adams, C. Manepally, and S.T. Green. "Thermal Conductivity, Edge Cooling, and Drift Degradation—Abstracted Model Sensitivity Analyses for Yucca Mountain." CNWRA Report. San Antonio, Texas: CNWRA. 2003.

Gute, G.D., G. Ofoegbu, F. Thomassy, S. Hsiung, G. Adams, A. Ghosh, B. Dasgupta, A.H. Chowdhury, and S. Mohanty. "MECHFAIL: A Total-system Performance Assessment Code Module for Evaluating Engineered Barrier Performance under Mechanical Loading Conditions." CNWRA 2003–06. San Antonio, Texas: CNWRA. 2003.

Harrar, J.E., H.F. Carley, W.F. Isherwood, and E. Raber. "Report of the Committee to Review the Use of J–13 Well Water in Nevada Nuclear Waste Storage Investigations." UCID–21867. Livermore, California: Lawrence Livermore National Laboratory. 1990.

Hill, B.E. and C.B. Connor. "Technical Basis for Resolution of the Igneous Activity Key Technical Issue." San Antonio, Texas: CNWRA. 2000.

Hill, B., C. Connor, M. Jarzemba, P. La Femina, M. Navarro, and W. Strauch, "1995 Eruptions of Cerro Negro Volcano, Nicaragua, and Risk Assessment for Future Eruptions." *Geological Society of America Bulletin*, October 1998. Vol. 110, No. 10. pp. 1,231–1,241. 1998.

Hooper, D. "First-Order Conceptual Model for Fluvial Remobilization of Tephra Along Fortymile Wash, Yucca Mountain, Nevada." San Antonio, Texas: CNWRA. 2004.

Incropera, F.P. and D.P. DeWitt. "Fundamentals of Heat and Mass Transfer." 3rd Edition. New York, New York: John Wiley and Sons. 1995.

Jain, V., G. Cragnolino, and L. Howard. "A Review Report on High Burnup Spent Nuclear Fuel—Disposal Issues." In NRC Review. San Antonio, Texas: CNWRA. 2004.

Jarzemba, M.S. "Stochastic Radionuclide Distributions after a Basaltic Eruption for Performance Assessment at Yucca Mountain." *Nuclear Technology.* 1997.

Kennedy, W.E. and D.L. Strenge. NUREG/CR–5512. "Residual Radioactive Contamination From Decommissioning: Technical Basis for Translating Contamination Levels to Annual Total Effective Dose Equivalent." Vol. 1. Washington, DC: NRC. October 1992.

Knauss, K.G., R.E. Martinelli, W.L. Bourcier, and H.F. Shaw. "Ti(IV) Hydroxyfluoride Aqueous Complexes: Equilibrium Constants Derived from Rutile Solubility Measurements Made from 100 to 300 °C." Livermore, California: Lawrence Livermore National Laboratory. 2000. (Draft)

Krumbein, W.C. "Application of Logarithmic Moments to Size Frequency Distribution of Sediments." *Journal of Sedimentary Petrology.* Vol. 6, No. 1. pp. 35–47. 1936.

Krumbein W.C. and G.D. Monk. "Permeability as a Function of the Size Parameters of Unconsolidated Sand." *Petroleum Technology*. Vol. 5, No. 4. pp. 1–11. 1942.

Kuntz, R., "Fluoride-Induced Corrosion of Drip Shield Dent and Localized Corrosion of Waste Package." *Presentation to Yucca Mountain Team Meeting, October 2003.*

Lake, L.W. "Enhanced Oil Recovery." Englewood Cliffs, New Jersey: Prentice Hall. 1989.

Lapwood, E.R. "Convection of a Fluid in a Porous Medium." *Proc. Camb. Phil. Soc*. Vol. 44. pp. 508–521. 1948.

Lin, C., B. Leslie, R. Codell, H. Arlt, and T. Ahn. "Potential Importance of Fluoride to Performance of the Drip Shield." Proceedings of the 10th International High Level Radioactive Waste Management Conference, Las Vegas, Nevada. March 30–April 2, 2003. Published on CD-ROM. LaGrange Park, Illinois: American Nuclear Society. 2003.

Manepally, C., R. Fedors, G. Adams, S. Green, and D. Gute. "Effects of Drift Degradation on Environmental Conditions in Drifts." *Presentation at the 2003 American Geophysical Union Fall Meeting, December 8-12, 2003. San Francisco, California*. 2003.

Manteufel, R.D. "Effects of Ventilation and Backfill on Mined Waste Disposal Facility." *Nuclear Engineering and Design*. Vol. 172. pp. 205–219. 1997.

Mohanty, S. "A Plan for Risk Analysis by the TSPAI KTI." San Antonio, Texas: CNWRA. 2003.

Mohanty, S., G. Adams, and M. Menchaca. "An Abstracted Model for Estimating Temperature and Relative Humidity in the Potential Repository at Yucca Mountain." Proceedings of the 2004 ASME Heat Transfer/Fluid Engineering Summer Conference, July 11–15, 2004. Charlotte, North Carolina. 2004.

Mohanty, S., T.J. McCartin, and D.W. Esh (coordinators). "Total-system Performance Assessment (TPA) Version 4.0 Code: Module Descriptions and User's Guide." San Antonio, Texas: CNWRA. 2002a.

Mohanty, S., R. Codell, J.M. Menchaca, R. Janetzke, M. Smith, P. LaPlante, M. Rahimi, and A. Lozano. "System-Level Performance Assessment of the Proposed Repository at Yucca Mountain Using the TPA Version 4.1 Code." CNWRA 2002–05. Rev. 1. San Antonio, Texas: CNWRA. 2002b.

Mohanty, S., R. Codell, R.W. Rice, J. Weldy, Y. Lu, R.M. Byrne, T.J. McCartin, M.S. Jarzemba, and G.W. Wittmeyer. "System-Level Repository Sensitivity Analyses Using TPA Version 3.2 Code." CNWRA 99–002. San Antonio, Texas: CNWRA. 1999.

Mohanty, S., G.A. Cragnolino, T. Ahn, D.S. Dunn, P.C. Lichtner, R.D. Manteufel, and N. Sridhar. "Engineered Barrier System Performance Assessment Code: EBSPAC Version 1.1, Technical Description and User's Manual." CNWRA 97–006. San Antonio, Texas: CNWRA. 1997.

NRC. "Risk Insights Baseline Report." ML0405601620. Washington, DC: NRC. April 2004. <www.nrc.gov/waste/hlw-disposal/reg-initiatives/resolve-key-tech-issues.html>

Nuclear Waste Policy Act of 1982. Pub. L. 97–425. 96 Stat. 2201. 1982.

Pabalan, R. and L. Yang. "Thermodynamic Modeling of Brine Chemistry in the In-Drift Environment of a Potential High-Level Nuclear Waste Repository at Yucca Mountain, Nevada." Poster presented at the 32nd International Geological Congress, August 20–28, 2004. Florence, Italy. 2004.

Panda, M.N. and L.W. Lake, "1994 Estimation of Single Phase Permeability from Parameters of Particle-Size Distribution." AAPG Bulletin. American Association of Petroleum Geologists. Vol. 78, No. 7. pp. 1,028–1,039. 1994.

Pensado, O., D.S. Dunn, G.A. Cragnolino, and V. Jain. "Passive Dissolution of Container Materials—Modeling and Experiments." CNWRA 2003–01. San Antonio, Texas: CNWRA. 2002.

Press, W.H., S.A. Teukolsky, W.T. Vettering, and B.P. Flannery. "Numerical Recipes." Second Edition. Cambridge University Press. 1992.

Ramsdell, Jr., J.V., C.E. Beyer, D.D. Lanning, U.P. Jenquin, R.A. Schwarz, D.L. Strenge, P.M. Daling, and R.T. Dahowski. NUREG/CR–6703. "Environmental Effects of Extending Fuel Burnup Above 60 GWd/MTU." Washington, DC: Pacific Northwest National Laboratory. January 2001.

Reardon, E. "K_d's—Can They Be Used to Describe Reversible Ion Sorption Reactions in Contaminant Migration?" *Ground Water.* Vol. 19, No. 3. pp. 279–286. 1981.

Sanders, C.E. and I.C. Gauld. NUREG/CR–6798, ORNL/TM–2001/259. "Isotopic Analysis of High-Burnup PWR Spent Fuel Samples From the Takahama-3 Reactor." Washington, DC: NRC. January 2003.

Searl, A., A. Nicholl, and P.J. Baxter. "Assessment of the Exposure of Islanders to Ash from the Soufriere Hills Volcano, Montserrat, British West Indies." *Occupational and Environmental Medicine*. Vol. 59. pp. 523–531. 2002.

Suzuki, T. "A Theoretical Model for Dispersion of Tephra." *Arc Volcanism: Physics and Tectonics*. D. Shimozuto and I. Yokoyama, Eds. Terra Scientific Publishing Company, pp. 95–113. 1983.

Wescott, R.G., M.P. Lee, N.A. Eisenberg, T.J. McCartin, and R.G. Baca, eds. NUREG–1464, "NRC Iterative Performance Assessment Phase 2." Washington, DC: NRC. October 1995.

Westrich, H. "The Solubility of LWR Core Debris in Sacrificial Floor Material." *J. Nuclear Materials*. Vol. 110. pp. 324–332. 1982.

Woods, A.W. "The Fluid Dynamics and Thermodynamics of Eruption Columns." *Bulletin of Volcanology*. Vol. 50. pp. 169–193. 1988.

Zhu, C. "A Case Against K_d-Based Transport Models: Natural Attenuation at a Mill Tailings Site." *Computers and Geosciences*. Vol. 29. pp. 351–359. 2003.

APPENDIX A

DERIVATION OF THE DRIP SHIELD AND WASTE PACKAGE INTERACTION CONTACT AREA

The following derivation conveys the methodology used to approximate the contact area between the drip shield and waste package in the event the drip shield fails under accumulated rockfall loads. The drip shield could fail by either structural buckling or material creep, subsequently causing the accumulated rockfall loads to be transferred to the waste package by way of the drip shield bulkhead. The intent of this derivation is to approximate the contact area as a function of the contact angle and the estimated allowable penetration depth. If the approximated contact stress (i.e., the applied load divided by the approximated contact area) is greater than 90 percent of the ultimate strength of the Alloy 22 waste package outer container, then the waste package is considered to have been breached.

As a first approximation, the drip shield and waste package contact area is defined as the projection of the actual contact surface area onto the x-z plane (Figures A–1 and A–2). The projected area is used because it has been assumed there are no surface tractions (i.e., no shear stresses created by friction) acting on the drip shield and waste package contact surface interface. In addition, the horizontally oriented component (i.e., x-component) of the pressure acting on the contact surface interface does not contribute to the support of the applied rockfall rubble load, which has been assumed to be vertically oriented (i.e., y-component only).

Referring to Figures A–1 and A–2, the variables used in the derivation are as follows:

a_{max} — projection length [m]

A — projected contact area [m^2]

b_o — maximum allowable penetration depth [m]

b^* — minimum penetration depth [m]

c — offset between the central axis of the waste package and the central axis of the drip shield bulkhead [m]

r_{wp} — waste package radius [m]

r_{ds} — drip shield bulkhead radius [m]

t_{bh} — drip shield bulkhead thickness [m]

w — projected contact width [m]

w_1 — projected contact width in the negative z-direction [m]

w_2 — projected contact width in the positive z-direction [m]

α — drip shield bulkhead and waste package contact angle [radians]

$_{max}\theta_{wp}$ — maximum angle of contact for the waste package [radians]

$_{max}\theta_{ds}$ — maximum angle of contact for the drip shield [radians]

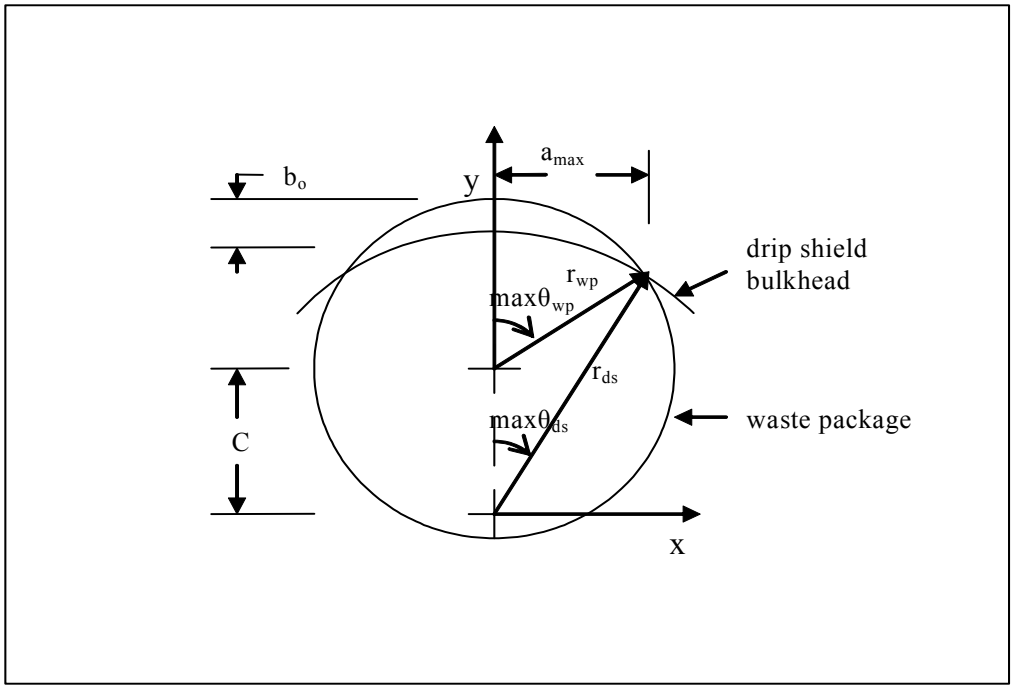

Figure A–1. Drip Shield Bulkhead Contact with the Waste Package Outer Barrier, x-y Plane

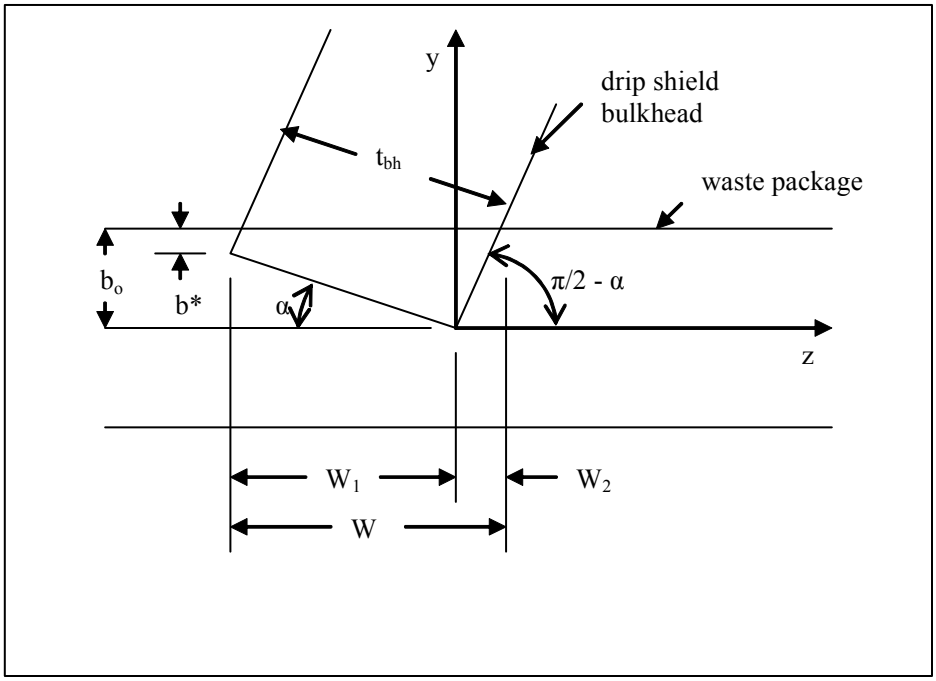

Figure A–2. Drip Shield Bulkhead Contact with the Waste Package Outer Barrier Showing the Bulkhead Penetration into the Barrier, y-z Plane

Before proceeding, it is worthwhile to note that b_o, r_{wp}, r_{ds}, t_{bh}, and α are either sampled or known quantities. As a result, it is desirable to cast the projected contact area, A, in terms of these variables. Also, it needs to be pointed out that r_{ds} varies as a function of θ_{ds} when the contact angle α is not zero. Because the contact angle is not likely to be greater than π/4 radians (i.e., 45°) and the range of potential rockfall rubble loads is relatively large {i.e., 40 to 160 tonnes/m [27 to 108 kip/ft]}, the dependency of r_{ds} on the contact angle and θ_{ds} is not likely to have a significant effect on the final estimate of potential waste package failures caused by interactions with the drip shield. Therefore, r_{ds} is assumed to remain constant. The radius of the drip shield bulkhead, r_{ds}, is important because it defines the radius of curvature of the contact area. Note the Titanium Grade 24 drip shield bulkhead is estimated to define the contact area curvature because it has a much higher yield stress than the Alloy 22 waste package outer container.

Based on the foregoing discussion and referring to Figures A–1 and A–2, the projected drip shield and waste package contact area is obtained in the following manner. First, the projected contact area can be formulated as

$$A = 2\int_0^{a_{max}} w(x)\,dx \tag{A–1}$$

where

$$w(x) = w_1 + w_2 \tag{A–2}$$

$$a_{max} = r_{ds}\,\sin(_{max}\theta_{ds}) \tag{A–3a}$$

or

$$a_{max} = r_{wp}\,\sin(_{max}\theta_{wp}) \tag{A–3b}$$

Because w can more conveniently be cast in terms of θ_{ds}, instead of x, the integral defined in Eq. (A–1) is adjusted accordingly. Specifically, because

$$x = r_{ds}\,\sin(\phi_{ds}) \tag{A–4a}$$

then

$$dx = r_{ds}\cos(\theta_{ds})\,d\theta_{ds} \tag{A–4b}$$

Therefore, Eq. (A–1) can be recast as

$$A = 2\int_0^{_{max}\theta_{ds}} w(\theta)\,r_{ds}\cos(\theta_{ds})\,d\theta_{ds} \tag{A–5}$$

Recognizing that

$$r_{ds}\cos(_{max}\theta_{ds}) = c + r_{wp}(_{max}\theta_{wp}) \tag{A–6a}$$

and

$$c = b_o + r_{ds} - r_{wp} \tag{A–6b}$$

it can be shown that, in conjunction with Eqs. (A–3a) and (A–3b),

$$\max\theta_{ds} = \cos^{-1}\left(1 + \frac{2\,b_o\,r_{wp} - b_o^2}{2\,r_{ds}\,r_{wp} - 2\,b_o\,r_{ds} - 2r_{ds}^2}\right) \tag{A–7}$$

The final task is to develop the projected contact width, *w,* in terms of θ_{ds}. Before proceeding, however, it is important to note that the contact projection width is discontinuous if the contact angle, ϕ, is small enough to allow penetration of the drip shield bulkhead trailing edge (defined by b^* and illustrated in Figure A–2). The contact projection width discontinuity occurs when

$$\alpha < \sin^{-1}\left(\frac{b_o}{t_{bh}}\right) \tag{A–8}$$

For the case where $\alpha \geq \sin^{-1}\left(\frac{b_o}{t_{bh}}\right)$, the projected contact width can be written in terms of the penetration depth, *b*, as follows

$$\begin{aligned} w &= w_1 + w_2 \\ &= \frac{b(\theta_{ds})}{\tan(\alpha)} + \frac{b(\theta_{ds})}{\tan\left(\frac{\pi}{2} - \alpha\right)} \\ &= \frac{2\,b(\theta_{ds})}{\sin(2\alpha)} \end{aligned} \tag{A–9}$$

Referring to Figure A–1, the penetration depth, b, can be written as

$$b = c + r_{wp}\cos(\theta_{wp}) - r_{ds}\cos(\theta_{ds}) \tag{A–10}$$

because

$$\theta_{wp} = \sin^{-1}\left[\frac{r_{ds}}{r_{wp}}\sin(\theta_{ds})\right] \tag{A–11}$$

The penetration depth can now be cast completely in terms of θ_{ds}. Specifically, substituting Eq. (A–10) into Eq. (A–9) and simplifying gives

$$b = b_o - r_{wp} + r_{ds}\left[1 - \cos(\theta_{ds})\right] + \left[r_{wp}^2 - r_{ds}^2 \sin^2(\theta_{ds})\right]^{1/2} \tag{A–12}$$

Now, substituting Eqs. (A–8) and (A–11) into Eq. (A–5) and performing the indicated integration gives an approximate projected contact area of

$$\begin{aligned} A = {} & \frac{4 r_{ds}}{\sin(2\alpha)}\left(b_o - r_{wp} + r_{ds}\right)\sin\left(\max\theta_{ds}\right) \\ & - \frac{4 r_{ds}^2}{\sin(2\alpha)}\left[\frac{1}{2}\sin\left(\max\theta_{ds}\right)\cos\left(\max\theta_{ds}\right) + \frac{\max\theta_{ds}}{2}\right] \\ & + \frac{4 r_{ds}\ r_{wp}}{\sin(2\alpha)}\left\{\frac{\sin\left(\max\theta_{ds}\right)}{2}\left[1 - \frac{r_{ds}^2}{r_{wp}^2}\sin^2\left(\max\theta_{ds}\right)\right]^{1/2} + \frac{1}{2}\frac{r_{wp}}{r_{ds}}\sin^{-1}\left[\frac{r_{ds}}{r_{wp}}\sin\left(\max\theta_{ds}\right)\right]\right\} \end{aligned} \tag{A–13}$$

For the case where $\alpha < \sin^{-1}\left(\frac{b_o}{t_{bh}}\right)$, a similar procedure is employed to approximate the projected contact area with the following notable changes. First, because the functionality of the projected contact width, w, is discontinuous for this scenario, the governing integral equation is recast as

$$A = \int_0^{\max\theta_{ds}} w(\theta)\, r_{ds} \cos\left(\theta_{ds}\right) d\theta_{ds} + 2\int_{\max\theta_{ds}}^{\max\theta_{ds}} w(\theta)\, r_{ds} \cos\left(\theta_{ds}\right) d\theta_{ds} \tag{A–14}$$

Now, using Eq.(A–7) and referring to Figure A–2, the drip shield angle corresponding to the projected contact width discontinuity can be written as

$$\max\theta_{ds}^* = \cos^{-1}\left(1 + \frac{2 b^*\ r_{wp} - \left(b^*\right)^2}{2 r_{ds}\ r_{wp} - 2 b^*\ r_{ds} - 2 r_{ds}^2}\right) \tag{A–15}$$

where

$$b^* = b_o - t_{bh}\sin(\alpha) \tag{A–16}$$

Next, for $0 \le \theta_{ds} \le {}_{max}\theta^{*}_{ds}$ the applicable projected contact width function is

$$
\begin{aligned}
w &= w_1 + w_2 \\
&= t_{bh}\cos(\alpha) + \frac{b_o - r_{wp} + r_{ds}\left[1-\cos(\theta_{ds})\right] + \left[r_{wp}^2 - r_{ds}^2\sin^2(\theta_{ds})\right]^{1/2}}{\tan\left(\frac{\pi}{2}-\alpha\right)} \\
&= t_{bh}\cos(\alpha) + \left\{b_o - r_{wp} + r_{ds}\left[1-\cos(\theta_{ds})\right] + \left[r_{wp}^2 - r_{ds}^2\sin^2(\theta_{ds})\right]^{1/2}\right\}\tan(\alpha)
\end{aligned}
\tag{A–17}
$$

The projected contact width function for ${}_{max}\theta^{*}_{ds} \le \theta_{ds} \le {}_{max}\theta_{ds}$ is the same as that used earlier [Eqs. (A–8) and (A–11)]. Substituting the applicable functions into Eq. (A–13) and performing the required integration gives the projected contact area between the drip shield and waste package for small contact angles $\left[\text{i.e., } \alpha < \sin^{-1}(b_o / t_{bh})\right]$ as

$$
\begin{aligned}
A = {} & 2t_{bh}\cos(\alpha)\sin\left({}_{max}\theta^{*}_{ds}\right) \\
& + 2\left(b_o - r_{wp} + r_{ds}\right)\tan(\alpha)\sin\left({}_{max}\theta^{*}_{ds}\right) \\
& - 2r_{ds}\tan(\alpha)\left[\frac{1}{2}\sin\left({}_{max}\theta^{*}_{ds}\right)\cos\left({}_{max}\theta^{*}_{ds}\right) + \frac{{}_{max}\theta^{*}_{ds}}{2}\right] \\
& + 2r_{wp}\tan(\alpha)\left\{\frac{\sin\left({}_{max}\theta^{*}_{ds}\right)}{2}\left[1-\frac{r_{ds}^2}{r_{wp}^2}\sin^2\left({}_{max}\theta^{*}_{ds}\right)\right]^{1/2} + \frac{1}{2}\frac{r_{wp}}{r_{ds}}\sin^{-1}\left[\frac{r_{ds}}{r_{wp}}\sin\left({}_{max}\theta^{*}_{ds}\right)\right]\right\} \\
& + \frac{4r_{ds}}{\sin(2\alpha)}\left(b_o - r_{wp} + r_{ds}\right)\left[\sin\left({}_{max}\theta_{ds}\right) - \sin\left({}_{max}\theta^{*}_{ds}\right)\right] \\
& - \frac{4r_{ds}^2}{\sin(2\alpha)}\left[\frac{1}{2}\sin\left({}_{max}\theta_{ds}\right)\cos\left({}_{max}\theta_{ds}\right) + \frac{{}_{max}\theta_{ds}}{2} - \frac{1}{2}\sin\left({}_{max}\theta^{*}_{ds}\right)\cos\left({}_{max}\theta^{*}_{ds}\right) - \frac{{}_{max}\theta^{*}_{ds}}{2}\right] \\
& + \frac{4r_{ds}\,r_{wp}}{\sin(2\alpha)}\left\{\frac{\sin\left({}_{max}\theta_{ds}\right)}{2}\left[1-\frac{r_{ds}^2}{r_{wp}^2}\sin^2\left({}_{max}\theta_{ds}\right)\right]^{1/2} + \frac{1}{2}\frac{r_{wp}}{r_{ds}}\sin^{-1}\left[\frac{r_{ds}}{r_{wp}}\sin\left({}_{max}\theta_{ds}\right)\right]\right\} \\
& - \frac{4r_{ds}\,r_{wp}}{\sin(2\alpha)}\left\{\frac{\sin\left({}_{max}\theta^{*}_{ds}\right)}{2}\left[1-\frac{r_{ds}^2}{r_{wp}^2}\sin^2\left({}_{max}\theta^{*}_{ds}\right)\right]^{1/2} + \frac{1}{2}\frac{r_{wp}}{r_{ds}}\sin^{-1}\left[\frac{r_{ds}}{r_{wp}}\sin\left({}_{max}\theta^{*}_{ds}\right)\right]\right\}
\end{aligned}
\tag{A–18}
$$